PROTEIN STRUCTURAL CHANGES AND TYROSYL RADICAL-MEDIATED ELECTRON TRANSFER REACTIONS IN RIBONUCLEOTIDE REDUCTASE AND MODEL COMPOUNDS

A Thesis
Presented to
The Academic Faculty

by

Adam R. Offenbacher

In Partial Fulfillment
of the Requirements for the Degree
Doctor of Philosophy in the
School of Chemistry and Biochemistry

Georgia Institute of Technology

May 2011

PROTEIN STRUCTURAL CHANGES AND TYROSYL RADICAL-MEDIATED ELECTRON TRANSFER REACTIONS IN RIBONUCLEOTIDE REDUCTASE AND MODEL COMPOUNDS

Approved by:

Dr. Bridgette A. Barry, Advisor
School of Chemistry and Biochemistry
Georgia Institute of Technology

Dr. Jim C. Spain
School of Civil and Environmental Engineering
Georgia Institute of Technology

Dr. Nils Kröger
School of Chemistry and Biochemistry
Georgia Institute of Technology

Dr. Paul H. Wine
School of Chemistry and Biochemistry
School of Earth and Atmospheric Sciences
Georgia Institute of Technology

Dr. Jake D. Soper
School of Chemistry and Biochemistry
Georgia Institute of Technology

Date Approved: December 7, 2010

To My Mom and Dad

ACKNOWLEDGMENTS

First and foremost, I would like to thank my advisor, Prof. Bridgette A. Barry, for her persistent guidance and support throughout my graduate school experience. Prof. Barry has taught me to be patient and has greatly improved my scientific methodology. Her passion for science is truly an inspiration. I only hope that our professional relationship grows stronger during the years to come. I wish to thank Prof. JoAnne Stubbe from Massachusetts Institute of Technology and Prof. Ólöf Einardóttir from University of California, Santa Cruz for the wonderful collaborations. I offer thanks to Profs. Christine Payne and Wendy Kelly for their selfless assistance. In addition, I would like to thank the past and current members of the Barry group: Dr. Ilya Vassiliev, Dr. Antonio de Riso, Dr. Jun Chen, Dr. Sascha Rexroth, Dr. Ian Cooper, Dr. Shana Bender, Dr. David Jenson, Dr. Robin Sibert, Dr. Cynthia Pagba, Ms. Tina Dreaden, Mr. Jamie Keough, and Mr. Brandon Polander for the interesting and educational discussions. Specifically, I send my gratitude to David for the thoughtful lunch and conversations, which persuaded me to choose Georgia Tech for graduate school. I wish to thank the professors and staff during my undergraduate studies at Ohio Northern University, especially Dr. Ron Peterson, Dr. Jeff Gray and Dr. David Kurtz for revealing my potential as a scientist. In addition, Mrs. Daws was a wonderful laboratory manager and friend. I wish to thank my GT friends, particularly Mr. Cameron Lippert, Mr. Chip Humphries, Dr. Scott Brombosz, Mr. Erik Dreaden, Mr. Michael Rood, Mr. Steve Arnstein, and Ms. Natalie Doss for all of the good times and the occasional “entertaining” discussions.

There are many family members I would like to thank. I, first, would like to thank my uncle, Jake, because I would not have made it here without the help. I thank my aunt, Donna, for her continual interest and curiosity in my studies. I thank my grandmother, Martha, for being a fun and loving person. I thank my grandmother, Mary, for her love and endless supply of delicious cookies, which got me through all of the late nights in lab and the rough patches. Her work ethic is surpassed by none. I acknowledge my grandfather Richard, whom I have always admired and loved, but who never had a chance to see me achieving my dreams. I will always be your little “skeeter”. To my brother, Nathan, and sister, Jennifer, you have already made me a very proud big brother. Yet, you have not even begun to reach the pinnacle of your success. For my wife, Gaëlle: je t’aime, mon amour! Tu es étonnante de toutes les manières possibles. Je veux passer le reste de ma vie avec toi. Most of all, I could not have even dreamed of attempting such endeavors without help from my parents. Thank you, mom and dad. I could not have accomplished a tenth without your support, love, and dedication. I love you all very much.

Throughout my life, I have had numerous people that have supported and inspired me. I can not imagine where I might be today without them. To those individuals whom I have not given due credit, I am eternally grateful.

TABLE OF CONTENTS

LIST OF TABLES

LIST OF FIGURES

Chapter 3

Chapter 4

Chapter 5

Chapter 6

Chapter 7

LIST OF ABBREVIATIONS

4-MP	4-Methoxyphenol
Δ9D	Stearoyl acyl carrier protein Δ^9 desaturase
AMP	Ampicillin
ATP	Adenosine triphosphate
BSA	Bovine serum albumin
C*c*O	Cytochrome *c* oxidase
CPET	Concerted proton electron transfer
CV	Cyclic voltammetry
dADP	Deoxyadenosine diphosphate
dATP	Deoxyadenosine triphosphate
dCTP	Deoxycytidine triphosphate
DEAE	Diethylaminoethyl cellulose
DFT	Density functional theory
dGDP	Deoxyguanosine diphosphate
dGTP	Deoxyguanosine triphosphate
DoM	Directed ortho-metalation
DOPA	3-,4-Dihydroxyphenylalanine
dNDP	Deoxyribonucleoside diphosphates
dTTP	Deoxythymidine triphosphate
E. coli	*Escherichia coli*
ENDOR	Electron nuclear double resonance
EPR	Electron paramagnetic resonance

ESEEM	Electron spin echo envelope modulation
ET	Electron transfer
FBL	Fitted base-line
FT-IR	Fourier-transform infrared
HAT	Hydrogen atom transfer
HEPES	4-(2-Hydroxyethyl)piperazine-1-ethanesulfonic acid
HU	Hydroxyurea
IPTG	Isopropyl β-D-1-thiogalactopyranoside
KIE	Kinetic isotope effect
MCT	Mercury cadmium telluride
MMOH	Methane monooxygenase hydroxylase
MOM	Methoxymethyl ether
NA	Natural abundance
NADH	Nicotinamide adenine dinucleotide (reduced form)
NDP	Nucleoside diphosphate
Nd:YAG	Neodymium:yttrium aluminium garnet
N-MHA	N-Methylhydroxylamine
NTP	Nucleoside triphosphate
OEC	Oxygen evolving complex
PCET	Proton-coupled electron transfer
PELDOR	Pulsed electron double resonance
PMSF	Phenylmethylsulfonyl fluoride
PSII	Photosystem II
PT	Proton transfer
QM/MM	Quantum mechanics/molecular mechanics

RNR	Ribonucleotide reductase
ROS	Reactive oxygen species
SDS-PAGE	Sodium dodecyl sulfate-polyacrylamide gel electrophoresis
SHE	Standard hydrogen electrode
SVD	Singular value decomposition
TRIS	Tris(hydroxymethyl)aminomethane
UVRR	Ultraviolet resonance Raman

SUMMARY

Tyrosyl radicals can facilitate proton-coupled electron transfer (PCET) reactions that are linked to catalysis in many biological systems. One such protein system is ribonucleotide reductase (RNR). This enzyme is responsible for the conversion of ribonucleotides to deoxyribonucleotides. The β2 subunit of class Ia RNRs contains a diiron cluster and a stable tyrosyl radical (Y122•). Reduction of ribonucleotides is dependent on reversible, long-distance PCET reactions involving Y122• located 35 Å from the active site. Protein conformational dynamics are postulated to precede diiron cluster assembly and PCET reactions in RNR. Using UV resonance Raman spectroscopy, we identified structural changes to histidine, tyrosine, and tryptophan residues with metal cluster assembly in β2. With a reaction-induced infrared spectroscopic technique, local amide bond structural changes, which are associated with the reduction of Y122•, were observed. Moreover, infrared spectroscopy of tyrosine-containing pentapeptide model compounds supported the hypothesis that local amide bonds are perturbed with tyrosyl radical formation. These findings demonstrate the importance of the amino acid primary sequence and amide bonds on tyrosyl radical redox changes. We also investigated the function of a unique tyrosine-histidine cross-link, which is found in the active site of cytochrome *c* oxidase (C*c*O). Spectrophotometric titrations of model compounds that mimic the cross-link were consistent with a proton transfer role in C*c*O. Infrared spectroscopic data support the formation of tyrosyl radicals in these model compounds. Collectively, the effect of the local structure and the corresponding protein dynamics involved in tyrosyl radical-mediated PCET reactions are illustrated in this work.

CHAPTER 1

INTRODUCTION

1.1. Biological Proton-Coupled Electron Transfer, Tyrosyl Radicals, and Protein Conformational Dynamics

A prerequisite for biological function in many enzyme systems, from photosynthesis to cellular respiration, is the coupling of catalysis to electron transfer processes.[1] In biology, electron transfer is often accompanied with proton transfer. Net proton-coupled electron transfer (PCET) processes can occur by either a concerted mechanism or stepwise transfer of an electron and a proton (see Figure 1.1).[2-4] In the consecutive, stepwise scheme, either subatomic particle may be transferred first. The transfer of a proton preceding an electron is designated as PT/ET, whereas the transfer of electron preceding proton is the ET/PT mechanism. If a proton transfer is in the rate-limiting step, a kinetic isotope effect, KIE, is observed upon deuterium exchange.[5-8] The determination of the exact mechanism may be complicated when the second step is very fast so that isolation of the intermediate, if one exists, is difficult. Concerted proton and electron transfer (CPET) occurs when the transfer of the electron and the proton is synchronous. A specific example of CPET is hydrogen-atom transfer (HAT), in which strong electronic coupling between donor and acceptor allows for simultaneous transfer of both proton and electron adiabatically.[9] In general, CPET mechanism for proton and electron motion is thermodynamically preferred, because it prevents the formation of charged species.[3] Model systems for elucidating PCET mechanisms have demonstrated the importance of proton transfer in the oxidation of amino acids in biology.[10,11]

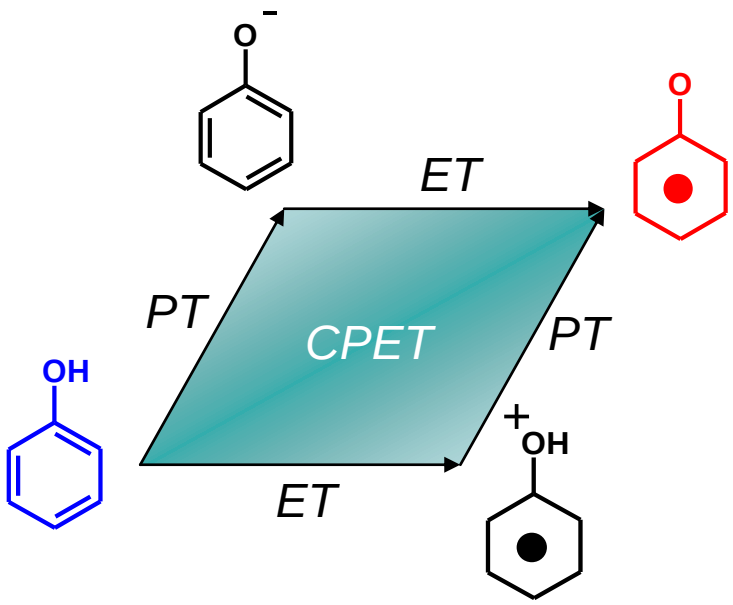

Figure 1.1. Diagram of proton-coupled electron transfer reactions. The example shown is the oxidation of phenol (blue) to a neutral phenoxyl radical (red). Phenol is the functional group of the amino acid, tyrosine. Oxidation of tyrosine may occur via PT/ET (top), ET/PT (bottom) or CPET (middle) mechanisms.

Oxidation of tyrosine (Figure 1.2) causes the loss of both a proton and an electron to generate a neutral tyrosyl radical. The unpaired electron spin of the tyrosine radical is delocalized over the 1′, 3′ and 5′ carbons and the phenoxyl oxgen.[12] The coupling of proton transfer to electron transfer is linked to the drop of the pK_A of the phenoxyl OH from ~10 in the reduced state to -2 in the radical state.[13] The reduction potential of protonated tyrosine in solution is pH dependent.[14-16] The midpoint potential for tyrosinate has been reported as ~700 mV for pH > 10 and, subsequently, this value was shown to increase linearly (+63 mV/pH unit) as the pH was decreased from 10 to 4.[16] Electrostatics, such as charge and hydrogen bonding interactions, are expected to modulate midpoint potentials of amino acids.[17] The importance of noncovalent

interactions on the midpoint potential of tyrosine and other aromatic amino acids has just begun to be illustrated.[15,16,18,19] The participation of the peptide (i.e. amide) bonds surrounding redox-active tyrosine residues in electron transfer reactions has also been investigated.[20-22] PCET reactions are dependent upon the pK_A and the midpoint potential of the amino acid residue(s) involved. These studies have demonstrated the importance of the environmental factors that control PCET reactions.

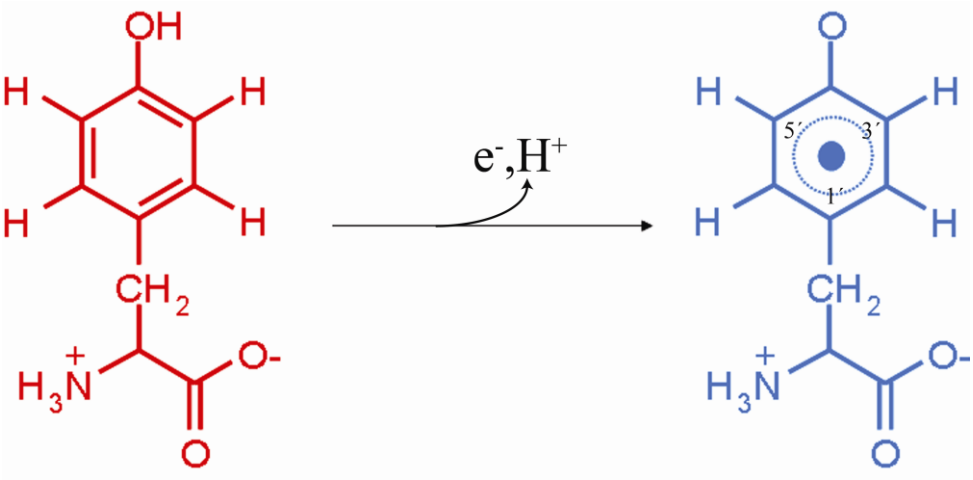

Figure 1.2. Scheme of the single electron oxidation of tyrosine (red) to tyrosyl radical (blue).

Tyrosyl radicals can participate in long-distance PCET reactions in many biological systems, such as photosystem II[23] (PSII), cytochrome *c* oxidase[24,25] (C*c*O), and ribonucleotide reductase[26] (RNR). These PCET processes are often required for catalysis. The biological process for the production of oxygen via photosynthesis is an excellent example. This system uses light-initiated PCET reactions to perform water oxidation. A tyrosyl radical, Y_Z•, in PSII has been proposed to facilitate such reactions.[27]

Modified tyrosine residues, such as those found in cytochrome *c* oxidase[28] (cross-linked tyrosine-histidine) and galactose oxidase[29,30] (cross-linked tyrosine-cysteine), have also been suggested to play a role in PCET reactions.

Tyrosine is not the only amino acid that may perform PCET reactions. Cysteine residues plays a role in PCET reactions for all classes of RNR enzymes.[31] In class III RNRs, a glycyl radical, necessary for substrate reduction, is generated by S-adenosylmethonine and an iron-sulfur protein.[32] In class I RNRs, a tryptophan residue (W48 in *E. coli*) has been proposed to participate in the conserved PCET pathway (as discussed in section 1.4). In addition, W48 may assist in generating Y122• during RNR activation under certain conditions.[33,34] Tryptophan radicals have also been observed in DNA photolyase,[35] galactose oxidase,[36] and cytochrome *c* peroxidase.[37] A tryptophan residue has been shown to mediate electron transfer in a genetically altered azurin protein.[38]

Many factors influence the rate at which electron transfer reactions occur. The semi-classical expression for the rate of electron transfer reactions is represented as $k_{ET} = \frac{4\pi^2 H_{D\text{-}A}^2}{h\sqrt{4\pi\lambda k_B T}} \exp[-(\Delta G^0 + \lambda)^2 / 4\lambda k_B T]$,[39,40] where k_B is the Boltzmann constant, T is temperature in Kelvin, ΔG^0 is the Gibb's free energy, λ is the reorganizational energy, h is Planck's constant, and $H_{D\text{-}A}$ is electronic coupling between the reactants and products in the transition state. Three important terms from this expression are $H_{D\text{-}A}$, ΔG^0 and λ. ΔG^0 is related to the redox potential difference between donor and acceptor pairs. λ, the reorganization energy, is the energy required to reorient the nuclear components from the reactant to transition state. The reorganization energy has both inner-sphere, λ_i, and

outer-sphere, λ_o, components. λ_i comprises nuclear perturbations (i.e. changes in bond lengths and angles) of the redox-centers, whereas λ_o comprises structural perturbations of the intervening medium. In small molecules, λ_o reflects the reorganization of polar solvent molecules. In proteins, however, this term may include conformational dynamics of the surrounding protein matrix. Although proteins vary in structure and function, λ has been determined in ~700 ± 100 mV range for an array of different proteins (reviewed in ref 26). It has been proposed that the protein matrix provides a rigid scaffold for the redox centers and thus reduces the reorganizational energy that can be significant in smaller molecules.

$H_{D\text{-}A}$ is the electronic coupling strength between reactants and products in the transition state. In the square potential barrier approximation, the probability of electron tunneling, $H_{D\text{-}A}^2$, decreases exponentially with distance ($r_{D\text{-}A}$) between donor (D) and acceptor (A) molecules: $H_{D-A} = H^{\circ}_{D-A} \exp[-\beta(r_{D-A} - r_0)]$.[41] The β term is a coefficient that describes the exponential decay of the electronic coupling with respect to distance (i.e. the barrier height). This parameter is dependent on the pathway of electron transfer; for proteins, the β value has been estimated in the ~1.0 – 1.4 A^{-1} range.[42] However, this range of β values can drastically alter the resulting calculated distance between acceptor and donor. Gray et al. have demonstrated experimentally that the secondary structural elements of proteins will modulate the efficiency of ET between redox centers (reviewed in 43).

In some biological systems, such as photosystem II, the distances between redox pairs may be quite large (i.e. $r_{D\text{-}A}$ > 10 Å) and thus direct wavefunction overlap between redox centers is insignificant. Therefore, the protein matrix must facilitate the electronic

interaction between donor and acceptor. The electronic states of the protein structure can bridge the redox centers. The barrier height is reduced to extend the D-A wavefunctions and this superexchange coupling effect allows for direct electron tunneling from acceptor to donor.[44] The expression of the electronic coupling term for these situations is slightly changed to account for the effect of covalent bonds (C), hydrogen bonds (H), and through-space jumps (TS): $H_{\mathrm{D-A}} \propto \prod \varepsilon_{\mathrm{C}} \prod \varepsilon_{\mathrm{H}} \prod \varepsilon_{\mathrm{TS}}$.[42,45] The mechanism by which the protein milieu mediates these long-distance electron transfer reactions is still not resolved.[46,47] The determination of the mechanism of ET reactions and elucidation of ET factors, λ and β, in biological systems is often not straightforward, because electron transfer reactions can be coupled to non-ET processes such as proton transfer (PT) or protein conformational changes.

Protein conformational dynamics have been postulated to precede or gate electron transfer reactions in many enzyme systems.[48] In photosystem II, protein conformational changes have been reported to precede oxidation reactions at the manganese cluster.[49,50] In ribonucleotide reductase, slow conformational changes have been hypothesized to gate nucleotide reduction.[51] Spectroscopic identification or characterization of these rate-limiting protein conformational changes in RNR has not been well studied. In this thesis, the mechanism of tyrosine-mediated electron transfer reactions using model compounds and the protein conformational dynamics that accompany or precede ET processes in ribonucleotide reductase are investigated.

1.2. Photosystem II of Photosynthesis

Photosystem II (PSII) is responsible for splitting water to produce molecular oxygen in plants, algae and cyanobacteria. This membrane-bound protein complex is found in the thylakoid membrane of photosynthetic organisms. Oxygen production is coupled to the translocation of protons from the stromal to the luminal side, which drives ATP synthesis. PSII is composed of more than 20 polypeptides. The redox-active cofactors (Figure 1.3) are primarily located in the intrinsically bound D1 and D2 subunits.[52,53] In addition, CP43 and CP47 are chlorophyll binding proteins that are closely associated with the D1 and D2 subunits.

Water oxidation in PSII occurs at the oxygen-evolving complex (OEC). This complex is composed of four manganese atoms, ligated by oxygens, and calcium. Although its binding site is controversial, chloride also plays a significant role in H_2O oxidation.[54,55] To initiate water oxidation, absorption of light produces a charge separation. Although the primary donor to $Pheo_{D1}$ is under debate, the excited state responsible for charge separation is most likely a chlorophyll molecule on the D1 subunit (Chl_{D1}).[56-58] The Chl_{D1} molecule has been proposed to reduce $Pheo_{D1}$ and the positive charge migrates to P_{680}^{+}, the chlorophyll dimer.[59] With a reduction potential of ~ 1.3 V,[60,61] P_{680}^{+} is considered the most oxidizing species in biology.

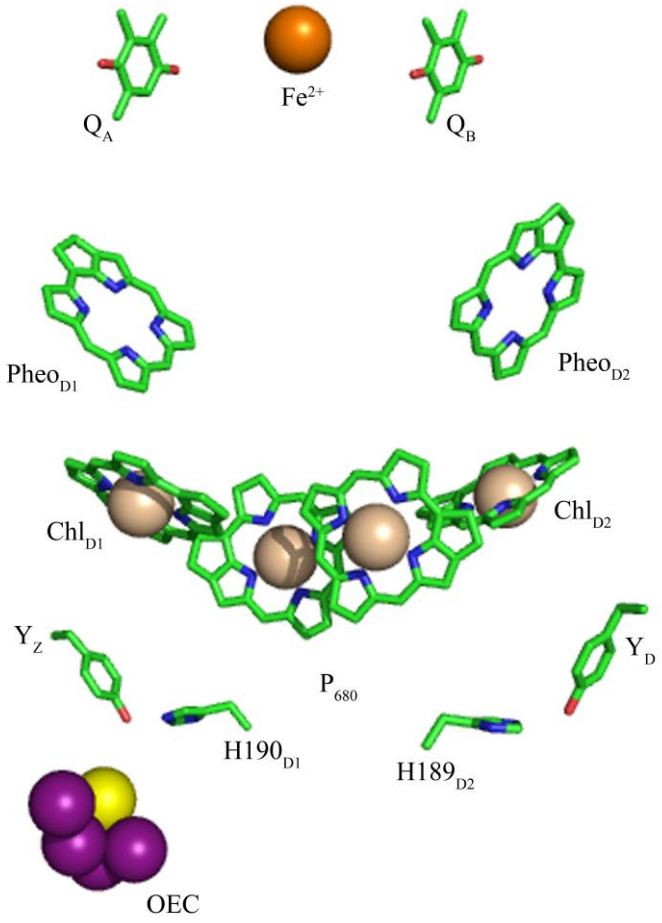

Figure 1.3. Arrangement of the redox-active cofactors in cyanobacterial PSII (PDB: 3BZ1). The OEC is composed of four manganese (purple spheres) atoms and one calcium (yellow sphere) atom. The "acceptor" side is at the top and the "donor" side is at the bottom. The tails of the chlorophyll, pheophytin, and plastoquinone molecules have been removed for clarity. The magnesium atoms of the chlorophyll molecules are shown as wheat spheres. The green, blue, and red colors represent carbon, nitrogen, and oxygen, respectively.

On the "acceptor" side, a strongly bound plastoquinone, Q_A, oxidizes the $Pheo_{D1}^-$ resulting in the $P_{680}^+Q_A^-$ state.[62,63] Consequently, Q_A^- transfers an electron to the weakly bound plastoquinone, Q_B. With a second charge separation event, the doubly-reduced Q_BH_2 dissociates from the quinone binding site out to the thylakoid membrane. Q_BH_2 eventually transfers electrons to the cytochrome b_6f complex.

On the "donor" side, P_{680}^+ is reduced by the redox-active tyrosine, Y161 (Y_Z)[64] of the D1 subunit, generating the transient, neutral radical (Y_Z•) on the nanosecond timescale.[65] Y_Z• subsequently oxidizes the manganese cluster[27] on the micro- to millisecond timescale.[66] The kinetics depend on the number of stored oxidizing equivalents (0 to 4) at the cluster. The manganese cluster cycles through five S (i.e. oxidation) states, S_0 – S_4, as described by the Kok cycle.[67,68] Molecular oxygen is released at the transient S_4 state. Excluding the S_4 state, all other S state advancements are induced by P_{680} photochemical oxidation. The S_4 state is of great interest, but has not yet been identified.[69-71] Proposals for the mechanism of water splitting, including the structure of the OEC, have been reviewed.[72]

The tyrosine residue, Y_Z, of photosystem II links the OEC to P_{680} and is essential for O_2 evolution. An analogous tyrosine residue is located in the D2 subunit, Y160 (Y_D). Both of these tyrosine residues are redox-active and both form neutral radicals (Y_Z• and Y_D•) when oxidized by P_{680}^+.[23,64,73-75] A comparison of the properties of these two similar and yet distinct tyrosine residues have been thoroughly reviewed, previously.[76]

Briefly, both of these residues share similar environments. Y_Z and Y_D are equidistant to P_{680} (both separated from P_{680} by ~13 – 14 Å).[52,53,77-79] Both tyrosine

residues are within hydrogen bonding distances to a histidine (D1-H190 for Y_Z and D2-H189 for Y_D).[53] The primary sequences, IY_ZPIG and IY_DPLG, are also similar.[52]

However, there are some properties that distinguish Y_Z and Y_D. The redox potential of Y_D is ~240 mV lower than that of Y_Z (~930 mV).[80-83] The decay rate of Y_D• is much slower (minutes to hours) than that of Y_Z• (microseconds to milliseconds).[84] Y_Z facilitates water oxidation; whereas, Y_D has been implemented in the assembly of the manganese cluster[85] and in photoprotection.[19,86] Together, the different properties of these two tyrosine residues in photosystem II underscore the importance of environmental factors on the utility of redox-active tyrosine residues in biology. The mechanism of electron transfer via tyrosine residues *in vitro* is discussed in more detail in Chapter 2.

1.3. Cytochrome *c* Oxidase

Cellular respiration is the process by which organisms generate a usable, sustainable source of energy from NADH. Cytochrome *c* oxidase (C*c*O) is the terminal membrane-bound enzyme in the electron transport chain of the mitochondrion and some bacteria. C*c*O plays a critical role in cellular respiration through the reduction of dioxygen to water, while preventing the generation of harmful reactive oxygen species (ROS).[87] Protons are translocated across the membrane to drive ATP synthesis. The reaction, $4H^+ + 4e^- + O_2 \rightarrow 2H_2O$, is exothermic and drives the active translocation of protons across the inner mitochondrial membrane.[88] Reduction of molecular oxygen is carried out at the heme a_3/Cu_B binuclear center (see Figure 1.4) and requires four

electrons.[89] Dioxygen *only* binds when the binuclear center is in the ferrous-cuprous state.

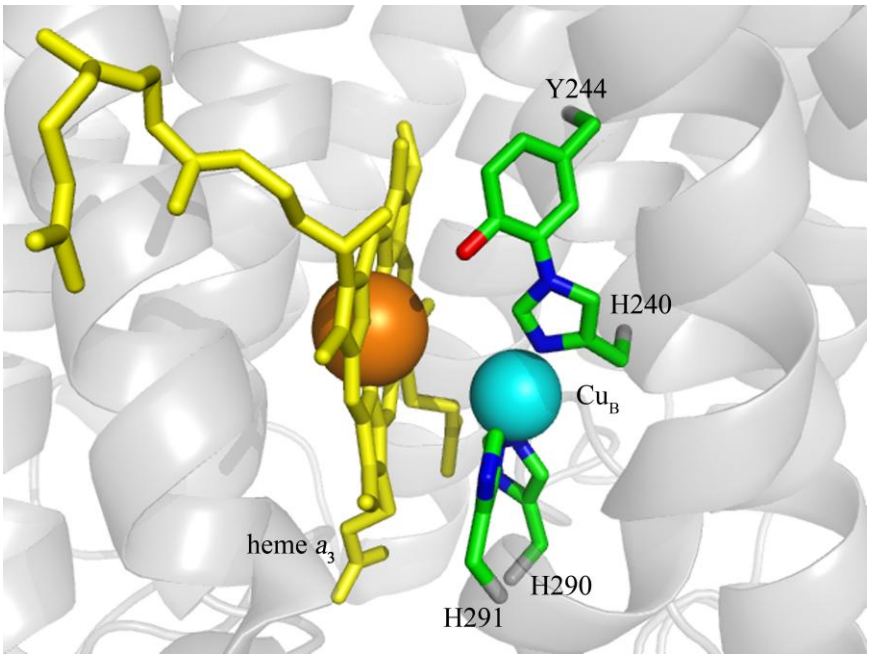

Figure 1.4. Structure of the heme a_3/Cu_B binuclear center of bovine heart cytochrome *c* oxidase (PDB: 2DYR). The ligands to Cu_B, His-240, His-290, His-291, are also shown. The orange sphere represents the iron of heme a_3 and the cyan sphere represents Cu_B.

The binuclear center donates three of the necessary reducing equivalents. Under fully reduced conditions, the iron of another C*c*O redox center, heme *a*, is responsible for the remaining electron. During steady-state turnover, however, in which the heme *a* iron is unable to provide this reducing equivalent, the source of the fourth electron is undefined. A novel, post-transcriptional covalent cross-link (Figure 1.4) involving the C5' of tyrosine (Y244; bovine heart numbering) and the ε-nitrogen of histidine 240 was established from X-ray crystallography.[28,90,91] H240 is one of the three histidine ligands to Cu_B. The importance of Y244 has been demonstrated through mutational studies, but

the biological function of this residue remains controversial.[24,25] Proton[92-94] and/or electron[95-99] donation to O_2 has been proposed.

Spectroscopic identification of the Y244 radical during turnover has been problematic. The study of the electronic structure and properties of the tyrosyl radical and its involvement in O_2 reduction remains to be fully elucidated. To identify the functional significance of this unique modification, model compounds have been synthesized (see Figure 1.5).[100-107] Physical and structural studies of active site model compounds may help to illustrate the function of this modified tyrosine in O_2 reduction. The functional significance of this cross-linked moiety will be discussed further in Chapter 3.

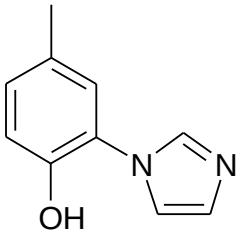

McCauley, 2000
Aki, 2002
Pratt, 2005

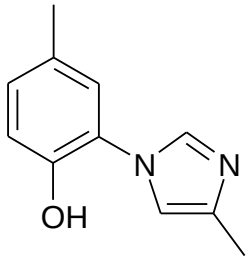

Kim, 2004

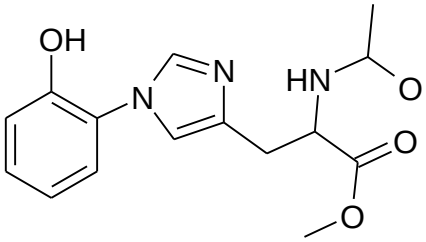

Cappuccio, 2002

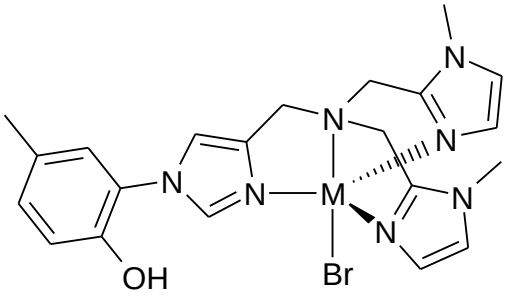

M = Cu^{2+} *or* Zn^{2+}
Nagano, 2005
Nagano, 2006

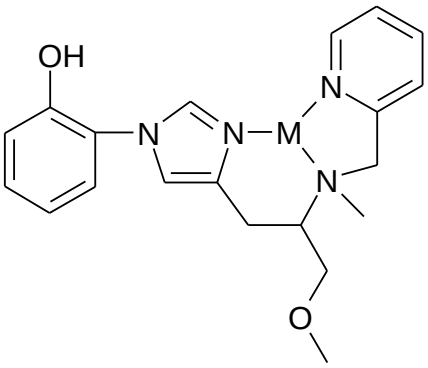

M = Cu^{2+}
White, 2007
Offenbacher, 2009

Figure 1.5. Structures of synthetic cytochrome *c* oxidase tyrosine-histidine model compounds.[100-107]

1.4. Ribonucleotide Reductase

Ribonucleotide reductases (RNRs) catalyze the reduction of ribonucleotides to 2′-deoxyribonucleotides and thus play a critical role in DNA biosynthesis and repair by providing the necessary monomers (Figure 1.6).[108-110] The process is initiated by abstraction of 3′-hydrogen atom using a transient active site cysteine radical. Loss of the 2′-hydroxyl group as H_2O leads to oxidation of two additional active site cysteines and release of the deoxynucleotide product. The reaction of the active state of the protein requires reduction of the disulfide bond by glutaredoxin (GR) or thioredoxin (TR) proteins.

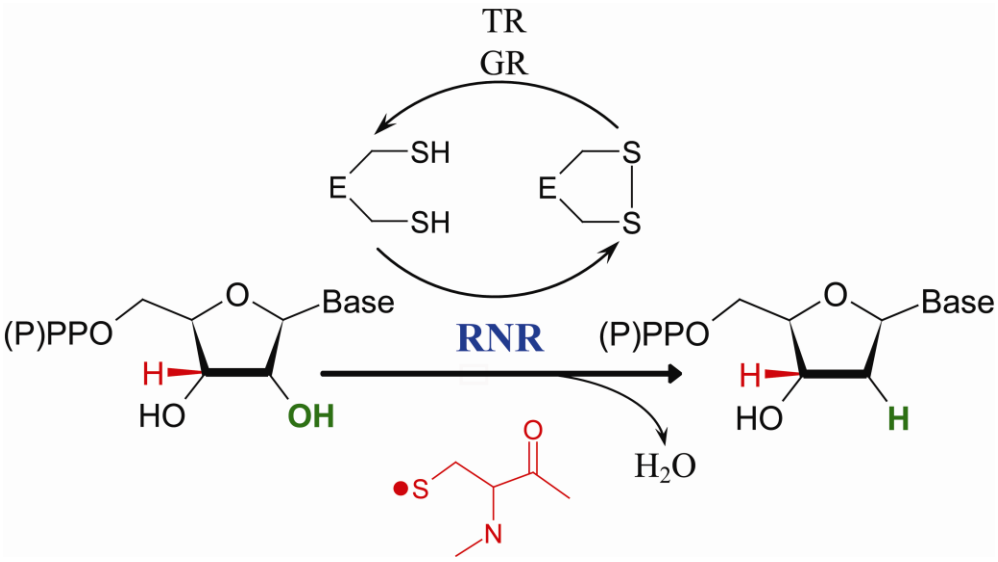

Figure 1.6. Schematic diagram of the ribonucleotide reductase catalytic reaction.

There is no other *de novo* pathway that circumvents ribonucleotide reductase for the production of these DNA precursors. Thus, RNR is indispensible for life in all organisms. Ribonucleotide reductase has gained a broad interest from all aspects of chemistry. First, in rapidly proliferating cells, RNR has been shown to be overexpressed

and directly correlated to tumor growth in cancer cells.[111,112] Thus, RNR has become a useful pharmaceutical target for anti-cancer drugs. Second, these proteins might have served as the evolutionary link between RNA and DNA.[113,114] Third, RNR is grouped within a family of nonheme diiron proteins with similar structural components, but different catalytic mechanisms.[115] The mechanism of assembly of the metal cluster is of interest. Another hallmark of ribonucleotide reductase is a long-range proton-coupled electron transfer pathway involving amino acid residues as the transient radical intermediates.[26,31] RNR provides a paradigm for the mechanistic elucidation of other biological systems. This thesis is aimed at understanding how structural dynamics control electron transfer and metal cluster assembly in RNR.

1.4.1 Three Classes of Ribonucleotide Reductase Enzymes

Deoxyribonucleoside 5′-di- or tri-phosphate production results from complex radical chemistry initiated by a transient radical centered at an active site cysteine (C439 in *E. coli*) residue. This transient radical is generated via proton-coupled electron transfer reactions from metallo-cofactors.

The RNR proteins comprise three classes, which are distinguished by their oxygen requirements, subunit composition, and radical initiation cofactors as shown in Figure 1.7. Class I enzymes contain a stable tyrosyl radical adjacent to a μ-oxo bridged diiron cluster. Class II RNRs initiate ribonucleotide reduction with a radical centered on adenosylcobalamin. Class III proteins utilize a stable glycyl radical facilitated by S-adenosylmethonine and an iron-sulfur protein. Class I is subdivided further into 3 subclasses Ia, Ib and Ic. Classes Ia and Ib both use tyrosyl radicals for thiyl radical

generation, whereas the equivalent residue in class Ic is replaced with a phenylalanine.[116] In lieu of a Y•, the recently discovered class Ic enzymes use a Fe^{III}–O–Mn^{IV} cofactor as a radical initiator.[117]

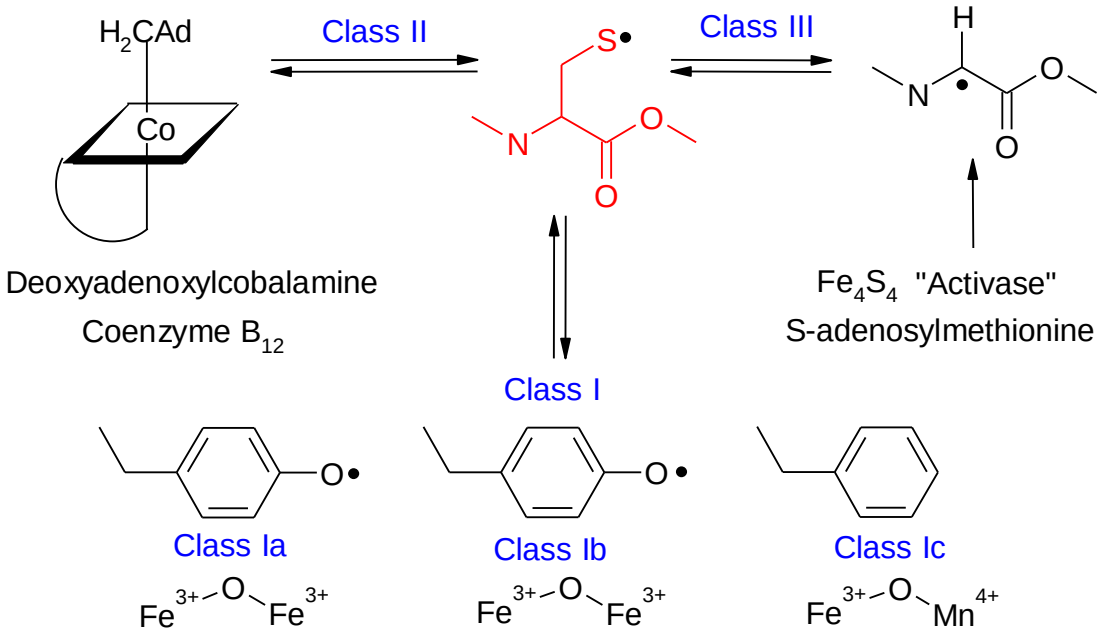

Figure 1.7. Diagram depicting the three classes of RNR required for generation of the transient cysteine radical.

Class Ia and Ib enzymes have identical radical initiation cofactors and both are composed of two homodimeric complexes $\alpha 2\beta 2$.[118] The radical propagation pathways for cysteine radical formation in the active site are also similar. The class Ia family is found in mammals, viruses, bacteriophages, and bacteria, whereas the class Ib is limited to particular bacteria.[109] The significant difference distinguishing these two subclasses is that class Ib enzymes lack a second allosteric regulation site, a feature of class Ia.[119] Unlike class Ia, the class Ib proteins are not inhibited by dATP. This characteristic has been linked to the absence of the ~50 amino acid terminus in the $\alpha 2$ subunit of class Ib.[120]

Some bacteria express both sets of genes (*nrdAB* for IA and *nrdEF* for Ib).[121] Although they appear to have similar aerobic ribonucleotide reduction activity,[122] the reason for expression of both gene sets is an interesting unresolved enigma.

1.4.2 RNR Reaction Mechanism

The radical-dependent catalytic mechanism has been proposed to be similar in all three classes.[123] C439• abstracts a hydrogen atom at the 3′-carbon of the ribose sugar (see Figure 1.8).[124]

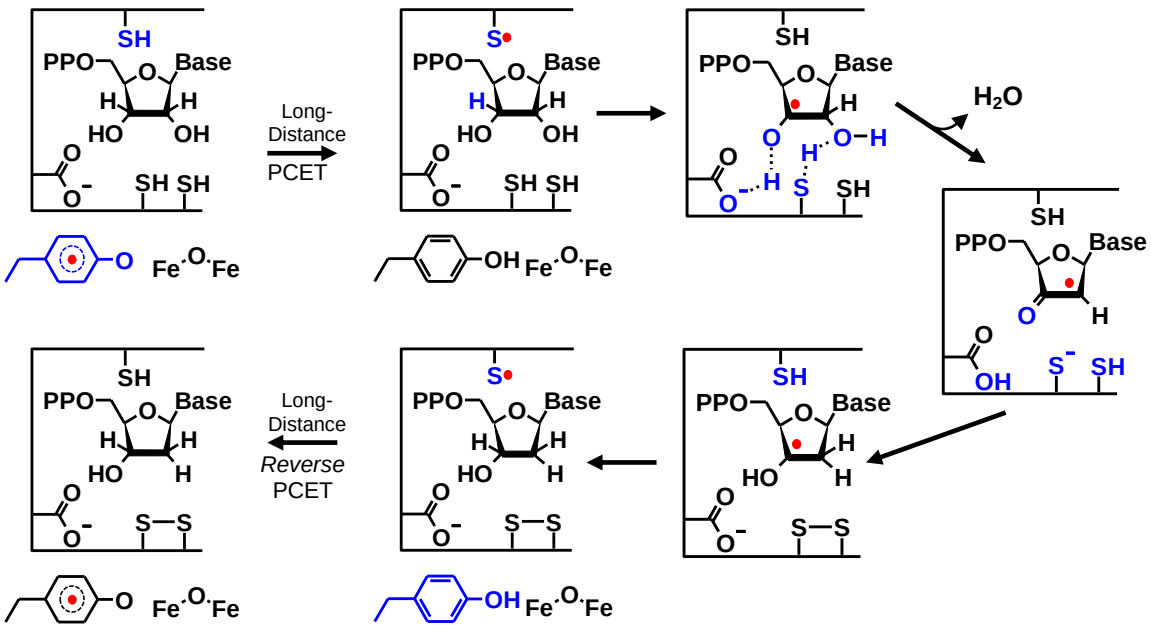

Figure 1.8. Proposed mechanism of ribonucleotides in α2 subunit of class Ia RNR.

After the abstraction, the 2′-hydroxyl group leaves as water, gaining a proton from another conserved active site cysteine (C225 or C462). These two catalytically essential cysteines are subsequently oxidized, forming a disulfide bond and a 2′-deoxy-

3′-nucleotide radical. Regeneration of the C439• produces the deoxyribonucleotide. Two other additional cysteines located outside of the active site, close to the carboxyl end,[31] re-reduce active site cystine, allowing multiple turnover events. Fully reduced α2 protein is regenerated through interactions with the thioredoxin and glutaredoxin systems. The RNR catalytic mechanism was deduced from studies of the class II enzyme, *Lactobacillus leichmannii*, which served as a prototype to generalize the RNR reaction mechanism in all classes.[125,126]

1.4.3 Class Ia RNR Subunit Composition

One focus of this thesis is the *Escherichia coli* class Ia enzyme, one of the most extensively studied RNR. Class Ia RNR, encompassing bacterial, mammalian and viral proteins, contains two homodimeric subunits, α2 and β2.[127] α2, formerly R1, is a 172 kDa dimer and houses the nucleotide (NDP or NTP) reduction site. RNR activity is highly regulated *in vivo* to ensure the appropriate balance of the deoxyribonucleotides required by the cell.[128] The α2 subunit is composed of two allosteric regulation sites. One site regulates specificity and the other controls the overall activity. Specificity is achieved through the binding of a particular effector, which induces a structural change at the active site of α2 and binding of the appropriate substrate.[119] The overall activity of RNR is stimulated in the presence of ATP or low concentrations of dATP and inhibited with high concentrations of dATP.[129] Thus, the relative cellular concentrations of these two species controls the rate at which nucleotide reduction takes place. The substrate specificity site, also referred to as the "high affinity" site, is the pocket where ATP, dATP, dTTP, and dGTP bind and regulate reduction of the precise nucleotides required

by the cell. An allosteric mechanism has been proposed that describes the relationship (see ref 108 for details). The general trend shows that binding of dGTP stimulates dADP production, whereas dTTP and dCTP stimulate dGDP formation and ATP/dATP binding favors pyrimidine reduction.

The small homodimer of 87 kDa, β2, contains a tyrosyl radical (Y•) located at position 122 adjacent to a μ-oxo bridged diferric cluster. This was the first reported case of a protein-containing tyrosyl radical in biology.[130] Y122• is absolutely required for turnover; mutation to a phenylalanine eliminates enzymatic activity.[131] Substrate analogs that trap the radical during the chemical reduction process have shown a stoichiometric decrease in Y122• content with the formation of substrate analog radical.[132-134] Site-specific replacement of Y356, a putative member of the electron transfer pathway, with 3-,4-dihydroxyphenylalanine (DOPA) has also demonstrated the importance of Y122•.[135] DOPA is a radical trap, because DOPA has a lower reduction potential than tyrosine. In the study,[135] $DOPA_{356}$• was formed concomitantly with Y122• reduction when DOPA356Y-β2 was mixed with α2, substrate, and effectors.

Y122• has an unusually long half-life of 2 weeks at 4°C,[136] even though tyrosyl radicals are strong oxidants. The typical lifetime of a tyrosyl radical in solution is on the μs timescale.[103] The midpoint potential versus the standard hydrogen electrode (SHE) for Y• in β2 and solution at pH 7.0 are ~1000[137] and ~950[14-16] mV, respectively. Thus, the reason for prolonged lifetime is not derived from redox stability. More likely, since Y122 is buried deep inside the protein and surrounded by a hydrophobic core, solvent inaccessibility is the main reason for enhanced stability. The stoichiometry of Y122 and Fe per β2 has also been determined. For the standard β2 purification protocol,[138] a typical

Y122•/β2 yield is 1.1 – 1.4 using the relation, $[Y\bullet] = \frac{A_{411nm} - \left[\frac{3\times(A_{416nm})+2\times(A_{406nm})}{5}\right]}{1784\,M^{-1}cm^{-1}}$.[139] *In vivo* studies using *Saccharomyces cerevisiae* determined a maximal 0.89 Y• in one β.[140] In addition, there are only 3 – 3.5 Fe atoms per dimer. The reason for the distribution in these values is not well understood.

Within class Ia, there are some differences between the mouse (i.e. mammalian) and *E. coli* (i.e. bacterial) RNRs. The tyrosyl radical in the mouse RNR (Y177) is hydrogen bonded,[141] whereas the *E. coli* tyrosyl radical (Y122) is not hydrogen bonded.[142] In both organisms, reduction of the stable radical is accomplished chemically through incubation of small reducing agents such as hydroxyurea,[143] hydrazine,[144] or hydroxylamine.[145,146] Incubation of the mouse small subunit, M2 (analogous to *E. coli* β2) with hydroxyurea reduces the radical and leads to a loss of iron.[147] In *E. coli*, however, hydroxyurea treatment forms a stable Met-β2 state, in which Y122 is reduced and the diiron center remains oxidized. The β2 structures of the two species appear similar, but distinct differences such as water arrangement and carboxylate flexibility in the mouse protein might account for the slight differences in comparison to the *E. coli* β2.[148] Moreover, since the tyrosyl radical in the mouse enzyme is hydrogen bonded to water, Y177• is more solvent accessible and the stability is less than that of Y122• in *E. coli*.[149]

1.4.3 Diiron Cluster Redox States and Assembly in Class Ia RNR Enzymes

There are four states of the *E. coli* β2 protein as depicted in the Figure 1.9 below. The crystal structures of three states have been resolved.[150-152] However, to this date,

there is no crystal structure and only limited other structural data[153] for the fully oxidized, control (Y122•-containing) β2 protein. The binuclear iron center has been studied using Raman, EPR, and Mössbauer spectroscopies and magnetic susceptibility.[136,154-158]

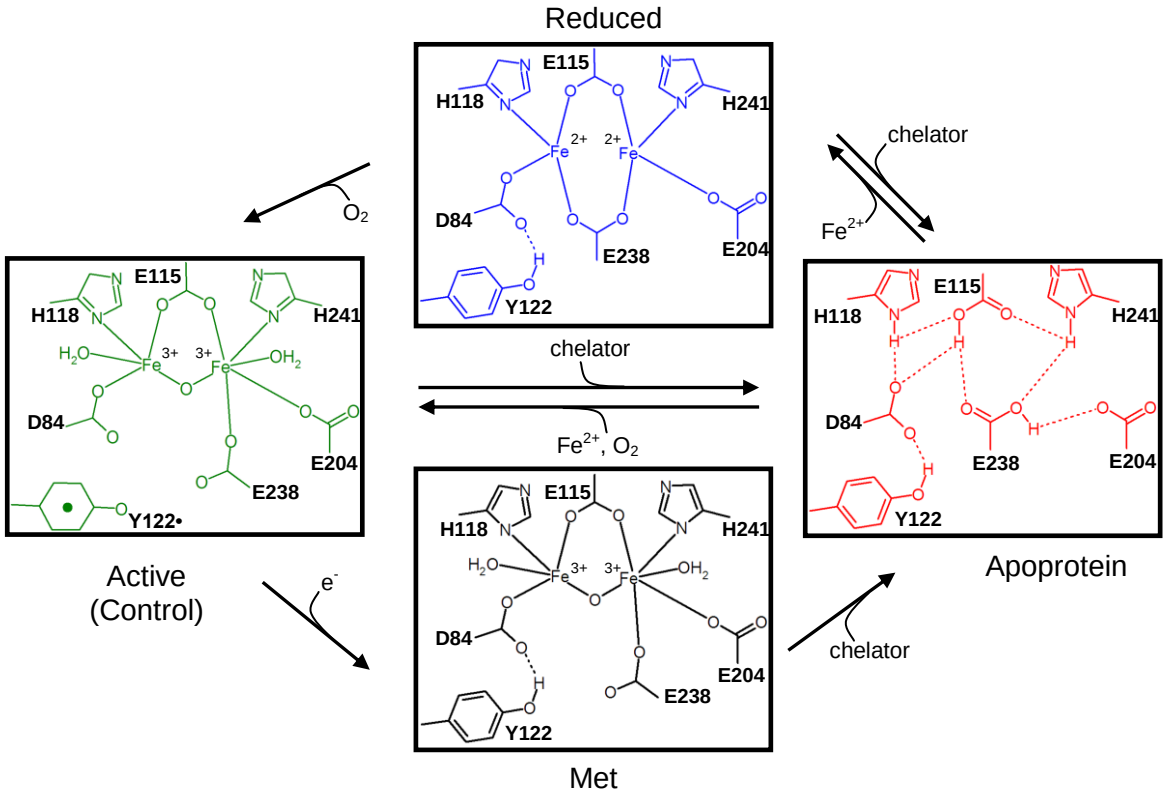

Figure 1.9. Diagram representing the different redox states of the class Ia RNR β2 protein.

In the active form, the antiferromagnetically coupled μ-oxo bridged binuclear iron center is in high spin, diferric state. The diferrous (reduced) β2 is formed through the anaerobic addition of diferrous ions to metal-free (Apo) β2. Apo-β2 may be formed through the chemical treatment with lithium 8-hydroxyquinoline-5-sulfonate, an iron chelator.[136] Titration of Apo-β2 with Fe^{2+} and oxygen spontaneously regenerates the

active state.[159] The iron may also be substituted with cobalt[160] or manganese[159], but these metals do not form Y122• when exposed to O_2.

Assembly of the diferric cluster of RNR has been proposed to be limited by protein conformational change(s).[161] In addition, metal binding has been shown to be regulated by allosteric effects.[162] Conformational changes involving the iron-ligating carboxylate residues accompany diiron cluster redox changes.[152,163]

1.4.4 Proton-Coupled Electron Transfer Pathway in Class Ia RNRs

In the presence of substrate and effectors, the subunits α2 and β2 are thought to form an active 1:1 complex (α2β2) with an affinity of $K_D \leq 0.2$ μM.[164] However, mammalians enzymes have shown to be in a preferred hexameric state (α6β6).[165] Recently, dATP inhibition was shown to be correlated with tetramer formation (α4β4) in *E. coli*.[166] This interaction is inhibited by biomimetic peptides that contain the carboxyl terminal amino residues of the β2 subunit.[167-169] The use of synthetic peptides for binding α2 has given new information concerning the mechanism of electron transfer (ET) between Y356 and α2.[170,171] Also, conformational dynamics of α2 during ET and turnover have been studied.[172] Nucleotide reduction requires the association of α2 and β2 with the presence of substrate and effectors. Because catalysis is initiated with a transient cysteine radical, the mechanism of C439• formation is an important question, which is just beginning to be elucidated.

Based upon a docking model of individual α2[31] and β2[150,153] *E. coli* structures, Y122• is ~35 Å from C439 at the active site. This distance has been supported by the *Salmonella typhimurium* class Ib holoenzyme structure[173] and pulsed electron double

resonance (PELDOR)[174] experiments. Assuming an electron tunneling model and that electron transfer is rate-limiting, nucleotide reduction would occur at 10^{-4} – 10^{-9} s^{-1}.[26] The rate projection accounts for a β range of 1.1 – 1.4 Å, which is the range for nearly all ET reactions in biology,[26] and assumes a favorable driving force for the oxidation of cysteine. The reduction potential of cysteine in solution is about 1.3 V.[175] Compared to the redox potential of ~1 V,[137] C439 oxidation by Y122• would be thermodynamically unfavorable. If the cysteine residue is deprotonated, the redox potential would drop to 770 mV, which is in a thermodynamically favorable range.[176] Since the pK_A of cysteine in solution is about 8.2,[177] deprotonation of C439 seems unlikely. However, the protein environment can significantly alter the pK_A and midpoint potential of the amino acids.[16,178] The exact mechanism for C439 oxidation in class Ia enzymes is not yet fully resolved.

1.4.6 Conformational Gating and Rate-Limiting Step in Nucleotide Reduction

The kinetics of nucleotide reduction have been explored both by Erickson[179,180] and Stubbe[51]. From these cases, the rate-limiting step is controversial. The identity of the rate-limiting step or process is crucial for the elucidation of the radical initiation mechanism in class I enzymes. Initial kinetics studies suggested that the oxidation of the active site cysteines, C225 and C462 (see Figure 1.8), following nucleotide reduction is kinetically competent.[179] In addition, these data supported an asymmetric complex of α2β2. The rate-limiting step for the overall reaction was proposed by Erickson to occur after the oxidation of the peripheral cysteines, C754 and C759.[180] These cysteine residues are proposed to be a shuttling system for reducing the active site cystine via thioredoxin

or glutaredoxin.[124,181,182] Stubbe, however, proposed a possible rate-limiting conformational gating step[51] preceding nucleotide reduction in addition to the slow post nucleotide reduction process.[180] The Y122• content was monitored using UV-visible spectroscopy along with the formation of dCDP from rapid chemical quenching. There was no significant change in Y122• during the course of the reaction when monitored with a 2 ms time resolution. Since the chemistry is fast (< 2 ms) and the overall nucleotide reduction is much slower (~ 100 ms), a physical gated step was hypothesized,[51] but there is no spectroscopic evidence for such an event during turnover.

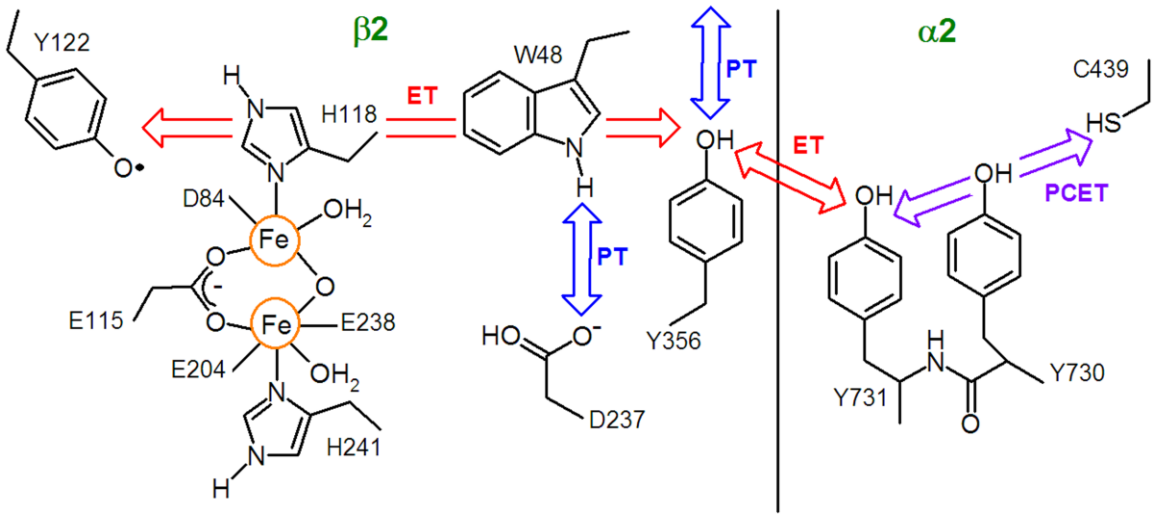

Figure 1.10. Proposed proton-coupled electron transfer pathway in ribonucleotide reductase class Ia enzymes.

Since nucleotide reduction occurs in the 2 – 14 s^{-1} range[180] and the putative rate-limiting step is postulated to be a conformation change preceding nucleotide reduction[51], the direct electron tunneling from C439 to Y122• model fails. An electron hopping pathway (Figure 1.10) has been proposed involving several amino acids as kinetic

intermediates.[26,31] This proposal has been supported by site-directed mutagenesis[131,183-186] and unnatural amino acid replacement[170,187,188] studies. To date, there has been no spectroscopic characterization of these intermediates during turnover for the wild-type enzyme.

As a first step in determining the identity of the rate-limiting step, we set out to explore how structural dynamics effect or mediate the electron transfer and activation processes of RNR. Structural dynamics have previously been shown to be important during electron transfer processes of other protein systems, such as photosystem I (PSI)[189,190] and photosystem II (PSII)[191,192], for example. In order to monitor such reactions, we have employed two novel vibrational techniques towards the study of RNR: reaction-induced Fourier-transform infrared (FT-IR) and ultraviolet resonance Raman (UVRR) spectroscopy.

1.5. Vibrational Spectroscopy

Vibrational spectroscopy offers complementary information to X-ray crystallographic studies such as changes in protonation state, electronic distribution, hydrogen bonding, and other electrostatic interactions of molecules. Two vibrational techniques, Fourier-transform infrared (FT-IR) and ultraviolet resonance Raman (UVRR) spectroscopies have been invaluable for the study of protein conformational dynamics in proteins.

1.5.1 Fourier Transform Infrared Spectroscopy

Fourier transform infrared (FT-IR) spectroscopy is sensitive to changes in normal vibrational modes of molecules.[193] Vibrational frequencies (υ) are associated with the force constant, *k*, of a covalent bond(s) involving two or more atoms of defined mass. This relationship[194] is expressed as $\upsilon = \frac{1}{2\pi}\sqrt{\frac{k}{\mu}}$, in which μ is the reduced mass. In a diatomic molecule the reduced mass is described as $\mu = \frac{m_1 m_2}{m_1 + m_2}$, where m_1 and m_2 are the masses of the two atoms. In the simplest approximation, the vibrations of a diatomic molecule may be represented by the harmonic oscillator model. Quantum mechanics expresses the allowed energy levels ($E(n)$) of a harmonic oscillator as $E(n) = h\upsilon(n + \frac{1}{2})$, where *h* is Planck's constant and *n* is the vibrational quantum number (n = 0, 1, 2, …). For a vibrational transition to occur, a change in the electric dipole moment is required. In a harmonic diatomic molecule, the selection rule $\Delta n = \pm 1$ is applicable. However, in an anharmonic molecule, weak transitions from $\Delta n = \pm 2, \pm 3, \ldots$ (i.e. overtone bands) may also be observed.

In larger (i.e. polyatomic) molecules, the description of the molecular transitions is more complicated than the harmonic diatomic molecule. The number of different types of vibrational motions available or possible for a polyatomic, nonlinear molecule can be explained with 3N–6 degrees of freedom, where N is the number of atoms in the defined system or molecule. A polyatomic, linear molecule has 3N – 5 degrees of freedom. The difficulty in describing the vibrations of polyatomic molecules is the calculation of the reduced mass for a specific normal mode. Calculating these vibrations is complicated

because, for a particular normal mode, vibrations can be coupled. However, molecules can be partitioned into functional groups. The frequencies for these group types allow for the identification of structural elements of a larger molecule using FT-IR spectroscopy. For instance, proteins are composed of amino acids connected by amide bonds, which primarily give rise to amide I (C=O stretching) and amide II (NH bending coupled with C–N stretching) vibrational bands. The frequency of the amide I mode may help to describe the secondary elements of proteins as α helices (1655 – 1660 cm^{-1}) or β sheets (1630 – 1640 cm^{-1}).[195]

Theoretical approaches such as density functional theory (DFT) may be used to calculate vibrational modes in small molecules. Proteins, however, are too large for the high level quantum mechanical methods such as DFT. Therefore, quantum mechanics/molecular mechanic (QM/MM) methods are often used. QM/MM calculations can provide quantitative information for FT-IR spectra, including geometry, electron density and charge distribution from the quantum mechanical part.

FT-IR spectroscopy has the ability to detect and distinguish subtle perturbations of the protonation state, electronic distribution, hydrogen bonding, and other electrostatic interaction(s). Thus, the technique can be used to monitor protein structural dynamics and to determine reaction mechanisms. Development of improved time-resolved FT-IR spectrometers has allowed the study of protein dynamics in real time.[196-198]

The application of FT-IR difference spectroscopy has emerged as a powerful tool to monitor reaction mechanisms in proteins. A small protein of 20 kDa (e.g. ubiquitin carrier protein) has around 10^4 modes of vibrations.[199] Thus, the protein FT-IR absorbance spectrum is broad and difficult to interpret small changes. FT-IR difference

spectroscopy, established with studies of the proton pump bacteriorhodopsin, emphasizes the changes that are only affected by the reaction.[200,201] There are some excellent reviews that discuss the application of FT-IR spectroscopy to proteins studies.[200,202-206] Since its emergence, FT-IR difference spectroscopy has been used to study the mechanisms of water oxidation of photosystem II[207,208] and dioxygen reduction in cytochrome *c* oxidase.[98,209,210] FT-IR difference spectroscopy has also been employed to monitor electron transfer reactions in bacterial reaction centers,[211] photosystem I,[212,213] and ribonucleotide reductase.[214]

In difference spectroscopy, a reaction is monitored by taking a snapshot before and after an event. The two snapshots are subtracted so that vibrational modes, which are not affected by the reaction or stimulus, are canceled out. Vibrational frequencies that shift in energy or change in amplitude are displayed in the difference spectrum. An example of the use of difference FT-IR spectroscopy is shown in Figure 1.11. In this example, the photolysis-induced FT-IR difference spectra of tyrosinate was monitored at 79 K. Tyrosyl radicals may be generated from tyrosinate samples with five 266 nm laser pulses of an Nd:YAG laser. FT-IR spectra collected of tyrosinate prior to photolysis were subtracted from spectra collected after photolysis (Figure 1.11, bottom spectrum) to yield the FT-IR difference spectrum. Photo-oxidation of tyrosinate has been shown to cause perturbations of the ring and CO stretching frequencies.[20,215,216] These spectral changes are discussed further in ensuing chapters.

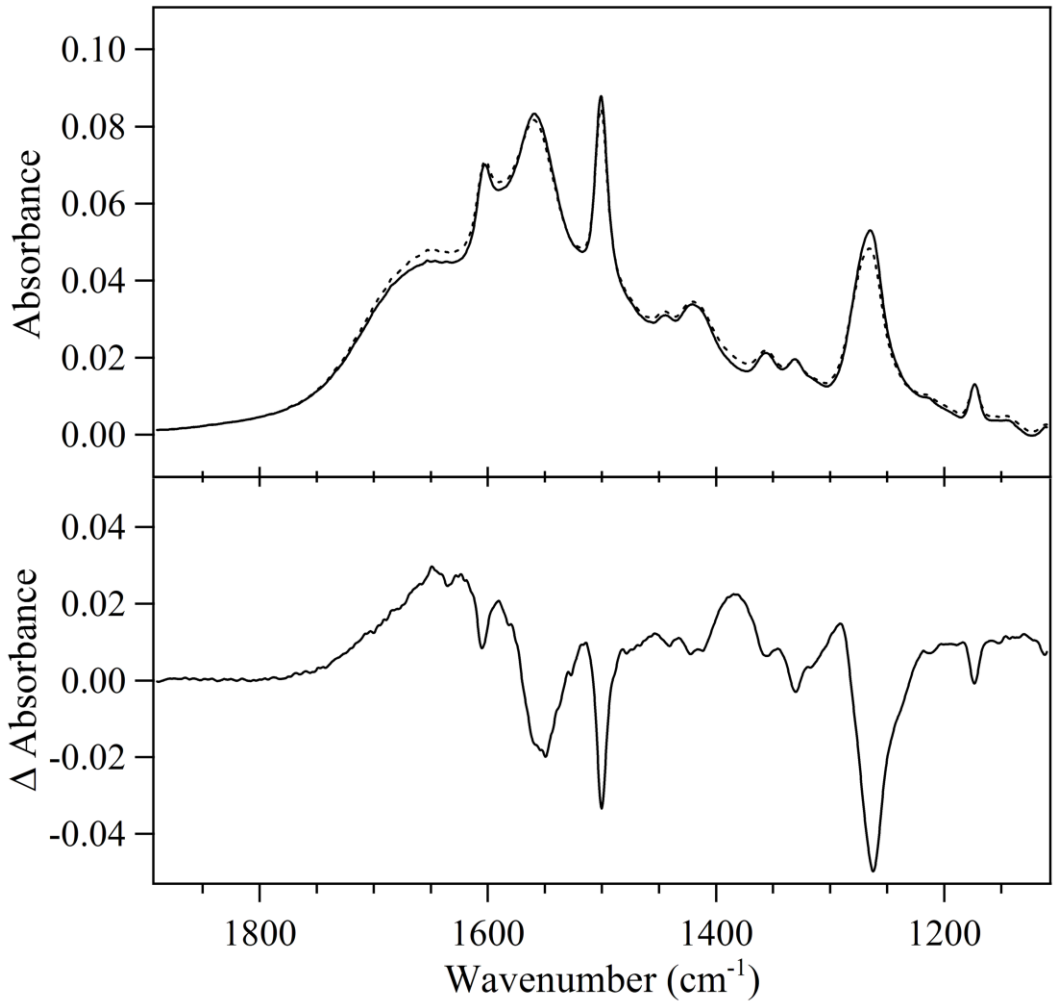

Figure 1.11. Diagram of difference spectroscopy as applied to monitoring structural changes during a reaction. The example shown here is the photo-oxidation of tyrosinate to generate the tyrosyl radical at 79 K. *Top*: FT-IR absorbance spectra of tyrosinate before (solid line) and after (dashed line) 5 laser pulses from the 266 nm output of Nd:YAG laser. *Bottom*: Photolysis-induced FT-IR difference spectrum of tyrosinate. The bottom spectrum was multiplied by 10 for clarity.

Assignments to vibrational modes may be accomplished through the comparison to model compounds and stable isotope labeling. Since a vibration is related to the reduced mass of the atoms involved in the motion, vibrational modes are sensitive to isotopes. Difference FT-IR spectroscopy with isotope incorporation has led to the assignment of crucial events and vibrational modes in the photosystems[213,217] and cytochrome *c* oxidase.[98,209,210]

1.5.2 Ultraviolet Resonance Raman Spectroscopy

Raman spectroscopy has proven to be a powerful technique for probing structural elements of aqueous biological samples and for providing conformational information of the target molecule due to the low Raman cross-section of water. This technique involves exciting the sample with a single wavelength and recording the resulting inelastic (i.e. Raman) scattered photons. Scattered radiation consists of Stokes and Anti-Stokes scattering, which correspond to the cases when the photon loses or gains energy, respectively, upon interaction with the molecule. The difference in energy between the frequency of incident radiation and Stokes/AntiStokes frequencies correlate to vibrational and rotational energies, v_n, (see Figure 1.12). Thus, the Raman spectrum displays analogous frequencies to infrared spectra. In contrast to infrared spectroscopy, for vibrational modes to be Raman active, the polarizability tensor (α) of the induced dipole must change during the course of the vibration. Dipole moments (μ) of atoms are induced by an electric field (E): $\mu = \alpha E$. The resulting signal intensity (I_n) of a Raman band of frequency, v_n, be expressed as: $I_n = \frac{2^7 \pi^5}{3^2 c^4} (v_s)^4 I_0 \sum_{if} \left| \alpha_{if} \right|^2$, where I_0 is the intensity of the

incident radiation, c is the speed of light, v_s is the frequency of the scattered light ($v_n = v_0 - v_s$), and v_0 is the frequency of the incident beam.[218] For the resonant Raman effect, the polarizability scattering tensor α can be expressed adiabatically as: $\alpha_{if} = \mathrm{A} + \mathrm{B} + \mathrm{C}$.[218,219] Of this equation, the A-term enhancement is caused from Frank-Condon electronic overlap of ground and excited states and results in only totally symmetric modes. In B-term enhancement, nontotally symmetric modes dominate and are caused through mixing of two different excited states. The C-term involves excitation of forbidden or weakly allowed 0-0 electronic transitions and provides enhancement of overtones and combination modes.

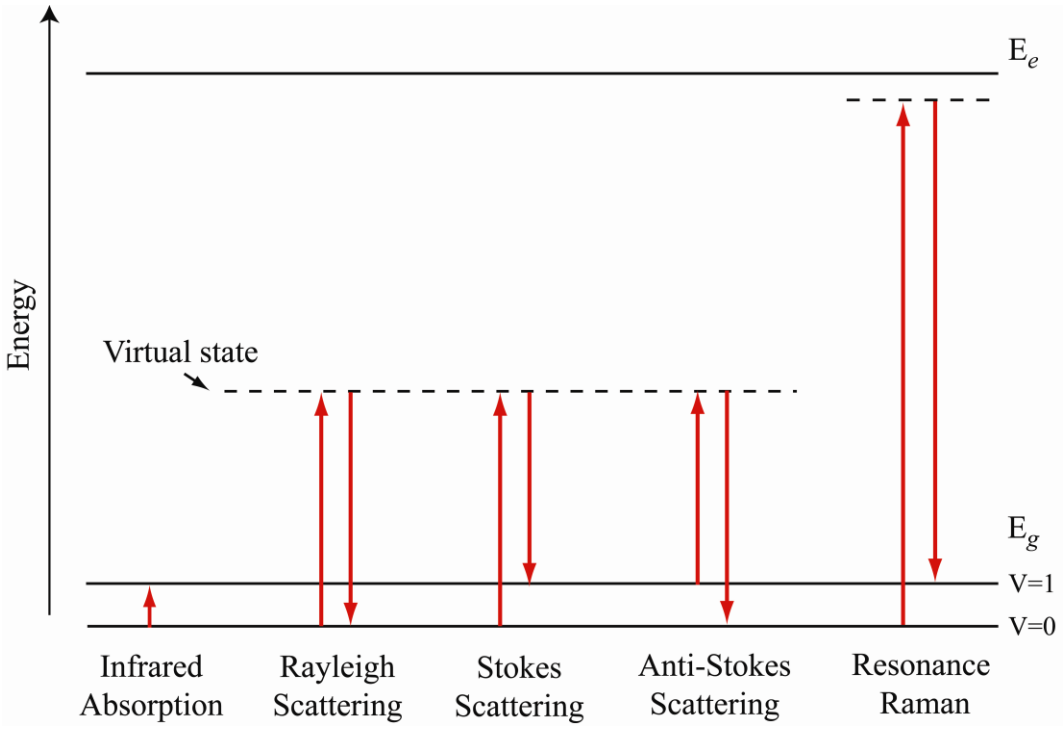

Figure 1.12. Energy level diagram representing the different Raman processes and infrared absorption scheme for reference. Adapted from reference [220].

Resonance Raman spectroscopy results from a resonant effect, in which the intensities for of Raman-active modes are selectively enhanced when the energy of the incident photons approaches an electronic transition (E_e). Thus, the technique permits the selective monitoring of specific chromophores in large biological systems. In additions, this resonance process allows for the use of concentrations as low as 10^{-8} M. The theory and principles of the resonance Raman effect have been well reviewed and described previously.[220-223]

Resonance Raman spectroscopy has been used in both visible and UV regions for a variety of applications.[224-226] Ultraviolet resonance Raman (UVRR) spectroscopy has been extended to study structure and dynamics in a number of protein systems.[227-230] In our lab, UVRR difference spectroscopy has been used to study the structural dynamics of PSI[190] and the electron transfer intermediates of PSII.[231] In RNR, Raman spectroscopy has previously been used to assign the hydrogen bonding state of Y• in the mouse and *E. coli* β2 proteins as well as to elucidate structural details of diiron center.[142] Prior to this thesis work, ultraviolet resonance Raman spectroscopy had not been applied to the study of RNR chemistry.

1.6 Electron Paramagnetic Resonance Spectroscopy

Electron paramagnetic resonance (EPR) spectroscopy uses microwave radiation to detect and study paramagnetic molecules, which include organic radicals, transition ions and triplet states. In the presence of a magnetic field (see Figure 1.13), the degeneracy of one unpaired electron spin is split into two spin states, $m_s = + ½$ and $m_s = - ½$, where m_s

is the quantum number for the *z* component of the electron spin. The splitting of degenerate states in the presence of an external magnetic field is called the Zeeman effect.[232] Resonance between the magnetic field-induced energy states occurs when $\Delta E = h\nu = g_e\mu_B B$ is met. In this equation, *h* is Planck's constant, *v* is microwave frequency (in GHz), g_e is the electron *g*-factor, μ_B is the Bohr magneton, and B is the applied magnetic field. The magnetic moment or *g*-factor of a free electron is 2.002322.[232] However, the local environment surrounding an electron perturbs the magnetic moment and thus, structural information can be obtained from the determined *g*-factor(s). In these cases, the resonance is represented as $\Delta E = g_e(1-\sigma)\mu_B B = g\mu_B B$, in which g is the *g*-factor for the radical and σ is the measure of the shielding from the surrounding environment. Additionally, the electron spin may be delocalized over an area of the molecule in organic radicals. For example, the resulting unpaired electron spin is delocalized over the 1′, 3′, and 5′ carbons of the phenoxyl ring and oxygen for the neutral tyrosyl radical generated from light-irradiated tyrosinate powder samples.[23,233]

The number of allowed values for the spin angular momentum, $\hat{\mathbf{S}}$, is given by (2*S*+1). With one unpaired electron (e.g. tyrosyl radical), the multiplicity allowed ($2*(^1/_2) + 1$) is 2 as shown in Figure 1.13. However, with two or more electrons, *S* can be 1, $^3/_2$, 2 … and the resulting multiplicity allowed is equal to 3, 4, 5… respectively. In all cases in this thesis work, *S* = ½ is valid and situations with higher *S* values will not be discussed further.

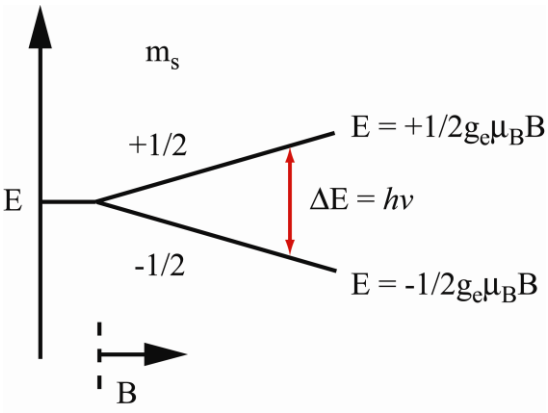

Figure 1.13. Energy diagram for a free electron as a function of the applied magnetic field (B). The m_s represents the quantum number for the spin moment of the electron oriented either parallel (m_s = - ½) or antiparallel (m_s = + ½) to the magnetic field. The red arrow illustrates the situation when the splitting of the energy level, induced by the applied magnetic field intensity, is in resonance with the microwave frequency.

The magnetic moment of the unpaired electron is sensitive to the orientation of any nearby magnetic dipole. The existence of a magnetic dipole, either electronic or nuclear, can cause splitting of the resonance and is referred to as hyperfine splitting. Much like for the electron spin angular momentum, the nuclear spin angular momentum ($\hat{\mathbf{I}}$) has ($2I$ + 1) number of allowed energy states. Figure 1.14 illustrates the effect of a nearby nuclear spin (I = ½) on the EPR spectrum for an unpaired electron (S = ½). The field experienced by an unpaired electron is the sum of the external, applied magnetic field (B_{app}) and the nuclear spin magnetic field (B_{loc}): $B_{loc} = B_{app} + a_1 m_{I1} + a_2 m_{I2} + ... a_n m_{In}$, in which a is the hyperfine splitting constant and m_I is the quantum number for the z component of the nuclear spin angular momentum. There are two types of hyperfine splitting interactions: isotropic and anisotropic. Isotropic hyperfine splitting is orientation independent; anisotropic hyperfine splitting is dependent on the orientation of the external magnetic field with respect to the molecular axis of the radical. The hyperfine

coupling values obtained from X-band and high-frequency EPR spectroscopies provide valuable information concerning the spin density delocalization and structural details of the environment surrounding the radical.

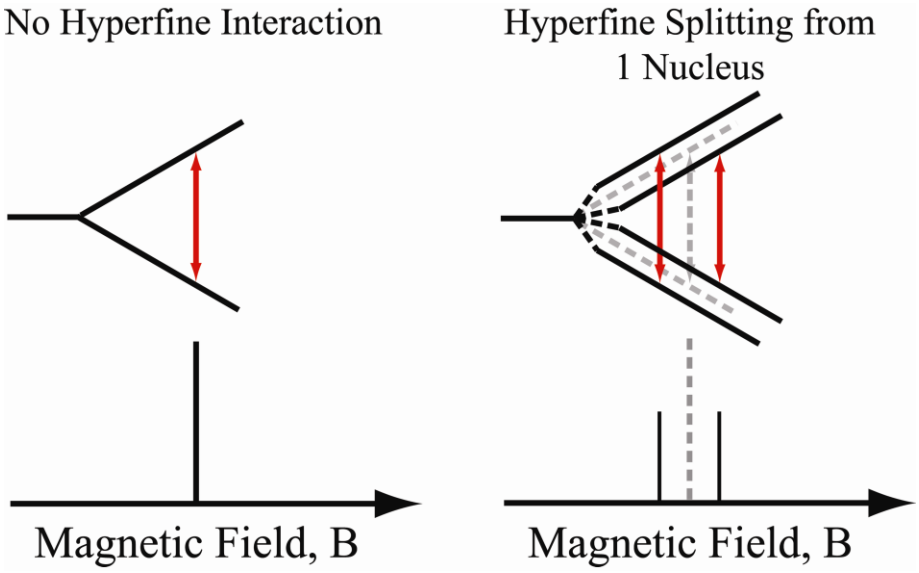

Figure 1.14. Diagram of electron energy levels in applied magnetic field (B) and corresponding expected EPR lines (*bottom*). *Right:* Hyperfine splitting of energy levels induced by nucleus of $I = ½$ (e.g. hydrogen atom). *a* is the hyperfine splitting constant for a particular nuclear spin. The dashed gray line (*bottom*, *right*) is the expected absorbance line if $a = 0$. The red arrow illustrates the situation when the splitting of the energy levels, induced by the applied magnetic field intensity, is in resonance with the microwave frequency.

For example, the EPR signal of Y122• in Figure 1.15II is centered at g ~ 2.0047[234] similar to that of a light generated crystalline tyrosyl radical (Figure 1.15I),[235] but exhibits a lineshape difference.[20] The spin distribution is delocalized at the phenolic oxygen and the 1′, 3′, and 5′ carbons of the tyrosyl radical ring,[236] similar to tyrosyl radicals in model tyrosinate powders.[233, 23] The differences between the model tyrosyl radical and Y122 EPR lineshape are attributed to the stressed angle (~30°)[237] of the

phenyl ring relative to the β-methylene protons. The spin delocalized on the 1′-carbon interacts with the β-methylene protons in an angular dependence[238] and results in the hyperfine splitting of tyrosyl radical EPR signals. β,β-{^{2}H}-tyrosine labeling causes the collapse of the Y122• doublet to a singlet.[236] The protons of the 3' and 5' carbons account for the remaining hyperfine splitting patterns.[130]

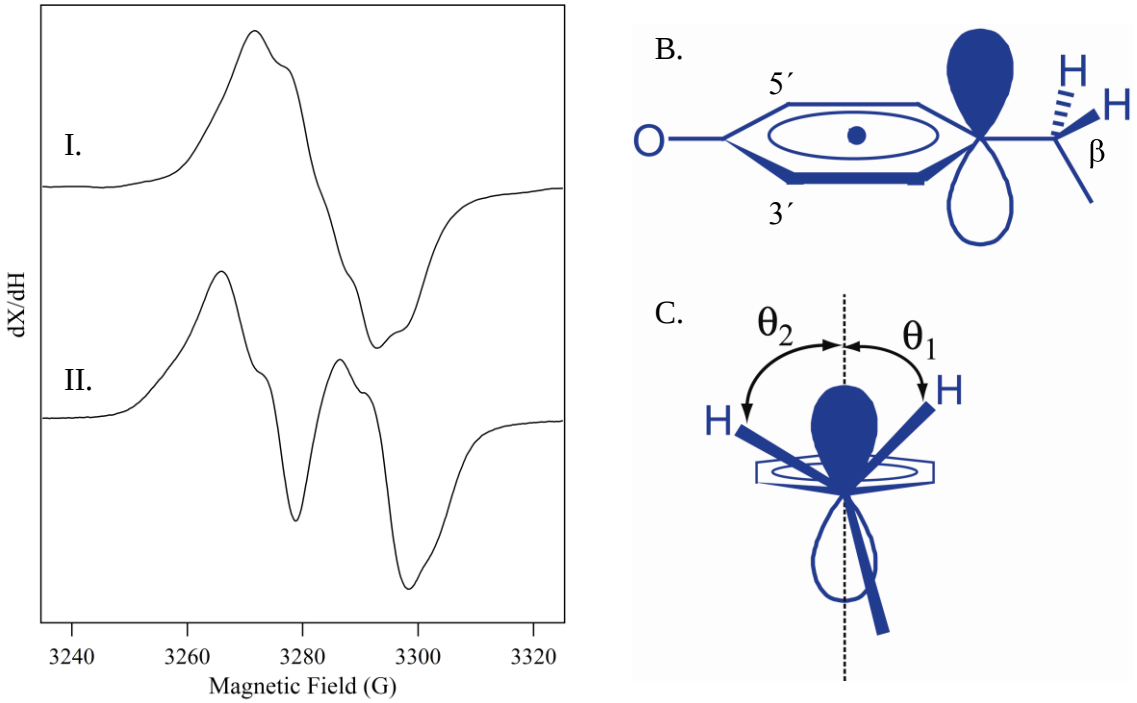

Figure 1.15. X-band EPR spectra of the tyrosyl radicals from (I) photolysis-induced tyrosinate samples and from (II) Y122• in ribonucleotide reductase. B) Diagram of tyrosyl radical. C) Schematic view of tyrosyl radical along C1′-Cβ bond. Figures B and C are adapted from reference 12.

EPR spectroscopy has been an invaluable tool towards the structural study of ribonucleotide reductase. This technique has been applied to characterize the spin delocalization of Y122• in β2,[236] to help develop the current proposed mechanism for nucleotide reduction using radical-trapping substrate analogs,[132,239,240] and to elucidate the

mechanism of the β2 activation process.[241,242] The structure of intermediate **X**, which is the intermediate proposed to be responsible for Y122 oxidation, has been studied extensively with EPR spectroscopy. Prior to the UV-Visible spectroscopy correlation for determining Y122•/β2,[139] EPR spectroscopy was used to first quantify the Y122• content in ribonucleotide reductase.[158] EPR spectroscopy can be used to determine second order reduction kinetics for β2-Y122• electron scavengers,[243,244] A high-field EPR study was among the first studies to characterize protein conformational changes linked with Y122 oxidation. A ring rotation along the Cα-Cβ bond of Y122 was proposed.[153]

1.7 Thesis Overview

In this thesis, conformational changes that accompany a PCET reaction and iron assembly have been identified in ribonucleotide reductase. To monitor such structural changes, FT-IR and UV resonance Raman spectroscopies have been used.

In Chapter 2, the mechanism of electron transfer involving tyrosine in synthesized pentapeptide (RSYTH, IYPIG, EYPIG, and RYPIG) model compounds was investigated. Structural changes at the amide bond were proposed from FT-IR spectroscopic data. These structural changes were shown to be dependent on the amino acid content of the peptide. The results suggested that the composition of the primary sequence in proteins may influence the redox properties of amino acid radicals in biological systems.

In Chapter 3, the role of the unique post-translational modified tyrosine-histidine cross-link in cytochrome *c* oxidase was studied in a synthesized model compound. Spectrophotometric titrations suggested that the cross-linked tyrosine residue plays a key

role in proton donation during O_2 reduction. EPR spectroscopic data suggest that the copper is not spin coupled to the light-generated phenoxyl radical. Cryogenic FT-IR spectroscopy led to the unambiguous assignment of υ(CO) mode of the phenoxyl radical in both the ligand and Cu-complex models. These data support that the cross-linked tyrosine residue may be oxidized at the Cu_B site in cytochrome *c* oxidase.

Chapter 4 describes the development of the pump injection apparatus used in the FT-IR spectroscopic studies of ribonucleotide reductase β2.

In Chapter 5, the reaction of the tyrosine radical-containing *E. coli* β2 protein with hydroxyurea, a well known Y122• reducing agent, was monitored. Using the FT-IR pump system, structural changes were observed for the β2 and hydroxyurea reaction. The results suggested that the amide I region in the β2 FT-IR spectra corresponds to local structural changes linked to Y122• redox changes.

In Chapter 6, the mechanism of Y122• reduction was investigated. FT-IR spectra of 1-{^{13}C}tyrosine-labeled β2 samples displayed loss of intensity at one of the amide I vibrational bands. These results support that the conclusion that the 1700 – 1600 cm^{-1} region exhibits local amide I structural changes.

In Chapter 7, the assembly of the metal cluster in β2 was studied using UV resonance Raman spectroscopy. The Apo-β2-minus-Met-β2 Raman data measured at pH 7.6 were consistent with the protonation of histidine. ^{15}N-histidine labeling studies supported these results. Tyrosine and tryptophan structural changes, consistent with changes in hydrogen-bonding interactions and orientation, were also observed. Protonation of histidine explains the unusual clustering of charged groups in iron-free β2 and provide further insight into the mechanism of PCET control during catalysis.

1.8 References

1. Reece, S. Y.; Hodgkiss, J. M.; Stubbe, J.; Nocera, D. G., Proton-coupled electron transfer: the mechanistic underpinning for radical transport and catalysis in biology. *Phil. Trans. R. Soc. B* **2006**, *361*, 1351-1364.

2. Cukier, R. I.; Nocera, D. G., Proton-coupled electron transfer. *Annu. Rev. Phys. Chem.* **1998**, *49*, 337-369.

3. Mayer, J. M.; Rhile, I. J., Thermodynamics and kinetics of proton-coupled electron transfer: stepwise vs. concerted pathways. *Biochim. Biophys. Acta* **2004**, *1655*, 51-58.

4. Huynh, M. H. V.; Meyer, T. J., Proton-coupled electron transfer. *Chem. Rev.* **2007**, *107*, 5004-5064.

5. Decornez, H.; Hammes-Schiffer, S., Model proton-coupled electron transfer reactions in solution: predictions of rates, mechanisms, and kinetic isotope effects. *J. Phys. Chem. A* **2000**, *104*, 9370-9384.

6. Shafirovich, V.; Dourandin, A.; Luneva, N. P.; Geacintov, N. E., The kinetic deuterium isotope effect as a probe of a proton coupled electron transfer mechanism in the oxidation of guanine by 2-aminopurine radicals. *J. Phys. Chem. B* **2000**, *104*, 137-139.

7. Weatherly, S. C.; Yang, I. V.; Thorp, H. H., Proton-coupled electron transfer in duplex DNA: driving force dependence and isotope effects on electrocatalytic oxidation of guanine. *J. Am. Chem. Soc.* **2001**, *123*, 1236-1237.

8. Hatcher, E.; Soudackov, A. V.; Hammes-Schiffer, S., Proton-coupled electron transfer in soybean lipoxygenase. *J. Am. Chem. Soc.* **2004**, *126*, 5763-5775.

9. Cukier, R. I., A theory that connects proton-coupled electron-transfer and hydrogen-atom transfer reactions. *J. Phys. Chem. B* **2002**, *106*, 1746-1757.

10. Kirby, J. P.; Roberts, J. A.; Nocera, D. G., Significant effect of salt bridges on electron transfer. *J. Am. Chem. Soc.* **1997**, *119*, 9230-9236.

11. Chang, C. J.; Chang, M. C. Y.; Damrauer, N. H.; Nocera, D. G., Proton-coupled electron transfer: a unifying mechanism for biological charge transport, amino acid radical initiation and propagation, and bond making/breaking reactions of water and oxygen. *Biochim. Biophys. Acta* **2004**, *1655*, 13-28.

12. Barry, B. A.; El-Deeb, M. K.; Sandusky, P. O.; Babcock, G. T., Tyrosine radicals in photosystem II and related model compounds. Characterization by isotopic labeling and EPR spectroscopy. *J. Biol. Chem.* **1990**, *265*, 20139-20143.

13. Dixon, W. T.; Murphy, D., Determination of the acidity constants of some phenol radical cations by means of electron spin resonance. *J. Chem. Soc., Faraday Trans. 2* **1976**, *72*, 1221-1229.

14. Harriman, A., Further comments on the redox potentials of tryptophan and tyrosine. *J. Phys. Chem.* **1987**, *91*, 6102-6104.

15. Tommos, C.; Skalicky, J. J.; Pilloud, D. L.; Wand, A. J.; Dutton, P. L., *De novo* proteins as models of radical enzymes. *Biochemistry* **1999**, *38*, 9495-9507.

16. Sibert, R.; Josowicz, M.; Porcelli, F.; Gianluigi, V.; Range, K.; Barry, B. A., Proton-coupled electron transfer in a biomimetic peptide as a model of enzyme regulatory mechanisms. *J. Am. Chem. Soc.* **2007**, *129*, 4393-4400.

17. Rhile, I. J.; Markle, T. F.; Nagao, H.; DiPasquale, A. G.; Lam, O. P.; Lockwood, M. A.; Rotter, K.; Mayer, J. M., Concerted proton-electron transfer in the oxidation of hydrogen-bonded phenols. *J. Am. Chem. Soc.* **2006**, *128*, 6075-6088.

18. Di Bilio, A. J.; Crane, B. R.; Wehbi, W. A.; Kiser, C. N.; Abu-Omar, M. M.; Carlos, R. M.; Richards, J. H.; Winkler, J. R.; Gray, H. B., Properties of photogenerated tryptophan and tyrosyl radicals in structurally characterized proteins containing rhenium(I) tricarbonyl diimines. *J. Am. Chem. Soc.* **2001**, *123*, 9495-9507.

19. Sibert, R.; Josowicz, M.; Barry, B. A., Control of proton and electron transfer in *de novo* designed, biomimetic β hairpins. *ACS Chem. Biol.* **2010**.

20. Ayala, I.; Range, K.; York, D.; Barry, B. A., Spectroscopic properties of tyrosyl radicals in dipeptides. *J. Am. Chem. Soc.* **2002**, *124*, 5496-5505.

21. Pujols-Ayala, I.; Sacksteder, C. A.; Barry, B. A., Redox-active tyrosine residues: role of the peptide bond in electron transfer. *J. Am. Chem. Soc.* **2003**, *125*, 7536-7538.

22. Vassiliev, I. R.; Offenbacher, A. R.; Barry, B. A., Redox-active tyrosine residues in pentapeptides. *J. Phys. Chem. B* **2005**, *109*, 23077-23085.

23. Barry, B. A.; Babcock, G. T., Tyrosine radicals are involved in the photosynthetic oxygen-evolving system. *Proc. Natl. Acad. Sci. U.S.A.* **1987**, *84*, 7099-7103.

24. Das, T. K.; Pecoraro, C.; Tomson, F. L.; Gennis, R. B.; Rousseau, D. L., The post-translational modification in cytochrome *c* oxidase is required to establish a functional environment of the catalytic site. *Biochemistry* **1998**, *37*, 14471-14476.

25. Pinakoulaki, E.; Pfitzner, U.; Ludwig, B.; Varotsis, C., The role of the cross-link his-tyr in the functional properties of the binuclear center in cytochrome *c* oxidase. *J. Biol. Chem.* **2002**, *277*, 13563-13568.

26. Stubbe, J.; Nocera, D. G.; Yee, C. S.; Chang, M. C. Y., Radical initiation in class I ribonucleotide reductase: long-range proton-coupled electron transfer? *Chem. Rev.* **2003**, *103*, 2167-2201.

27. Boerner, R. J.; Barry, B. A., Isotopic labeling and EPR spectroscopy show that a tyrosine residue is the terminal electron donor, Z, in manganese-depleted photosystem II preparations. *J. Biol. Chem.* **1993**, *268*, 17151-17154.

28. Ostermeier, C.; Harrenga, A.; Ermler, U.; Michel, H., Structure at 2.7 Å resolution of the *Paracoccus denitrificans* two-subunit cytochrome *c* oxidase complexed with an antibody F_v fragment. *Proc. Natl. Acad. Sci. U.S.A.* **1997**, *94*, 10547-10553.

29. Whittaker, M. M.; Whittaker, J. W., A tyrosine-derived free radical in apogalactose oxidase. *J. Biol. Chem.* **1990**, *265*, 9610-9613.

30. Ito, N.; Phillips, S. E.; Yadav, K. D. S.; Knowles, P. F., Crystal structure of a free radical enzyme, galactose oxidase. *J. Mol. Biol.* **1994**, *238*, 794-814.

31. Uhlin, U.; Eklund, H., Structure of ribonucleotide reductase protein R1. *Nature* **1994**, *370*, 533-539.

32. Sun, X.; Eliasson, R.; Pontis, E.; Andersson, J.; Buist, G.; Sjöberg, B.-M.; Reichard, P., Generation of the anaerobic *Escherichia coli* ribonucleotide reductase requires a specific activating enzyme. *J. Biol. Chem.* **1995**, *270*, 2443-2446.

33. Baldwin, J.; Krebs, C.; Ley, B. A.; Edmondson, D. E.; Huynh, B. H.; Bollinger, J. M., Jr., Mechanism of rapid electron transfer during oxygen activation in the R2 subunit of *Escherichia coli* ribonucleotide reductase. 1. Evidence for a transient tryptophan radical. *J. Am. Chem. Soc.* **2000**, *122*, 12195-12206.

34. Krebs, C.; Chen, S.; Baldwin, J.; Ley, B. A.; Patel, U.; Edmondson, D. E.; Huynh, B. H.; Bollinger, J. M., Jr., Mechanism of rapid electron transfer during oxygen activation in the R2 subunit of *Escherichia coli* ribonucleotide reductase. 2. Evidence for and consequences of blocked electron transfer in the W48F variant. *J. Am. Chem. Soc.* **2000**, *122*, 12207-12219.

35. Kim, S. T.; Sancar, A.; Essenmacher, C.; Babcock, G. T., Time-resolved EPR studies with DNA photolyase: excited-state FADHo abstracts an electron from Trp-306 to generate FADH-, the catalytically active form of the cofactor. *Proc. Natl. Acad. Sci. U.S.A.* **1993**, *90*, 8023-8027.

36. Baron, A. J.; Stevens, C.; Wilmot, C.; Seneviratne, K. D.; Blakeley, V.; Dooley, D. M.; Phillips, S. E.; Knowles, P. F.; McPherson, M. J., Structure and mechanism of galactose oxidase. The free radical site. *J. Biol. Chem.* **1994**, *269*, 25095-25105.

37. Sivaraja, M.; Goodin, D. B.; Smith, M.; Hoffman, B. M., Identification by ENDOR of Trp191 as the free-radical site in cytochrome *c* peroxidase compound ES. *Science* **1989**, *245*, 738-740.

38. Shih, C.; Museth, A. K.; Abrahamsson, M.; Blanco-Rodriguez, A. M.; Di Bilio, A. J.; Sudhamsu, J.; Crane, B. R.; Ronayne, K. L.; Towrie, M.; A., V. J.; Richards, J. H.; Winkler, J. R.; Gray, H. B., Tryptophan-accelerated electron flow through proteins. *Science* **2008**, *320*, 1760-1762.

39. Marcus, R. A.; Sutin, N., Electron transfers in chemistry and biology. *Biochim. Biophys. Acta* **1985**, *811*, 265-322.

40. Marcus, R. A., Electron transfer reactions in chemistry. Theory and experiment. *Rev. Mod. Phys.* **1993**, *65*, 599-610.

41. Hopfiled, J. J., Electron transfer between biological molecules by thermally activated tunneling. *Proc. Natl. Acad. Sci. U.S.A.* **1974**, *71*, 3640-3644.

42. Beratan, D. N.; Betts, J. N.; Onuchic, J. N., Protein electron transfer rates set by the bridging secondary and tertiary structure. *Science* **1991**, *252*, 1285-1288.

43. Gray, H. B.; Winkler, J. R., Electron tunneling through proteins. *Quart. Rev. Biophys.* **2003**, *36*, 341-372.

44. Gray, H. B.; Winkler, J. R., Electron transfer in proteins. *Annu. Rev. Biochem.* **1996**, *65*, 537-561.

45. Beratan, D. N.; Onuchic, J. N.; Betts, J. N.; Bowler, B. E.; Gray, H. B., Electron tunneling pathways in ruthenated proteins. *J. Am. Chem. Soc.* **1990**, *112*, 7915-7921.

46. Moser, C. C.; Keske, J. M.; Warncke, K.; Farid, R. S.; Dutton, P. L., Nature of biological electron transfer. *Nature* **1992**, *355*, 796-802.

47. Winkler, J. R.; Gray, H. B., Electron tunneling in proteins: role of the intervening medium. *J. Biol. Inorg. Chem.* **1997**, *2*, 399-404.

48. Davidson, V. L., What controls the rates of interprotein electron-transfer reactions. *Acc. Chem. Res.* **2000**, *33*, 87-93.

49. Haumann, M.; Liebisch, P.; Müller, C.; Barra, M.; Grabolle, M.; Dau, H., Photosynthetic O_2 formation tracked by time-resolved X-ray experiments. *Science* **2005**, *310*, 1019-1021.

50. Barry, B. A.; Cooper, I. B.; De Riso, A.; Brewer, S. H.; Vu, D. M.; Dyer, R. B., Time-resolved vibrational spectroscopy detects protein-based intermediates in the photosynthetic oxygen-evolving cycle. *Proc. Natl. Acad. Sci. U.S.A.* **2006**, *103*, 7288-7291.

51. Ge, J.; Yu, G.; Ator, M. A.; Stubbe, J., Pre-steady-state and steady-state kinetic analysis of *E. coli* class I ribonucleotide reductase. *Biochemistry* **2003**, *42*, 10071-10083.

52. Loll, B.; Kern, J.; Saenger, W.; Zouni, A.; Biesiadka, J., Towards complete cofactor arrangement in the 3.0 Å resolution structure of photosystem II. *Nature* **2005**, *438*, 1040-1044.

53. Guskov, A.; Kern, J.; Gabdulkhakov, A.; Broser, M.; Zouni, A.; Saenger, W., Cyanobacterial photosystem II at 2.9-Å resolution and the role of quinones, lipids, channels and chloride. *Nat. Struct. Mol. Biol.* **2009**, *16*, 334-342.

54. Yocum, C. F., The calcium and chloride requirements for photosynthetic water oxidation. In *Manganese Redox Enzymes*, Pecoraro, V. L., Ed. VCH Publishers: New York, 1992; pp 71-83.

55. Olesen, K.; Andreasson, L.-E., The function of the chloride ion in photosynthetic oxygen evolution. *Biochemistry* **2003**, *42*, 2025-2035.

56. Diner, B. A.; Rappaport, F., Structure, dynamics, and energetics of the primary photochemistry of photosystem II of oxygenic photosynthesis. *Annu. Rev. Plant Biol.* **2002**, *53*, 551-580.

57. Groot, M. L.; Pawlowicz, N. P.; van Wilderen, L.; Breton, J.; van Stokkum, I. H. M.; van Grondelle, R., Initial electron donor and acceptor in isolated photosystem II reaction centers identified with femtosecond mid-IR spectroscopy. *Proc. Natl. Acad. Sci. U.S.A.* **2005**, *102*, 13087-13092.

58. Holzwarth, A. R.; Müller, M. G.; Reus, M.; Nowaczyk, M.; Sander, J.; Rögner, M., Kinetics and mechanism of electron transfer in intact photosystem II and in the isolated reaction center: pheophytin is the primary electron acceptor. *Proc. Natl. Acad. Sci. U.S.A.* **2006**, *103*, 6895-6900.

59. Diner, B. A.; Schlodder, E.; Nixon, P. J.; Coleman, W. J.; Rappaport, F.; Lavergne, J.; Vermaas, W. F. J.; Chisholm, D. A., Site-directed mutations at D1-His198 and D2-His197 of photosystem II in *Synechocystis* PCC 6803: sites of

primary charge separation and cation and triplet stabilization. *Biochemistry* **2001**, *40*, 9265-9281.

60. Rappaport, F.; Guergova-Kuras, M.; Nixon, P. J.; Diner, B. A., Kinetics and pathways of charge recombination in photosystem II. *Biochemistry* **2002**, *41*, 8518-8527.

61. Grabolle, M.; Dau, H., Energetics of primary and secondary electron transfer in photosystem II membrane particles of spinach revisited on basis of recombination-fluorescence measurements. *Biochim. Biophys. Acta* **2005**, *1708*, 209-218.

62. Nuijs, A. M.; Vangorkom, H. J.; Plijter, J. J.; Duysens, L. N. M., Primary charge separation and excitation of chlorophyll *a* in photosystem II particles from spinach as studied by picosecond absorbency-difference spectroscopy. *Biochim. Biophys. Acta* **1986**, *848*, 167-175.

63. Trissl, H. W.; Leibl, W., Primary charge separation in photosystem II involves two electrogenic steps. *FEBS Lett.* **1989**, *244*, 85-88.

64. Debus, R. J.; Barry, B. A.; Sithole, I.; Babcock, G. T., Directed mutagenesis indicates that the donor to P_{680}^{+} in photosystem II is Tyr-161 of the D1 polypeptide. *Biochemistry* **1988**, *27*, 9071-9074.

65. Gerken, S.; Brettel, K.; Schlodder, E.; Witt, H. T., Optical characterization of the immediate donor to chlorophyll a_{II}^{+} in O_2-evolving photosystem II complexes. *FEBS Lett.* **1988**, *237*, 69-75.

66. Dekker, J. P.; Plijter, J. J.; Ouwehand, L.; Gorkom, H. J. V., Kinetics of manganese redox transitions in the oxygen-evolving apparatus of photosynthesis. *Biochim. Biophys. Acta* **1984**, *325*, 483-503.

67. Joliot, P.; Barbieri, G.; Chabaud, R., A new model of photochemical centers in system-2. *Photochem. Photobiol.* **1969**, *10*, 309-329.

68. Kok, B.; Forbush, B.; McGloin, M., Cooperation of charges in photosynthetic O_2 evolution-I. A linear four step mechanism. *Photochem. Photobiol.* **1970**, *11*, 457-475.

69. Dau, H.; Haumann, M., Reaction cycle of photosynthetic water oxidation in plants and cyanobacteria. *Science* **2006**, *312*, 1471-1472.

70. Junge, W.; Clausen, J.; Penner-Hahn, J. E.; Yocum, C. F.; Dau, H.; Haumann, M., Photosynthetic oxygen production. *Science* **2006**, *312*, 1470-1472.

71. Penner-Hahn, J. E.; Yocum, C. F., Photosynthetic oxygen production: response. *Science* **2006**, *312*, 1471-1472

72. McEvoy, J. P.; Brudvig, G. W., Water-splitting chemistry of photosystem II. *Chem. Rev.* **2006**, *106*, 4454-4483.

73. Debus, R. J.; Barry, B. A.; Babcock, G. T.; McIntosh, E. M., Site-specific mutagenesis identifies a tyrosine radical involved in the photosynthetic oxygen-evolving complex. *Proc. Natl. Acad. Sci. U.S.A.* **1988**, *85*, 427-430.

74. Vermaas, W. F. J.; Rutherford, A. W.; Hansson, Ö., Site-directed mutagenesis in photosystem II of the cyanobacterium *Synechocystis sp.* PCC 6803: donor D is a tyrosine residue in the D2 protein. *Proc. Natl. Acad. Sci. U.S.A.* **1988**, *85*, 8477-8481.

75. Noren, G. H.; Barry, B. A., The YF161D1 mutant of *Synechocystis* 6803 exhibits an EPR signal from a light-induced photosystem II radical. *Biochemistry* **1992**, *31*, 3335-3342.

76. Diner, B. A.; Britt, R. D., Photosystem II: the light-driven water; plastoquinone oxidoreductase. In *Advances in Photosynthesis and Respiration*, Wydrzynski, T. J.; Satoh, K., Eds. Springer: Dordrecht, The Netherlands, 2005; p 205.

77. Zouni, A.; Witt, H.-T.; Kern, J.; Fromme, P.; Kraß, N.; Saenger, W.; Orth, P., Crystal structure of photosystem II from *Synechococcus elongatus* at 3.8 Å resolution. *Nature* **2001**, *409*, 739-743.

78. Kamiya, N.; Shen, J.-R., Crystal structure of oxygen-evolving photosystem II from *Thermosynechococcus vulanus* at 3.7 Å resolution. *Proc. Natl. Acad. Sci. U.S.A.* **2003**, *100*, 98-103.

79. Ferreira, K. N.; Iverson, T. M.; Maghlaoui, K.; Barber, J.; Iwata, S., Architecture of the photosynthetic oxygen-evolving center. *Science* **2004**, *303*, 1831-1837.

80. Boussac, A.; Etienne, A. L., Midpoint potential of signal II (slow) in tris-washed photosystem II particles. *Biochim. Biophys. Acta* **1984**, *766*, 576-581.

81. Metz, J. G.; Nixon, P. J.; Rögner, M.; Brudvig, G. W.; Diner, B. A., Directed alteration of the D1 polypeptide of photosystem II: evidence that tyrosine-161 is the redox component, Z, connecting the oxygen-evolving complex to the primary electron donor P680. *Biochemistry* **1989**, *28*, 6960-6969.

82. Vass, I.; Styring, S., pH-dependent charge equilibria between tyrosine-D and the S states in photosystem II. Estimation of relative midpoint redox potentials. *Biochemistry* **1991**, *30*, 830-839.

83. Ishikita, H.; Knapp, E. W., Function of redox-active tyrosine in photosystem II. *Biophys. J.* **2006**, *90*, 3886-3896.

84. Rutherford, A. W.; Boussac, A.; Faller, P., The stable tyrosyl radical in photosystem II: why D? *Biochim. Biophys. Acta* **2004**, *1655*, 222-230.

85. Ananyev, G. M.; Sakiyan, I.; Diner, B. A.; Dismukes, G. C., A functional role for tyrosine-D in assembly of the inorganic core of the water oxidase complex of photosystem II and the kinetics of water oxidation. *Biochemistry* **2002**, *41*, 974-980.

86. Rova, M.; Mamedov, F.; Magnuson, A.; Fredriksson, P.-O.; Styring, S., Coupled activation of the donor and the acceptor side of photosystem II during photoactivation of the oxygen evolving cluster. *Biochemistry* **1998**, *37*, 11039-11045.

87. Ferguson-Miller, S.; Babcock, G. T., Heme/copper terminal oxidases. *Chem. Rev.* **1996**, *96*, 2889-2907.

88. Wikström, M. K. F., Proton pump coupled to cytochrome c oxidase in mitochondrion. *Nature* **1977**, *266*, 271-273.

89. Ludwig, B.; Bender, E.; Arnold, S.; Hüttemann, M.; Lee, I.; Kadenbach, B., Cytochrome *c* oxidase and the regulation of oxidative phosphorylation. *ChemBioChem* **2001**, *2*, 392-403.

90. Yoshikawa, S.; Shinzawa-Itoh, K.; Nakashima, R.; Yanoe, R.; Yamashita, E.; Inoue, N.; Yao, M.; Fei, M. J.; Libeu, C. P.; Mitzushima, T.; Yamaguchi, H.; Tomizaki, T.; Tsukihara, T., Redox-coupled crystal structure changes in bovine heart cytochrome *c* oxidase. *Science* **1998**, *280*, 1723-1731.

91. Soulimane, T.; Buse, G.; Bourenkov, G. P.; Bartunik, H. D.; Huber, R.; Than, M. E., Structure and mechanism of the aberrant ba_3-cytochrome *c* oxidase from *Thermus thermophilus*. *EMBO J.* **2000**, *19*, 1766-1776.

92. Gennis, R. B., Multiple proton-conducting pathways in cytochrome oxidase and a proposed role for the active-site tyrosine. *Biochim. Biophys. Acta* **1998**, *1365*, 241-248.

93. Proshlyakov, D. A.; Pressler, M. A.; Babcock, G. T., Dioxygen activation and bond cleavage by mixed-valence cytochrome *c* oxidase. *Proc. Natl. Acad. Sci. U.S.A.* **1998**, *95*, 8020-8025.

94. Sucheta, A.; Szundi, I.; Einarsdóttir, Ó., Intermediates in the reaction of fully reduced cytochrome *c* oxidase with dioxygen. *Biochemistry* **1998**, *37*, 17905-17914.

95. Blomberg, M. R. A.; Sieghbahn, P. E. M.; Babcock, G. T.; Wikström, M., O-O bond splitting mechanism in cytochrome oxidase. *J. Inorg. Biochem.* **2000**, *80*, 261-269.

96. Proshlyakov, D. A.; Pressler, M. A.; DeMaso, C.; Leykam, J. F.; Dewitt, D. L.; Babcock, G. T., Oxygen activation and reduction in respiration: involvement of redox-active tyrosine 244. *Science* **2000**, *290*, 1588-1591.

97. Tomson, F.; Bailey, J. A.; Gennis, R. B.; Unkefer, C. J.; Li, Z. H.; Silks, L. A.; Martinez, R. A.; Donohoe, R. J.; Dyer, R. B.; Woodruff, W. H., Direct infrared detection of the covalently ring linked his-tyr structure in the active site of the heme-copper oxidases. *Biochemistry* **2002**, *41*, 14383-14390.

98. Nyquist, R. M.; Heitbrink, D.; Bolwien, C.; Gennis, R. B.; Heberle, J., Direct observation of protonation reactions during the catalytic cycle of cytochrome *c* oxidase. *Proc. Natl. Acad. Sci. U.S.A.* **2003**, *100*, 8715-8720.

99. Svistunenko, D. A.; Wilson, M. T.; Cooper, C. E., Tryptophan or tyrosine? On the nature of the amino acid radical formed following hydrogen peroxide treatment of cytochrome *c* oxidase. *Biochim. Biophys. Acta* **2004**, *1655*, 372-380.

100. Elliott, G. I.; Konopelski, J. P., Complete *N*-1 regiocontrol in the formation of *N*-arylimidazoles. Synthesis of the active site his-tyr side chain coupled dipeptide of cytochrome *c* oxidase. *Org. Lett.* **2000**, *2*, 3055-3057.

101. McCauley, K. M.; Vrtis, J. M.; Dupont, J.; van der Donk, W. A., Insights into the functional role of the tyrosine-histidine linkage in cytochrome *c* oxidase. *Org. Lett.* **2000**, *122*, 2403-2404.

102. Aki, M.; Ogura, T.; Naruta, Y.; Le, T. H.; Sato, T.; Kitagawa, T., UV resonance Raman characterization of model compounds of Tyr^{244} of bovine cytochrome *c* oxidase in its neutral, deprotonated anionic, and deprotonated neutral radical forms: effects of covalent binding between tyrosine and histidine. *J. Phys. Chem. A* **2002**, *106*, 3436-3444.

103. Cappuccio, J. A.; Ayala, I.; Elliott, G. I.; Szundi, I.; Lewis, J.; Konopelski, J. P.; Barry, B. A.; Einarsdóttir, Ó., Modeling the active site of cytochrome oxidase: synthesis and characterization of a cross-linked histidine-phenol. *J. Am. Chem. Soc.* **2002**, *124*, 1750-1760.

104. Kim, S. H.; Aznar, C.; Brynda, M.; Silks, L. A.; Michalczyk, R.; Unkefer, C. J.; Woodruff, W. H.; Britt, R. D., An EPR, ESEEM, structural NMR, and DFT study of a synthetic model for the covalently ring-linked tyrosine-histidine structure in the heme-copper oxidases. *J. Am. Chem. Soc.* **2004**, *126*, 2328-2338.

105. Nagano, Y.; Liu, J.; Naruta, Y.; Kitagawa, T., UV resonance Raman study of model complexes of the CuB site of cytochrome *c* oxidase. *J. Mol. Struct.* **2005**, *735-736*, 279-291.

106. Pratt, D. A.; Pesavento, R. P.; van der Donk, W. A., Model Studies of the histidine-tyrosine cross-link in cytochrome *c* oxidase reveal the flexible substituent effect of the imidazole moiety. *Org. Lett.* **2005**, *7*, 2735-2738.

107. Nagano, Y.; Liu, J.; Naruta, Y.; Ikoma, T.; Tero-Kubota, S.; Kitagawa, T., Characterization of the phenoxyl radical in model complexes for the Cu_B site of cytochrome *c* oxidase: steady-state and transient absorption measurements, UV resonance Raman spectroscopy, EPR spectroscopy, and DFT calculations for M-BIAIP. *J. Am. Chem. Soc.* **2006**, *128*, 14560-14570.

108. Thelander, L.; Reichard, P., Reduction of ribonucleotides. *Annu. Rev. Biochem.* **1979**, *48*, 133-158.

109. Jordan, A.; Reichard, P., Ribonucleotide reductases. *Annu. Rev. Biochem.* **1998**, *67*, 71-98.

110. Stubbe, J.; van der Donk, W. A., Protein radicals in enzyme catalysis. *Chem. Rev.* **1998**, *98*, 705-762.

111. Fan, H.; Villegas, C.; Wright, J. A., Ribonucleotide reductase R2 component is a novel malignancy determinant that cooperates with activated oncogenes to determine transformation and malignant potential *Proc. Natl. Acad. Sci. U.S.A.* **1996**, *93*, 14036-14040.

112. Zhou, B.-S.; Tsai, P.; Ker, R.; Tsai, J.; Ho, R.; Yu, J.; Shih, J.; Yen, Y., Overexpression of transfected human ribonucleotide reductase M2 subunit in human cancer cells enhances their invasive potential. *Clin. Exp. Metastasis* **1998**, *16*, 43-49.

113. Reichard, P., From RNA to DNA, why so many ribonucleotide reductases? *Science* **1993**, *260*, 1773-1777.

114. Stubbe, J., Ribonucleotide reductases: the link between an RNA and DNA world? *Curr. Opin. Struct. Biol.* **2000**, *10*, 731-736.

115. Solomon, E. I.; Brunold, T. C.; Davis, M. I.; Kemsley, J. N.; Lee, S.-K.; Lehnert, N.; Neese, F.; Skulan, A. J.; Yang, Y.-S.; Zhou, J., Geometric and electronic structure/function correlations in non-heme iron enzymes. *Chem. Rev.* **2000**, *100*, 235-350.

116. Högbom, M.; Stenmark, P.; Voevodskaya, N.; McClarty, G.; Gräslund, A.; Nordlund, P., The radical site in Chlamydial ribonucleotide reductase defines a new R2 subclass. *Science* **2004**, *305*, 245-248.

117. Jiang, W.; Yun, D.; Saleh, L.; Barr, E. W.; Xing, G.; Hoffart, L. M.; Maslak, M.-A.; Krebs, C.; Bollinger, J. M., Jr., A manganese(IV)/iron(III) cofactor in *Chlamydia trachomatis* ribonucleotide reductase. *Science* **2007**, *316*, 1188-1191.

118. Jordan, A.; Pontis, E.; Atta, M.; Krook, M.; Gibert, I.; Barbé, J.; Reichard, P., A second class I ribonucleotide reductase in Enterobacteriaceae: characterization of the *Salmonella typhimurium* enzyme. *Proc. Natl. Acad. Sci. U.S.A.* **1994**, *91*, 12892-12896.

119. Eriksson, M.; Uhlin, U.; Ramaswamy, S.; Ekberg, M.; Regnström, K.; Sjöberg, B.-M.; Eklund, H., Binding of allosteric effectors to ribonucleotide reductase protein R1: reduction of active-site cysteines promotes substrate binding. *Structure* **1997**, *5*, 1077-1092.

120. Eliasson, R.; Pontis, E.; Jordan, A.; Reichard, P., Allosteric regulation of the third ribonucleotide reductase (*nrdEF* enzyme) from Enterobacteriaceae. *J. Biol. Chem.* **1996**, *271*, 26582-26587.

121. Jordan, A.; Aragall, E.; Gibert, I.; Barbé, J., Promoter identification and expression analysis of *Salmonella typhimurium* and *Escherichia coli nrdEF* operons encoding one of two class I ribonucleotide reductase present in both bacteria. *Mol. Microbiol.* **1996**, *19*, 777-790.

122. Jordan, A.; Gibert, I.; Barbé, J., Two different operons for the same function: comparison of the *Salmonella typhimurium nrdAB* and *nrdEF* genes. *Gene* **1995**, *167*, 75-79.

123. Eklund, H.; Uhlin, U.; Färnegårdh, M.; Logan, D. T.; Nordlund, P., Structure and function of the radical enzyme ribonucleotide reductase. *Prog. Biophys. Mol. Biol.* **2001**, *77*, 177-268.

124. Mao, S. S.; Holler, T. P.; Bollinger, J. M., Jr.; Booker, S.; Johnston, M. I.; Stubbe, J., A model for the role of multiple cysteine residues involved in ribonucleotide reduction: amazing and still confusing. *Biochemistry* **1992**, *31*, 9733-9743.

125. Stubbe, J.; Ackles, D.; Segal, R.; Blakley, R. L., On the mechanism of ribonucleoside triphosphate reductase from *Lactobacillus leichmannii*. Evidence for 3' C--H bond cleavage. *J. Biol. Chem.* **1981**, *256*, 4843-4846.

126. Ashley, G. W.; Harris, G.; Stubbe, J., The mechanism of *Lactobacillus leichmannii* ribonucleotide reductase. Evidence for 3' carbon-hydrogen bond

cleavage and a unique role for the coenzyme B12. *J. Biol. Chem.* **1986**, *261*, 3958-3964.

127. Brown, N. C.; Canellakis, Z. N.; Lundin, B.; Reichard, P.; Thelander, L., Ribonucleoside diphosphate reductase. Purification of the two subunits, proteins B1 and B2. *Eur. J. Biochem.* **1969**, *9*, 561-573.

128. Kunz, B. A.; Kohalmi, S. E.; Kunkel, T. A.; Mathews, C. K.; McIntosh, E. M.; Reidy, J. A., International commission for protection against environmental mutagens and carcinogens. Deoxyribonucleoside triphosphate levels: a critical factor in the maintenance of genetic stability. *Mutat. Res.* **1994**, *318*, 1-64.

129. Brown, N. C.; Reichard, P., Role of effector binding in allosteric control of ribonucleoside diphosphate reductase. *J. Mol. Biol.* **1969**, *46*, 39-55.

130. Sjöberg, B.-M.; Reichard, P.; Gräslund, A.; Ehrenberg, A., The tyrosine free radical in ribonucleotide reductase from *Escherichia coli*. *J. Biol. Chem.* **1978**, *253*, 6863-6865.

131. Larsson, Å.; Sjöberg, B.-M., Identification of the stable free radical tyrosine residue in ribonucleotide reductase. *EMBO J.* **1986**, *5*, 2037-2040.

132. Stubbe, J.; van der Donk, W. A., Ribonucleotide reductases: radical enzymes with suicidal tendencies. *Chem. Biol.* **1995**, *2*, 793-801.

133. van der Donk, W. A.; Stubbe, J.; Gerfen, G. J.; Bellew, B. F.; Griffin, R. G., EPR investigations of the inactivation of *E. coli* ribonucleotide reductase with 2'-azido-2'-deoxyuridine 5'-diphosphate: evidence for the involvement of the thiyl radical of C225-R1. *J. Am. Chem. Soc.* **1995**, *117*, 8909-8916.

134. van der Donk, W. A.; Gerfen, G. J.; Stubbe, J., Direct EPR spectroscopic evidence for an allylic radical generated from (E)-2'-fluoromethyl-2'-deoxycytidine 5'-diphosphate by *E. coli* ribonucleotide reductase. *J. Am. Chem. Soc.* **1998**, *120*, 4252-4253.

135. Seyedsayamdost, M. R.; Stubbe, J., Site-specific replacement of Y_{356} with 3,4-dihydroxyphenylalanine in the β2 subunit of *E. coli* ribonucleotide reductase. *J. Am. Chem. Soc.* **2006**, *128*, 2522-2523.

136. Atkin, C. L.; Thelander, L.; Reichard, P.; Lang, G., Iron and free radical in ribonucleotide reductase: exchange of iron and Mössbauer spectroscopy of the protein B2 subunit of the *Escherichia coli* enzyme. *J. Biol. Chem.* **1973**, *248*, 7464-7472.

137. Silva, K. E.; Elgren, T. E.; Que, L., Jr.; Stankovich, M. T., Electron transfer properties of the R2 protein of ribonucleotide reductase from *Escherichia coli*. *Biochemistry* **1995**, *34*, 14093-14103.

138. Salowe, S. P.; Stubbe, J., Cloning, overproduction, and purification of the B2 subunit of ribonucleoside-diphosphate reductase. *J. Bacteriol.* **1986**, *165*, 363-366.

139. Sneeden, J. L.; Loeb, L. A., Mutations in the R2 subunit of ribonucleotide reductase that confer resistance to hydroxyurea. *J. Biol. Chem.* **2004**, *279*, 40723-40728.

140. Ortigosa, A. D.; Hristova, D.; Perlstein, D. L.; Zhang, A.; Huang, M.; Stubbe, J., Determination of the *in vivo* stoichiometry of tyrosyl radical in ββ' in *Saccharomyces cervisiae* ribonucleotide reductase. *Biochemistry* **2006**, *45*, 12282-12294.

141. Schmidt, P. P.; Andersson, K. K.; Barra, A.-L.; Thelander, L.; Gräslund, A., High field EPR studies of mouse ribonucleotide reductase indicate hydrogen bonding of the tyrosyl radical. *J. Biol. Chem.* **1996**, *271*, 23615-23618.

142. Backes, G.; Sahlin, M.; Sjöberg, B.-M.; Loehr, T. M.; Sanders-Loehr, J., Resonance Raman spectroscopy of ribonucleotide reductase. Evidence for a deprotonated tyrosyl radical and photochemistry of the binuclear iron center. *Biochemistry* **1989**, *28*, 1923-1929.

143. Karlsson, M.; Sahlin, M.; Sjöberg, B.-M., *Escherichia coli* ribonucleotide reductase. Radical susceptibility to hydroxyurea is dependent on the regulatory state of the enzyme. *J. Biol. Chem.* **1992**, *267*, 12622-12626.

144. Han, J.-Y.; Swarts, J. C.; Sykes, A. G., Kinetic study on the hydrazine and phenylhydrazine reductions of the *Escherichia coli* R2 subunit of ribonucleotide reductase. *Inorg. Chem.* **1996**, *35*, 4629-4634.

145. Lam, K.-Y.; Fortier, D. G.; Thomson, J. B.; Sykes, A. G., Kinetics of inactivation of the tyrosine radical of the B2 subunit of *E. coli* ribonucleotide reductase. *J. Chem. Soc., Chem. Commun.* **1990**, 658-660.

146. Swarts, J. C.; Aquino, M. A. S.; Han, J.-Y.; Lam, K.-Y.; Sykes, A. G., Kinetic studies on the reduction of the tyrosyl radical of the R2 subunit of *E. coli* ribonucleotide reductase. *Biochim. Biophys. Acta* **1995**, *1247*, 215-224.

147. McClarty, G. A.; Chan, A. K.; Choy, B. K.; Wright, J. A., Increased ferritin gene expression is associated with increased ribonucleotide reductase gene expression and the establishment of hydroxyurea resistance in mammalian cells. *J. Biol. Chem.* **1990**, *265*, 7539-7547.

148. Strand, K. R.; Karlsen, S.; Kolberg, M.; Røhr, Å. K.; Görbitz, C. H.; Andersson, K. K., Crystal structural studies of changes in the native dinuclear iron center of ribonucleotide reductase protein R2 from mouse. *J. Biol. Chem.* **2004**, *279*, 46794-67801.

149. van Dam, P. J.; Willems, J.-P.; Schmidt, P. P.; Pötsch, S.; Barra, A.-L.; Andersson, K. K.; Gräslund, A., High-frequency EPR and pulsed Q-band ENDOR studies on the origin of the hydrogen bond in tyrosyl radicals of ribonucleotide reductase R2 proteins from mouse and herpes simplex virus type-1. *J. Am. Chem. Soc.* **1998**, *120*, 5080-5085.

150. Nordlund, P.; Sjöberg, B.-M.; Eklund, H., Three-dimensional structure of the free radical protein of ribonucleotide reductase. *Nature* **1990**, *345*, 593-598.

151. Åberg, A.; Nordlund, P.; Eklund, H., Unusual clustering of carboxyl side chains in the core of iron-free ribonucleotide reductase. *Nature* **1993**, *361*, 276-278.

152. Logan, D. T.; Su, X.-D.; Åberg, A.; Regnström, K.; Hajdu, J.; Eklund, H.; Nordlund, P., Crystal structure of reduced protein R2 of ribonucleotide reductase: the structural basis for oxygen activation at a dinuclear iron site. *Structure* **1996**, *4*, 1053-1064.

153. Högbom, M.; Galander, M.; Andersson, M.; Kolgerg, M.; Hofbauer, W.; Lassmann, G.; Nordlund, P.; Lendzian, F., Displacement of the tyrosyl radical cofactor in ribonucleotide reductase obtained by single-crystal high-field EPR and 1.4-Å x-ray data. *Proc. Natl. Acad. Sci. U.S.A.* **2003**, *100*, 3209-3214.

154. Petersson, L.; Gräslund, A.; Ehrenberg, A.; Sjöberg, B.-M.; Reichard, P., The iron center in ribonucleotide reductase form *Escherichia coli*. *J. Biol. Chem.* **1980**, *255*, 6706-6712.

155. Sjöberg, B.-M.; Gräslund, A.; Sanders-Loehr, J.; Loehr, T. M., Ribonucleotide reductase: a structural study of the dimeric iron site. *Biochem. Biophys. Res. Commun.* **1980**, *94*, 793-799.

156. Sjöberg, B.-M.; Loehr, T. M.; Sanders-Loehr, J., Raman spectral evidence for a μ-oxo bridge in the binuclear iron center of ribonucleotide reductase. *Biochemistry* **1982**, *21*, 96-102.

157. Sahlin, M.; Petersson, L.; Gräslund, A.; Ehrenberg, A.; Sjöberg, B.-M.; Thelander, L., Magnetic interaction between the tyrosyl free radical and the antiferromagnetically coupled iron center in ribonucleotide reductase. *Biochemistry* **1987**, *26*, 5541-5548.

158. Lynch, J. B.; Juarez-Garcia, C.; Münck, E.; Que, L. J., Mössbauer and EPR studies of the binuclear iron center in ribonucleotide reductase from *Escherichia coli*. A new iron-to-protein stoichiometry. *J. Biol. Chem.* **1989**, *264*, 8091-8096.

159. Atta, M.; Nordlund, P.; Åberg, A.; Eklund, H.; Fontecave, M., Substitution of manganese for iron in ribonucleotide reductase from *Escherichia coli*. Spectroscopic and crystallographic characterization. *J. Biol. Chem.* **1992**, *267*, 20682-20688.

160. Elgren, T. E.; Ming, L.-J.; Que, L. J., Spectroscopic studies of Co(II)-reconstituted ribonucleotide reductase R2 from *Escherchia coli*. *Inorg. Chem.* **1994**, *33*, 891-894.

161. Tong, W. H.; Chen, S.; Lloyd, S. G.; Edmondson, D. E.; Huynh, B. H.; Stubbe, J., Mechanism of assembly of the diferric cluster-tyrosyl radical cofactor of *Escherichia coli* ribonucleotide reductase from the diferrous form of the R2 subunit. *J. Am. Chem. Soc.* **1996**, *118*, 2107-2108.

162. Pierce, B. S.; Hendrich, M. P., Local and global effects of metal binding within the small subunit of ribonucleotide reductase. *J. Am. Chem. Soc.* **2005**, *127*, 3613-3623.

163. Andersson, M. E.; Högbom, M.; Rinaldo-Matthis, A.; Blodig, W.; Liang, Y.; Persson, B.-O.; Sjöberg, B.-M.; Su, X.-D.; Nordlund, P., Structural and mutational studies of the carboxylate cluster in iron-free ribonucleotide reductase R2. *Biochemistry* **2004**, *43*, 7966-7972.

164. Lycksell, P.-O.; Ingemarson, R.; Davis, M. I.; Gräslund, A.; Thelander, L., ^{1}H NMR studies of mouse ribonucleotide reductase: the R2 protein carboxyl-terminal tail, essential for subunit interaction, is highly flexible but becomes rigid in the presence for protein R1. *Biochemistry* **1994**, *33*, 2838-2842.

165. Kashlan, O. B.; Scott, C. P.; Lear, J. D.; Coopermann, B. S., A comprehensive model for the allosteric regulation of mammalian ribonucleotide reductase. Functional consequences of ATP- and dATP- induced oligomerization of the large subunit. *Biochemistry* **2002**, *41*, 462-474.

166. Rofougaran, R.; Crona, M.; Vodnala, M.; Sjöberg, B.-M.; Hofer, A., Oligomerization status directs overall activity regulation of the *Escherichia coli* class Ia ribonucleotide reductase. *J. Biol. Chem.* **2008**, *283*, 35310-35318.

167. Dutia, B. M.; Frame, M. C.; Subak-Sharpe, J. H.; Clark, W. N.; Marsden, H. S., Specific inhibition of herpes virus ribonucleotide reductase by synthetic peptides. *Nature* **1986**, *321*, 439-444.

168. Yang, F. D.; Spanevello, R. A.; Celiker, I.; Hirschmann, R.; Rubin, H.; Coopermann, B. S., The carboxyl terminus heptapeptide of the R2 subunit of mammalian ribonucleotide reductase inhibits enzyme activity and can be used to purify the R1 subunit. *FEBS Lett.* **1990**, *272*, 61-64.

169. Climent, I.; Sjöberg, B.-M.; Huang, C. Y., Carboxyl-terminal peptides as probes for *Escherichia coli* ribonucleotide reductase subunit interaction: kinetic analysis of inhibition studies. *Biochemistry* **1991**, *30*, 5164-5171.

170. Reece, S. Y.; Seyedsayamdost, M. R.; Stubbe, J.; Nocera, D. G., Direct observation of a transient tyrosine radical competent for initiating turnover in a photochemical ribonucleotide reductase. *J. Am. Chem. Soc.* **2007**, *129*, 13828-13830.

171. Reece, S. Y.; Seyedsayamdost, M. R.; Stubbe, J.; Nocera, D. G., Photoactive peptides for light-initiated tyrosyl radical generation and transport into ribonucleotide reductase. *J. Am. Chem. Soc.* **2007**, *129*, 8500-8509.

172. Reece, S. Y.; Lutterman, D. A.; Seyedsayamdost, M. R.; Stubbe, J.; Nocera, D. G., Re(bpy)$(CO)_3$CN as a probe of conformational flexibility in a photochemical ribonucleotide reductase. *Biochemistry* **2009**, *48*, 5832-5838.

173. Uppsten, M.; Färnegårdh, M.; Domkin, V.; Uhlin, U., The first holocomplex structure of ribonucleotide reductase gives new insight into its mechanism of action. *J. Mol. Biol.* **2006**, *359*, 365-377.

174. Seyedsayamdost, M. R.; Chan, C. T. Y.; Mugnaini, V.; Stubbe, J.; Bennati, M., PELDOR spectroscopy with DOPA-β2 and NH_2Y-α2s: distance measurements between residues involved in the radical propagation pathway of *E. coli* ribonucleotide reductase. *J. Am. Chem. Soc.* **2007**, *129*, 15748-15749.

175. Surdhar, P. S.; Armstrong, D. A., Reduction potentials and exchange reactions of thiyl radicals and disulfide anion radicals. *J. Phys. Chem.* **1987**, *91*, 6532-6537.

176. Stubbe, J., Protein structure. Controlling radical reactions. *Nature* **1994**, *370*, 502.

177. Lide, D. R., *Handbook of Chemistry and Physics*. 72nd ed.; CRC Press: Boca Ranton, FL, 1991.

178. Barry, B. A.; Einarsdóttir, Ó., Insights into the structure and function of redox-active tyrosines from model compounds. *J. Phys. Chem. B* **2005**, *109*, 6972-6981.

179. Erickson, H. K., Formation of the cystine between cysteine 225 and cysteine 462 from ribonucleoside diphosphate reductase is kinetically competent. *Biochemistry* **2000**, *39*, 9241-9250.

180. Erickson, H. K., Kinetics in the pre-steady state of the formation of cystines in ribonucleoside diphosphate reductase: evidence for an asymmetric complex. *Biochemistry* **2001**, *40*, 9631-9637.

181. Lin, A. N. I.; Ashley, G. W.; Stubbe, J., Location of the redox-active thiols of ribonucleotide reductase: sequence similarity between the *Escherchia coli* and *Lactobacillus leichmannii* enzymes. *Biochemistry* **1987**, *26*, 6905-6909.

182. Åberg, A.; Hahne, S.; Karlsson, M.; Larsson, Å.; Ormö, M.; Ahgren, A.; Sjöberg, B.-M., Evidence for two different classes of redox-active cysteines in ribonucleotide reductase of *Escherichia coli*. *J. Biol. Chem.* **1989**, *264*, 12249-12252.

183. Rova, U.; Goodtzova, K.; Ingemarson, R.; Behraven, G.; Gräslund, A.; Thelander, L., Evidence by site-directed mutagenesis supports long-range electron transfer in mouse ribonucleotide reductase. *Biochemistry* **1995**, *34*, 4267-4275.

184. Ekberg, M.; Sahlin, M.; Eriksson, M.; Sjöberg, B.-M., Two conserved tyrosine residues in protein R1 participate in an intermolecular electron transfer in ribonucleotide reductase. *J. Biol. Chem.* **1996**, *271*, 20655-20659.

185. Ekberg, M.; Pötsch, S.; Sandin, E.; Thunnissen, M.; Nordlund, P.; Sahlin, M.; Sjöberg, B.-M., Preserved catalytic activity in an engineered ribonucleotide reductase R2 protein with a nonphysiological radical transfer pathway. The importance of hydrogen bond connections between the participating residues. *J. Biol. Chem.* **1998**, *273*, 21003-21008.

186. Rova, U.; Adrait, A.; Pötsch, S.; Gräslund, A.; Thelander, L., Evidence by mutagenesis that Tyr370 of the mouse ribonucleotide reductase R2 protein is the connecting link in the intersubunit radical transfer pathway. *J. Biol. Chem.* **1999**, *274*, 23746-23751.

187. Chang, M. C. Y.; Yee, C. S.; Nocera, D. G.; Stubbe, J., Site-specific replacement of a conserved tyrosine in ribonucleotide reductase with an aniline amino acid: a mechanistic probe for redox-active tyrosine. *J. Am. Chem. Soc.* **2004**, *126*, 16702-16703.

188. Seyedsayamdost, M. R.; Xie, J.; Chan, C. T. Y.; Schultz, P. G.; Stubbe, J., Site-specific insertion of 3-aminotyrosine into subunit $\alpha 2$ of *Escherichia coli* ribonucleotide reductase: direct evidence for involvement of Y_{730} and Y_{731} in radical propagation. *J. Am. Chem. Soc.* **2007**, *129*, 15060-15071.

189. Bender, S. L.; Barry, B. A., Light-induced dynamics in photosystem I electron transfer. *Biophys. J.* **2008**, *95*, 3927-3934.

190. Chen, J.; Bender, S. L.; Keough, J. M.; Barry, B. A., Tryptophan as a probe of photosystem I electron transfer reactions: a UV resonance Raman study. *J. Phys. Chem. B* **2009**, *113*, 11367-11370.

191. Diner, B. A.; Babcock, G. T., Structure, dynamics, and energy conversion efficiency in photosystem II. In *Oxygenic photosynthesis: the light reactions*, Ort, D. R.; Yocum, C. F., Eds. Kluwer Academic Publishers: Dordrecht, 1996.

192. Ehrenberg, A., Protein dynamics and reactions of photosystem II. *Biochim. Biophys. Acta* **2004**, *1655*, 231-234.

193. Wilson, E. B.; Decium, J. C.; Cross, P. C., *Molecular vibrations: the theory of infrared and Raman vibrational spectra*. Dover Publications: New York, 1980.

194. Silbey, R. J.; Alberty, R. A., *Physical chemistry*. 3rd ed.; Wiley: New York, 2001.

195. Susi, H.; Timashef, S. N.; Stevens, L., Infrared spectra and protein conformations in aqueous solutions I. The amide I band in H_2O and D_2O solutions. *J. Biol. Chem.* **1967**, *242*, 5460-5466.

196. Engelhard, M.; Gerwert, K.; Hess, B.; Siebert, F., Light-driven protonation changes of internal aspartic acids of bacteriorhodopsin: an investigation of static and time-resolved infrared difference spectroscopy using {4-^{13}C}aspartic acid labeled purple membrane. *Biochemistry* **1985**, *24*, 400-407.

197. Gerwert, K.; Souvignier, G.; Hess, B., Simultaneous monitoring of light-induced changes in protein side-group protonation, chromophore isomerization, and backbone motion of bacteriorhodopsin by time-resolved Fourier-transform infrared spectroscopy. *Proc. Natl. Acad. Sci. U.S.A.* **1990**, *87*, 9774-9778.

198. Braiman, M. S.; Bousche, O.; Rothschild, K. J., Protein dynamics in the bacteriorhodopsin photocycle: submillisecond Fourier transform infrared spectra of the L, M, and N photointermediates. *Proc. Natl. Acad. Sci. U.S.A.* **1991**, *88*, 2388-2392.

199. Kötting, C.; Gerwert, K., Proteins in action monitored by time-resolved FTIR spectroscopy. *ChemPhysChem* **2005**, *6*, 881-888.

200. Rothschild, K. J.; Zagaeski, M.; Cantore, W. A., Conformational changes of bacteriorhodopsin detected by Fourier transform infrared difference spectroscopy. *Biochem. Biophys. Res. Commun.* **1981**, *103*, 483-489.

201. Bagley, K.; Dollinger, G.; Eisenstein, L.; Singh, A. K.; Zimanyi, L., Fourier transform infrared difference spectroscopy of bacteriorhodopsin and its photoproducts. *Proc. Natl. Acad. Sci. U.S.A.* **1982**, *79*, 4972-4976.

202. Heberle, J.; Fitter, J.; Sass, H. J.; Büldt, G., Bacteriorhodopsin: the functional details of a molecular machine are being resolved. *Biophys. J.* **2000**, *85*, 229-248.

203. Vogel, R.; Fan, G.-B.; Sheves, M.; Siebert, F., The molecular origin of the inhibition of transduction activation in rhodopsin lacking the 9-methyl group of the retinal chromophore: a UV−Vis and FTIR spectroscopic study. *Biochemistry* **2000**, *39*, 8895-8908.

204. Zscherp, C.; Barth, A., Reaction-induced infrared difference spectroscopy for the study of protein reaction mechanisms. *Biochemistry* **2001**, *40*, 1875-1883.

205. Schweitzer-Stenner, R., Advances in vibrational spectroscopy as a sensitive probe of peptide and protein structure: a critical review. *Vib. Spectrosc.* **2006**, *42*, 98-117.

206. Berthomieu, C.; Hienerwadel, R., Fourier transform infrared (FTIR) spectroscopy. *Photosynth. Res.* **2009**, *101*, 157-170.

207. Noguchi, T.; Ono, T.; Inoue, Y., Detection of structural changes upon S1-to-S2 transition in the oxygen evolving manganese cluster in photosystem II by light-induced Fourier-transform infrared difference spectroscopy. *Biochemistry* **1992**, *31*, 5953-5956.

208. Steenhuis, J. J.; Barry, B. A., Protein and ligand environments of the S_2 state in photosynthetic oxygen evolution: a difference FT-IR study. *J. Phys. Chem. B* **1997**, *101*, 6652-6660.

209. Hellwig, P.; Pfitzner, U.; Behr, J.; Rost, B.; Pesavento, R. P.; van der Donk, W. A.; Gennis, R. B.; Michel, H.; Ludwig, B.; Mäntele, W., Vibrational modes of tyrosines in cytochrome *c* oxidase from *Paracoccus denitrificans*: FTIR and electrochemical studies on Tyr-D_4-labeled and on Tyr280His and Tyr35Phe mutant enzymes. *Biochemistry* **2002**, *41*, 9116-9125.

210. Iwaki, M.; Puustinen, A.; Wikström, M. K. F.; Rich, P. R., FTIR spectroscopy and isotope labeling of the P_M intermediate of *Paracoccus denitrificans* cytochrome *c* oxidase. *Biochemistry* **2004**, *43*, 14370-14378.

211. Breton, J.; Thibodeau, D. L.; Berthomieu, C.; Mäntele, W.; Verméglio, A.; Nabedryk, E., Probing the primary quinone environment in photosynthetic bacterial reaction centers by light-induced FTIR difference spectroscopy. *FEBS Lett.* **1991**, *278*, 257-260.

212. Breton, J.; Nabedryk, E.; Leibl, W., FTIR study of the primary electron donor of photosystem I (P700) revealing delocalization of the charge in P700+ and localization of the triplet character in ^{3}P700. *Biochemistry* **1999**, *38*, 11585-11592.

213. Kim, S.; Barry, B. A., Identification of carbonyl modes of P_{700} and P_{700}^{+} by *in situ* chlorophyll labeling in photosystem I. *J. Am. Chem. Soc.* **2000**, *122*, 4980-4981.

214. Offenbacher, A. R.; Vassiliev, I. R.; Seyedsayamdost, M. R.; Stubbe, J.; Barry, B. A., Redox-linked structural changes in ribonucleotide reductase. *J. Am. Chem. Soc.* **2009**, *131*, 7496-7497.

215. Tripathi, G. N. R.; Schuler, R. H., The resonance Raman spectrum of phenoxyl radical. *J. Chem. Phys.* **1984**, *81*, 113-122.

216. Johnson, C. R.; Ludwig, B.; Asher, S. A., Ultraviolet resonance Raman characterization of photochemical transients of phenol, tyrosine, and tryptophan. *J. Am. Chem. Soc.* **1986**, *108*, 905-912.

217. MacDonald, G. M.; Bixby, K. A.; Barry, B. A., A difference Fourier-transform infrared study of two redox-active tyrosine residues in photosystem II. *Proc. Natl. Acad. Sci. U.S.A.* **1993**, *90*, 11024-11028.

218. Albrecht, A. C., On the theory of Raman intensities. *J. Chem. Phys.* **1961**, *34*, 1476-1484.

219. Tang, J. A., A. C., Studies in Raman intensity theory. *J. Chem. Phys.* **1968**, *49*, 1144-1154.

220. Spiro, T. G., Resonance Raman spectroscopy: a new structure probe for biological chromophores. *Acc. Chem. Res.* **1974**, *7*, 339-344.

221. Johnson, B. B.; Peticolas, W. L., The resonant Raman effect. *Ann. Rev. Phys. Chem.* **1976**, *27*, 465-491.

222. Spiro, T. G.; Stein, P., Resonance effects in vibrational scattering from complex molecules. *Ann. Rev. Phys. Chem.* **1977**, *28*, 501-521.

223. Chapmion, P. M.; Korenowski, G. M.; Albrecht, A. C., On the vibronic theory of resonance Raman scattering. *Solid State Commun.* **1979**, *32*, 7-12.

224. Hu, S. Z.; Morris, I. K.; Singh, J. P.; Smith, K. M.; Spiro, T. G., Complete assignment of cytochrome c resonance Raman spectra via enzymatic reconstitution with isotopically labeled hemes. *J. Am. Chem. Soc.* **1993**, *115*, 12446-12458.

225. Gable, J. E.; Schlamadinger, D. E.; Cogen, A. L.; Gallo, R. L.; Kim, J. E., Fluorescence and UV resonance Raman study of peptide-vesicle interactions of human cathelicidin LL-37 and its F6W and F17W mutants. *Biochemistry* **2009**, *48*, 11264-11272.

226. Taniguchi, T.; Watanabe, T.; Sugiyama, N.; Subramani, A. K.; Wagata, H.; Masushita, N.; Yoshimura, M., Identifying defects in ceria-based nanocrystals by UV resonance Raman spectroscopy. *J. Phys. Chem. C* **2009**, *113*, 19789-19793.

227. Chi, Z.; Chen, X. G.; Holtz, J. S. W.; Asher, S. A., UV resonance Raman-selective amide vibrational enhancement: quantitative methodology for determining protein secondary structure. *Biochemistry* **1998**, *37*, 2854-2864.

228. Balakrishnan, G.; Weeks, C. L.; Ibrahim, M.; Soldatova, A. V.; Spiro, T. G., Protein dynamics from time resolved UV Raman spectroscopy. *Curr. Opin. Struct. Biol.* **2008**, *18*, 623-629.

229. El-Mashtoly, S. F.; Takahashi, H.; Kurokawa, H.; Sato, A.; Shimizu, T.; Kitagawa, T., Resonance Raman investigation of redox-induced structural changes of protein and heme in the sensor domain of Ec DOS protein. *J. Raman Spectrosc.* **2008**, *39*, 1614-1626.

230. Shafaat, H. S.; Sanchez, K. M.; Neary, T. J.; Kim, J. E., Ultraviolet resonance Raman spectroscopy of a beta-sheet peptide: a model for membrane protein folding. *J. Raman Spectrosc.* **2009**, *40*, 1060-1064.

231. Chen, J.; Barry, B. A., Ultraviolet resonance Raman microprobe spectroscopy of photosystem II. *Photochem. Photobiol.* **2008**, *84*, 815-818.

232. Weil, J. A.; Bolton, J. R.; Wertz, J. E., *Electron paramagnetic resonance. Elementary theory and practical applications*. John Wiley and Sons, Inc. : New York, 1994.

233. Sealy, R. C.; Harman, L.; West, P. R.; Mason, R. P., The electron spin resonance spectrum of the tyrosyl radical. *J. Am. Chem. Soc.* **1985**, *107*, 3401-3406.

234. Ehrenberg, A.; Reichard, P., Electron spin resonance of the iron-containing protein B2 from ribonucleotide reductase. *J. Biol. Chem.* **1972**, *247*, 3485-3488.

235. Fasanella, E. L.; Gordy, W., Electron spin resonance of an irradiated single crystal of L-tyrosine-HCl. *Proc. Natl. Acad. Sci. U.S.A.* **1969**, *62*, 299-304.

236. Bender, C. J.; Sahlin, M.; Babcock, G. T.; Barry, B. A.; Chandrashekar, T. K.; Salowe, S. P.; Stubbe, J.; Lindström, B.; Petersson, L.; Ehrenberg, A.; Sjöberg, B.-M., An ENDOR study of the tyrosyl free radical in ribonucleotide reductase from *Escherichia coli*. *J. Am. Chem. Soc.* **1989**, *111*, 8076-8083.

237. Sahlin, M.; Gräslund, A.; Ehrenberg, A.; Sjöberg, B.-M., Structure of the tyrosyl radical in bacteriophage T4-induced ribonucleotide reductase. *J. Biol. Chem.* **1982**, *257*, 366-369.

238. McConnell, H. M.; Heller, C.; Cole, T.; Fessenden, R. W., Radiation damage in organic crystals. I. $CH(COOH)_2$ in malonic acid. *J. Am. Chem. Soc.* **1960**, *82*, 766-775.

239. Sjöberg, B.-M.; Gräslund, A.; Eckstein, F., A substrate radical intermediate in the reaction between ribonucleotide reductase from *Escherichia coli* and 2'-azido-2'-deoxynucleoside diphosphates. *J. Biol. Chem.* **1983**, *258*, 8060-8067.

240. Ator, M.; Salowe, S. P.; Stubbe, J.; Emptage, M. H.; Robins, M. J., 2'-Azido-2'-deoxynucleotide interaction with *E. coli* ribonucleotide reductase: generation of a new radical species. *J. Am. Chem. Soc.* **1984**, *106*, 1886-1887.

241. Bollinger, J. M., Jr.; Edmondson, D. E.; Huynh, B. H.; Filley, J.; Norton, J. R.; Stubbe, J., Mechanism of assembly of the tyrosyl radical-dinuclear iron cluster cofactor of ribonucleotide reductase. *Science* **1991**, *253*, 292-298.

242. Bollinger, J. M., Jr.; Tong, W. H.; Ravi, N.; Huynh, B. H.; Edmondson, D. E.; Stubbe, J., Mechanism of assembly of the tyrosyl radical-diiron(III) cofactor of *E. coli* ribonucleotide reductase. 2. Kinetics of the excess Fe^{2+} reaction by optical, EPR, and Mössbauer spectroscopies. *J. Am. Chem. Soc.* **1994**, *116*, 8015-8023.

243. Lassmann, G.; Thelander, L.; Gräslund, A., EPR stopped-flow studies of the reaction of the tyrosyl radical of protein R2 from ribonucleotide reductase with hydroxyurea. *Biochem. Biophys. Res. Commun.* **1992**, *188*, 879-887.

244. Pötsch, S.; Sahlin, M.; Langelier, Y.; Gräslund, A.; Lassmann, G., Reduction of the tyrosyl radical and the iron center in protein R2 of ribonucleotide reductase from mouse, herpes simplex virus and *E. coli* by *p*-alkoxyphenol. *FEBS Lett.* **1995**, *374*, 95-99.

CHAPTER 2

REDOX-ACTIVE TYROSINE RESIDUES IN PENTAPEPTIDES

by

Ilya R. Vassiliev[*], Adam R. Offenbacher[†] and Bridgette A. Barry[†]

* - Deceased

† - School of Chemistry and Biochemistry and the Petit Institute for Bioengineering and Bioscience, Georgia Institute of Technology, Atlanta, GA 30332

This work was a result of the Research Experience for Undergraduates (REU) internship with Dr. Barry and resulted in the following publication that granted me a co-authorship.

Reprinted with permission from the Journal of Physical Chemistry B

Vassiliev, I. R.; Offenbacher, A. R.; Barry, B. A. "Redox-Active Tyrosine Residues in Pentapeptides." *J. Phys. Chem. B* **2005**, *109*, 23077-23085.

2.1 Abstract

Tyrosyl radicals are important in long-range electron transfer in several enzymes, but the protein environmental factors that control midpoint potential and electron-transfer rate are not well understood. To develop a more detailed understanding of the effect of protein sequence on their photophysical properties, we have studied the spectroscopic properties of tyrosyl radicals at 85 K. Tyrosyl radical was generated by UV-photolysis of pentapeptides in polycrystalline samples. The sequence of the pentapeptides was chosen to mimic peptide sequences found in redox-active tyrosine containing enzymes, ribonucleotide reductase and photosystem II. From EPR studies, we report that the EPR line shape of the tyrosyl radical depends on peptide amino acid content. We also present the first evidence for a component of the tyrosyl radical EPR signal, which decays on the seconds time scale at 85 K. We suggest that this transient results from a spontaneous, small conformational rearrangement in the radical. From FT-IR studies, we show that amide I vibrational bands (1680 – 1620 cm^{-1}) and peptide bond skeletal vibrations (1230 – 1090 cm^{-1}) are observed in the photolysis spectra of tyrosine-containing pentapeptides. From these data, we conclude that oxidation of the tyrosine aromatic ring perturbs the electronic structure of the peptide bond in tyrosine-containing oligopeptides. We also report composition dependent alterations in these bands. These results support the previous suggestion[1] that spin delocalization can occur from the tyrosine aromatic ring into the peptide bond. We hypothesize that these composition-dependent effects are mediated either by electrostatics or by changes in conformer preference in the peptides. Our findings suggest that primary structure influences the functional properties of redox-active tyrosines in enzymes.

2.2 Introduction

The aromatic side chain of tyrosine can participate in long-distance electron-transfer reactions in enzymes. In many cases, these electron-transfer reactions are essential steps in the enzyme's catalytic mechanism. For example, one-electron oxidation/reduction of a tyrosine side chain occurs in prostaglandin H synthase,[2] galactose oxidase,[3] ribonucleotide reductase (RNR)[4] and photosystem II (PSII).[5,6] While there have been previous model compound studies of tyrosyl and phenoxyl radical structure (see, for example, refs 1, 7-12, 13), the influence of peptide bond formation on the structure, function, and redox potential of the radical is not well understood.

EPR (electron paramagnetic resonance) studies have shown that the unpaired electron spin of the tyrosyl radical is primarily located on the aromatic ring, with maximum densities at the 1′, 3′ and 5′ positions.[1,11,12,14,15] Similar spin density distributions have been reported for the Y122• and Y160• radicals in RNR and PSII.[4,11,16-18]

However, it is clear that the protein environment of the tyrosine can control the function of the redox active amino acid.[19,20] One mechanism of redox potential control is suggested by recent DFT (density functional theory) calculations on tyrosyl radical, which report that spin density delocalizes to the terminal groups of tyrosine.[1] Of particular interest is the fact that the amount of spin density delocalization was predicted to be conformation-dependent. This conformation dependence offers a method for midpoint potential control,[21,20] because there is a correlation between increased spin delocalization and decreases in midpoint potential (reviewed in ref 22). In previous DFT calculations, the amount of spin density on the amino nitrogen of tyrosyl radical was

predicted to be 0.016 in the Boltzmann averaged conformation.[1] The predicted ^{14}N hyperfine interaction is less than ~0.4 G for X-band EPR. Thus, this amount of spin density delocalization is small and would not be detected by field-swept EPR techniques alone.[1] Interestingly, a coupling, which was attributed to the amide nitrogen, was detected in previous ESEEM studies of a PSII tyrosyl radical.[23] A possible, small amount of spin density delocalization in tyrosyl radical is thus easily reconcilable with previous conclusions that the sum of the spin density on the aromatic ring and the oxygen is close to one.[11,12,15]

While this predicted amount of spin density delocalization to terminal groups is small, it may be significant, particularly if it is sensitive to conformation or electrostatics. The significance could arise from control of midpoint potential, as discussed above, or from a directional control mechanism.[20] Because it is difficult to detect a small hyperfine splitting with field swept EPR spectroscopy, we used Fourier transform infrared (FT-IR) spectroscopy to test this theoretical prediction.[1] In this technique, UV photolysis pulses are applied to produce a tyrosyl radical, and FT-IR spectra are collected before and after illumination and are subtracted to construct a photolysis-induced difference spectrum. This spectrum is exquisitely sensitive to small changes in force constant. DFT calculations predicted that spin density delocalization would upshift the frequency of the amino NH bending mode.[1,24] Such an upshift was indeed detected in the photolysis FT-IR spectrum of tyrosyl radical, and the vibrational band was shown to be ^{15}N sensitive, as expected.[1] In addition, when tyrosyl radical was generated by photolysis in some tyrosine-containing dipeptides, a contribution to the FT-IR spectrum from the amide I and II (peptide bond) vibrational bands was observed.[1] Taken together, these results

suggest that spin density delocalization occurs in tyrosinate and tyrosine-containing dipeptides.

The question addressed in this paper is whether spin density delocalization can occur when tyrosyl radicals are formed in oligopeptides and, if so, whether this effect is sensitive to amino acid content.[1,25] Accordingly, we report the results of EPR and FT-IR studies of tyrosyl radicals generated in pentapeptides. The primary sequences of the pentapeptides used in our study were based on sequences containing redox-active tyrosine residues in two enzymes PS II and RNR (Figure 2.1).[26,27]

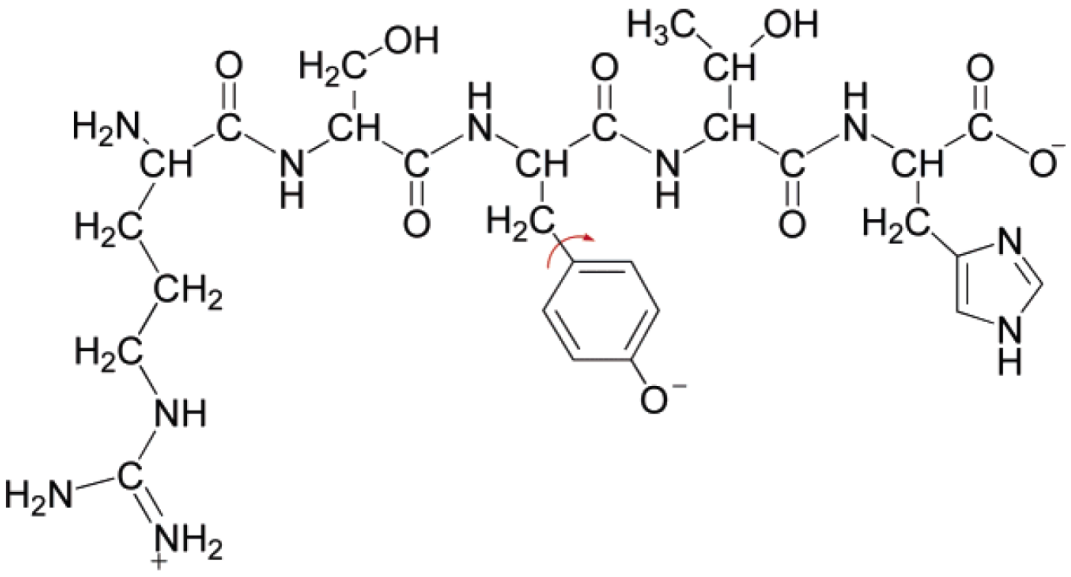

Figure 2.1. Structure of pentapeptide RSYTH, which is the sequence surrounding the tyrosyl radical in the R2 subunit of *Escherichia coli* RNR. The arrow shows the rotation of the aromatic ring along the $C_{1'}$-C_β bond.

2.3 Materials and Methods

2.3.1 Materials

L-Tyrosine (denoted as Y in the figures), boric acid, sodium hydroxide, and hydrochloric acid were purchased from Sigma (St. Louis, MO). Polyalanine (MW 1000-5000) was purchased from MP Biomedicals, LLC (Aurora, OH). The tyrosine-containing dipeptide IY and a control dipeptide, RE, were purchased from Bachem (King of Prussia, PA). The tyrosine-containing pentapeptides, IYPIG, EYPIG, RYPIG, and RSYTH were purchased from Sigma-Genosys (The Woodlands, TX). The pentapeptide samples were purified by the manufacturer on Discovery Bio Wide Pore C-18 column (mobile phase A, 0.1% TFA/water; mobile phase B, 0.1% TFA/acetonitrile). The purity of each sample was assessed from the chromatograms, monitored at 214 nm, and was reported in the range from 94 to 99% homogeneity. The UV-visible absorption spectra of the samples were recorded at 100 μM concentration in 1 cm quartz cuvettes on a Hitachi U-3000 spectrophotometer (Figure 2.2). As shown in Figure 2.2, the spectra of pentapeptides, tyrosinate, and the dipeptide, IY, were similar. The extinction coefficients of these compounds at 266 nm (used as the excitation wavelength for generation of tyrosyl radicals) were also similar, with values between 890 and 1000 M^{-1} cm^{-1}.

The sequences of pentapeptides were chosen to maximize the solubility of the synthesized peptides. The pentapeptide, IYPIG, represents the sequence containing the redox-active tyrosine, Y160, in a cyanobacterial PSII D1 subunit (NCBI entry, NP_682634[26]). Two other pentapeptides, EYPIG and RYPIG, are variants of the D1 sequence, in which the amino terminal isoleucine has been replaced by a glutamic acid or an arginine. This change in amino acid content should have the effect of modulating

peptide charge. The *Protparam*-predicted isoelectric points are 4.0 for EYPIG, 5.5 for IYPIG, and 8.8 for RYPIG (http://us.expasy.org/tools/protparam.html). The pentapeptide, RSYTH, shown in Figure 2.1, is based on the amino acid sequence containing the redox-active tyrosine, Y122, in the R2 subunit of Class I RNR from *E. coli* (NCBI entry, 1MXR_B[27]).

For EPR and FT-IR spectroscopic studies, the samples were dissolved in 10 mM borate-NaOH buffer, pH 11.00 ± 0.05. The sample concentration was 100 mM for FT-IR spectroscopy (unless indicated otherwise), and 16 mM for EPR spectroscopy.

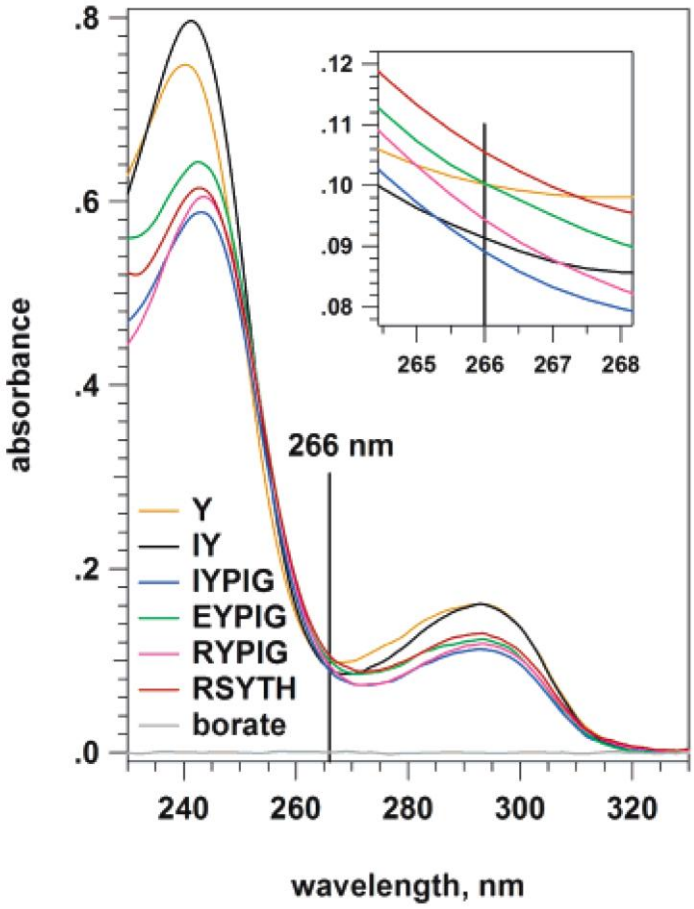

Figure 2.2. Room temperature absorption spectra of tyrosinate, dipeptide IY, pentapeptides (relative to borate buffer) and borate buffer (relative to water) measured at 1 cm path length. The inset shows the spectral absorption at 266 nm wavelength, which is the wavelength used for photolysis.

2.3.2 NMR Spectroscopy

NMR spectra of pentapeptides were recorded at room temperature on a Bruker DRX-500 NMR spectrometer operating at 500.13 MHz using a 5 mm probe equipped with Z gradients. The water peak was suppressed using a standard Watergate sequence. The samples were suspended in 10 mM borate-NaOH buffer, pH 11, containing 10% (v/v) D_2O (purchased from Cambridge Isotope Laboratories, Andover, MA). The Shigemi (Allison Park, PA) sample tubes were susceptibility matched to D_2O.

2.3.3 EPR Spectroscopy

EPR spectra were recorded in polycrystalline samples at 85 K on a Bruker EMX 6/1 (Billerica, MA) X-band EPR spectrometer with ST-9605 cavity and a Dewar insert (Wilmad Glass, Buena, NJ). The samples were placed into fused quartz sample tubes (3 mm i.d.) and frozen to 85 K under a flow of cooled nitrogen gas inside of the Dewar. A strong pitch EPR standard, g = 2.0028 ± 0.0002 (Bruker) was used for the cavity calibration and for calculation of the field offset. After recording of a background EPR spectrum for each sample, the spectrometer was switched to a time sweep with magnetic field set to 3271.5 G, and trains of flashes were fired at 6.5 s intervals from a Surelite III Nd:YAG laser (Continuum, Santa Clara, CA; wavelength, 266 nm quadrupled output; flash energy, 115 mJ; pulse width, 7 ns). The energy density incident at the EPR cavity was 234 mJ cm^{-2}, and it was attenuated as necessary with a 44% transmittance beam splitter, with a concave lens, and by increasing the laser Q-switch delay. The flash energy was measured with a Scientech (Boulder, CO) Vector S310 meter with a PHD50 pyroelectric detector. Another EPR spectrum was collected after completion of the flash

sequence, and the pre-illumination background was subtracted from this spectrum to present in Figure 2.2. A photolysis spectrum of the borate buffer was then subtracted. The spectrometer settings were as follows: microwave frequency, 9.21 GHz; power, 200 μW; modulation amplitude, 2 G; modulation frequency, 100 kHz; time constant, 81.92 ms; conversion time, 81.92 ms; number of scans, 8. Control experiments showed that there was no microwave power saturation under these conditions (data not shown). In the time-sweep mode, data acquisition parameters were the same, except that the magnetic field was set to 3271.5 G, the time constant was changed to 2.56 ms, and the conversion time was changed to 40.96 ms. Representative EPR spectra and kinetic traces are presented in the figures. The variation in EPR amplitudes from experiment to experiment was in the 10–15% range.

2.3.4 FT-IR Spectroscopy

FT-IR spectra were recorded at 85 K on a Nicolet Magna 550 II spectrometer with a MCT-A detector (Nicolet, Madison, WI) in a rapid scan mode. 6 μL liquid samples were placed between a pair of CaF_2 windows separated by a 6 μm spacer in a liquid nitrogen cryostat (R. G. Hansen & Associates, Santa Barbara, CA). 3062 interferograms were collected within 620 s at 4 cm^{-1} resolution and 2.53 cm s^{-1} mirror velocity. Three hundred seconds after the start of data collection, the sample was illuminated by a train of five laser flashes from a Surelite I or III Nd:YAG laser (Continuum, Santa Clara, CA; wavelength, 266 nm quadrupled output; flash energy, 34 mJ; pulse width, 7 ns) at a frequency of 10 Hz. The energy density incident at the IR sample was 58 mJ cm^{-2}; where indicated it was attenuated with a 44% transmittance beam splitter, with a concave lens,

and by increasing the laser Q-switch delay. Lower energy and fewer flashes were sufficient to saturate the signal compared to the EPR experiments. This was due to the short (6 μm) path length of the FT-IR sample. The set of interferograms was Fourier transformed in Omnic v.5.2 software (Nicolet, Madison, WI) using Happ-Genzel apodization, two levels of zero filling, and a Mertz phase correction. Processed data were averaged in Igor Pro v. 5.03 (Wavemetrics, Lake Oswego, OR) to produce the single beam spectra before (T_1) and after (T_2) illumination. Photolysis spectra, associated with the production of the radical (Figures 2.6 – 2.9) were calculated as $\Delta A = -\log(T_2/T_1)$. The photolysis spectrum (spline interpolated) of the borate buffer was interactively subtracted from the photolysis spectrum of each sample. For some differential spectra acquired at low excitation energy density, a smooth polynomial-fitted baseline was also subtracted from the data. The ground state absorption spectra (Figure 2.5) were calculated through ratio of the single beam spectrum (before photolysis) to an open beam background, which was recorded with no sample in the cryostat. The borate buffer absorbance spectrum was then interactively subtracted. All FT-IR data were obtained on three different samples and were averaged. The peak positions were determined with the Igor Pro "FindPeak" operation, which searches for a minimum or a maximum by analyzing the smoothed first and second derivatives of the waveforms.

2.4 Results and Discussion

2.4.1 EPR Spectroscopy of the Tyrosyl Radical

Tyrosyl radicals were generated by UV irradiation of polycrystalline samples at 85 K and detected by EPR spectroscopy. UV photolysis of an alkaline tyrosinate solution gave rise to an EPR signal (Figure 2.3, panel Ib) with an apparent *g* value of 2.0045 and a line shape similar to those previously reported for tyrosyl radical.[1,11,12] This component of the radical signal was stable between 77 and 100 K (see next section for details). The EPR line shape and the *g* value of the radical produced in the IY dipeptide (Figure 2.3, panel Ic) were similar to those observed in tyrosinate (Figure 2.3, panel Ib) and to data previously reported.[1] Some perturbation of the EPR line shape was observed when Y and IY were compared to three pentapeptides, IYPIG (Figure 2.3, panel Id), EYPIG (Figure 2.3, panel Ie) and RYPIG (Figure 2.3, panel If). The EPR spectra of these three pentapeptides were similar. However, the EPR spectrum of the R2-based pentapeptide, RSYTH (Figure 2.3, panel Ig) was distinct from the PSII-based peptides and was more similar to the spectrum generated in tyrosinate (Figure 2.3, panel Ib) or in the dipeptide IY (Figure 2.3, panel Ic). The *g* values of all tyrosine-containing samples were indistinguishable (range: 2.0042 – 2.0045), given the precision of the X-band spectrometer, which was calibrated with a strong pitch EPR standard.

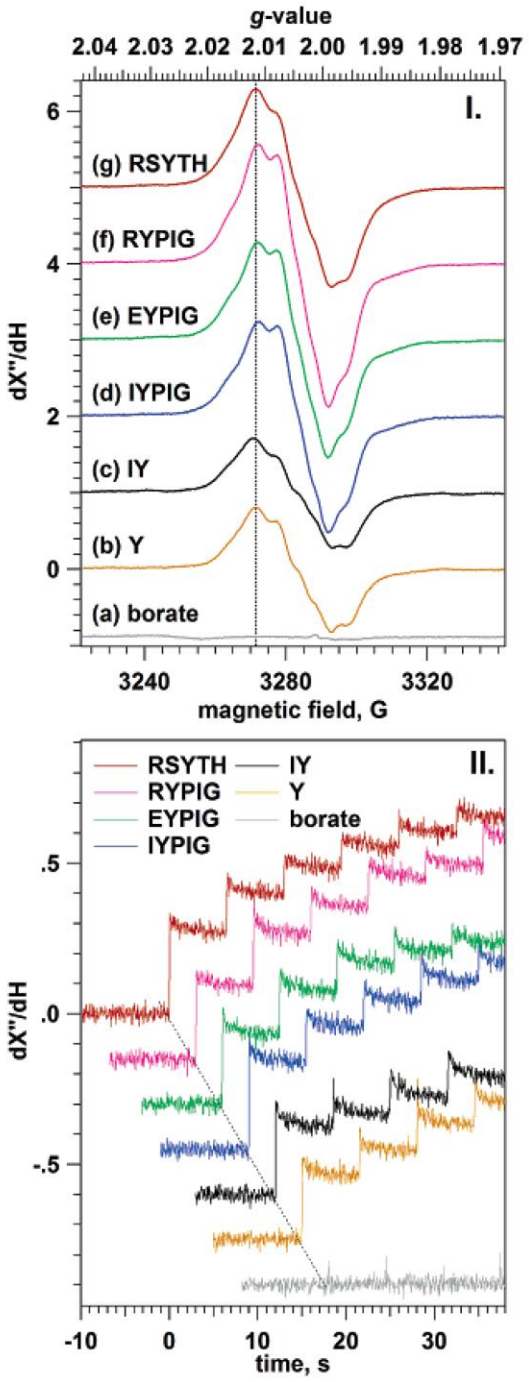

Figure 2.3. Panel I: 85 K EPR spectra of tyrosyl radicals generated by UV photolysis of tyrosinate Y (b), an isoleucine-tyrosine IY dipeptide (c), and the pentapeptides IYPIG, EYPIG, RYPIG and RSYTH (d-g). The spectra are displayed with vertical offsets. The sample concentration was 16 mM. The photolysis spectrum of borate buffer (a) was subtracted from all presented spectra (b-g). The vertical line indicates the peak position at 3271.5 G at which the kinetics (see panel II) were monitored. Panel II: Initial time course of the EPR amplitude at 3271.5 G upon multiple flash excitations. The traces are displayed with vertical and horizontal offsets.

We conclude that a tyrosyl radical is generated in all the pentapeptide compounds. However, the spectra reveal small differences, when the R2- and PSII-based peptides are compared. The EPR line shape results from hyperfine coupling of the unpaired electron with the 3´ and 5´ ring protons and with the β-protons of the methylene group. The hyperfine interaction with the β-protons depends on the dihedral angle (θ) (Figure 2.1) and is thus sensitive to rotation at the C_1-C_β single bond.[11,13,28,29] Recent DFT calculations[24] on tyrosinate and tyrosyl radical have predicted that two conformers of tyrosinate are populated at room temperature, with ring dihedral angles of +168° (conformer A) and -69° (conformer B). These conformers will be frozen in at low temperatures, where large scale conformational rearrangement is prevented. On the other hand, there is only one conformer of tyrosyl radical populated at room temperature, conformer A with a ring dihedral angle of 165°. For the radical, conformer B is predicted to be 2.5 kcal/mol higher in energy when compared to conformer A.[24] Therefore, we predict that when photolysis is carried out at 85 K, the initial, populated radical states have ring dihedral angles that are representative of the tyrosinate ground state (+168 and -69°).[24] Note that the initially populated B conformational state is predicted to be unstable in the radical and should decay at higher temperatures. These predictions are in good agreement with previous experimental results.[28,29] Therefore, we hypothesize that the spectral differences observed in Figure 2.3, panel I, may be due to small composition-dependent differences in the population of allowed tyrosyl radical conformers.

2.4.2 Stability of the Tyrosyl Radical at Cryogenic Temperatures

Tyrosyl radical generated by UV illumination at room temperature has a lifetime of 77 μs.[30] To estimate the radical stability at 85 K, the amplitude of the EPR signal was monitored at a single field position (3271.5 G, shown in Figure 2.3, panel I, by the vertical line). Following a laser flash, the EPR amplitude reached a maximum within a time period shorter than conversion time (40.96 ms) of the spectrometer's digitizer, and then decayed slightly on the seconds time scale to a steady-state level. Each consecutive flash in the 50-flash sequence resulted in a smaller amplitude increment (Figure 2.3, panel II). The interval between the flashes in this experiment was 6.5 s (to allow acquisition of 50 traces within the 8192-point acquisition limit of the spectrometer digitizer). Neither the decay nor the stable component was observed in photolysis experiments on the borate buffer alone (Figure 2.3, panel Ia and IIa).

The series of 50 kinetic segments was analyzed by a global exponential fit using Igor Pro, and the best fit resolved a decaying component, with a lifetime varying from 1 to 2 s between the samples, and a stable (nondecaying) component. The stable component has the EPR line shape shown in Figure 2.3, panel I. The lifetime of the decaying component showed no apparent correlation with the sample type. Also, the global fit residual plots indicate that the lifetime does not vary from flash to flash (data not shown). Among the six compounds, the contribution of the minor decaying component to the overall amplitude varied from 13% to 22% for the 1st flash to 1% to 6% for the 50th flash. This corresponds to a 20 – 60% decrease in its absolute amplitude over the course of the multiple flash experiments. The stable component was very stable at liquid nitrogen temperature as the photoinduced EPR signal, (Figure 2.3, panel I)

decreases only by 3 – 5% in its amplitude and does not change its line shape upon sample storage for 24 h at 77 K.

To obtain a better resolution of the kinetic components, tyrosinate samples were illuminated with trains of five flashes with longer (50 s) intervals between the flashes (Figure 2.4, panel I). Three different photon densities were employed in the 266 nm photolysis pulse. Note that the spectral line width of tyrosyl radical was independent of photolysis photon density, given the difference in signal-to-noise ratio (data not shown). Because the light-exposed sample area was larger at the lowest energy (due to use of a concave lens), the signals were first normalized to the initial amplitude (derived from a two-exponential fit), and then all five traces were analyzed by global multiexponential fitting.

Figure 2.4, panel I, shows the experimental data, the global fit curves, and the residuals of the fit. By analyzing the residuals and the standard deviations, we found that the best fit to these data is provided by a two-exponential function with a stable (nondecaying) component. In addition to the 1 – 2 s component found with the shorter interval between the flashes (Figure 2.3, panel II), a component with a lifetime of ca. 20 s was found in this analysis. Figure 2.4, panel II, shows the dependence of amplitudes on a flash number for each of the energy densities.

These data show that the fast decaying components are not caused by a photochemical or thermal artifact. Should the fast component(s) result from such an artifact, one would expect a higher contribution at higher energies. However, this is not the case, as seen from Figure 2.4, panel II. The contribution of the fastest, 0.7 s component was similar at all excitation energies.

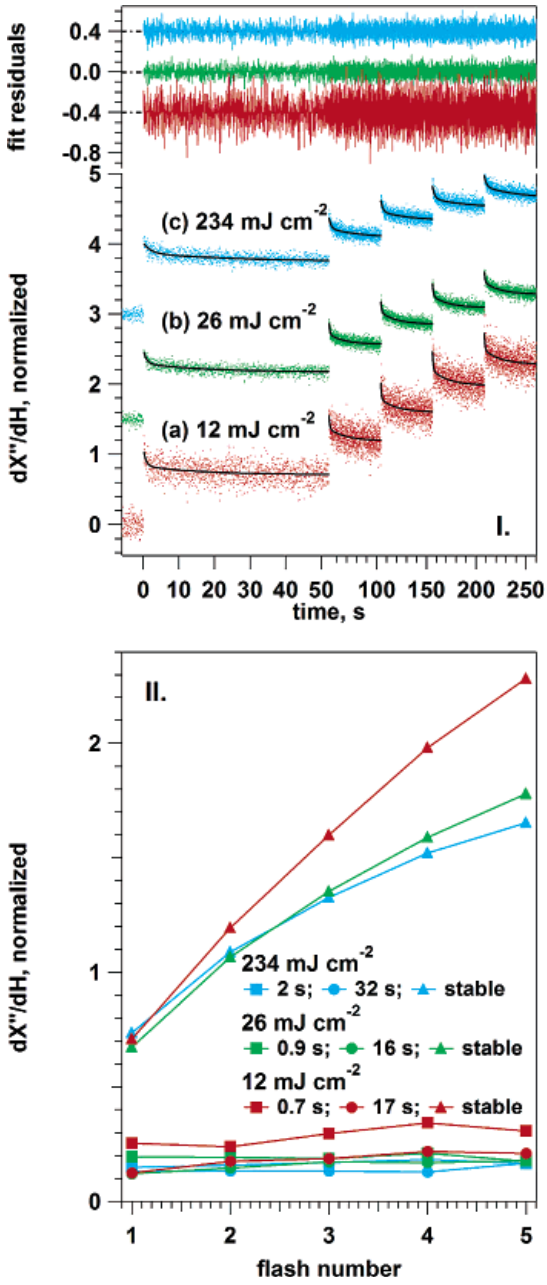

Figure 2.4. Panel I: Initial time course of the EPR amplitude at 3271.5 G upon multiple flash excitation of tyrosinate at three different energy densities. The sample concentration was 16 mM. The traces are displayed with vertical offsets, and the time scale of the first trace is horizontally expanded. Each signal is an average of data from three different samples and is normalized to its initial amplitude. Solid lines represent the global (two-exponential and a stable component) fits, with the residuals represented on an expanded vertical scale at the top of the panel in matching colors (see Materials and Methods for details). Panel II: The flash number dependencies of the normalized amplitudes of the two decaying components and the stable component. These kinetic components were derived from global analysis of the EPR signal kinetics in tyrosinate samples. Data were acquired at 85 K.

We conclude that all three EPR kinetic phases arise from tyrosyl radical. Because our DFT calculations[24] and previous experimental work from other groups[28,29] point to the existence of an unstable radical conformer (see above), we interpret the relaxing phases as slight, spontaneous conformational rearrangements in a small radical population. To explain our results, these conformational rearrangements must slightly alter the EPR amplitude at the monitoring field and must be allowed at cryogenic temperatures.

2.4.3 Ground-State FT-IR Spectra

Figure 2.5 shows the ground state spectra of tyrosinate (a), an IY dipeptide (b), and the four pentapeptides (c-f). The first two spectra are similar to previously reported spectra.[1] The most prominent difference observed in the dipeptide is the presence of a strong absorption in the amide I region (1680 – 1620 cm^{-1}), which overlaps with the OH bending band of water.[31] In the pentapeptides (Figure 2.5, parts c-f), an amide I band is also observed, as expected. The amide I band is assignable to the C=O stretching vibration of the peptide bond. This band has been used to predict secondary structural content due to its sensitivity to hydrogen bonding.[32] For pentapeptides, we expect that at room temperature there is no single, well-defined conformation, but rather that there exists an ensemble of structures, which interconvert rapidly.[33,34]

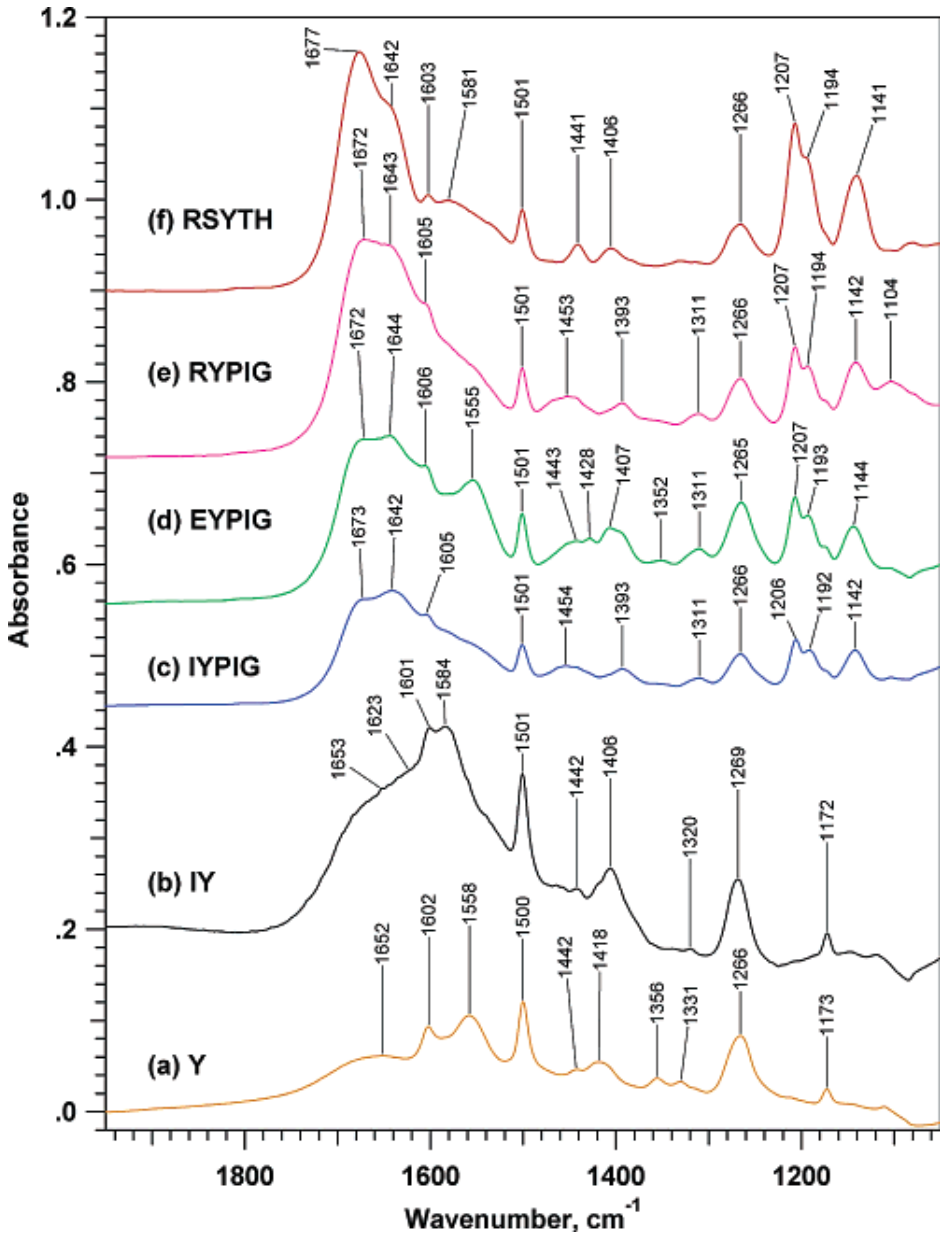

Figure 2.5. Ground-state FT-IR spectra of tyrosinate Y (a), the dipeptide IY (b) and the pentapeptides IYPIG (c), EYPIG (d), RYPIG (e), and RSYTH (f) at 85 K. The sample concentration was 100 mM. The data are displayed with vertical offsets.

When the amide I regions of the different pentapeptides are compared at cryogenic temperatures, the FT-IR absorption spectra (Figure 2.5, parts c-f) show only small frequency variations, which are probably caused by changes in relative amplitude in this region. For example, all the spectra show two similar components between 1677 and 1672 and 1644 – 1642 cm^{-1} (Figure 2.5, parts c-f). Because no large frequency variations are observed, these FT-IR absorption data provide no evidence for large changes in the average, trapped cryogenic conformation as a function of amino acid content. However, small changes in average conformation cannot be ruled out. In addition, these data provide no evidence for intermolecular hydrogen bonding,[32] which would occur if higher molecular weight oligomers were formed. Note that the pentapeptide samples (Figure 2.5, parts c-f) also exhibit bands in the 1200 – 1050 cm^{-1} region, which may be assigned to skeletal stretching vibrations of the peptide bond (see discussion below).[35,36] As expected, these bands are not present in tyrosinate or in the IY dipeptide (Figure 2.5, parts a and b).

2.4.3 Differential FT-IR Spectra

Figure 2.6 shows the photolysis-induced difference spectra of tyrosinate (a), a dipeptide IY (b), and two pentapeptides, IYPIG (c) and RSYTH (d), which are based on the sequences of the redox-active tyrosine domains in PSII and RNR, respectively. These spectra will reflect vibrational perturbations due to oxidation of tyrosinate to produce the radical. Figure 2.7 compares the spectrum of IYPIG (a) with those of EYPIG (b) and RYPIG (c), which are variants of the PSII sequence in which the terminal isoleucine has

been replaced by a glutamic acid or an arginine. This substitution will modulate the peptide charge.

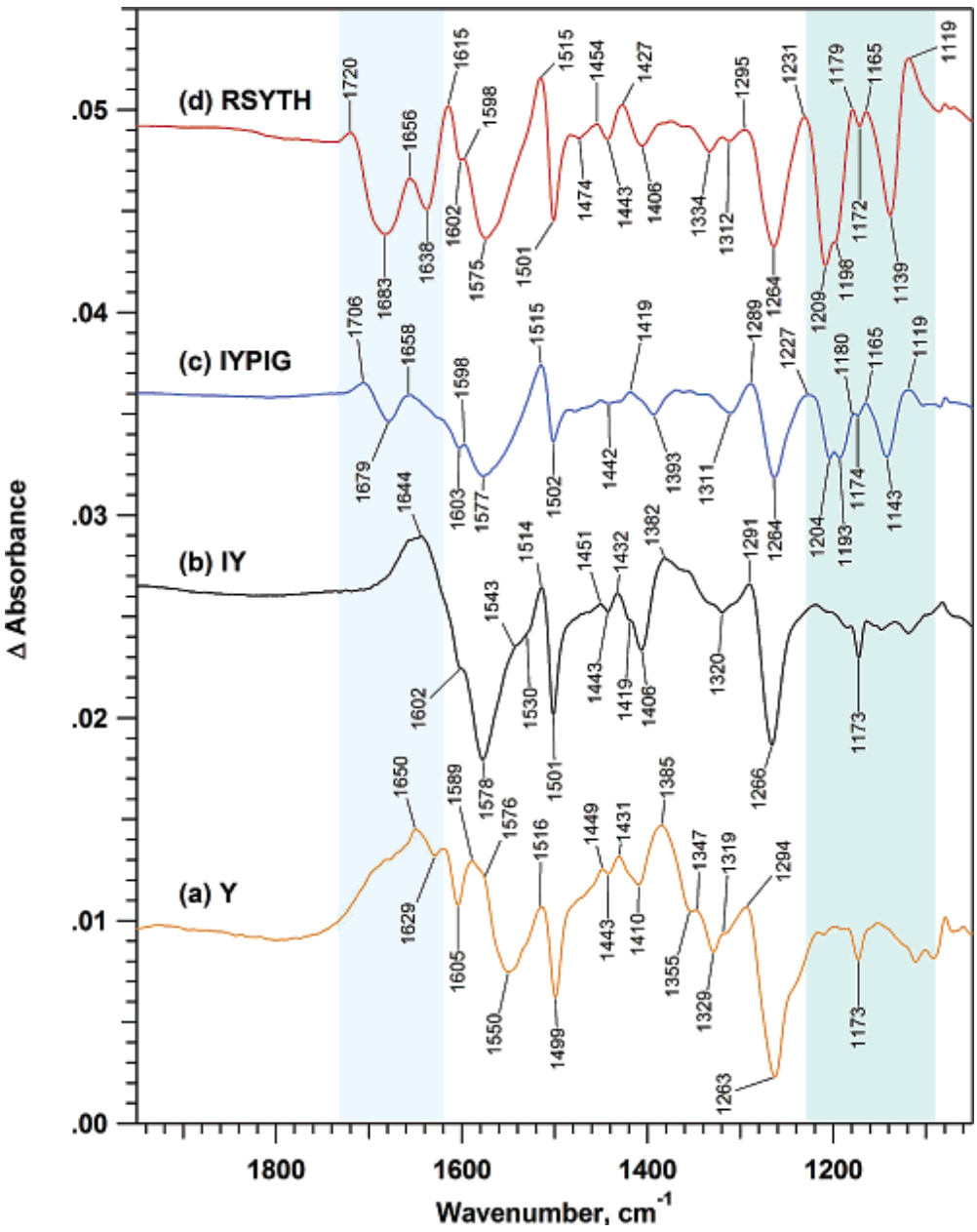

Figure 2.6. Photolysis-induced difference FT-IR spectra of Y (a), the dipeptide IY (b), and pentapeptides IYPIG (c) and RSYTH (d). Data were acquired at 85 K. The sample concentration was 100 mM in $^{1}H_2O$. The photolysis spectrum of borate buffer (Figure 2.7f) was subtracted from each spectrum. The spectra are displayed with vertical offsets. The shaded areas represent regions assigned to the peptide backbone.

The spectra of two control peptides, RE (d) and polyalanine (e), and of the borate buffer (f) are also shown in Figure 2.7 (parts d-f). As expected, photolysis produces no vibrational bands in any of the borate, RE, or polyalanine samples, which do not contain tyrosine.

Assignments of the differential absorbance bands observed in the tyrosine-containing samples are based on correlations with previously published data[1,9,10,25,37-40] and our recent density functional calculations of tyrosyl radical.[24] Unique vibrational bands of tyrosinate (Figure 2.6a) are observed as negative spectral features. Negative bands from tyrosinate are observed at 1605 – 1602 (υ_{8a}/NH_2 bend), 1502 – 1499 (υ_{19a}), 1266 – 1263 ($\upsilon_{7a'}$) and 1174 – 1172 (υ_{9a}) cm^{-1}. To summarize, two symmetric ring stretching (υ_{8a}, υ_{19a}) bands and the CO stretching ($\upsilon_{7a'}$) and CH bending (υ_{9a}) vibrational modes are observed in the photolysis spectra of tyrosinate (Figure 2.6a).[1,30] These bands are also observed in the dipeptide (Figure 2.6b) and all the pentapeptide samples (Figure 2.6, parts c and d; Figure 2.7, parts a-c) at similar frequencies. In the dipeptide and pentapeptides, oxidation also perturbs the frequency of a negative band at 1578 – 1575 cm^{-1} (Figure 2.6, parts b-d). This band may be assigned to a combination of the ring υ_{8b} stretching vibration, a carboxylate stretching mode, and an NH_2 bending mode.[24] The corresponding band is observed at 1550 cm^{-1} in the tyrosinate samples (Figure 2.6, a).[1,24] Oxidation of tyrosine is known to perturb the frequency of the CO stretching and ring stretching vibrations.[1,9,10] Unique vibrational modes of the radical will be positive bands in the photolysis spectra. A tyrosyl radical NH_2 bending/CO_2 stretching band[1,24] contributes to the spectrum at ~1640 cm^{-1}; this band overlaps a positive contribution from the OH_2 bending mode of the solvent. The broad υ_{8a} stretching vibration of the

radical is observed at ~1560 – 1550 cm^{-1}, where it also overlaps other spectral contributions. A positive band at 1516 – 1514 cm^{-1} is observed in all samples and corresponds to $\upsilon_{7a'}$ (the CO stretching) vibration of the radical.[1,24] Observation of tyrosinate and tyrosyl radical bands in the photolysis-derived FT-IR spectrum confirms that a tyrosyl radical is generated in each sample, as expected from the EPR results presented in Figure 2.3, panel I. The relative amplitudes of the ~1515 and ~1265 cm^{-1} bands give a measure of radical yield under the FT-IR conditions.

In our previous work, ^{15}N sensitive bands in the photolysis spectrum of tyrosinate at 1647/1627/1603 cm^{-1} were assigned to NH_2 bending modes. The observation of these bands was attributed to a delocalization of spin to the amino group.[1] In the photolysis spectrum of dipeptides, candidates for amide I (C=O stretch)[35] and amide II (combination CN stretch, NH bend)[35] bands were observed. For example, in the dipeptide HY, derivative-shaped bands at 1628 (-)/1620 (+) and 1548 (+)/ 1531 (-) cm^{-1} were assigned to amide I (C=O stretching) and amide II (C-N stretching, NH bending) modes, respectively.[1] In the dipeptide IY, a 1543 (+)/1531 (-) cm^{-1} shoulder was assigned to an amide II band and an inflection point at 1622 cm^{-1} was suggested to arise from an amide I band (see ref 1 and also Figure 2.6b). Observation of amide I and II bands in dipeptides was attributed to spin delocalization to the amide bond.[1] In dipeptides, there is no transition dipole coupling to complicate spectral interpretation, and the amide I band is observed at low frequency relative to the amide I band in polypeptides and proteins.

As shown in Figures 2.6 and 2.7, all the pentapeptide spectra exhibit a ~1543 cm^{-1} shoulder on the CO stretching band, which may be assignable to an amide II vibration. In addition, all pentapeptides (Figures 2.6 and 2.7) display derivative-shaped bands in the

1680 – 1620 cm^{-1} polypeptide amide I region.[35] These derivative-shaped bands have a negative component between 1684 and 1679 cm^{-1} and a positive component between 1658 and 1648 cm^{-1}. This observation is consistent with a perturbation of the amide I force constant by oxidation of the aromatic ring. Interestingly, in RSYTH, an additional 1638 (-)/ 1615 (+) cm^{-1} band (Figure 2.6, d) is also observed in the amide I region. This is an indicator of composition-specific interactions between the tyrosyl radical and the amide bond.

All pentapeptides also exhibit derivative-shaped bands in the photolysis spectra in the 1230 – 1090 cm^{-1} region (Figure 2.6, parts c and d; Figure 2.7, parts a-c), which are not present in the tyrosinate and in the dipeptide. These bands of the photolysis spectra result from perturbation of three spectral bands in the ground-state spectra at 1207 – 1206, 1194 – 1192, and 1144 – 1141 cm^{-1} (Figure 2.5, parts c-f). In the pentapeptides, these bands overlap the 1173 – 1172 cm^{-1} band (CH bending υ_{9a}), which are also present in spectra of tyrosinate and the dipeptide IY. In the photolysis spectrum of IYPIG (Figure 2.6c), the 1204/1193 cm^{-1} pair shifts down to 1180/1165 cm^{-1} and the 1143 band shifts to 1119 cm^{-1}. In the photolysis spectrum of RSYTH (Figure 2.6d), the 1209/1198 cm^{-1} pair shifts to 1179/1165 cm^{-1} and the 1139 band shifts to 1119 cm^{-1}.

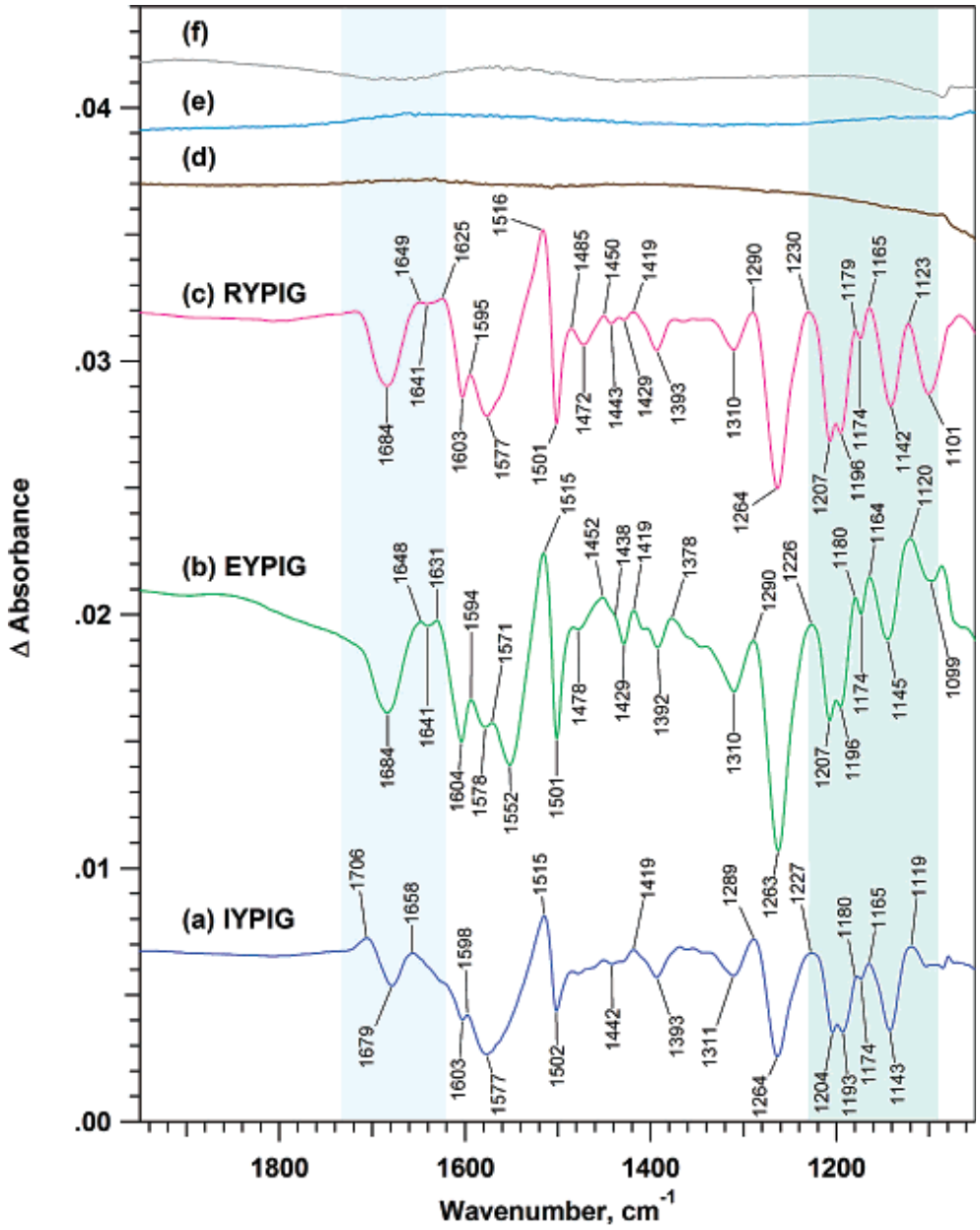

Figure 2.7. Photolysis-induced difference FT-IR spectra of IYPIG (a), EYPIG (b) and RYPIG (c), two control peptides, RE (d) and polyalanine (e), and borate buffer (f). The sample concentration was 100 mM, except for polyalanine, where the concentration was estimated as ~15–75 mM, based on the molecular mass range provided by the manufacturer. The photolysis spectrum of borate buffer (f) was subtracted from each pentapeptide's spectrum (a-c), but the control spectra (d-e) are presented without the buffer subtraction. Data were acquired at 85 K. The spectra are displayed with vertical offsets. The shaded areas represent regions assigned to the peptide backbone.

Assignments in this spectral region are complex. In previous Raman and infrared studies, spectral bands in the 1200 – 1050 cm^{-1} were assigned to CH_3 rocking vibrations, along with C–C and C–N backbone skeletal stretches.[35,41] Other spectral contributions are also possible. The higher frequency bands are similar in frequency to the calculated frequencies for the NC^{α} and the $C^{\alpha}C^{\beta}$ stretch in polyalanine, while the third band is close in its frequency to NC^{α} and $C^{\alpha}C^{\beta}$ stretching vibrations observed in polyglycine.[35] A 1204 cm^{-1} band in collagen was attributed either to amide III or CH_2 wagging vibration.[42] Note that the ground state spectrum of polyalanine has weak and relatively broad bands at 1213 and 1190 cm^{-1} (not shown), which were not perturbed, as expected, in photolysis spectrum (Figure 2.7e).

Taken together, these reports suggest that the 1230 – 1090 cm^{-1} region is associated with the vibrations of the peptide backbone. To explain their appearance in the photolysis spectrum, we propose that oxidation of the aromatic ring alters the force constants of these normal modes, as well as the force constants of the amide I and II bands. The frequencies of some of these bands do not exhibit marked composition dependency. In EYPIG (Figure 2.7b), the bands are observed at 1207/1196 cm^{-1}, 1180/1164 cm^{-1} and 1145/1120 cm^{-1}, while in RYPIG (Figure 2.7c) the bands are observed at 1207/1196, 1179/1165, and 1142/1123 cm^{-1}. However, we note the presence of a composition specific band at 1101 cm^{-1} in RYPIG (Figure 2.7c) and less prominent 1099 cm^{-1} band in EYPIG (Figure 2.7b); these bands are not noticeable in the other pentapeptides. Similar frequencies (1105 and 1108 cm^{-1}) were reported in Raman and infrared spectra of polyalanine.[35]

The spectra in Figure 2.7b also provide evidence for perturbation of an amino acid side chain, adjacent to the redox-active tyrosine. In the spectrum of EYPIG, a variant of the D1 sequence, in which the amino terminal isoleucine has been replaced by a glutamic acid to add extra negative charge, differential features at 1571 (+)/1552 (-) and 1438 (+)/1429 (-) are observed (Figure 2.7b). These unique bands are not present either in the IYPIG pentapeptide based on the original D1 sequence or in the RYPIG peptide in which isoleucine has been replaced by arginine to add extra positive charge. These frequencies are consistent with oxidation-induced perturbation of the asymmetric and symmetric stretching vibration of the adjacent carboxylic acid side chain.[43]

2.4.4 Differential FT-IR Spectra of Pentapeptides in D_2O

The photolysis-induced FT-IR difference spectra of pentapeptides dissolved in D_2O are displayed in Figure 2.8. In all pentapeptide spectra in Figure 2.8, derivative shapes at 1710–1703 (+)/1677–1675 (-)/1654–1651 (+) cm^{-1} are observed, which are not present in the tyrosinate samples (Figure 2.8e). The intensity of the $\upsilon_{7a'}$ mode for the tyrosyl radical in the spectra in Figure 2.8a–e is lower in D_2O media compared to H_2O. The observed 1628 (-)/1612 (+) cm^{-1} derivative-shaped peak in RSYTH peptide further supports the proposal of composition-specific interactions with the tyrosyl radical.

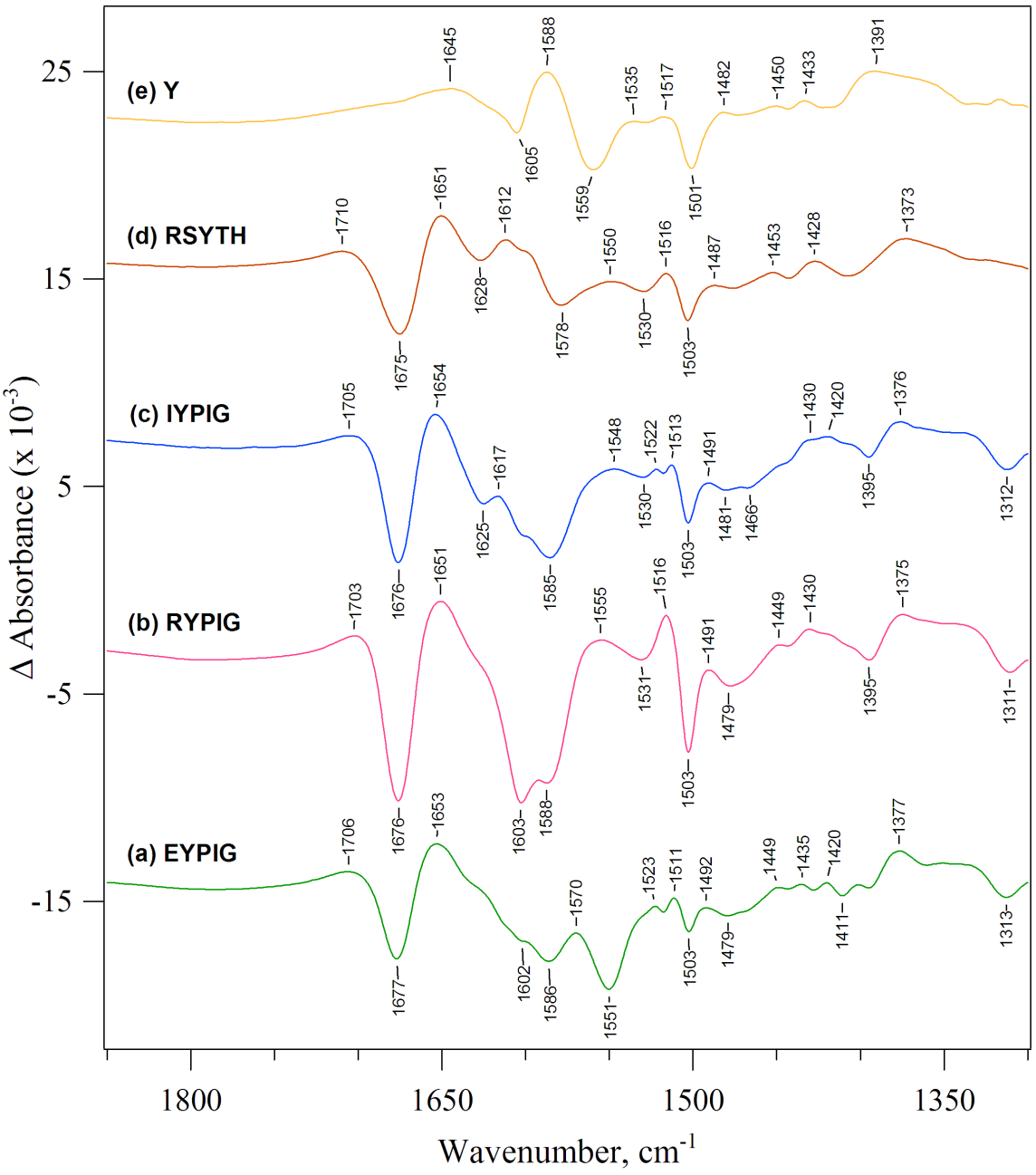

Figure 2.8. Photolysis-induced difference FT-IR spectra of EYPIG (a), RYPIG (b), IYPIG (c), RSYTH (d), and Y (e). The sample concentrations were 50 mM in 5 mM Na-borate, pD 11.0. Data were acquired at 79 K. The spectra are displayed with vertical offsets. The spectra are averages of 3 sets of different samples.

2.4.5 Photolysis Spectra Observed at Lower Photon Densities and at Lower Sample Concentrations

To rule out the possibility that bands in the photolysis spectra are due to multi photon processes, secondary products, and sample decomposition, we report FT-IR photolysis spectra of tyrosinate and two pentapeptides at excitation energy densities[8,25] times lower than used in the FT-IR experiments described above. As seen from Figure 2.9, panel I, the spectra collected at the two different energy densities consist of the same set of differential bands, although the signal-to-noise ratio is lower in the case of low excitation energy. At lower signal-to-noise, a background contribution from the ground-state absorption spectrum becomes more obvious. This background contribution resembles a roll in the differential spectrum baseline. Importantly, the sets of spectral features in the amide I region and in 1230 – 1090 cm^{-1} region are well resolved in both IYPIG (Figure 2.9b) and RSYTH (Figure 2.9c) at significantly lower energy densities.

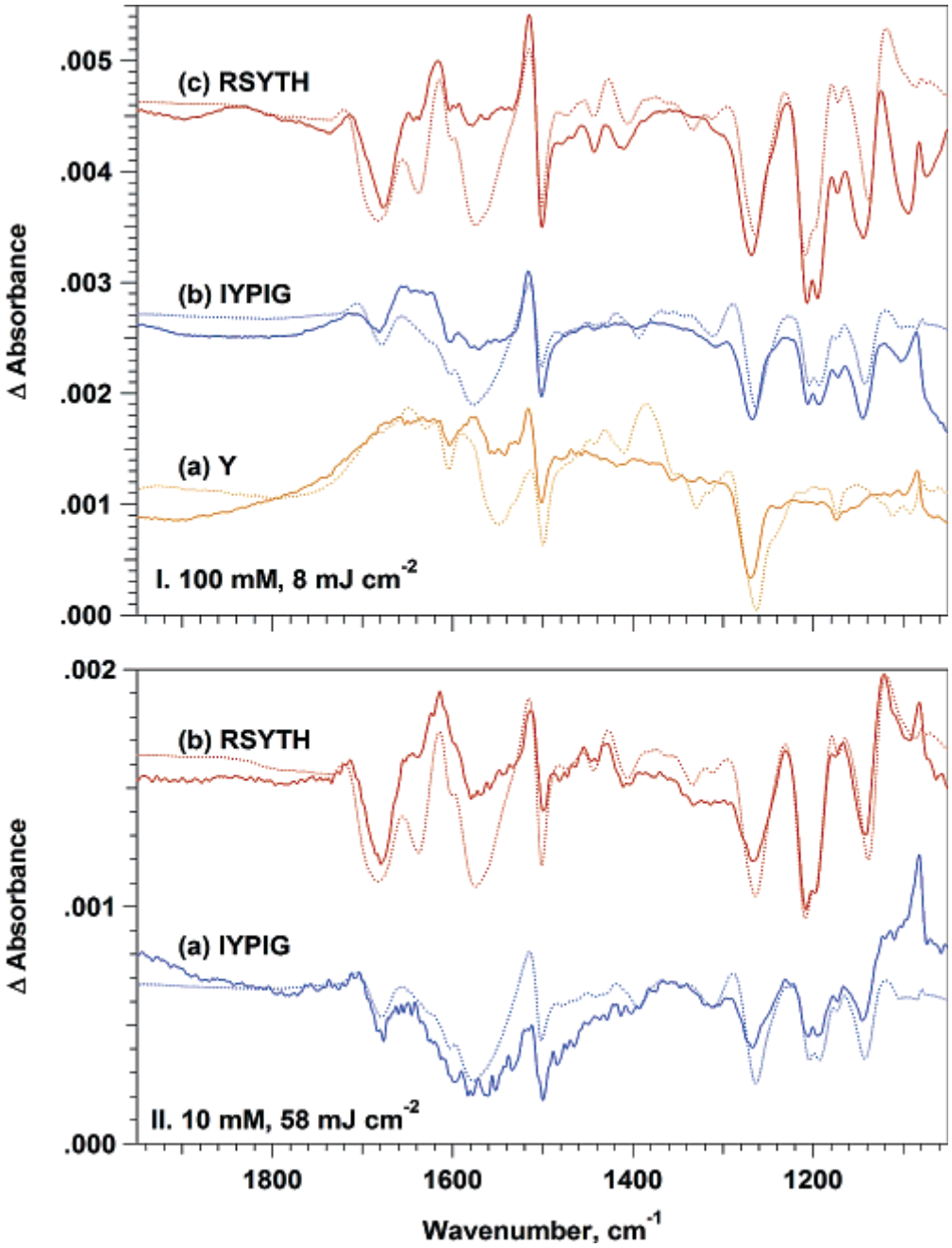

Figure 2.9. Panel I: Photolysis-induced difference FT-IR spectra of tyrosinate Y (a, solid line), IYPIG (b, solid line) and RSYTH (c, solid line) with lower photon density (8 mJ cm^{-2}) in the photolysis pulse. The dotted lines show the spectra of the corresponding pentapeptides, acquired with the standard excitation energy (58 mJ cm^{-2}). Panel II: Photolysis-induced difference FT-IR spectra of IYPIG (a, solid line) and RSYTH (b, solid line) at a concentration of 10 mM. Dotted lines represent the spectra of the corresponding pentapeptides at 100 mM on an arbitrary scale for presentation purposes. See Figure 2.6 for correct scale. Data were acquired at 85 K. The spectra are displayed with vertical offsets.

To verify whether any of the observed differential spectral features could be related to aggregation of the pentapeptides at a concentration of 100 mM, differential FT-IR spectra of two pentapeptides, IYPIG and RSYTH, were also acquired at 10 mM (Figure 2.9, panel II). The observed similarity of the 10 and 100 mM photolysis spectra (except for the difference in signal-to-noise) indicates that the differential bands do not arise from artifacts due to molecular aggregation. Another independent verification that aggregation does not occur in these peptides under these conditions (borate buffer, pH 11) is the one dimensional NMR spectrum, which is sensitive to oligomeric state.[44] Figure 2.10 shows ^{1}H NMR spectra of two pentapeptides, IYPIG (a, b) and RSYTH (c, d) at 10 and 100 mM concentrations. The common features of these spectra include peaks in the 6.5 – 7.0 ppm range, which can be ascribed to aromatic ring protons, and sets of peaks at 4.2 ppm (α-proton) and at 2.7 ppm (β-protons).[45] The unique peak at ~7.5 ppm in RSYTH can be ascribed to ring protons of histidine residue, and unique features in the 0.7 – 0 .9 ppm range in IYPIG can be ascribed to the α-protons in isoleucine.[45] Most importantly, the observed ^{1}H NMR peak line widths for the two pentapeptides, IYPIG and RSYTH are indistinguishable at 10 and 100 mM concentrations, and therefore there is no evidence of the line broadening associated with peptide oligomerization. These NMR results support conclusions reached from our analysis of the ground state FT-IR spectrum (see discussion earlier).

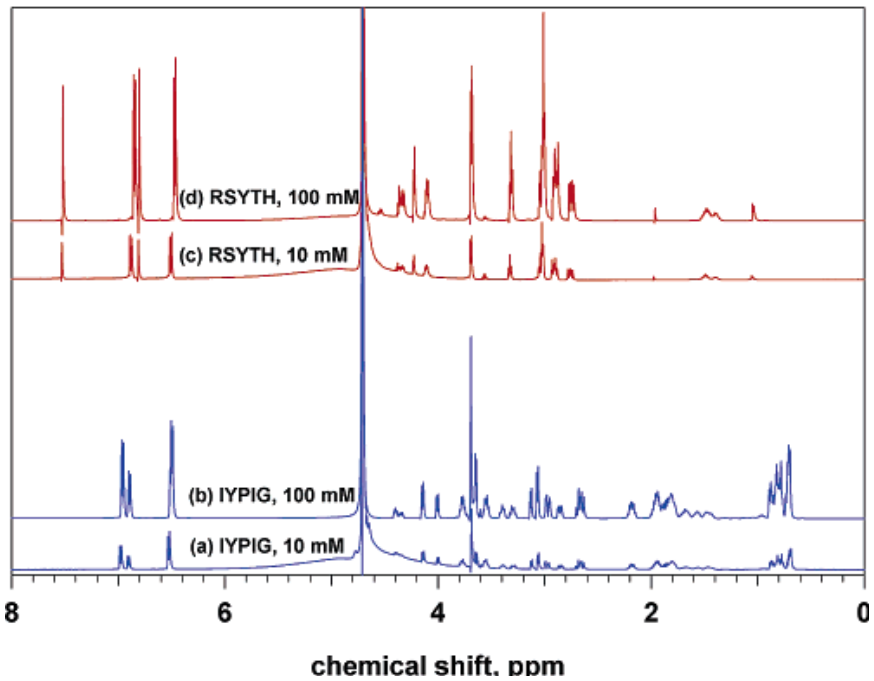

Figure 2.10. Room temperature ^{1}H NMR spectra of 10 mM IYPIG (a), 100 mM IYPIG (b), 10 mM RSYTH (c), and 100 mM RSYTH (d). The spectra are displayed with vertical offsets.

2.5 Conclusions

In this paper, we report several novel findings concerning the photophysical properties of tyrosyl radicals in peptides. First, we find that the EPR line shape of the radical depends on peptide amino acid content. Second, we present evidence for a decaying component of the EPR signal of tyrosyl radical. We assign this transient to a spontaneous, small structural rearrangement in the radical. Third, we show that amide I vibrational modes and peptide bond skeletal stretch bands are observed in the photolysis spectra of tyrosine-containing pentapeptides. From these data, we conclude that oxidation of the tyrosine aromatic ring perturbs the electronic structure of the peptide bond in tyrosine-containing oligopeptides. Fourth, we report composition-dependent

alterations in these bands, suggesting that the perturbative mechanism depends either on conformation or electrostatics.

We interpret the perturbative mechanism to be spin density delocalization to the amide group, in agreement with previous DFT calculations.[1,20,21] Other possible mechanisms for this perturbation can be considered. One possibility is that an intermolecular interaction between the pentapeptides perturbs the amide bond. However, such an interpretation is not supported by the finding that the photolysis spectra, acquired at 10 and 100 mM, are similar. It is also not supported by the NMR spectra, reported here and recorded at these two concentrations. A second possibility is that there is an intramolecular change in hydrogen bonding, which is induced by photolysis, and that this hydrogen bonding involves the peptide bond. However, a direct interaction between the tyrosyl radical and the peptide nitrogen is very unlikely, due to steric constraints. A third possibility is that conformational rearrangement or changes in solvation may underlie the observed perturbation. These possibilities cannot be excluded, but because the experiments were conducted at cryogenic temperatures, these changes must be subtle, if they occur. Note that a solvation shell perturbation upon tyrosinate oxidation has been previously reported.[1] Our work suggests that primary structure has an impact on the structure and function of redox-active tyrosine residues. Secondary and tertiary structural interactions are also expected to influence reactivity; in future work, the impact of these additional control mechanisms on tyrosyl radicals will be explored.

2.6 Acknowledgments

This work was supported by NIH Grant GM43273. The authors thank Dr. Leslie Gelbaum and Ms. Robin Sibert for their help in collection and processing of NMR data.

2.7 References

1. Ayala, I.; Range, K.; York, D.; Barry, B. A., Spectroscopic properties of tyrosyl radicals in dipeptides. *J. Am. Chem. Soc.* **2002**, *124*, 5496-5505.

2. Tsai, A.-L.; Kulmacz, R. J.; Palmer, G., Spectroscopic evidence for reaction of prostaglandin H synthase-1 tyrosyl radical with arachidonic acid. *J. Biol. Chem.* **1995**, *270*, 10503-10508.

3. Whittaker, M. M.; DeVito, V. L.; Asher, S. A.; Whittaker, J. W., Resonance Raman evidence for tyrosine involvement in radical site of galactose oxidase. *J. Biol. Chem.* **1989**, *264*, 7104-7106.

4. Sjöberg, B.-M.; Reichard, P.; Gräslund, A.; Ehrenberg, A., The tyrosine free radical in ribonucleotide reductase from *Escherichia coli*. *J. Biol. Chem.* **1978**, *253*, 6863-6865.

5. Barry, B. A.; Babcock, G. T., Tyrosine radicals are involved in the photosynthetic oxygen-evolving system. *Proc. Natl. Acad. Sci. U.S.A.* **1987**, *84*, 7099-7103.

6. Boerner, R. J.; Barry, B. A., Isotopic labeling and EPR spectroscopy show that a tyrosine residue is the terminal electron donor, Z, in manganese-depleted photosystem II preparations. *J. Biol. Chem.* **1993**, *268*, 17151-17154.

7. Land, E. J.; Porter, G.; Strachan, E., Primary photochemical processes in aromatic molecules. Part 6.-The absorption spectra and acidity constants of phenoxyl radicals. *Trans. Faraday Soc.* **1961**, *51*, 1885-1893.

8. Dixon, W. T.; Moghimi, M.; Murphy, D., Substituent effects in the e.s.r. spectra of phenoxyl radicals. *J. Chem. Soc., Faraday Trans. 2* **1974**, *70*, 1713-1720.

9. Tripathi, G. N. R.; Schuler, R. H., The resonance Raman spectrum of phenoxyl radical. *J. Chem. Phys.* **1984**, *81*, 113-121.

10. Johnson, C. R.; Ludwig, M.; Asher, S. A., Ultraviolet resonance Raman characterization of photochemical transients of phenol, tyrosine and tryptophan. *J. Am. Chem. Soc.* **1986**, *108*, 912-915.

11. Barry, B. A.; El-Deeb, M. K.; Sandusky, P. O.; Babcock, G. T., Tyrosine radicals in photosystem II and relate model compounds. Characterization by isotopic labeling and EPR spectroscopy. *J. Biol. Chem.* **1990**, *265*, 20139-20143.

12. Hulsebosch, R. J.; van den Brink, J. S.; Nieuwenhuis, S. A. M.; Gast, P.; Raap, J.; Lugtenburg, J.; Hoff, A. J., Electronic structure of the neutral tyrosine radical in frozen solution. Selective ^{2}H-, ^{13}C-, and ^{17}O-isotope labeling and EPR spectroscopy at 9 and 35 GHz. *J. Am. Chem. Soc.* **1997**, *119*, 8685-8694.

13. Svistunenko, D.; Cooper, C., A new method of identifying the site of tyrosyl radicals in proteins. *Biophys. J.* **2004**, *87*, 582-595.

14. Gräslund, A.; Sahlin, M., Electron paramagnetic resonance and nuclear magnetic resonance studies of class I ribonucleotide reductase. *Annu. Rev. Biophys. Biomol. Struct.* **1996**, *25*, 259-286.

15. Babcock, G. T.; Espe, M.; Hoganson, C.; Lydakis-Simantiris, N.; McCracken, J.; Shi, W. J.; Syring, S.; Tommos, C.; Warncke, K., Tyrosyl radicals in enzyme catalysis: Some properties and a focus on photosyntheic water oxidation. *Acta Chem. Scand.* **1997**, *51*, 533-540.

16. Warncke, K.; McCracken, J.; Babcock, G. T., Structure of the YD tyrosine radical in photosystem II as revealed by 2H electron spin echo envelope modulation (ESEEM) spectroscopic analysis of hydrogen hyperfine interactions. *J. Am. Chem. Soc.* **1994**, *116*, 7332-7340.

17. Tommos, C.; Tang, X.-S.; Warncke, K.; Hoganson, C. W.; Styring, S.; McCracken, J.; Diner, B. A.; Babcock, G. T., Spin-density distribution, conformation, and hydrogen bonding of the redox-active tyrosine YZ in photosystem II from multiple-electron magnetic-resonance spectroscopies: Implications for photosynthetic oxygen evolution. *J. Am. Chem. Soc.* **1995**, *117*, 10325-10335.

18. Hoganson, C. W.; Sahlin, M.; Sjöberg, B.-M.; Babcock, G. T., Electron magnetic resonance of the Tyrosyl radical in ribonucleotide reductase from *Escherichia coli*. *J. Am. Chem. Soc.* **1996**, *118*, 4672-4679.

19. Hoganson, C. W.; Babcock, G. T., Protein-tyrosyl radical interactions in photosystem II studied by electron spin resonance and electron nuclear double resonance spectroscopy: Comparison with ribonucleotide reductase and in vitro tyrosine. *Biochemistry* **1992**, *31*, 11874-11880.

20. Barry, B. A.; Einarsdóttir, Ó., Insights into the structure and function of redox-active tyrosines from model compounds. *J. Phys. Chem. B* **2005**, *109*, 6972-6981.

21. Pujols-Ayala, I.; Barry, B. A., Tyrosyl radicals in photosystem II. *Biochim. Biophys. Acta* **2004**, *165*, 205-216.

22. Tripathi, G. N. R.; Schuler, R. H., Structure of the *p*-aminophenoxyl radical. *J. Chem. Soc., Faraday Trans.* **1993**, *89*, 4177-4180.

23. Campbell, K. A.; Peloquin, J. M.; Diner, B. A.; Tang, X.-S.; Chisholm, D. A.; Britt, R. D., The τ-Nitrogen of D2 histidine 189 is the hydrogen bond donor to the tyrosine radical Y_D•. *J. Am. Chem. Soc.* **1997**, *119*, 4787-4788.

24. Range, K.; Ayala, I.; York, D.; Barry, B. A., Normal modes of redox-active tyrosine: Conformation dependence and comparison to experiment. *J. Phys. Chem. B* **2006**, *110*, 10970-10981.

25. Pujols-Ayala, I.; Sacksteder, C. A.; Barry, B. A., Redox-active tyrosine residues: Role for the peptide bond in electron transfer. *J. Am. Chem. Soc.* **2003**, *125*, 7536-7538.

26. Högbom, M.; Galander, M.; Andersson, M.; Kolberg, M.; Hofbauer, W.; Lassmann, G.; Nordlund, P.; Lendzian, F., Displacement of the tyrosyl radical cofactor in ribonucleotide reductase obtained by single-crystal high-field EPR and 1.4-Å X-ray data. *Proc. Natl. Acad. Sci. U.S.A.* **2003**, *100*, 3209-3214.

27. Kamiya, N.; Shen, J. R., Crystal structure of oxygen-evolving photosystem II from *Thermosynechococcus vulcanus* at 2.7-Å resolution. *Proc. Natl. Acad. Sci. U.S.A.* **2003**, *100*, 98-103.

28. Warncke, K.; Babcock, G. T.; McCracken, J., Static conformational distributions in the solid state: Analysis and application to angular dispersion in side chain orientations in model tyrosine in aqueous glass. *J. Phys. Chem. B* **1996**, *100*, 4654-4661.

29. Warncke, K.; Perry, M. S., Redox state dependence of rotamer distributions in tyrosine and neutral tyrosyl radical. *Biochim. Biophys. Acta* **2001**, *1545*, 1-5.

30. Cappuccio, J. A.; Ayala, I.; Elliott, G. I.; Szundi, I.; Lewis, J.; Konopelski, J. P.; Barry, B. A.; Einarsdóttir, Ó., Modeling the active site of cytochrome oxidase: Synthesis and characterization of a cross-linked histidine-phenol. *J. Am. Chem. Soc.* **2002**, *124*, 1750-1760.

31. Bellamy, L. J., *The infrared spectra of complex molecules*. Chapman and Hall: London, 1980; Vol. II.

32. Torii, H.; Tasumi, M., Theoretical analyses of the amide I infrared bands of globular proteins. In *Infrared spectroscopy of biomolecules*, Mantsch, H. H.; Chapman, D., Eds. Wiley-Liss: New York, 1996; p 1.

33. Bogusky, M. J.; Naylor, A. M.; Pitzenberger, S. M.; Nutt, R. F.; Brady, S. F.; Colton, C. D.; Sisko, J. T.; Anderson, P. S.; Veber, D. F., NMR and molecular modeling characterization of RGD containing peptides. *Int. J. Pept. Protein Res.* **1992**, *39*, 63-76.

34. Meirovitch, H.; Meirovitch, E., New theoretical methodology for elucidating the solution structure of peptides from NMR data. 3. Solvation effects. *J. Phys. Chem. B* **1996**, *100*, 5123-5133.

35. Krimm, S.; Bandekar, J., Vibrational spectroscopy and conformation of peptides, polypeptides and proteins. *Adv. Protein Chem.* **1986**, *38*, 181-364.

36. Nauman, D., FT-infrared and FT-Raman spectroscopy in biomedical research. In *Infrared and Raman spectroscopy of biological materials*, Gremlich, H.-U.; Yan, B., Eds. Marcel Dekker: New York, 2001; pp 323-377.

37. Takeuchi, H.; Watanabe, N.; Satoh, Y.; Harada, I., Effects of hydrogen bonding on the tyrosine Raman bands in the 1300-1150 cm^{-1} region. *J. Raman Spectrosc.* **1989**, *20*, 233-237.

38. Chipman, D. M.; Liu, R.; Zhou, X.; Pulay, P., Structure and fundamental vibrations of the phenoxyl radical. *J. Phys. Chem.* **1994**, *100*, 5023-5035.

39. Mukherjee, A.; McGlashen, M. L.; Spiro, T. G., Ultraviolet resonance Raman spectroscopy and general valence force field analysis of phenolate and phenoxyl radical. *J. Phys. Chem.* **1995**, *99*, 4912-4917.

40. Nwobi, O.; Higgins, J.; Zhou, X.; Liu, R., Density functional calculation of phenoxyl radical and phenolate anion: An examination of the performance of DFT methods. *Chem. Phys. Lett.* **1997**, *272*, 155-161.

41. Ford, S. J.; Wen, Z. Q.; Hecht, L.; Barron, L. D., Vibrational Raman optical activity of alanyl peptide oligomers: A new perspective on aqueous solution conformation. *Biopolymers* **1994**, *34*, 303-313.

42. Jackson, M.; Mantsch, H. H., Biomedical infrared spectroscopy. In *Infrared spectroscopy of biomolecules*, Mantsch, H. H.; Chapman, D., Eds. Wiley-Liss: New York, 1996; p 311.

43. Hutchinson, R. S.; Steenhuis, J. J.; Yocum, C. F.; Razeghifard, M.; Barry, B. A., Deprotonation of the 33-kDa, extrinsic, manganese-stabilizing subunit accompanies photooxidation of manganese in photosystem II. *J. Biol. Chem.* **1999**, *274*, 31987-31995.

44. Cavanagh, J.; Fairbrother, W. J.; Palmer, A. G. I.; Skelton, N. J., *Protein NMR spectroscopy: Principles and practice*. Academic Press: San Diego, CA, 1996.

45. Wüthrich, K., *NMR of proteins and nucleic acids*. John Wiley & Sons: New York, 1986.

CHAPTER 3

A SPECTROSCOPIC INVESTIGATION OF A TRIDENTATE CU-COMPLEX MIMIKING THE TYROSINE-HISTIDINE CROSS-LINK OF CYTOCHROME OXIDASE

by

[1]Adam Offenbacher, [2]Kimberley N. White, [2]Indranil Sen, [2]Allen G. Oliver, [2]Joseph P. Konopelski, [1]Bridgette A. Barry and [2]Ólöf Einarsdóttir

[1]School of Chemistry and Biochemistry and the Petit Institute for Bioengineering and Bioscience, Georgia Institute of Technology, Atlanta, GA 30332

[2]Department of Chemistry and Biochemistry, University of California Santa Cruz, California 95064

Reprinted with permission from the Journal of Physical Chemistry B

Offenbacher, A.; White, K. N.; Sen, I.; Oliver, A. G.; Konopelski, J. P.; Barry, B. A.; Einarsdóttir, Ó. "A Spectroscopic Investigation of a Tridentate Cu-Complex Mimicking the Tyrosine-Histidine Cross-Link of Cytochrome *c* Oxidase." *J. Phys. Chem. B* **2009**, *113*, 7407-7417.

3.1 Abstract

Heme-copper oxidases have a crucial role in the energy transduction mechanism, catalyzing the reduction of dioxygen to water. The reduction of dioxygen takes place at the binuclear center, which contains heme a_3 and Cu_B. The X-ray crystal structures have revealed that the C6′ of tyrosine 244 (bovine heart numbering) is cross-linked to a nitrogen of histidine 240, a ligand to Cu_B. The role of the cross-linked tyrosine at the active site still remains unclear. In order to provide insight into the function of the cross-linked tyrosine, we have investigated the spectroscopic and electrochemical properties of chemical analogues of the Cu_B–His–Tyr site. The analogues, a tridentate histidine–phenol cross-linked ether ligand and the corresponding Cu-containing complex, were previously synthesized in our laboratory.[1] Spectrophotometric titrations of the ligand and the Cu-complex indicate a pK_A of the phenolic proton of 8.8 and 7.7, respectively. These results are consistent with the cross-linked tyrosine playing a proton delivery role at the cytochrome *c* oxidase active site. The presence of the phenoxyl radical was investigated at low temperature using electron paramagnetic resonance (EPR) and Fourier transform infrared (FT-IR) difference spectroscopy. UV photolysis of the ligand, without bound copper, generated a narrow g = 2.0047 signal, attributed to the phenoxyl radial. EPR spectra recorded before and after UV photolysis of the Cu-complex showed a g = 2 signal characteristic of oxidized copper, suggesting that the copper is not spin-coupled to the phenoxyl radical. An EPR signal from the phenoxyl radical was not observed in the Cu-complex, either due to spin relaxation of the two unpaired electrons or to masking of the narrow phenoxyl radical signal by the strong copper contribution. Stable isotope (^{13}C) labeling of the phenol ring (C1′) Cu-complex, combined with photoinduced difference FT-IR spectroscopy, revealed bands at 1485 and 1483 cm^{-1} in the ^{12}C-minus-^{13}C-isotope-edited spectra of the ligand and Cu-complex, respectively. These bands are attributed to the radical υ_{7a} stretching frequency and are shifted to 1468 and 1472 cm^{-1}, respectively, with $^{13}C1'$ labeling. These results show that a radical is generated in both the ligand and

the Cu-complex and support the unambiguous assignment of a vibrational band to the phenoxyl radical υ_{7a} stretching mode. These data are discussed with respect to a possible role of the cross-linked tyrosine radical in cytochrome *c* oxidase.

3.2 Introduction

Cytochrome *c* oxidase (C*c*O), the terminal enzyme in the respiratory electron transfer chain, plays a crucial role in energy transduction through the catalytic reduction of molecular oxygen to water.[2] This reaction drives the translocation of four protons across the inner mitochondrial or bacterial plasma membrane and generates the electrochemical proton gradient necessary for ATP synthesis.[3] The reduction of O_2 to water takes place at the heme a_3/Cu_B binuclear site while avoiding the release of harmful, reactive oxygen species. The enzyme contains two additional redox centers, heme *a* and Cu_A. X-ray crystallographic studies on a variety of C*c*O enzymes[4-6] and protein chemical analysis[7] have identified a unique covalent cross-link between C5' of tyrosine 244 (bovine heart numbering) and the ε-nitrogen of histidine 240, a ligand to Cu_B. Mutational studies have revealed that this highly conserved, modified tyrosine is required for C*c*O enzymatic activity, although its specific biological function is under debate.[8,9]

In the catalytic mechanism of O_2 reduction, scission of the O-O bond forms a so-called **P** intermediate with the heme a_3 iron in an oxyferryl state ($Fe_{a3}^{4+}=O^{2-}$).[10-12] The heme a_3 iron and Cu_B donate three of the four electrons required for the bond breakage. Under mixed-valence conditions, in which heme a_3 and Cu_B are reduced and heme *a* and Cu_A are oxidized, the origin of the fourth electron is still unknown. It has been proposed that due to its local proximity to the active site and its terminal location in the proton K-

channel, the cross-linked tyrosine may act as an electron[13-17] and proton donor to O_2.[11,18,19]

Several infrared (IR) spectroscopic studies of cytochrome *c* oxidase from *Rhodobacter sphaeroides*,[16] *Paracoccus denitrificans*[20-23] and bovine heart[21,24,25] have been carried out, but definitive assignment of spectral contributions from the tyrosine-histidine radical has been problematic. A previous EPR study on C*c*O incubated with H_2O_2[26] attributed a $g = 2$ signal to the cross-linked tyrosine. However, subsequent work showed that this signal may arise from a tryptophan cation radical[25,27-29] or another, unmodified tyrosyl radical.[17,30,31] Budiman et al. have proposed a radical migration pathway[31] from the tyrosine-histidine radical to tyrosine 129 (bovine heart numbering).

These results suggest that the cross-linked tyrosine may play a role in O_2 reduction to water. To define its functional significance, several groups have synthesized and studied model compounds, which mimic the tyrosine-histidine cross-link[1,32-38] or the heme a_3/Cu_B binuclear site.[39-44] In a recent study, a functional C*c*O model was used to support the idea that the cross-linked tyrosine is essential for the catalytic reduction of O_2 under steady-state conditions.[45] Although these studies have afforded a better understanding of some of the physicochemical properties of the cross-link, little is known about the electronic structure of the Cu-coordinated tyrosine-histidine moiety.

Nagano and coworkers were the first to present vibrational assignments for a light-induced phenoxyl radical of a tyrosine-histidine-Cu_B model complex using resonance Raman spectroscopy.[37,46] Recently, we reported the synthesis and structural characterization of two analogs of the active site of cytochrome *c* oxidase, a tridentate cross-linked histidine-phenol ligand and its corresponding Cu-complex.[1] Using

spectrophotometric titrations, we showed that the acidity of the phenolic proton of the ligand is lower when compared to *p*-cresol. Subsequent Cu-coordination produced an additional decrease in pK_A, which is consistent with the proposed proton delivery role of the cross-linked tyrosine. In contrast to the ligand, the phenoxyl radical was not detected in the time-resolved optical absorption spectra recorded at room temperature of the copper-containing compound.[1]

In this study, we use stable isotopes to show that a phenoxyl radical is generated in a copper-containing histidine-phenol cross-linked model compound and assign vibrational bands to the radical and singlet forms.

3.3 Materials and Methods

3.3.1 Materials

L-Tyrosine, Tris(hydroxymethyl)aminomethane hydrochloride, acetonitrile, sodium hydroxide, and hydrochloric acid were purchased from Sigma (St. Louis, MO). $^{13}C_{4'}$-Tyrosine (98–99 %) was obtained from Cambridge Isotope Laboratories (Andover, MA).

3.3.2 Synthesis

Synthesis of the unlabeled ligand **1** and copper complex **2** have already been described.[1] Whereas our previous synthesis relied on commercial 2-bromophenol as the starting material, preparation of the ^{13}C-labeled ligand **3** necessitated the use of 1-^{13}C-

phenol (99% ^{13}C) as the starting material and required development of an alternative route to the key aryllead(IV) reagent.

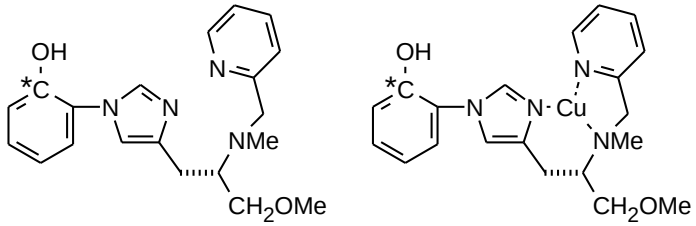

1 * = natural abundance
3 * = ^{13}C enriched

2 * = natural abundance
4 * = ^{13}C enriched

Phenol in the presence of bromine and acetic acid yields, not unexpectedly, predominantly *p*-brominated material. Consequently, our attention was turned to directed ortho-metalation (DoM)[47] for specific C-2 activation. Considerable precedent exists in the literature for utilizing MOM protection as a directing group for *o*-metalation of phenolic compounds.[48,49] Protection of the ^{13}C-phenol to provide **5** proceeded smoothly. However, extensive experimentation was necessary to identify a sufficiently selective and efficient method for the *o*-metalation. Success was achieved with *t*-BuLi in Et_2O at low temperature to yield trimethylstannane derivative **6** in 85% yield. Transmetalation of **6** afforded the desired aryllead(IV) reagent **7.**

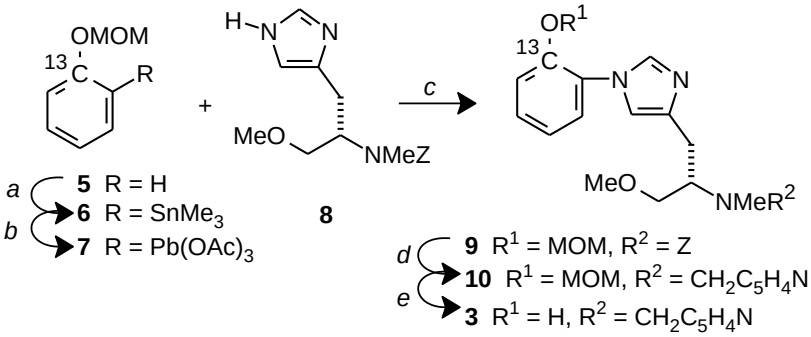

a) *t*-BuLi, $ClSnMe_3$, -25 °C, 90%; *b*) $Pb(OAc)_4$, cat. $Hg(O_2CCF_3)_2$, 86%;
c) cat. $Cu(OAc)_2$, 68%; *d*) 1) cyclohexadiene, Pd/C, 99%,
2) picolyl carboxaldehyde, $Na(OAc)_3BH$, 66%; *e*) $HCl_{(g)}$, then NaOH, 83%

The synthesis of the ^{13}C-labeled ligand **3** proceeded in an identical fashion to the synthesis of the non-labeled ligand **1**.[1] Aryllead reagent **7** was coupled to previously synthesized Z-protected *N*-methyl histidinol methyl ether (**8**) to afford **9**. Removal of the Cbz protection group and reductive amination installed the pyridine residue, yielding **10**. Finally, MOM-deprotection gave the ^{13}C-labeled ligand **3** in an overall yield of 29% from **5**. Addition of copper to ligand **3** under identical conditions as for the non-labeled ligand **1**[1] afforded a dark blue solution that yielded needles (**4**) suitable for single crystal X-ray analysis and biophysical studies. The ^{12}C-ligand (**1**) and the Cu-complex (**2**) will hereafter be referred to as the "ligand" and the "Cu-complex"; the corresponding isotopically labeled compounds will be referred to as the ^{13}C-labeled ligand and Cu-complex.

3.3.3 Spectrophotometric Titrations

The pK_A values of the ^{13}C-labeled ligand and the corresponding Cu-complex were determined from the UV-visible spectra recorded on a Hewlett-Packard (8452) diode array spectrophotometer over the pH ranges 3.3–9.2 and 4.9–8.7, respectively. The values were compared to those obtained for the corresponding unlabeled compounds.[1] Due to limited solubility, the ^{13}C-labeled ligand and the Cu-complex were dissolved in 80% aqueous/20% acetonitrile mixtures in the presence of 0.1 M KCl. The spectra were analyzed by singular value decomposition (SVD) and global pK_A fitting as previously described[35] to determine the pK_A values and the intermediate spectra.

3.3.4 Electrochemical Titrations

Electrochemical experiments were carried out with a CH Instrument 440 electrochemical workstation at room temperature using a glassy carbon working electrode, Ag/AgCl (saturated with 0.1 M KCl) reference electrode and a platinum wire counter electrode.[50] The experiments were carried out in the presence of 10 mM Na-phosphate, pH 7.0 (0.2 M KCl).

3.3.5 EPR Spectroscopy

EPR spectra on samples in fused quartz sample tubes were recorded at 100 K on a Bruker (Billerica, MA) EMX 6/1 X-band EPR spectrometer, equipped with a ST-9605 cavity and a Wilmad (Buena, NJ) liquid nitrogen dewar.[35,51] The unlabeled ligand and Cu-complex were prepared as 50 mM solutions in 35% acetonitrile/65% 10 mM Tris-HCl, pH 8.5 (ligand) or in 20% acetonitrile/80% 10 mM Tris-HCl, pH 6.2 (Cu-complex). Tyrosinate samples (50 mM) were prepared in 10 mM Tris-HCl, pH 11.0. The Cu-complex was unstable at high pH values, and limited solubility precluded the examination of 50 mM tyrosine and ligand solutions at pH 6.2. These high concentrations were necessary for comparison to the Fourier transform infrared (FT-IR) experiments.

Tyrosyl or phenoxyl radicals were generated by photolysis with the 266 nm output from a Surelite III Nd:YAG laser (Continuum, Santa Clara, CA). The pulse energy was 70–80 mJ at a frequency of 10 Hz, and 50 flashes were employed. The spectrometer conditions were as follows: microwave frequency, 9.21 GHz; microwave power, 200 μW; modulation frequency, 100 kHz; modulation amplitude, 3 G; time

constant, 2.6 s; conversion time, 1.3 s. Microwave power dependence experiments (Figure 3.3) showed that there was no saturation of the signals from any of the samples under these conditions. The final photolysis-induced EPR spectrum was generated by subtracting background signals observed before photolysis using the Igor Pro v. 5.03 (Wavemetrics, Lake Oswego, OR) software.

3.3.6 FT-IR Spectroscopy

FT-IR spectra were obtained with a Nicolet Magna 550 II spectrometer, equipped with an MCT-A detector (Nicolet, Madison, WI). Samples were sandwiched between two CaF_2 windows, partitioned by a 6 μm spacer, and cooled to 79 K using a Hansen (R.G. Hansen & Associates, Santa Barbara, CA) liquid nitrogen cryostat prior to data collection. Sample conditions and preparations were similar to those described above for the EPR experiments, with the tyrosinate samples prepared at pH 11, and the ligand and Cu-complex at pH 8.5 and 6.2, respectively. Data were recorded before and after photolysis for 120 s at 4 cm^{-1} resolution and with a 2.5 cm s^{-1} mirror velocity. After 2 minutes of data collection, the samples were illuminated with 5 (tyrosinate and the ^{12}C- and ^{13}C-labeled ligands) or 50 (^{12}C- and ^{13}C-labeled Cu-complexes, buffer blank) 266 nm laser flashes using a Surelite III Nd:YAG laser (Continuum, Santa Clara, CA) with pulse energies of 70 – 80 mJ (at 10 Hz). The data were processed using Omnic v. 5.2 software (Nicolet, Madison, WI), a Happ-Genzel apodization function, two levels of zero filling, and a Mertz phase correction. FT-IR absorption spectra and FT-IR light-minus-dark difference spectra were generated in Igor Pro v. 5.03 as previously described.[52] To construct the absorption spectrum, the single beam spectrum was ratioed to an open beam

background, the absorbance was calculated, and the appropriate buffer blank interactively subtracted from the data.

3.4 Results

3.4.1 Structure of the Cu-complex

The structure of the ^{13}C-labeled Cu-tridentate ether complex was determined by single crystal X-ray analysis (Figure 3.1). As mentioned above, an alternative route toward synthesizing the aryllead(IV) reagent had to be developed because of the necessity to use different starting materials for the ^{12}C-complex (2-bromophenol) and the ^{13}C-labeled ligand (1-^{13}C-phenol). There are four molecules of the complex and associated perchlorate anion in the unit cell of the primitive, acentric, orthorhombic space group $P2_12_12_1$. The copper atom is coordinated in a square-planar geometry by three nitrogens of the ligand and a chlorine atom. The equatorial chloride forms a weak bond to copper in the adjacent monomeric unit (Cu–Cl: 2.76 Å). An analysis of the bond distances and angles about the C1', which was substituted with ^{13}C, reveals that the structure is within experimental error identical to our previously characterized ^{12}C-analogue.[1] The very slight variations observed in the derived parameters (bond distances and angles) are due to statistical variation (Table 3.1).

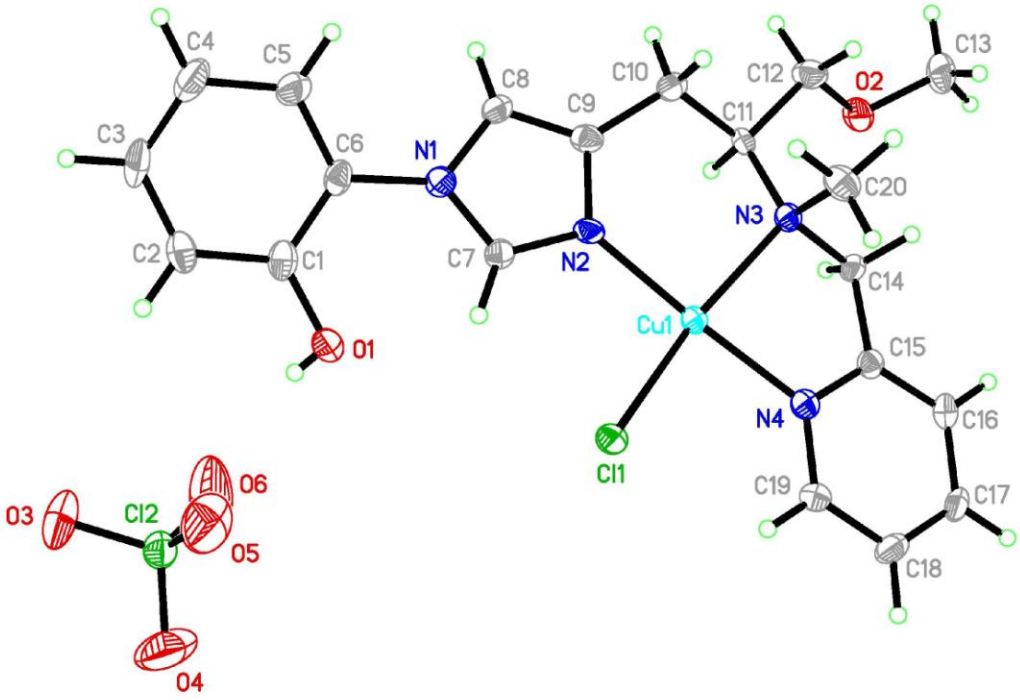

Figure 3.1. X-ray crystal structure of the ^{13}C-labled Cu-complex.

Table 3.1. Comparison of Bond Length and Angles at C1´

C^{13}					
O(1)—C(1)	1.355(5)	C(1)—C(2)	1.398(6)	C(1)—C(6)	1.394(5)
O(1)—C(1)—C(6)	118.9(3)	O(1)—C(1)—C(2)	122.6(4)	C(6)—C(1)—C(2)	118.5(4)
C^{12}					
O(1)—C(1)	1.358(3)	C(1)—C(2)	1.395(4)	C(1)—C(6)	1.403(4)
O(1)—C(1)—C(6)	118.7(2)	O(1)—C(1)—C(2)	122.7(2)	C(6)—C(1)—C(2)	118.7(2)

3.4.2 Spectrophotometric titrations

SVD and global pK_A fitting of the UV-visible spectra recorded for the ^{13}C-labeled ligand over a wide pH range revealed three pK_A values, 4.5, 7.4, and 8.8, which are attributed to the pyridine, imidazole, and phenol, respectively. These are identical within experimental error to our previously observed pK_A values for the unlabeled ligand.[1] A single pK_A of 7.7 was observed for the ^{13}C-labeled Cu-complex, which is consistent with a pK_A of 7.8 observed for the ^{12}C- analogue.[1]

3.4.3 Electrochemical Titrations

Cyclic voltammetry studies were performed on tyrosine, the natural abundance ligand, and the Cu-complex to access the effect of the cross-link and Cu^{2+} on the redox properties of the phenolate/phenoxyl radical couple. Parts A, B, and C of Figure 3.2 show the cyclic voltammograms for the tyrosine, ligand, and Cu-complex, respectively. The cyclic voltammetry showed irreversible behavior, with anodic redox potentials of 0.67, 0.78 and 0.73 eV, respectively (950, 1060, and 1010 mV versus NHE electrode), attributed to the oxidation of tyrosine or phenol to the corresponding radicals in tyrosine, the ligand and the Cu-complex, respectively. A peak with a redox potential of 0.42 eV in the Cu-complex is assigned to the Cu(II)/Cu(I) couple; this peak is absent in the ligand.

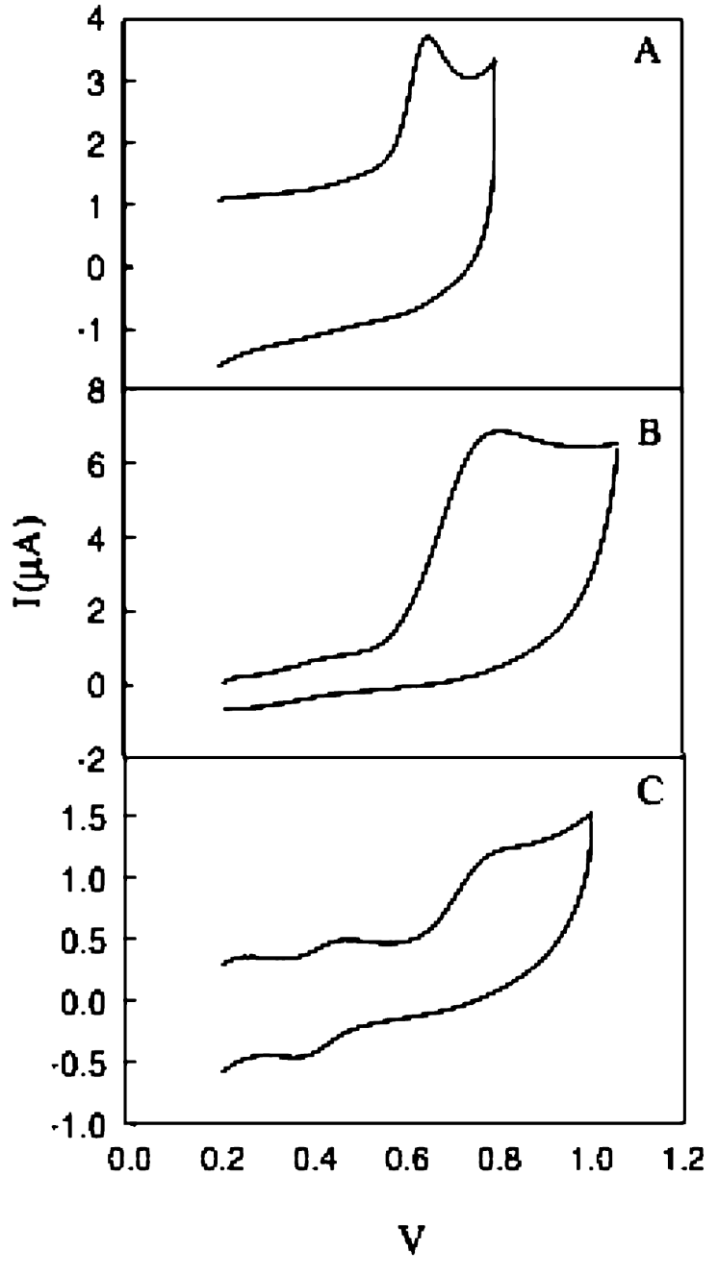

Figure 3.2. Cyclic voltammograms of the natural abundance tyrosine (A), ligand (B), and Cu-complex (C). The electrochemical experiments were carried out with a CH Instrument 440 electrochemical workstation at room temperature using a glassy carbon working electrode, Ag/AgCl (saturated with 0.1 M KCl) reference electrode, and a platinum wire counter electrode.[50] The experiments were carried out in the presence of 10 mM Na-phosphate pH 7.0 (0.2 M KCl).

3.4.4 EPR Spectra

Figure 3.4 depicts the photolysis-induced EPR spectra (after photolysis-minus-before photolysis) derived from the natural abundance Cu-complex (panel A), ligand (panel B), and tyrosinate (panel C). For comparison, a photolysis-induced blank, acquired on the 35% acetonitrile/65% 10 mM Tris-HCl, pH 8.5, buffer alone is shown in Figure 3.4D. Figure 3.5 exhibits the EPR spectra of the ligand (panel A) and tyrosinate (panel B) on an expanded scale, displaying spectral line shapes. The UV photolysis of tyrosinate at 100 K generated an EPR signal (Figure 3.4C and 3.5B) similar to the previously reported spectra,[53,54] with a *g* value of 2.0044. A previous EPR study of tyrosinate demonstrated that upon oxidation, the spin density is located on the phenoxyl oxygen and carbons 1', 3', and 5' on the phenoxyl ring.[53] In the tyrosyl radical, the spectrum is dominated by hyperfine couplings to the C1' and C3' hydrogens, as well as conformation-sensitive couplings to the beta-methylene hydrogens.[53] At 1 mM concentrations, tyrosyl radicals exhibited a similar EPR lineshape at pH 5 and 11, although the signal intensity at pH 5 is ~50% of the amplitude observed at pH 11.[55] In previous work, the change in signal intensity was attributed to the increase in midpoint potential of tyrosine at low pH values.

Photolysis of the ligand also generated a stable EPR signal (Figure 3.5A) with a similar *g* value (2.0047) to the neutral tyrosyl radical.[51] The EPR spectrum of the ligand is similar to the spectrum we previously reported for a related His-phenol cross-linked compound.[35] Therefore, the EPR signal of the ligand suggests the formation of a neutral phenoxyl radical. The EPR line shape of the ligand (Figure 3.5A) lacks the hyperfine structure present in the tyrosinate spectrum (Figure 3.5B) due to the absence of beta-

methylene protons. Moreover, spin quantization under non-saturating conditions showed that the radical yield is a factor of ~4 lower in the ligand, compared to tyrosinate.

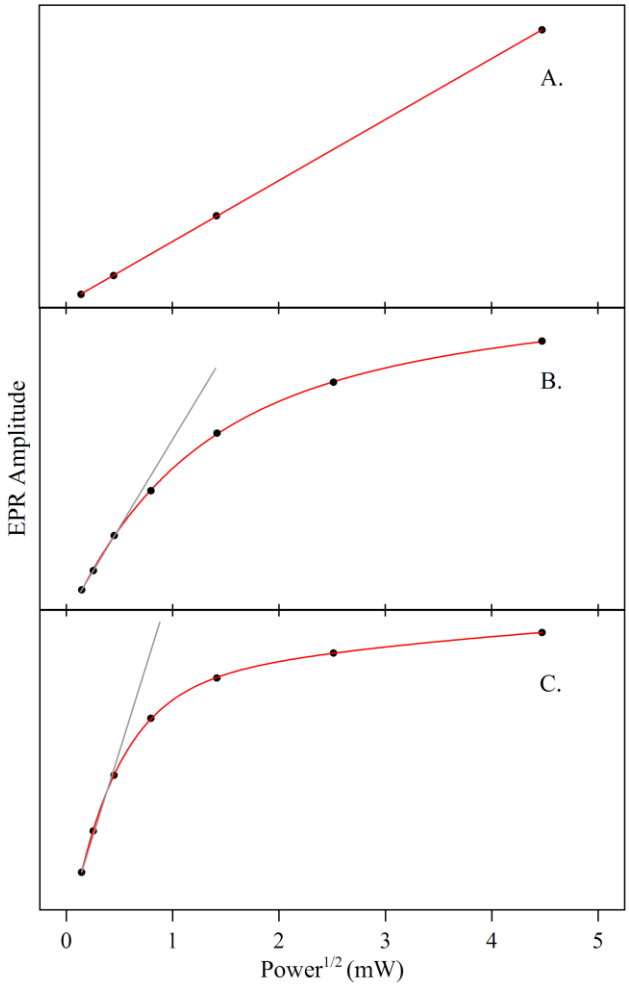

Figure 3.3. Power saturation curves of (A) Cu-complex, (B) ligand, and (C) tyrosinate EPR amplitudes after photolysis. EPR spectra were recorded after photolysis (see Materials and Methods for details) as a function of the microwave power and the integrated amplitudes of each signal (black dots) were plotted against the square root of the microwave power ($Power^{1/2}$). The thin gray line is a reference for determining the non-saturated power conditions.

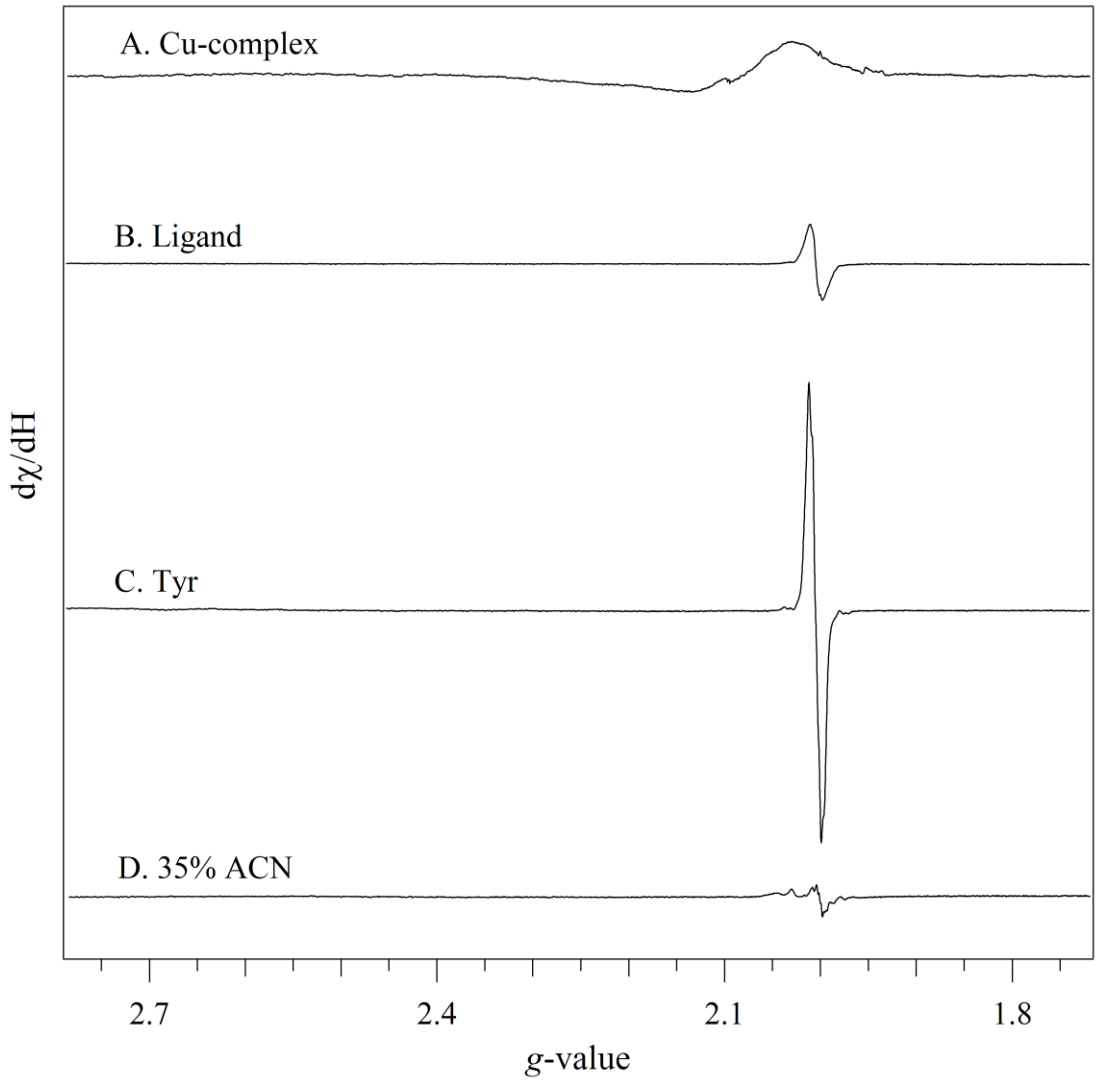

Figure 3.4. EPR spectra of radicals generated by UV photolysis of (A) the Cu-complex, (B) the ligand, and (C) tyrosinate. Panel D shows the results of photolysis of a buffer blank, containing 35% acetonitrile in 10 mM Tris buffer. To generate these data, the spectrum obtained before photolysis was subtracted from one obtained after photolysis. The temperature was 100 K (see Materials and Methods for details). In (A and B), eight trials were averaged, and in panels C and D, four trials were averaged.

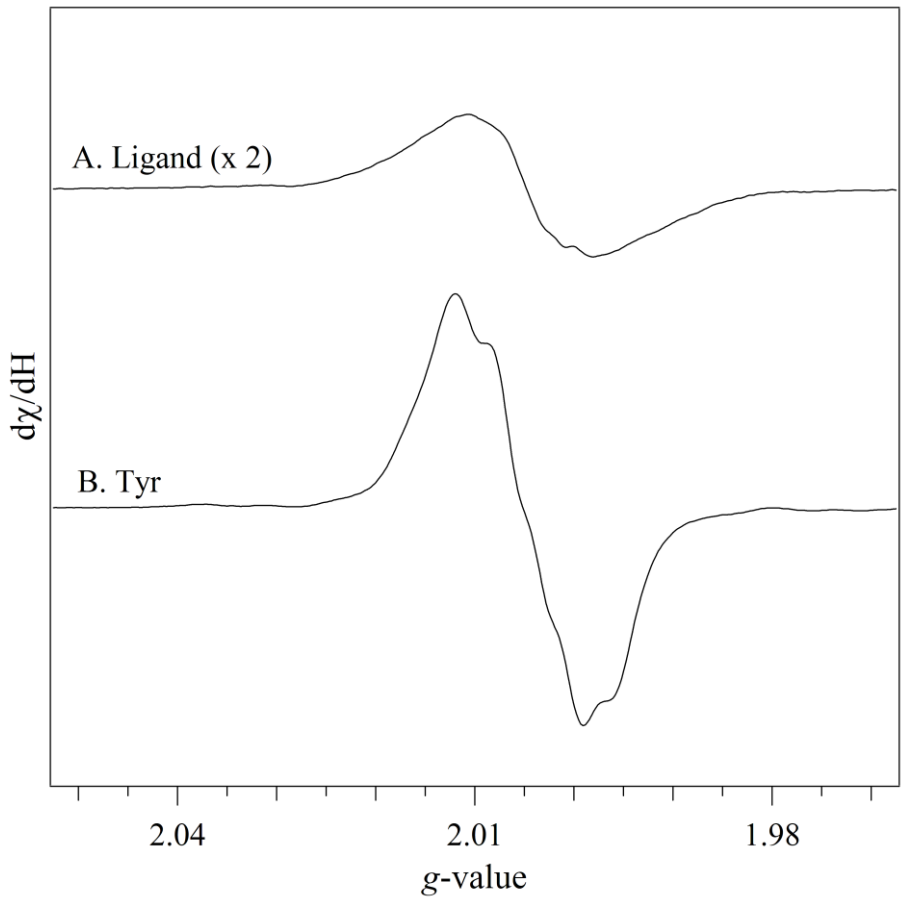

Figure 3.5. EPR spectra of radicals generated by UV photolysis of (A) the ligand and (B) tyrosinate. The spectra are reproduced from Figure 3.4B and C, respectively, but on an expanded scale. For presentation purposes, in this figure, the spectrum for the ligand (Figure 3.4A) is multiplied by a factor of 2. The temperature was 100 K (see Materials and Methods section and Figure 3.4 legend).

Note that our EPR results differ from previous reports in which cross-linked compounds are based on *p*-cresol and in which hyperfine couplings to the equivalent –CH_3 protons dominate the EPR spectrum.[33,36,46] In earlier work, including our EPR simulations of the His–phenol cross-linked radical, it was concluded that the spin distribution on the phenoxyl radical is only modestly perturbed by the imidazole cross-link.[35,36,56] However, our previous time-resolved optical absorption spectra of the ligand[1] and the related cross-linked His–phenol compound[35] have shown that the imidazole cross-link causes a substantial red shift of the radical's electronic spectrum.

In the Cu-complex, the intense EPR signal from Cu^{2+} was observed both before and after photolysis (Figure 3.6), indicating that the oxidation state of the metal ion does not change. Photolysis was associated with only a small change in the amplitude of this copper signal (Figure 3.6, solid line, repeated from Figure 3.4), which is due to a background artifact created during subtraction of the spectra. A small baseline artifact was also apparent when experiments were conducted at lower Cu-complex concentrations, at which the expected copper hyperfine splittings could be observed (data not shown). The observation of a Cu^{2+} EPR signal after photolysis (Figure 3.6) indicates either that the resulting phenoxyl radical is not spin-coupled to the metal ion or that the phenoxyl radical produced by photolysis of the Cu-complex remains somehow undetectable by EPR. Our analysis of the FT-IR intensities (see below) suggests that the radical yield in the copper complex decreases by a factor of 40. This is supported by our time-resolved optical spectrum of the Cu-complex, which failed to show an ~480 nm peak, attributed to the phenoxyl radical in analogous spectra of the ligand[1] and the related cross-linked His–phenol compound.[35] Nagano et al.[37] also did not observe a distinct band

in the transient optical spectrum of their Cu-bound *ortho*-imidazole-bound *para*-cresol-based model compound.

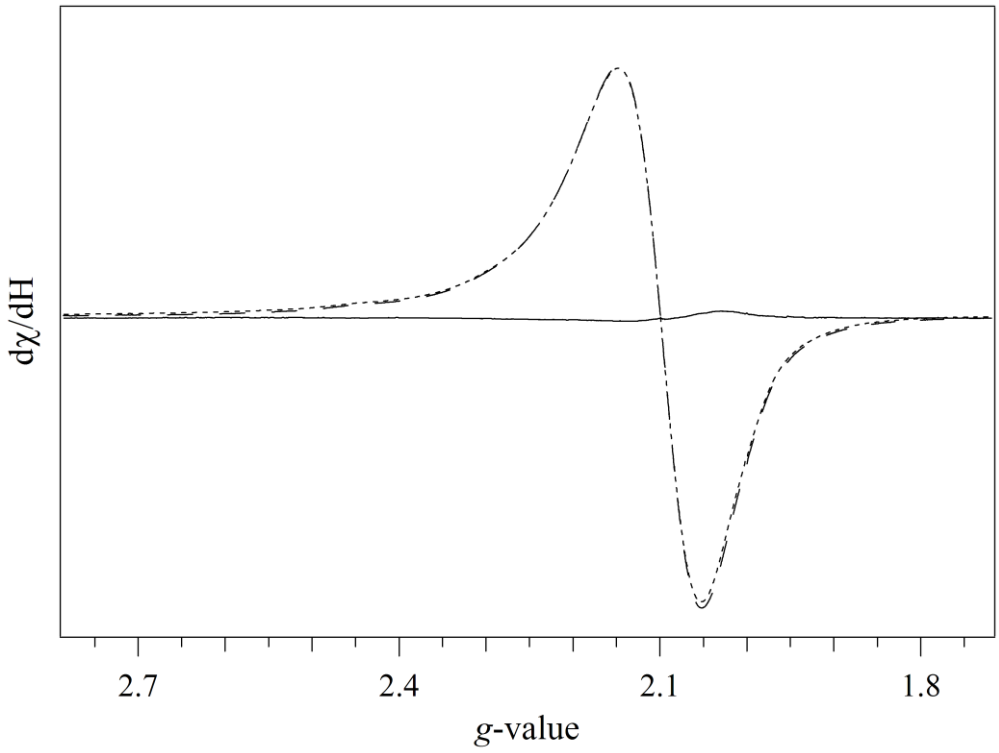

Figure 3.6. EPR spectra generated before (dashed line) and after (dotted line) photolysis of the Cu-complex. The temperature was 100 K (see Materials and Methods section and Figure 3.4 legend). The spectrum shown in the solid line is the after photolysis-minus-before photolysis difference spectrum (repeated from Figure 3.4A). To generate the final data, eight trials were averaged.

3.4.5 FT-IR Spectroscopy

Photolysis-induced difference FT-IR spectroscopy was employed to monitor structural changes induced by oxidation. The FT-IR absorption spectra for tyrosinate and the ^{12}C- and ^{13}C-labeled ligands and Cu-complexes were recorded (Figure 3.7). The FT-IR data were acquired before and after UV photolysis and then subtracted to generate the

difference FT-IR spectra shown in Figure 3.8. Under the conditions employed in our FT-IR measurements, the phenol ring is expected to be unprotonated in tyrosinate (pK_A 10), primarily protonated (~67%) in the ligands (pK_A 8.9) and protonated in the Cu-complexes (pK_A 7.7–7.8). The limited solubility of tyrosine and the ligand at high concentrations, necessary for the FT-IR experiments, and the limited stability of the copper complex precluded the use of the same pH for all of the experiments.

Tyrosyl radical formation is expected to perturb vibrational bands of the phenol ring (υ_{8a} and υ_{19a}) as well as the frequency of the CO vibrational band (υ_{7a}).[57,58] Negative bands in the difference spectra arise from vibrational bands unique to the ground (singlet) state of tyrosinate/phenol, whereas positive bands correspond to vibrational bands of the neutral tyrosyl/phenoxyl radical species. Only vibrational bands, which are perturbed by the oxidation of the phenol ring, will contribute to the photolysis-induced difference spectrum. As expected, photolysis of the blank (Figure 3.8A) resulted in no defined difference spectrum.

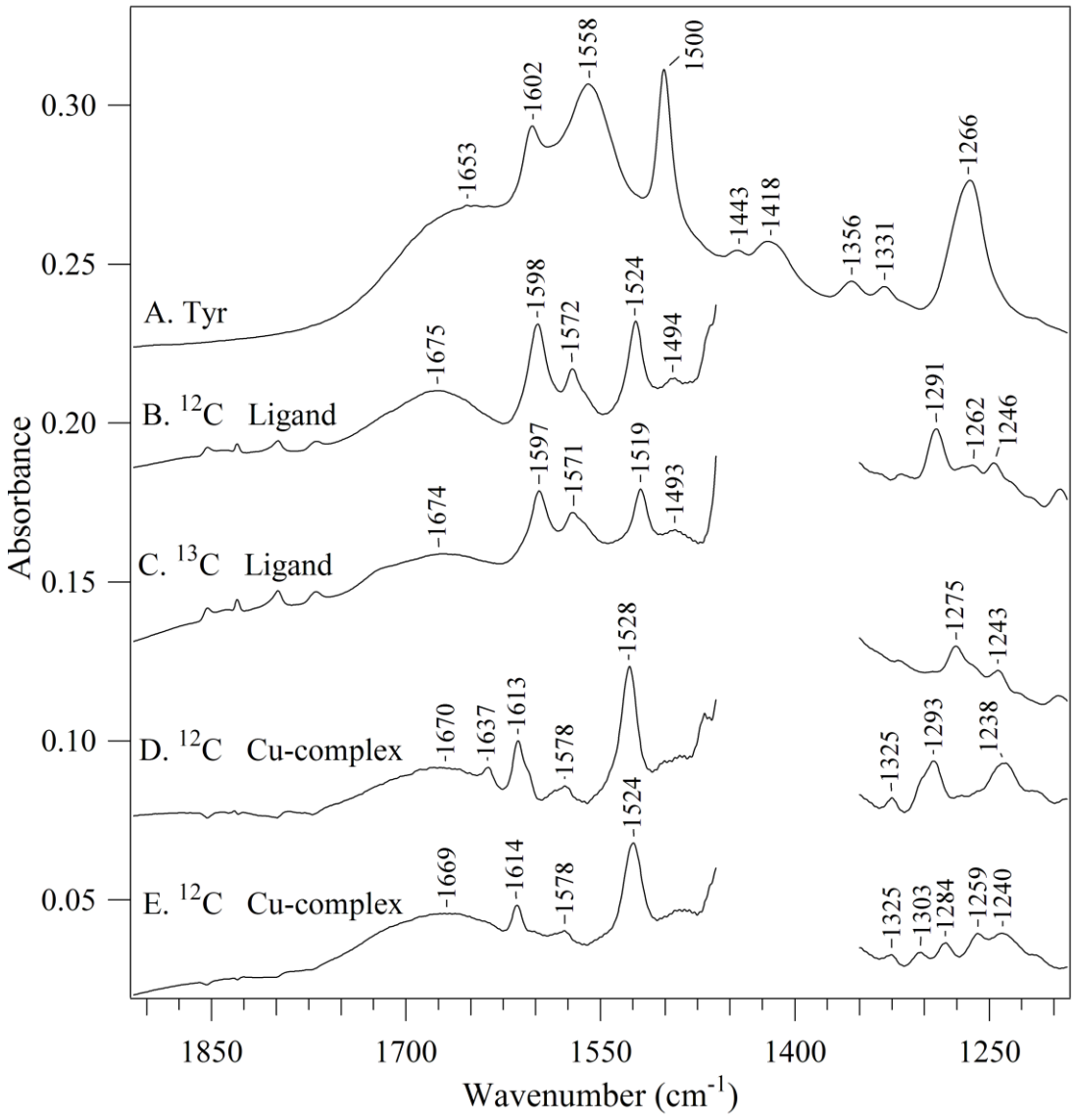

Figure 3.7. FT-IR absorbance spectra of tyrosinate (A), the natural abundance ligand (B), the ^{13}C ligand (C), the natural abundance Cu-complex (D), and the ^{13}C Cu-complex. The concentrations were 50 mM. The temperature was 79 K. Data were recorded at 4 cm^{-1} resolution (120 s; 2.5 cm s^{-1} mirror velocity). The buffer was 10 mM Tris-HCl pH 11.0 (A), 35% acetonitrile/65% 10 mM Tris-HCl pH 8.5 (B, C), or 20% acetonitrile/80% 10 mM Tris-HCl pH 6.2 (D, E). The buffer spectrum was interactively subtracted. For clarity, the spectral region between 1460 and 1350 cm^{-1} in panels B-E was removed due to acetonitrile absorption. The final spectra are averages of data obtained from 5 (A), 8 (B), 9 (C), 24 (D), or 23 (E) different trials.

3.4.6 Ring and CO Stretching Vibrations of Tyrosinate/Phenol

In Figure 3.8B, negative bands of tyrosinate, corresponding to the bands perturbed in the singlet state, are observed at 1605 (υ_{8a}), 1500 (υ_{19a}) and 1263 ($\upsilon_{7a'}$) cm^{-1}. These vibrational assignments are based upon previous reports.[51,52,59,60] The assignments of other vibrational bands have been discussed.[35,51,60] A similar set of bands, with different frequencies, are observed for the ^{12}C-ligand (Figure 3.8C) and Cu-complex (Figure 3.8E). To assign these bands to ring and CO stretching frequencies, ^{13}C labeling of the CO ring carbon was performed in tyrosinate (C4'), the ligand (C1') (Figure 3.8D), and the Cu-complex (C1') (Figure 3.8F). All three vibrational bands, υ_{8a}, υ_{19a}, and $\upsilon_{7a'}$, are predicted to be sensitive to labeling at this ring position.[60] Isotope-edited spectra (double difference spectra), ^{12}C (light – dark)-minus-^{13}C (light – dark) were constructed to identify the frequencies of these isotope sensitive bands (Figure 3.9). In the isotope-edited spectra, the singlet bands from the ^{12}C-compound are negative; the ^{13}C-isotope shifted bands are positive. These bands are marked in Figure 3.9 with dotted lines.

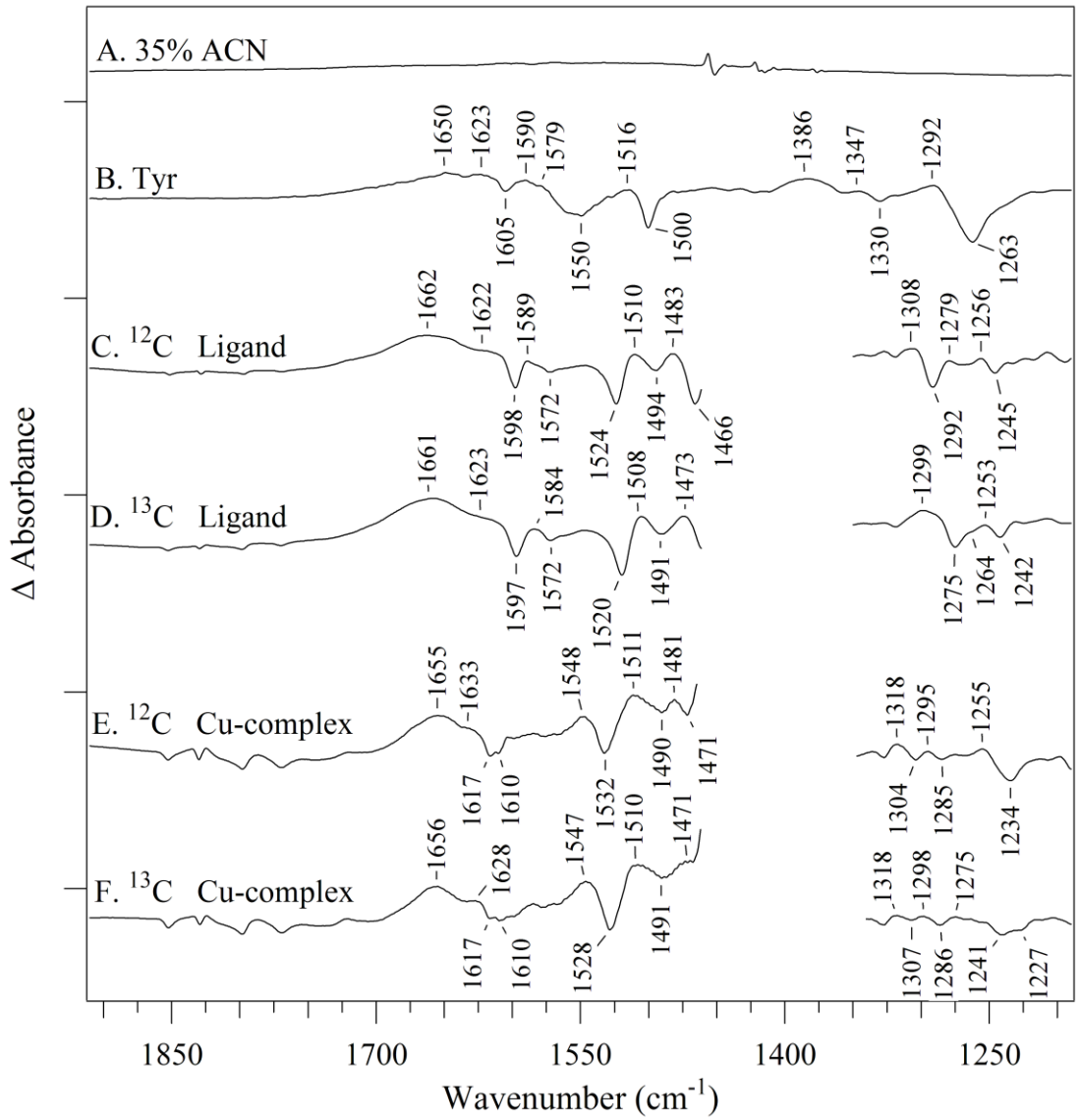

Figure 3.8. Photolysis-induced difference FT-IR spectra recorded from: (A) a blank (35% acetonitrile in 10 mM Tris buffer), (B) tyrosinate, (C) natural abundance ligand, (D) ^{13}C-ligand, (E) natural abundance Cu-complex, and (F) ^{13}C Cu-complex. The temperature was 79 K (see Materials and Methods for details). For clarity, the spectral region between 1460 and 1350 cm^{-1} in panels B-E was removed due to acetonitrile absorption. The final spectra are derived from 1 (A), 5 (B), 8 (C), 9 (D), 24 (E) or 23 (F) different trials. Tick marks on the *y*-axis correspond to 22.5 x 10^{-3} absorbance unit.

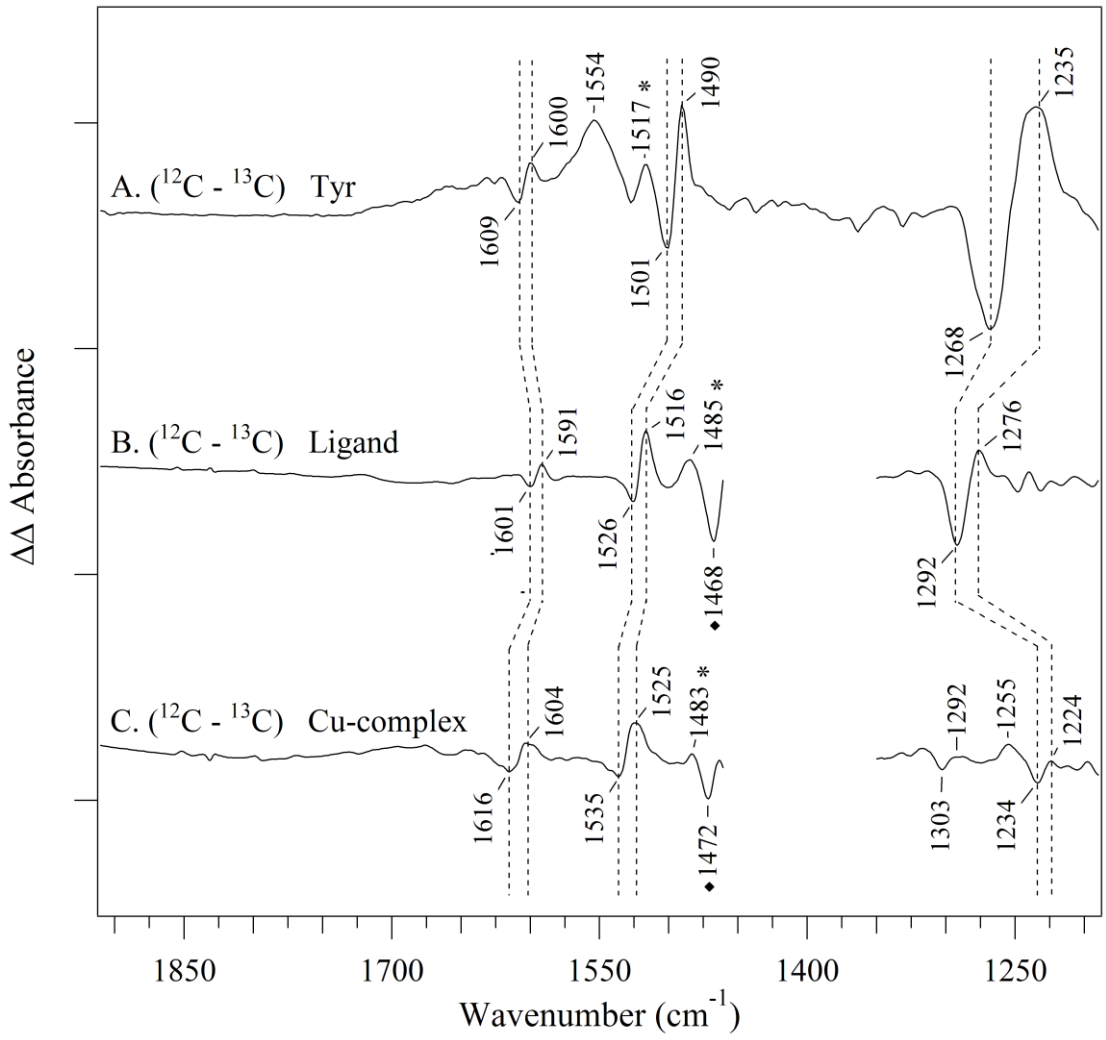

Figure 3.9. Isotope-edited, ^{12}C (light – dark)-minus-^{13}C (light – dark), FT-IR spectra, showing vibrational bands sensitive to ^{13}C labeling. The data were derived from tyrosinate (A), the ligand (B), and the Cu-complex (C). The ^{12}C-minus-^{13}C-isotope-edited FT-IR spectrum of the ligand (B) is the subtraction of Figure 3.8D from Figure 3.8C. The ^{12}C-minus-^{13}C-isotope-edited FT-IR spectrum of the Cu-complex is the subtraction of Figure 3.8F from Figure 3.8E. Tick marks on the *y*-axis correspond to 15 x 10^{-3} absorbance unit. For clarity, the spectral region between 1460 and 1350 cm^{-1} in panels B-E was removed due to acetonitrile absorption. The tyrosinate spectrum (A) was reproduced from reference.[51]

Isotope editing was also used to identify the analogous bands in the difference FT-IR spectra of the ligand and Cu-complex. From the isotope-edited spectrum of the ligand (Figure 3.9B), the negative bands at 1601, 1526, and 1292 cm^{-1} are attributed to υ_{8a}, υ_{19a} and $\upsilon_{7a'}$, respectively, with ^{13}C-isotope shifts (positive bands) to 1591, 1516, and 1276 cm^{-1}, respectively (Table 3.2 and Figure 3.9B). Our related, His–phenol cross-linked compound exhibited negative features at 1592, 1511, and 1265 cm^{-1}, which were assigned to perturbation of the singlet υ_{8a}, υ_{19a}, and $\upsilon_{7a'}$ bands, respectively, in the photolysis-induced FT-IR spectrum.[35] In the isotope-edited spectrum of the ^{12}C Cu-complex (Figure 3.9C), these same three vibrational modes appear at 1616, 1535, and 1234 cm^{-1}, with similar isotope shifts as those observed in the ligand (Table 3.2).

Table 3.2. Assignments of Vibrational Frequencies[a] with ^{13}C-Isotope Shifts

tyrosinate[b]			ligand		Cu-complex		
	(Δexp[c])	(Δcalc[d])		(Δexp[c])		(Δexp[c])	assignment
1609	-9	-6	1601	-10	1616	-12	υ_{8a}
1501	-11	-9	1526	-10	1535	-10	υ_{19a}
1268	-33	-24	1292	-16	1234	-10	υ_{7a}
tyrosyl radical•			ligand•		Cu-complex•		
	(Δexp[c])	(Δcalc[d])		(Δexp[c])		(Δexp[c])	assignment
1554	N.D.[e]	0	N.O.[f]		N.O.[f]		υ_{8a}
1517	N.D.[e]	-27	1485	-17	1234	-11	υ_{7a}

[a]Frequencies are in cm^{-1}. See Materials and Methods for experimental details. [b]Tyrosinate assignments based on previous isotope-edited spectra and DFT calculations.[51,60] [c]This work; derived from double difference spectra (Figure 3.9). [d]See ref 60. [e]N.D., not determined. [f]N.O., not observed

For the ligand in the singlet state, histidine–phenol cross-linking downshifts the highest energy, υ_{8a} phenol ring stretching mode and upshifts the υ_{19a} ring stretching mode (Table 3.2). Copper complexation upshifts both ring stretching modes relative to the non-metal-bound compound. Previously, changes in the frequency of the $\upsilon_{7a'}$ CO mode have been reported as a function of hydrogen bonding and protonation state of the phenol ring.[59] For a protonated phenol, the CO stretching vibration is observed between 1275 and 1265 cm^{-1} in proton donating states, with less intensity and at lower frequency (1240 and 1230 cm^{-1}) in proton accepting states, and at ~1255 cm^{-1} in non-hydrogen bonded states. For a deprotonated phenol, the CO vibrational band was reported at 1266 cm^{-1}. As mentioned above, under the conditions employed in our FT-IR measurements, the phenol ring is expected to be unprotonated in tyrosinate, protonated (67%) in the ligand and protonated in the Cu-complex. The upshift in CO frequency for the ligand (1292 cm^{-1}) compared to that of tyrosine (1268 cm^{-1}) is therefore larger than expected, based on the expected change in protonation. The upshift is attributed to a strengthening of the C–O single bond due to contribution of the C–C stretch to the 7a´ mode in the cross-linked ligand. For an *ortho*-substituted amino phenol in a solid, a mode at 1290 cm^{-1} is predicted.[61]

In the ^{12}C-minus-^{13}C isotope edited spectra, the decrease in the CO frequency and intensity of the $\upsilon_{7a'}$ mode of the Cu-complex (1234 cm^{-1}) (Figure 3.9C), compared to the ligand (1292 cm^{-1}) (Figure 3.9B), is attributable to the expected change in protonation, if the COH group of the Cu-complex is hydrogen bonded as a proton acceptor. The origin of the derivative-shaped band at 1303/1292 cm^{-1} and the positive band at 1255 cm^{-1} in the Cu-complex (Figure 3.9C) is under investigation, but the observation of multiple ^{13}C-

sensitive bands in this region suggests some heterogeneity in the CO frequency, and possibly, in the interactions of the phenolic OH group with the Cu^{2+} ion in the Cu-complex. An alternative pairing of the negative 1234 cm^{-1} with the positive 1255 cm^{-1} band is considered less likely, due to the expectation that ^{13}C labeling will downshift the band,[60] and that the negative 1234 cm^{-1} band arises from the singlet state.

3.4.7 Ring and CO Stretching Vibrations of the Radical

Unique vibrational bands arising from the radical are observed as positive bands in the photoinduced difference spectra in Figure 3.8. In the ^{12}C-minus-^{13}C isotope-edited spectra (Figure 3.9), the natural abundance bands from the radical are positive (∗) and the ^{13}C-shifted bands are negative (♦). The positive band at ~1517 cm^{-1} for tyrosine (Figure 3.9A, ∗) is assigned to the tyrosyl radical υ_{7a} CO stretching band on the basis of multiple isotopic labeling experiments and DFT calculations.[51,60] The frequency of the $^{13}C4'$ shifted band is not obvious in the isotope-edited spectrum (Figure 3.9A) and may overlap with the negative υ_{19a} vibrational band at 1501 cm^{-1}. A ^{13}C-isotope shift of 27 cm^{-1} is predicted (Table 3.2).[60]

On the basis of the isotope-edited spectra (Figure 3.9B and 3.9C, ∗), the bands at 1485 and 1483 cm^{-1}, are attributed to the υ_{7a} CO stretching in the ligand and Cu-complex, respectively. These bands shift to 1468 and 1472 cm^{-1} with ^{13}C labeling (Figure 3.9B and 3.9C, ♦; Table 3.2). The isotope-edited spectra in Figure 3.9 provide unambiguous support for the conclusion that a radical is generated by photolysis in both the ligand and the copper complex. In turn, this result confirms that the failure to observe a free radical

signal in the EPR experiment is most likely due to the large background signal from the Cu^{2+} ion and/or the low photolysis yield of the radical.

The $\upsilon_{7a'}$ CO frequency is substantially downshifted in the ligand radical (Figure 3.9B) compared to the frequency observed in the tyrosyl radical (Figure 3.9A). Because the imidazole cross-linking does not significantly change the unpaired spin density distribution,[35] this effect may be caused by a decrease in the paired π-electron density in the CO bond or an inductive effect on the ionic character of the CO bond. However, the CO frequency in the radical state is not significantly shifted by copper (Figure 3.9B and 3.9C), suggesting that the CO frequency shifts observed in the radical states of the ligand and Cu-complex are not mediated by the partial negative charge on the phenolic oxygen.

In our previous studies on the related, histidine–phenol cross-linked compound, we suggested that the radical CO stretching vibration might arise from bands at 1522 or 1498 cm^{-1}.[35] However, ^{13}C isotope-sensitive bands with these frequencies are not observed in the data presented here for the ligand or the Cu-complex. Attribution of a 1487 cm^{-1} band, observed previously in our histidine–phenol cross-linked compound,[35] to the CO stretching vibration is consistent with the data presented here.

3.4.8 Yield of the Radical in the Ligand and Copper Complex

To estimate the yield of the radical the amplitudes of bands in the isotope-edited spectra (Figure 3.9) were compared after correction for any differences in concentration, flash number, flash energy, and gain. Our EPR measurements (Figure 3.5) suggest that the radical yield is decreased by a factor of 4, when tyrosinate is compared to the ligand. The FT-IR data in Figure 3.9A (tyrosinate) and B (ligand) were collected on different FT-

IR spectrometers. However, analysis of the intensities of the CO $\upsilon_{7a'}$ band in Figure 3.9A (tyrosinate, 1268/1235 cm^{-1}) and B (ligand, 1292/1276 cm^{-1}) is qualitatively consistent with the EPR measurement. The FT-IR comparison predicts a 2.5-fold decrease in the ligand radical yield compared to tyrosine. A similar comparison was conducted for Figure 3.9B (ligand) and C (copper complex), which were collected on the same FT-IR spectrometer but with a different number of flashes (5, Figure 3.9B; 50, Figure 3.9C). Analysis of the intensities of the CO $\upsilon_{7a'}$ band in Figure 3.9B (ligand, 1292/1276 cm^{-1}) and C (1234/1224 cm^{-1}) gives a 40-fold decrease in the copper complex radical yield compared to that of the ligand.

3.4.9 Other Vibrational Bands

The broad ~1650 and ~1620 cm^{-1} peaks in the tyrosinate difference spectrum (Figure 3.8B) have previously been assigned to an overlap of solvent bands and perturbed NH_2 bending modes.[51,60,62] The photoinduced difference spectra of the natural abundance and ^{13}C-labeled ligand and Cu-complexes (Figure 3.8C–F) contain a similar series of broad peaks in the ~1660–1650 cm^{-1} region. However, these compounds do not contain any NH bands that can be perturbed upon oxidation. Therefore, in the case of the ligand and the Cu-complex, these broad bands are attributed to changes in solvent interactions alone.

The υ_{8a} ring stretching mode of the tyrosyl radical is expected between 1550 and 1560 cm^{-1}.[51,58,60] A candidate for this band is observed at 1554 cm^{-1} in the isotope-edited spectrum from tyrosinate (Figure 3.9A); however, the magnitude of the experimental isotope shift has not been established.[60] DFT calculations predict that the υ_{8a} ring

stretching mode of the radical will be insensitive to ring 4' labeling.[60,63] In agreement with this expectation, the υ_{8a} ring stretching mode is not observed in the isotope-edited spectra derived from the ligand and the Cu-complex (Figure 3.9B and C).

Some vibrational bands are observed in the ^{12}C- and ^{13}C-labeled ligands and Cu-complexes but are absent in the tyrosinate difference spectrum (Figure 3.8). These bands may arise from a perturbation of the imidazole cross-link upon radical formation. One such band appears at 1511–1508 cm^{-1} (pos.)/1494–1490 cm^{-1} (neg.) in the ligands and Cu-complexes (Figure 3.8C–F). The analogous positive peak may be at 1522 cm^{-1} in our related phenol-histidine cross-linked model.[35]

3.5 Discussion

3.5.1 Spectrophotomotmetric titrations

Our previous spectrophotmetric titrations on the natural abundance ligand and its copper complex[1] and those presented here for the ^{13}C-labeled ligand and Cu-complex have measured the pK_A of the phenolic proton. These studies indicate that the ligand pK_A of 8.8 and the Cu-complex pK_A of 7.8 are significantly lower than the pK_A of tyrosine.[35] These results are consistent with the cross-linked tyrosine facilitating proton delivery at the enzyme active site. These data are in agreement with previous studies on other model compounds,[33,38,64] which gave a pK_A value of 8.65 for a tripodal chelating ligand, containing an *ortho*-imidazole-phenol linkage, and a pK_A of 8 for a corresponding Zn-complex. For the ligand, a lower phenolic pK_A compared to unperturbed tyrosine or phenol would be expected, either through an inductive electron-withdrawing effect or

through resonance stabilization of the phenolate anion by the N-linked imidazole.[42,38] Further reduction would be expected upon coordination of the cross-linked imidazole to the copper because copper will withdraw electron density from the imidazole and stabilize the phenolate anion.[64]

3.5.2 Electrochemical titrations

The 670 mV potential of tyrosine (950 mV vs SHE electrode) is similar to that reported previously at pH 7.0.[65] At pH 7.0, our electrochemical data indicate that the redox potentials of the ligand phenol and the Cu-complex phenol are 110 and 60 mV more positive than that of tyrosine, respectively, consistent with imidazole withdrawing electron density from the phenolate ring.[33] The 110 mV increase in the redox potential of the ligand over that of tyrosine is similar to that observed previously between the oxidation potential of 2-imidazol-1-yl-4-methylphenol and p-cresol (66 mV) recorded at pH 11.5.[33] The moderate increase in the potential of the Cu-complex (60 mV) compared to that of unperturbed tyrosine and the lowering of the phenolic proton pK_A may ensure proton delivery during dioxygen reduction. The change in pK_A will allow re-reduction of the tyrosyl radical following its oxidation during the splitting of the dioxygen bond.[33]

3.5.3 EPR

UV photolysis of polycrystalline samples of the ligand clearly generated a paramagnetic species as indicated by a relatively narrow EPR signal with a corresponding isotropic *g* value of 2.0047. This observed *g*-value is in good agreement with the *g* value of tyrosyl radical and suggests the formation of a neutral phenoxyl radical in the ligand.

This result also suggests that the spin distribution of the photolysis-induced phenoxyl radical is not noticeably perturbed upon addition of an *o*-substituted imidazole group. Our previous EPR simulations on the related histidine–phenol cross-linked compound corroborate this idea.[35] DFT calculations have also shown that *o*-substitution yields only minor effects on the spin distribution of the deprotonated cross-linked tyrosine radical, consistent with our results.[56,66] EPR studies of other tyrosine–histidine model compounds have confirmed this conclusion.[36]

Previously, it was proposed that the S = 1/2 tyrosyl radical in cytochrome *c* oxidase might spin couple with the S = 1/2 Cu_B.[67,11] This would result in no Cu_B^{2+} EPR signal as observed for the magnetically-coupled Cu-tyrosyl radical in galactose oxidase.[68,69] However, Collman and co-workers have shown that a tyrosyl radical near a binuclear site analog does not necessarily spin couple with Cu_B.[45] The absence of a phenoxyl radical EPR signal for the Cu-complex presented here is consistent with tyrosine–histidine–Cu_B model studies with[45] or without[46] a heme group. Nagano and co-workers[46] observed no EPR phenoxyl radical signal for a copper ligated 2-[4-[[bis-(1-methyl-1*H*-imidazol-2-ylmethyl)amino]methyl]-1*H*-imidazol-1-yl]-4-methylphenol compound, Cu^{II}-**BIAIP**, upon light excitation in a temperature range from 4 to 90 K. This lack of a phenoxyl radical EPR signal was attributed to a weak signal intensity stemming from spin relaxation of the two unpaired interacting electrons.[46] From the relative intensities of the tyrosinate, ligand and Cu-complex EPR signals in our studies, it is evident that production of a phenoxyl radical species in the Cu-complex will be masked by the broad EPR signal from Cu^{2+} itself (Figures 3.4 and 3.6). Thus conventional continuous-wave X-band EPR spectroscopy alone is too insensitive for the

detection of such a paramagnetic species. The absence of a phenoxyl radical in our time-resolved optical absorption spectra generated following UV photolysis of the Cu-complex was attributed to possibly quenching by the copper.[1]

A tyrosine radical has been identified in the $\mathbf{P_M}$ and the **F•** oxyferryl intermediates of *P. denitrificans* using EPR spectroscopy;[31] these intermediates were generated upon addition of stoichiometric amounts of hydrogen peroxide to the oxidized enzyme at high and low pH, respectively. This radical has been assigned to tyrosine 129 (Tyr 167 *in P. denitrificans*) based on a multifrequency EPR (34 and 285 GHz) study of various tyrosine variants close to the binuclear center. However, because mutation of this tyrosine does not severely impact the turnover activity of the enzyme, it may not be involved in direct electron donation at the binuclear center during dioxygen turnover.[28,31]

3.5.4 FT-IR spectroscopy

Photolysis-induced FT-IR difference spectra were acquired to gain structural information and provide insight into the functional role of the tyrosine–histidine moiety in C*c*O. FT-IR spectroscopy detects changes in force constants, which are associated UV photolysis and phenoxyl radical generation. Unique positive vibrational modes were detected in the ligand and the Cu-complex compared to the tyrosyl radical, indicating that that the *o*-substituted imidazole force constants are perturbed upon oxidation of the phenoxyl group. This conclusion is supported by our previous FT-IR studies of a related cross-linked histidine–phenol analog[35] and by previous *ab initio* calculations[66] for histidine-substituted tyrosine models. We also observed a large spectral shift (~100 nm) in the time-resolved optical absorption difference spectra between the radical generated

in the ligand and unperturbed tyrosyl radical,[1] which may suggest significant mixing of the imidazole and phenoxyl electronic states in the ligand.

With oxidation, the frequencies of the radicals in the ligand and the Cu-complex are essentially identical and thus the copper does not seem to dramatically alter the electronic structure of the radical species. This observation is consistent with resonance Raman data reported for the biomimetic cross-linked **BIAIP** ligand and Cu^{II}-**BIAIP** compound although the resonance Raman frequencies reported for the 7a mode are significantly higher than those reported here.[46] Stable isotope labeling of the C1' carbon in the present study aided in the assignment of the CO frequency of the cross-linked phenoxyl radical in the ligand and the Cu-complex. Our assignments are consistent with FT-IR vibrational assignments for the tyrosine-histidine radical in cytochrome *c* oxidase. A band at 1489 cm^{-1} in the Raman spectrum of the $\mathbf{P_M}$ state of cytochrome bo_3 was tentatively assigned to the υ(CO) of the tyrosine-histidine radical.[70] In previous FT-IR difference studies, a frequency of 1479 cm^{-1} in the $\mathbf{P_M}$-minus-**O** spectrum of both the *R. sphaeroides*[16] and *P. denitrificans*[21] enzymes was attributed to the CO stretching vibration of the tyrosyl radical. Recently, based on isotope labeling, a band at 1519 cm^{-1} was identified as the phenoxyl radical ring stretching frequency of the cross-linked tyrosine in the $\mathbf{P_M}$-minus-**O** FT-IR difference spectrum of *P. denitrificans* C*c*O.[23] Nyquist and co-workers attributed bands at 1528 and 1517 cm^{-1} to the C–C ring stretching frequencies of the tyrosine–histidine radical in *R. sphaeroides* cytochrome *c* oxidase.[16] However, previous Raman spectroscopic studies of *ortho*-imidazole-bound *para*-cresol-based model compounds, with and without copper, have attributed bands around 1530–1533 cm^{-1} to the CO stretching vibration.[34,37,46] The good agreement

between the vibrational assignments presented here for the ligand and the Cu-complex and those observed in the spectra of the $\mathbf{P_M}$ intermediate of cytochrome *c* oxidase from different species provides further support for the presence of a tyrosyl radical in the $\mathbf{P_M}$ intermediate of cytochrome oxidase. These data indicate that these compounds are useful markers for future assignments of additional, tyrosine-histidine cross-link vibrational bands in C*c*O.

Several experimental results argue against the FT-IR bands in the Cu-complex resulting from a dissociated ligand in solution rather than the Cu-complex. First, the time-resolved optical absorption spectrum of the ligand shows a band at ~500 nm, while the spectrum of the Cu-complex does not. The spectrophotometric titrations of the ligand and the Cu-complex give significantly different pK_A values for the phenolic proton (8.8 for the ligand and 7.7 for the Cu-complex); the additional pK_A values of 4.5 and 7.4, attributed to the pyridine and imidazole, are not observed in the Cu-complex, arguing against a dissociated ligand being present in the Cu-complex sample. A phenoxyl radical signal is observed in the EPR spectrum of the photoinduced ligand, while this signal is absent in the Cu-complex. Moreover, while the vibrational frequencies attributed to the C–O stretch of the cross-linked phenoxyl radical are similar in the ligand and the Cu-complex, the C–O stretches for the phenolate anion in the two compounds are significantly different. Furthermore, we expect the Cu-imidazole bond to be stable at pH 6.2 and only at significantly lower pH might the imidazole become protonated and the Cu-bond break. A Jahn-Teller effect would be most prominent in the axial (dz^2) direction and not along the equatorial Cu-imidazole bond.

In summary, our studies show that a Cu^{2+} EPR signal is detected in the Cu complex both before and after following photolysis. Stable isotope (^{13}C) labeling of the phenol ring provides unequivocal support for the formation of the phenoxyl radical in both the ligand and the Cu-complex, following UV photolysis. Together, these results indicate that the C–O stretching frequency of the cross-linked tyrosyl radical would be expected at ~1480–1490 cm^{-1} rather than that in the 1530–1535 cm^{-1}. Together, our EPR and FT-IR results suggest that Cu_B^{2+} at the active site of cytochrome *c* oxidase is not spin-coupled to the cross-linked tyrosyl radial. Collman and co-workers have shown that a stable Fe^{III}-superoxide-Cu^{I} cytochrome *c* oxidase model compound reacts inter-molecularly with exogenous Tyr244 mimic compounds. This reaction leads to the formation of a phenoxyl radical and an oxyferryl ($Fe^{IV}=O^{2-}$)-cupric species, which is analogous to that observed in the **P** intermediate of the enzyme.[44] Moreover, mutagenesis of the cross-linked tyrosine to phenylalanine or histidine leads to essentially an inactive enzyme, reflecting the importance of this residue.[8,71] The absence of an EPR signal from the cross-linked tyrosyl radical in current EPR studies on cytochrome *c* oxidase has been suggested to be due to the migration of the cross-linked tyrosine radical to tyrosine 129 (Tyr 167 in *P. denitrificans*).[31,17] This pathway would compensate for the expected thermodynamic barrier to the fourth electron reduction reaction.[72] MacMillan et al. have suggested that tryptophan 126 (Trp 272 in *P. denitrificans*) may be an important intermediate on this pathway.[28] Our results demonstrate that the fourth electron required for dioxygen bond cleavage may originate from the cross-linked tyrosine, with the radical ultimately ending up on tyrosine 129 by the way of tryptophan 126.

3.6 Acknowledgement

This work was supported by the National Institutes of Health grant GM53788 (Ó.E.), and GM 43273 (B.A.B.). The single crystal X-ray diffraction data in this work were recorded on an instrument supported by the National Science Foundation, Major Research Instrumentation (MRI) Program under Grant No. CHE-0521569. We would like to thank Sulolit Pradhan and Shaowei Chen for assistance with the electrochemical measurements.

3.7 References

1. White, K. N.; Sen, I.; Szundi, I.; Landaverry, Y. R.; Bria, L. E.; Konopelski, J. P.; Olmstead, M. M.; Einarsdóttir, Ó. Synthesis and structural characterization of cross-linked histidine-phenol Cu(II) complexes as cytochrome *c* oxidase active site models. *Chem. Commun.* **2007**, 3252-3254.

2. Ferguson-Miller, S.; Babcock, G. T. Heme/copper terminal oxidases. *Chem. Rev.* **1996**, *96*, 2889-2907.

3. Wikström, M. K. F. Proton pump coupled to cytochrome *c* oxidase in mitochondrion. *Nature (London)* **1977**, *266*, 271-273.

4. Ostermeier, C.; Harrenga, A.; Ermler, U.; Michel, H. Structure at 2.7 Å resolution of the *Paracoccus denitrificans* two-subunit cytochrome *c* oxidase complexed with an antibody F_v fragment. *Proc. Natl. Acad. Sci. U.S.A.* **1997**, *94*, 10547-10553.

5. Yoshikawa, S.; Shinzawa-Itoh, K.; Nakashima, R.; Yanoe, R.; Yamashita, E.; Inoue, N.; Yao, M.; Fei, M. J.; Libeu, C. P.; Mitzushima, T.; Yamaguchi, H.; Tomizaki, T.; Tsukihara, T. Redox-coupled crystal structure changes in bovine heart cytochrome *c* oxidase. *Science* **1998**, *280*, 1723-1731.

6. Soulimane, T.; Buse, G.; Bourenkov, G. P.; Bartunik, H. D.; Huber, R.; Than, M. E. Structure and mechanism of the aberrant ba_3-cytochrome *c* oxidase from *Thermus thermophilus*. *EMBO J.* **2000**, *19*, 1766-1776.

7. Buse, G.; Soulimane, T.; Dewor, M.; Meyer, H. E.; Blüggel, M. Evidence for a copper-coordinated histidine–tyrosine cross-link in the active site of cytochrome oxidase. *Protein Sci.* **1999**, *8*, 958-990.

8. Das, T. K.; Pecoraro, C.; Tomson, F. L.; Gennis, R. B.; Rousseau, D. L. The post-translational modification in cytochrome *c* oxidase is required to establish a functional environment of the catalytic site. *Biochemistry* **1998**, *37*, 14471-14476.

9. Pinakoulaki, E.; Pfitzner, U.; Ludwig, B.; Varotsis, C. The role of the cross-link His-Tyr in the functional properties of the binuclear center in cytochrome *c* oxidase. *J. Biol. Chem.* **2002**, *277*, 13563-13568.

10. Ogura, T.; Hirota, S.; Proshlyakov, D. A.; Shinzawa-Itoh, K.; Yoshikawa, S.; Kitagawa, T. Time-resolved resonance Raman evidence for tight coupling between electron transfer and proton pumping of cytochrome *c* oxidase upon the change from the Fe^{V} oxidation level to the Fe^{IV} oxidation level. *J. Am. Chem. Soc.* **1996**, *118*, 5443-5449.

11. Proshlyakov, D. A.; Pressler, M. A.; Babcock, G. T. Dioxygen activation and bond cleavage by mixed-valence cytochrome *c* oxidase. *Proc. Natl. Acad. Sci. U.S.A.* **1998**, *95*, 8020-8025.

12. Fabian, M.; Wong, W. W.; Gennis, R. B.; Palmer, G. Mass spectrometric determination of dioxygen bond splitting in the "peroxy" intermediate of cytochrome *c* oxidase. *Proc. Natl. Acad. Sci. U.S.A.* **1999**, *96*, 13114-13117.

13. Blomberg, M. R. A.; Siegbahn, P. E. M.; Babcock, G. T.; Wikström, M. K. F. O–O bond splitting mechanism in cytochrome oxidase. *J. Inorg. Biochem.* **2000**, *80*, 261-269.

14. Proshlyakov, D. A.; Pressler, M. A.; DeMaso, C.; Leykam, J. F.; Dewitt, D. L.; Babcock, G. T. Oxygen activation and reduction in respiration: Involvement of redox-active tyrosine 244. *Science* **2000**, *290*, 1588-1591.

15. Tomson, F.; Bailey, J. A.; Gennis, R. B.; Unkefer, C. J.; Li, Z. H.; Silks, L. A.; Martinez, R. A.; Donohoe, R. J.; Dyer, R. B.; Woodruff, W. H. Direct infrared detection of the covalently ring linked His-Tyr structure in the active site of the heme-copper oxidases. *Biochemistry* **2002**, *41*, 14383-14390.

16. Nyquist, R. M.; Heitbrink, D.; Bolwien, C.; Gennis, R. B.; Heberle, J., Direct observation of protonation reactions during the catalytic cycle of cytochrome *c* oxidase. *Proc. Natl. Acad. Sci U.S.A.* **2003**, *100*, 8715-8720.

17. Svistunenko, D. A.; Wilson, M. T.; Cooper, C. E. Tryptophan or tyrosine? On the nature of the amino acid radical formed following hydrogen peroxide treatment of cytochrome *c* oxidase. *Biochim. Biophys. Acta* **2004**, *1655*, 372-380.

18. Gennis, R. B. Multiple proton-conducting pathways in cytochrome oxidase and a proposed role for the active-site tyrosine. *Biochim. Biophys. Acta* **1998**, *1365*, 241-248.

19. Sucheta, A.; Szundi, I.; Einarsdóttir, Ó. Intermediates in the reaction of fully reduced cytochrome *c* oxidase with dioxygen. *Biochemistry* **1998**, *37*, 17905-17914.

20. Hellwig, P.; Pfitzner, U.; Behr, J.; Rost, B.; Pesavento, R. P.; van der Donk, W. A.; Gennis, R. B.; Michel, H.; Ludwig, B.; Mäntele, W. Vibrational modes of tyrosines in cytochrome *c* oxidase from *Paracoccus denitrificans*: FTIR and electrochemical studies on Tyr-D_4-labeled and on Tyr280His and Tyr35Phe mutant enzymes. *Biochemistry* **2002**, *41*, 9116-9125.

21. Iwaki, M.; Puustinen, A.; Wikström, M. K. F.; Rich, P. R. ATR-FTIR spectroscopy of the P_M and F intermediates of bovine and *Paracoccus denitrificans* cytochrome *c* oxidase. *Biochemistry* **2003**, *42*, 8809-8817.

22. Iwaki, M.; Puustinen, A.; Wikström, M. K. F.; Rich, P. R. ATR-FTIR spectroscopy and isotope labeling of the P_M intermediate of *Paracoccus denitrificans* cytochrome *c* oxidase. *Biochemistry* **2004**, *43*, 14370-14378.

23. Iwaki, M.; Puustinen, A.; Wikström, M. K. F.; Rich, P. R. Structural and chemical changes of the P_M intermediate of *Paracoccus denitrificans* cytochrome *c* oxidase revealed by IR spectroscopy with labeled tyrosines and histidine. *Biochemistry* **2006**, *45*, 10873-10885.

24. Iwaki, M.; Breton, J.; Rich, P. R. ATR-FTIR difference spectroscopy of the P_M intermediate of bovine cytochrome *c* oxidase. *Biochim. Biophys. Acta* **2002**, *1555*, 116-121.

25. Rich, P. R.; Rigby, S. E. J.; Heathcote, P. Radicals associated with the catalytic intermediates of bovine cytochrome *c* oxidase. *Biochim. Biophys. Acta* **2002**, *1557*,137-146.

26. MacMillan, F.; Kannt, A.; Behr, J.; Prisner, T.; Michel, H. Direct evidence for a tyrosine radical in the reaction of cytochrome *c* oxidase with hydrogen peroxide. *Biochemistry* **1999**, *38*, 9179-9184.

27. Rigby, S. E. J.; Jünemann, S.; Rich, P. R.; Heathcote, P. Reaction of bovine cytochrome *c* oxidase with hydrogen peroxide produces a tryptophan cation radical and a porphyrin cation radical. *Biochemistry* **2000**, *39*, 5921-5928.

28. MacMillan, F.; Budiman, K.; Angerer, H.; Michel, H. The role of tryptophan 272 in the *Paracoccus denitrificans* cytochrome *c* oxidase. *FEBS Lett.* **2006**, *580*, 1345-1349.

29. Weirtz, F. G.; Richter, O.-M. H.; Ludwig, B.; de Vries, S. Kinetic resolution of a tryptophan-radical intermediate in the reaction cycle of *Paracoccus denitrificans* cytochrome *c* oxidase. *J. Biol. Chem.* **2007**, *282*, 31580-31591.

30. Chen, Y. R.; Gunther, R. P.; Mason, R. P. An electron spin resonance spin-trapping investigation of the free radicals formed by the reaction of mitochondrial cytochrome *c* oxidase with H_2O_2. *J. Biol. Chem.* **1999**, *274*, 3308-3314.

31. Budiman, K.; Kannt, A.; Lyubenova, S.; Richter, O. H.; Ludwig, B.; Michel, H.; MacMillan, F. Tyrosine 167: The origin of the radical species observed in the reaction of cytochrome *c* oxidase with hydrogen peroxide in *Paracoccus denitrificans*. *Biochemistry* **2004**, *43*, 11709-11716.

32. Elliott, G. I.; Konopelski, J. P. Complete *N*-1 regiocontrol in the formation of *N*-arylimidazoles. Synthesis of the active site His-Tyr side chain coupled dipeptide of cytochrome *c* oxidase. *Org. Lett.* **2000**, *2*, 3055-3057.

33. McCauley, K. M.; Vrtis, J. M.; Dupont, J.; van der Donk, W. A. Insights into the functional role of the tyrosine-histidine linkage in cytochrome *c* oxidase. *J. Am. Chem. Soc.* **2000**, *122*, 2403-2404.

34. Aki, M.; Ogura, T.; Naruta, Y.; Le, T. H.; Sato, T.; Kitagawa, T. UV resonance Raman characterization of model compounds of Tyr244 of bovine cytochrome *c* oxidase in its neutral, deprotonated anionic, and deprotonated neutral radical forms: Effects of covalent binding between tyrosine and histidine. *J. Phys. Chem. A* **2002**, *106*, 3436-3444.

35. Cappuccio, J. A.; Ayala, I.; Elliott, G. I.; Szundi, I.; Lewis, J.; Konopelski, J. P.; Barry, B. A.; Einarsdóttir, Ó. Modeling the active site of cytochrome oxidase: Synthesis and characterization of a cross-linked histidine-phenol. *J. Am. Chem. Soc.* **2002**, *124*, 1750-1760.

36. Kim, S. H.; Aznar, C.; Brynda, M.; Silks, L. A.; Michalczyk, R.; Unkefer, C. J.; Woodruff, W. H.; Britt, R. D. An EPR, ESEEM, structural NMR, and DFT study of a synthetic model for the covalently ring-linked tyrosine-histidine structure in the heme-copper oxidases. *J. Am. Chem. Soc.* **2004**, *126*, 2328-2338.

37. Nagano, Y.; Liu, J.; Naruta, Y.; Kitagawa, T. UV resonance Raman study of model complexes of the Cu_B site of cytochrome *c* oxidase. *J. Mol. Struct.* **2005**, *735*, 279-291.

38. Pratt, D. A.; Pesavento, R. P.; van der Donk, W. A. Model studies of the histidine-tyrosine cross-link in cytochrome *c* oxidase reveal the flexible substituent effect of the imidazole moiety. *Org. Lett.* **2005**, *7*, 2735-2738.

39. Kamaraj, K.; Kim, E.; Galliker, B.; Zakharov, L. N.; Rheingold, A. L.; Zuberbühler, A. D.; Karlin, K. D. Copper(I) and copper(II) complexes possessing cross-linked imidazole-phenol ligands: Structures and dioxygen reactivity. *J. Am. Chem. Soc.* **2003**, *125*, 6028-6029.

40. Collman, J. P.; Decréau, R. A.; Zhang, C. Synthesis of cytochrome *c* oxidase models bearing a Tyr244 mimic. *J. Org. Chem.* **2004**, *69*, 3546 - 3549.

41. Liu, J. G.; Naruta, Y.; Tani, F.; Chishiro, T.; Tachi, Y. Formation and spectroscopic characterization of the dioxygen adduct of a heme-Cu complex possessing a cross-linked tyrosine-histidine mimic: Modeling the active site of cytochrome *c* oxidase. *Chem. Commun.* **2004**, 120-121.

42. Kim, E.; Kamaraj, K.; Galliker, B.; Rubie, N. D.; Moënne-Loccoz, P.; Kaderli, S.; Zuberbühler, A. D.; Karlin, K. D. Dioxygen reactivity of copper and heme-copper complexes possessing an imidazole-phenol cross-link. *Inorg. Chem.* **2005**, *44*, 1238-1247.

43. Liu, J. G.; Naruta, Y.; Tani, F. A functional model of the cytochrome *c* oxidase active site: Unique conversion of a heme-μ-peroxo-Cu^{II} intermediate into heme-superoxo/Cu^{I}. *Angew. Chem. Int. Ed.* **2005**, *44*, 1836-1840.

44. Collman, J. P.; Decréau, R. A.; Sunderland, C. J. Single-turnover intermolecular reaction between a Fe^{III}–superoxide–Cu^{I} cytochrome *c* oxidase model and exogeneous Tyr244 mimics. *Chem. Commun.* **2006**, 3894-3896.

45. Collman, J. P.; Devaraj, N. K.; Decréau, R. A.; Yang, Y.; Yan, Y. L.; Ebina, W.; Eberspacher, T. A.; Chidsey, C. E. D. A cytochrome *c* oxidase model catalyzes oxygen to water reduction under rate-limiting electron flux. *Science* **2007**, *315*, 1565-1568.

46. Nagano, Y.; Liu, J.; Naruta, Y.; Ikoma, T.; Tero-Kubota, S.; Kitagawa, T. Characterization of the phenoxyl radical in model complexes for the Cu_B site of cytochrome *c* oxidase: Steady-state and transient absorption measurements, UV resonance Raman spectroscopy, EPR spectroscopy, and DFT calculations for M-BIAIP. *J. Am. Chem. Soc.* **2006**, *128*, 14560-14570.

47. Snieckus, V. Directed ortho metalation. Tertiary amide and O-carbamate directors in synthetic strategies for polysubstituted aromatics. *Chem. Rev.* **1990**, *90*, 879-933.

48. Kaiser, F.; Schwink, L.; Velder, J.; Schmalz, H. G. Studies towards the total synthesis of mumbaistatin: Synthesis of highly substituted benzophenone and anthraquinone building blocks. *Tetrahedron* **2003**, *59*, 3201-3217.

49. Seganish, W. M.; DeShong, P. Application of directed orthometalation toward the synthesis of aryl siloxanes. *J. Org. Chem.* **2004**, *69*, 6790-6795.

50. Deng, F.; Chen, S. Electrochemical quartz crystal microbalance studies of the rectified quantized charging of gold nanoparticle multilayers. *Langmuir* **2007**, *23*, 936-941.

51. Ayala, I.; Range, K.; York, D.; Barry, B. A. Spectroscopic properties of tyrosyl radicals in dipeptides. *J. Am. Chem. Soc.* **2002**, *124*, 5496-5505.

52. Vassiliev, I. R.; Offenbacher, A. R.; Barry, B. A. Redox active tyrosine residues in pentapeptides. *J. Phys. Chem. B* **2005**, *109*, 23077-23085.

53. Barry, B. A.; El-Deeb, M. K.; Sandusky, P. O.; Babcock, G. T. Tyrosine radicals in photosystem II and related model compounds. Characterization by isotopic labeling and EPR spectroscopy. *J. Biol. Chem.* **1990**, *256*, 20139-20143.

54. Hulsebosch, R. J.; van den Brink, J. S.; Nieuwenhuis, A. M.; Gast, P.; Rapp, J.; Lugtenburg, J.; Hoff, A. J., Electronic structure of the neutral tyrosine radical in frozen solution. Selective ^{2}H-, ^{13}C-, and ^{17}O-isotope labeling and EPR spectroscopy at 9 and 35 GHz. *J. Am. Chem. Soc.* **1997**, *119*, 8685-8694.

55. Sibert, R.; Josowicz, M.; Porcelli, F.; Veglia, G.; Range, K.; Barry, B. A. Proton-coupled electron transfer in a biomimetic peptide as a model of enzyme regulatory mechanisms. *J. Am. Chem. Soc.* **2007**, *129*, 4393-4400.

56. Himo, F.; Erikson, L. A.; Blomberg, M. R. A.; Siegbahn, P. E. M. Substituent effects on OH bond strength and hyperfine properties of phenol, as model for modified tyrosyl radicals in proteins. *Int. J. Quantum Chem.* **2000**, *76*, 714-723.

57. Tripathi, G. N. R.; Schuler, R. H. The resonance Raman spectrum of phenoxyl radical. *J. Chem. Phy.* **1984**, *81*, 113-121.

58. Johnson, C. R.; Ludwig, M.; Asher, S. A. Ultraviolet resonance Raman characterization of photochemical transients of phenol, tyrosine, and tryptophan. *J. Am. Chem. Soc.* **1986**, *108*, 905-912.

59. Takeuchi, H.; Watanabe, N.; Satoh, Y.; Harada, I. Effects of hydrogen bonding on the tyrosine Raman bands in the 1300-1150 cm^{-1} region. *J. Raman Spectrosc.* **1989**, *20*, 233-237.

60. Range, K.; Ayala, I.; York, D.; Barry, B. A. Normal modes of redox-active tyrosine: Conformation dependence and comparison to experiment. *J. Phys. Chem. B* **2006**, *110*, 10970-10981.

61. Agashe, M. S.; Jose, C. I. Analysis of complex hydroxyl absorptions of amino- and dimethylamino-phenols. *J. Chem. Soc., Faraday Trans. 2* **1976**, *73*, 1227-1231.

62. McCracken, J.; Vassiliev, I. R.; Yang, E. C.; Range, K.; Barry, B. A. ESEEM studies of peptide nitrogen hyperfine coupling in tyrosyl radicals and model peptides. *J. Phys. Chem. B* **2007**, *111*, 6586-6592.

63. McDonald, W.; Einarsdóttir, Ó. Solvent effects on the vibrational frequencies of phenolate anion, *para*-cresolate anion and their radicals. *J. Phys. Chem. A* **2008**, *112*, 11400-11413.

64. Pesavento, R. P.; Pratt, D. A.; Jeffers, J.; van der Donk, W. A. Model studies of the Cu_B site of cytochrome *c* oxidase utilizing a Zn(II) complex containing an imidazole–phenol cross-linked ligand. *Dalton Trans.* **2006**, *27*, 3326-3337.

65. Harriman, A. Further comments on the redox potentials of tryptophan and tyrosine. *J. Phys. Chem.* **1987**, *91*, 6102-6104.

66. Bu, Y.; Cukier, R. I. Structural character and energetics of tyrosyl radical formation by electron/proton transfers of a covalently linked histidine-tyrosine: A model for cytochrome *c* oxidase. *J. Phys. Chem. B* **2005**, *109*, 22013-22026.

67. Palmer, G. Current issues in the chemistry of cytochrome *c* oxidase. *J. Bioenerg. Biomembr.* **1993**, *25*, 145-153.

68. Whittaker, M. M.; Whittaker, J. W. The active site of galactose oxidase. *J. Biol. Chem.* **1988**, *263*, 6074-6080.

69. Whittaker, M. M.; Whittaker, J. W. A tyrosine-derived free radical in apogalactose oxidase. *J. Biol. Chem.* **1990**, *265*, 9610-9613.

70. Uchida, T.; Mogi, T.; Kitagawa, T. Resonance Raman studies of oxo intermediates in the reaction of pulsed cytochrome *bo* with hydrogen peroxide. *Biochemistry* **2000**, *39*, 6669-6678.

71. Pfitzner, U.; Odenwals, A.; Ostermann, T.; Weingard, L.; Ludwig, B.; Richter, O. H. Cytochrome *c* oxidase (heme aa_3) from *Paracoccus denitrificans*: Analysis of mutations in putative proton channels of subunit I. *J. Bioenerg. Biomembr.* **1998**, *30*, 89-97.

72. Blomberg, M. R. A.; Siegbahn, P. E. M.; Wikström, M. K. F. Metal-bridging mechanism for O-O bond cleavage in cytochrome *c* oxidase. *Inorg. Chem.* **2003**, *42*, 5231-5243.

CHAPTER 4

DEVELOPMENT OF A REACTION-INDUCED FT-IR SPECTROSCOPIC TECHNIQUE

by

Adam R. Offenbacher, Ilya R. Vassiliev, and Bridgette A. Barry

School of Chemistry and Biochemistry and the Parker H. Petit Institute for Bioengineering and Bioscience, Georgia Institute of Technology, Atlanta, Georgia 30332

4.1 Introduction and Background

In the chapters to follow, a reaction-induced FT-IR spectroscopic technique has been employed for the identification of protein conformational dynamics, which are coupled to redox changes of the ribonucleotide reductase β2 tyrosyl radical. In this chapter, a brief overview of the reaction-induced FT-IR syringe pump, which we have developed, is presented.

As introduced in Chapter 1, class Ia ribonucleotide reductase (RNR) enzymes exploit transient amino acid radicals, which perform long-distance proton-coupled electron transfer (PCET) reactions, to facilitate ribonucleotide reduction (reviewed in 1). The oxidation of C439 (*Escherichia coli* numbering) initiates this reduction process. Formation of C439• is mediated by a stable tyrosyl radical, Y122•, which is located 35 Å away. Spectroscopic identification of transient intermediates in the proposed PCET pathway[2] (Y122• – W48 – Y356 – Y731 – Y730 – C439), during turnover in the wild-type RNR, has not yet been successful. The caveat is that the PCET reactions occur quickly and are masked by slow, rate-limiting conformational change(s).[3] This pre-steady-state and steady-state kinetic analysis of the RNR reaction has underscored the importance of protein conformational dynamics in biological PCET reactions. Prior to this thesis work, structural information for the electron transfer events in RNR was limited. A previous high-field electron paramagnetic resonance (EPR)[4] study suggested a redox-linked rotation of Y122 along the C_α–C_β bond in the wild-type enzyme.

The conformational gating process in RNR limits the information that may be ascertained from the PCET reactions. The use of non-natural amino acids has allowed for the elucidation of PCET mechanistic details in RNR by switching the rate-limiting step

from a conformational gating to an electron transfer process. For instance, fluorotyrosine has been utilized in RNR and other enzymes, such as photosystem II (PSII),[5] because compared to tyrosine, fluorination of the tyrosine ring perturbs the pK_A and/or midpoint potential.[6,7] The role of Y356, which is the proposed interprotein electron transfer link between subunits $\alpha 2$ and $\beta 2$, has been investigated with site-specific replacement with 3-nitrotyrosine,[8] aniline,[9] and 3,4-dihydroxyphenylalanine[10] (DOPA). It was concluded that nucleotide reduction proceeds independent of the protonation state of the Y356, suggesting that electron shuttling from Y731 to Y356 is not mediated by hydrogen atom transfer (HAT).[7,11] Using a suppressor tRNA/aminoacyl-tRNA synthetase method, incorporation of 3-aminotyrosine into Y730 and Y731 in $\alpha 2$ subunit was possible.[12] In these modified 3-NH_2Y_{730} and 3-NH_2Y_{731} $\alpha 2$ samples, nucleotide reduction was observed and the data supported a hydrogen atom transfer mechanism in this subunit. The use of these non-natural amino acid residues has demonstrated the ability to probe intra- and inter-subunit proton-coupled electron transfer reactions of RNR. The function of the protein conformational dynamics that interplay with PCET processes in ribonucleotide reductase, however, was not addressed in these studies.

Protein conformational changes are postulated to play a central role in controlling proton-coupled electron transfer reactions.[13] Protein structural dynamics have been implicated in affecting electron transfer reactions required for photosynthetic reaction centers.[14] For example, the rate-limiting step in initial charge separation of photosynthesis has been correlated to protein structural dynamics.[15] Protein conformation changes surrounding the Mn_4Ca cluster of oxygen-evolving complex (OEC) are proposed to precede oxidation changes to the cluster.[16] These previous studies

have established the utility of the protein matrix dynamics in modulating electron transfer reactions.

Vibrational spectroscopy has emerged as a powerful tool to monitor protein dynamics and electron transfer mechanisms in biological systems.[17] Specifically, Fourier-transform infrared (FT-IR) spectroscopy has been used to identify structural dynamics and to elucidate reaction mechanisms of proteins (see refs 18-20, for example). The amide (i.e. peptide) bonds of the protein backbone yield several vibrational bands, of which the amide I and II modes are the most intense and useful bands for functional studies of the proteins.[21] The amide I band, which is found in the 1600–1700 cm^{-1} region, results mostly from C=O stretching vibrations of the peptide backbone. This amide vibration is very sensitive to perturbations in molecular geometry and hydrogen bonding of the atoms involving this mode.[22,23] The frequency of the amide I mode may help to describe protein conformational changes in proteins. Protein structural components can be assigned to α helices (1655 – 1660 cm^{-1}) or β sheets (1630 – 1640 cm^{-1}) using FT-IR analysis.[24] The amide II band, which is found in the 1480–1575 cm^{-1} region, results mostly from a coupling of CN stretching and in-plane bending of the N–H group.

FT-IR spectroscopy has the ability to detect and distinguish subtle changes, such as perturbations of the protonation state, electronic distribution, hydrogen bonding, and other electrostatic interaction(s). Thus, the technique can be used to probe protein structural dynamics and to determine reaction mechanisms. Development of improved time-resolved FT-IR spectrometers has allowed the study of protein dynamics in real time.[25-27] Time-resolved FT-IR and FT-IR difference spectroscopic studies were initiated

with the work by Rothschild, Siebert, and Gerwert on the light-driven proton pumping reactions in bacteriorhodopsin.[25,28,29]

FT-IR difference spectroscopy provides a means to study perturbations sensitive to a chemical- or photolysis-induced reaction. This difference technique emphasizes *only* the changes that are affected by the reaction.[28,30] There are some excellent reviews that discuss the application of FT-IR spectroscopy to proteins studies.[20,31-34] The technique has been extended towards the studies of water oxidation in photosystem II[35,36] and dioxygen reduction in cytochrome *c* oxidase.[37-39] Most of the successful FT-IR difference spectroscopic studies of enzymes have focused on light-initiated reactions. The application of reaction-induced FT-IR spectroscopy to non-photo-inducible proteins/enzymes, however, has not been widely reported. The limited number of studies is partially attributed to the lack of affordable, commercially available stopped-flow FT-IR instruments. Here, we describe the development of a reaction-induced FT-IR spectroscopic technique to identify protein conformational dynamics linked to PCET reactions in ribonucleotide reductase.

4.2 Description of Instrument

4.2.1 Sample Cell

The hallmark of our stopped-flow setup (Figure 4.1) is the fabricated sample flow cell. The sample cell is composed of two 32 x 3 mm CaF_2 windows, which are sandwiched together. One of the windows has been customized with a pair of through

holes (1.5 mm diameter) separated by 19 mm. The windows were customized by and purchased from Spectral Systems, LLC (Hopewell Junction, NY).

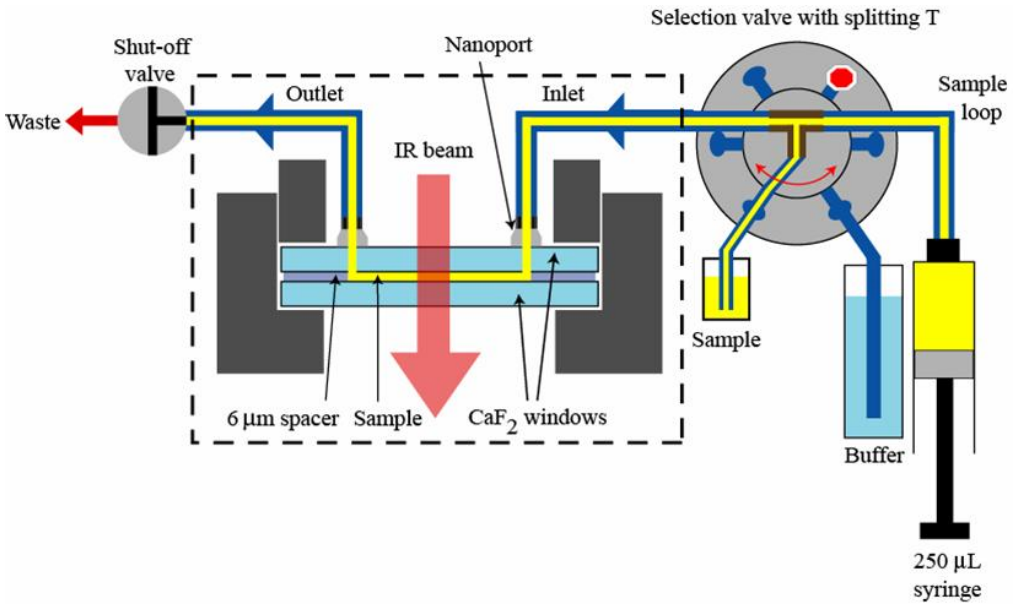

Figure 4.1. Diagram of the syringe-pump setup developed for the reaction-induced FT-IR experiments. The dashed line represents the flow-cell holder in the FT-IR instrument.

The two windows are separated by a 6 μm spacer composed of a Mylar material, which was donated by Steiner Films (Williamstown, MA). The spacer itself is stabilized in place by a thin layer of clear vacuum grease. By using a spacer, the pathlengths for the experiments are controlled by the thickness of the spacer material. Thus, the pathlength can be altered easily by changing the thicknesses of the spacer. For the majority of the RNR experiments, 6 μm has been used, but we have material in the 6 – 12 μm thicknesses range.

A pair of coned nanoports from Upchurch Scientific (Oak Harbor, WA) was bonded to the surface of the customized window at the location of the two through holes.

With the complementary coned nut, these connections allow for unobstructed flow rates with minimal dead volume.

4.2.2 Pump

The syringe pump that delivers the samples to the sample cell was purchased from FIAlab Instruments (Bellevue, WA). The microCSP-3000 syringe pump is computer automated with a 24,000 increment step motor, which drives the syringe piston at rates from 1.5 to 600 s per full stroke.

4.3 Experiments

4.3.1 RNR β2 Inhibitor Selection

Ribonucleotide reductase has been proposed as the rate-limiting step in DNA biosynthesis. This enzyme is overexpressed during tumor growth in cancer cells. Therefore, RNR has become an attractive target for anti-cancer pharmaceuticals.[40] The four main groups of drugs that target RNR activity are substrate analogs, peptidomimetic inhibitors, tyrosyl radical scavengers and iron chelators. Substrate analogs,[41] such as Cytarabine and gemcitabine, are suicidal inhibitors, which bind to nucleotide binding site and react to generate unusual products leading to the inactivation of RNR. Gemcitabine (2',2'-difluoro-2'-deoxycytidine, dFdC), which is currently used for pancreatic cancer and non-small cell lung cancer therapy,[40] induces the concomitant loss of tyrosyl radical in β2 and formation of a stable radical in the α2 subunit.[42] Peptidomimetic inhibitors, which match or mimic the carboxyl terminus of the β2 subunit, compete with binding of β2 to

α2 and prevent the formation of the active α2β2 complex.[43,44] An iron chelator, Triapine® (3-aminopyridine-2-carboxaldehyde thiosemicarbazone, 3-AP), is in Phase II clinical trials for the treatment of cervical carcinoma and has been shown to bind to the iron cluster in RNR and to consequently reduce Y122• (see ref 40 and refs therein).

The most popular and well-studied RNR inhibitors are radical scavengers, such as hydroxyurea, N-methylhydroxylamine, hydrazine and 4-methoxyphenol. These Y122• reducing agents are not postulated to have a binding site in β2.[45-47] Hydroxyurea (HU), specifically, has previously been widely used in cancer therapy for several decades, especially for the treatment of chronic and acute myeloid leukemias and refractory malignant lymphoma.[48,49] HU has also been effective as a therapy agent against HIV.[50] In mammalian enzymes, hydroxyurea has been shown to reduce the diferric cluster in addition to the Y•.[51] 4-methoxyphenol (or 4-hydroxyanisole) has been shown to be a potent inhibitor for RNR and has been used in the past for the treatment of melanomas, although the target may be towards tyrosinase activity.[52] The kinetics for the reduction of Y122• by these radical scavengers have been extensively studied and are summarized in Table 4.1.

The rate constants for the reduction of Y122• in β2 with these exogenous electron donors have only been well described in $^{1}H_2O$. For our reaction-induced FT-IR spectroscopic studies, we exchange β2 samples in $^{2}H_2O$ to eliminate spectral overlap of the amide I vibrations with the bending modes of $^{1}H_2O$ (~1650 cm^{-1}). Thus, in Chapters 5 and 6, we have determined the second-order rate constants for the reduction of Y122• using hydroxyurea, N-methylhydroxylamine, and 4-methoxyphenol in $^{2}H_2O$. Also, we

have examined these reaction kinetics at 20°C, because hydroxyurea has been shown to exhibit a temperature dependence.[53]

Table 4.1: Second-order kinetic rate constants (k_{obs}) for the reduction of Y122•.

β2 inhibitors	k_{obs} ($M^{-1}s^{-1}$) at p^{1}H 7.6	Reference
	Hydroxamic Acids	
Hydroxyurea	0.41 [b] - 0.46 [a] (25°C);	54, 55
	0.36 [b] (20°C)	56
N-Methylhydroxylamine	0.41 [a] (25°C)	55
	Alkoxyphenols	
4-Methoxyphenol	0.9 [b] (20°C)	56
4-Ethoxyphenol	0.8 [b] (20°C)	56
4-Allyloxyphenol	1.3 [b] (20°C)	56
	Others	
Didox[c]	0.010 [a] (25°C)	55
Catechol	3.2 [a] (25°C)	55
Hydrazine	0.013 [a] (25°C)	57
Phenylhydrazine	0.18 [a] (25°C)	57

[a] Monitored with UV/Vis spectroscopy [b] Monitored with EPR spectroscopy [c] 3,4-Dihydroxybenzohydroxamic acid

For our initial experiments, presented here and in Chapter 5, we have studied the reaction of the β2 protein with hydroxyurea. This reaction is among the most studied for exogenous reduction of Y• in ribonucleotide reductase. From the rate constant of the reaction of β2 and HU that we determined in ^2H_2O at 20°C (0.028 ± 0.003 $M^{-1}s^{-1}$),[58] we have derived the FT-IR reaction scheme shown in Figure 4.3. For the hydroxyurea

reaction, we estimate ~ 60% of Y122• is reduced (using [HU] = 50 mM) over the 10 minute data collection.

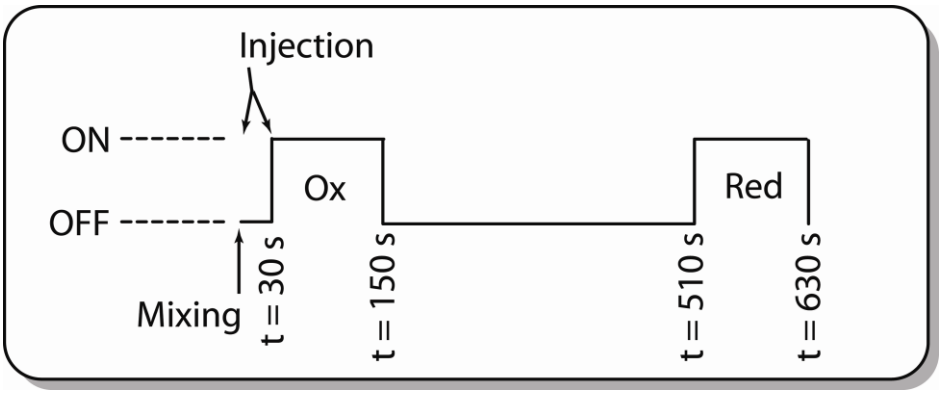

Figure 4.2. Reaction scheme for the reaction-induced FT-IR experiments using our sample flow cell. Following manual mixing of oxidized, control β2 and reducing agent (see text for details), the syringe pump injects the sample into the flow cell. After the 30 second injection, FT-IR data collection is turned "ON" for 2 minutes and these initial data points are averaged and dubbed "Ox" (or oxidized). Following a six minute incubation, data collection is turned "OFF" to allow for hydroxyurea-induced reduction of Y122•. Then, FT-IR data collection is turned "ON" for 2 minutes and these final data points are averaged and dubbed "Red" (i.e. reduced). To generate the FT-IR difference spectra (see Figure 4.7; for example), the FT-IR absorbance spectra of "reduced" are subtracted from "oxidized".

The kinetics for the reactions, displayed in Table 4.1, do not provide a thorough mechanism of action. A detailed analysis of the mechanism of RNR inhibitors and development and application of techniques to monitor the reaction of these inhibitors is required for the design of new anti-cancer treatments. Thus, we applied our reaction-induced FT-IR spectroscopic technique to describe the details for these reactions (see Chapter 6). In the following sections, experiments are described to test the validity of our designed reaction-induced FT-IR syringe pump.

4.3.2 Photosystem II

For the validation of our flow-cell, we have performed preliminary FT-IR absorption measurements of $^{2}H_2O$-exchanged Tris-washed photosystem II, which was isolated from spinach, as a standard. The FT-IR absorbance spectrum for this PSII sample in $^{2}H_2O$ buffer is shown in Figure 4.3. The spectrum is similar to previous reports, in which a conventional FT-IR spectrometer was used.[59]

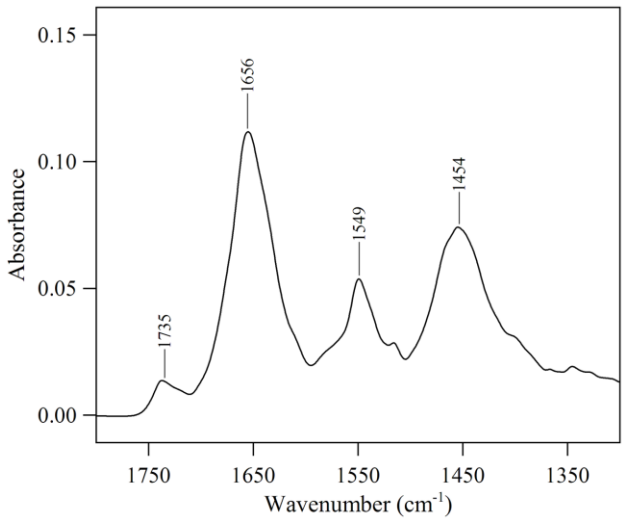

Figure 4.3. FT-IR absorbance spectra of photosystem II complexes collected at 20°C with the 6 μm pathlength of the sample cell and reaction-induced FT-IR syringe pump setup. PSII samples were exchanged in 5 mM Tris-^{2}HCl, p^{2}H 7.6. The data were collected and analyzed by Dr. Ilya R. Vassiliev.

There are several inherent benefits associated with this flow-cell system as compared to a standard set of FT-IR windows with the conventional system. First, the sample compartment of IR spectrometer remains closed and constantly purged with nitrogen gas. This allows for rapid sample collection, while maintaining the IR beam path free of H_2O and CO_2 vapor. Multiple replicates of the experiments can be performed on

samples within several minutes while they remain in a stable state. Second, the experiments are performed at fixed pathlengths of the IR cell, which allows for the results from different experiments at identical sample concentration to be quantitatively analyzed. These pilot experiments demonstrate the reliability of monitoring FT-IR absorption spectra of proteins on shorter time scale compared to conventional FT-IR systems.

4.3.3 BSA Control

FT-IR absorbance spectra of bovine serum albumin (BSA) collected in $^{2}H_2O$-based buffer are shown in Figure 4.4A. The BSA FT-IR spectra are similar to, but with better signal-to-noise than reported previously.[60] We have performed consecutive FT-IR measurements on a series of BSA samples (Figure 4.4A) from high to low concentration. The sample cell was cleaned between BSA data collections with 600 μL of buffer (5 mM Tris-^{2}HCl). The integrity of these cleaning steps is illustrated in Figure 4.8. The shape of the BSA spectra was reproducible at different concentrations and the amplitude of amide I band displayed a linear dependence on BSA concentrations in the 6.25 to 25 mg mL^{-1} range (Figure 4.4B). These data confirm that the pathlength (6 μm) and protein concentrations used in the reaction-induced FT-IR spectroscopic setup obey Beer's law.

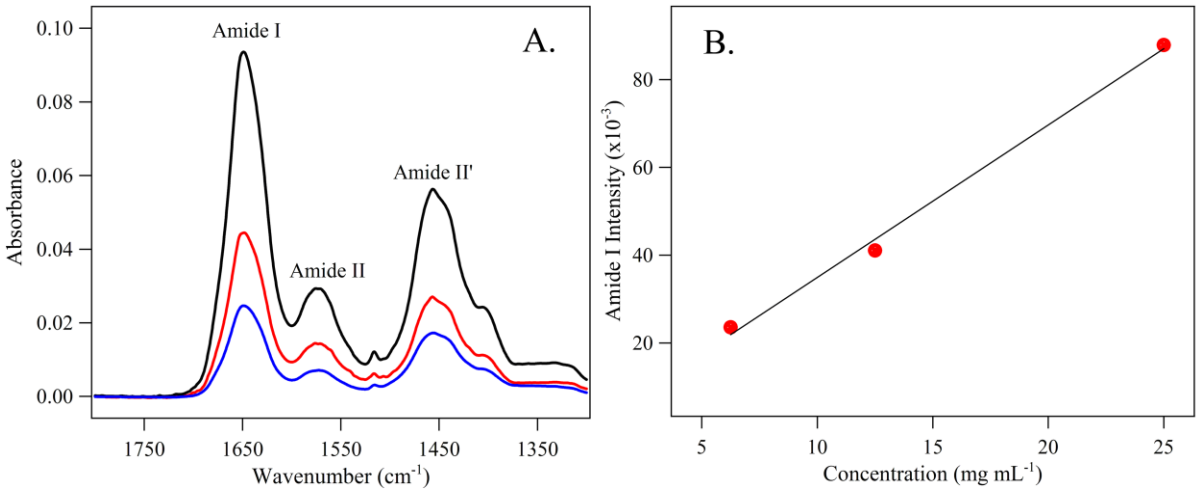

Figure 4.4. Dependence of amide I amplitude on the concentration of BSA. FT-IR spectra (A) of BSA were recorded in 5 mM Tris-^{2}HCl, p^{2}H 7.6 and were performed in duplicate. In (B), the intensity of the amide I bands from (A) were plotted against the concentration (in mg/mL).

The FT-IR absorbance spectrum of the reaction of BSA with hydroxyurea at 250 μM in ^2H_2O is shown in Figure 4.5A. The reaction conditions were setup to mimic the β2 reaction with hydroxyurea (Section 4.3.4). A 225 μL sample of 278 μM BSA was manually mixed (by pipette) with 25 μL of 500 mM hydroxyurea and was immediately injected into the flow-cell using the syringe pump. Following injection, two minutes of data were recorded before and after a six minute incubation time. The FT-IR difference spectrum for the reaction of BSA with hydroxyurea is displayed in Figure 4.5B. As expected, there are no significant spectral changes observed.

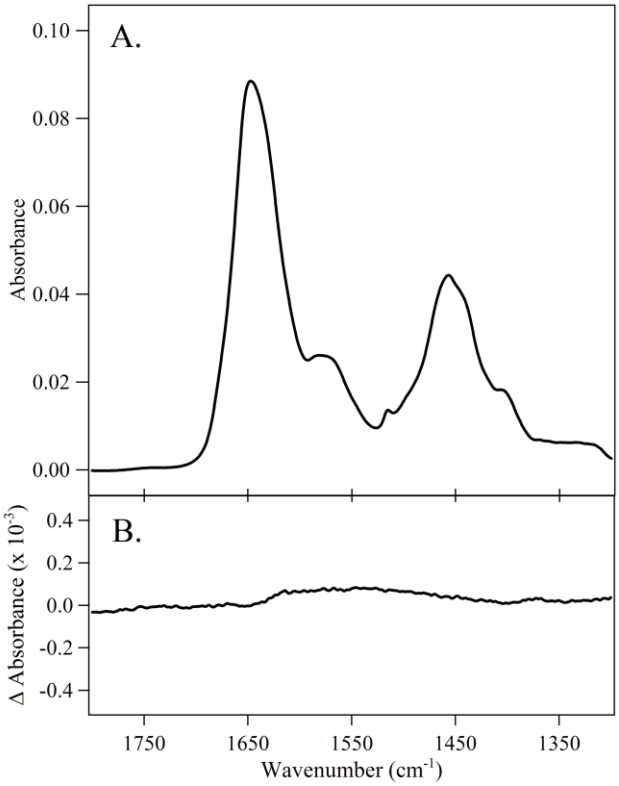

Figure 4.5. FT-IR spectra of the reaction of BSA with hydroxyurea at 20°C. A) FT-IR absorbance spectrum of BSA and hydroxyurea. B) FT-IR difference spectrum of "after"-"before". Two minutes of data were collected before and after a six minute incubation. The "before" spectrum was acquired immediately following the injection into the sample cell. The protein samples were prepared at 250 μM concentrations (final) in 5 mM Tris-^{2}HCl and the final hydroxyurea concentrations were 50 mM. The spectra are averages of 5 different samples.

4.3.4 RNR and Hydroxyurea in ^2H_2O

The first reported FT-IR absorbance spectrum of the *E. coli* β2 subunit of ribonucleotide reductase is shown in Figure 4.6. The ^2H_2O-based buffer single beam spectrum was subtracted from the β2 single beam spectrum to generate the β2 infrared absorbance spectrum in Figure 4.6.

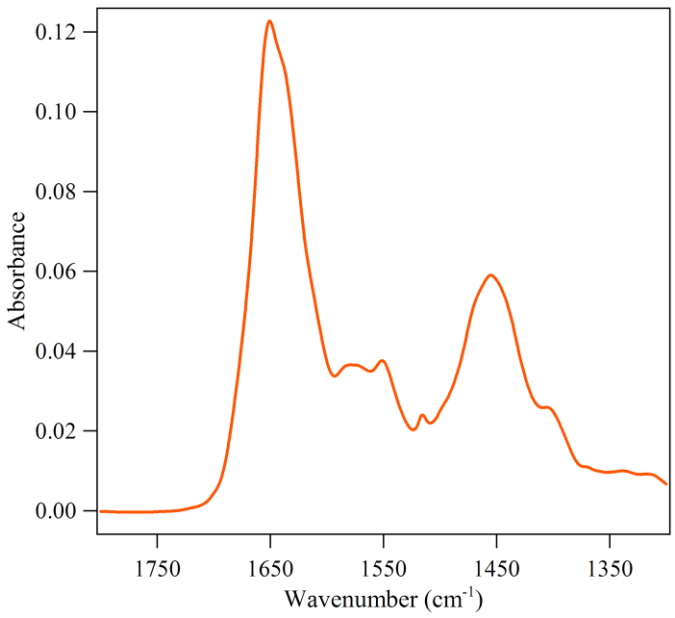

Figure 4.6. FT-IR absorbance spectrum of hydroxyurea reaction with ribonucleotide reductase β2 subunit in $^{2}H_2O$, collected at 20°C. The protein samples were exchanged into 5 mM Hepes, p^{2}H 7.6 buffer. The protein concentrations were 250 μM and hydroxyurea was 50 mM. The spectra are averages of 7 different samples.

The corresponding reaction-induced FT-IR difference spectra of β2 and hydroxyurea reactions are displayed in Figure 4.7. The data are generated from 1:1 subtraction of the "oxidized" – "reduced" FT-IR absorbance spectra (Figure 4.6). The reactions were performed in 5 mM Hepes (dotted line) and 5 mM Tris-^{2}HCl (solid line) buffers at p^{2}H 7.6. The confidence of the labeled peaks (in cm^{-1}) in Figure 4.7 is confirmed by the reproducibility of the spectral contributions using different buffer systems. Assignment of the observed vibrational modes in Figure 4.7 is discussed in detail in Chapters 5 and 6.

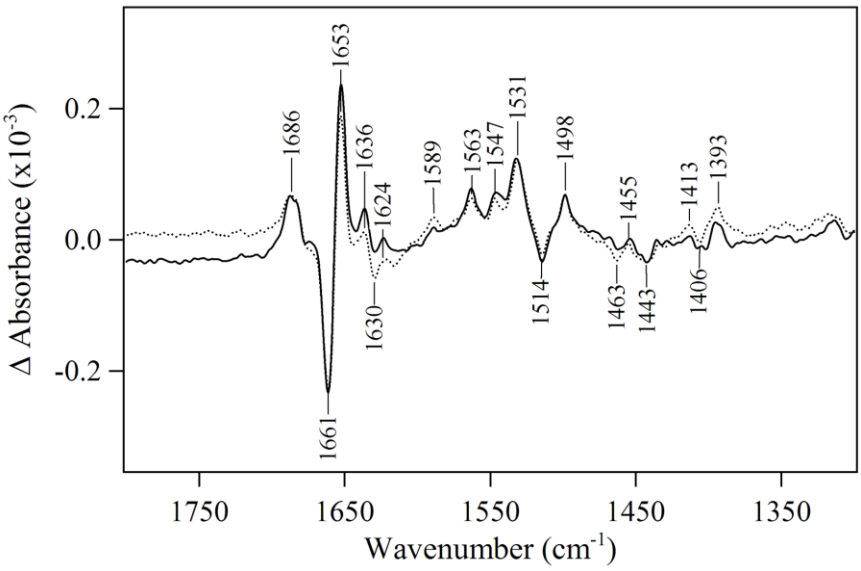

Figure 4.7. FT-IR difference spectra of hydroxyurea reaction with ribonucleotide reductase β2 subunit in ^2H_2O, collected at 20°C. Spectra were generated by subtracting "oxidized"-minus-"reduced" β2 FT-IR absorbance spectra. The protein samples were exchanged into 5 mM Hepes, p^{2}H 7.6 (dotted line) or 5 mM Tris, p^{2}H 7.6 (solid line) buffer. The protein concentrations were 250 μM and hydroxyurea was 50 mM. The spectra are averages of 7 (dotted line) and 8 (solid line) different samples.

4.3.5 Washing Procedure

One concern with this system is the ability to wash sample from the flow cell windows between experiments. Contamination from experiment to experiment could cause undesirable vibrational signals. The cleaning procedure consists of two steps: cleaning the sample injection lines (400 μL of ^2H_2O-buffer) followed by the sample flow cell (600 μL of ^2H_2O-buffer) itself. Figure 4.8 shows the effectiveness of the cleaning procedure. A FT-IR spectrum of the appropriate buffer is collected, followed by the collection of the β2 sample (dashed line) FT-IR spectrum. Following the cleaning protocol, another FT-IR spectrum of the buffer is recorded. Subtraction of the buffer FT-IR spectra as after-minus-before washing generates the solid line in Figure 4.8.

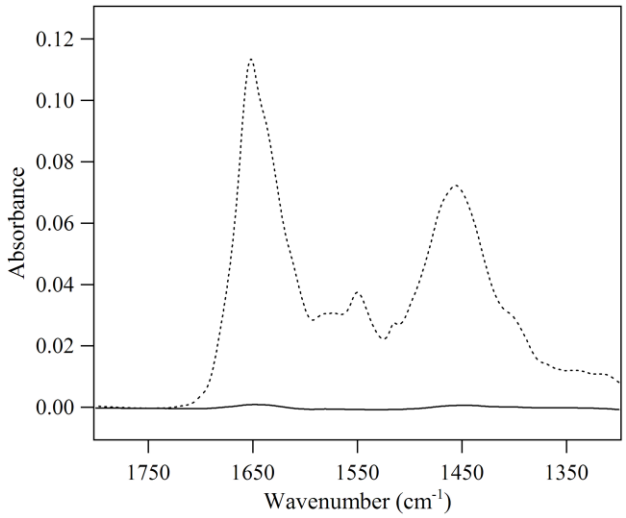

Figure 4.8. FT-IR spectra to describe washing experiment of the reaction-induced FT-IR syringe pump technique.

It follows from these measurements that the cleaning protocol is sufficient for complete displacement of the residual sample from the previous injection. In conclusion, the initial experiments, presented here, demonstrate to the capabilities of this reaction-induced FT-IR spectroscopic technique for the efficient study of protein conformational dynamics and electron transfer reactions in ribonucleotide reductase and other biological systems.

4.4 References

1. Stubbe, J.; Nocera, D. G.; Yee, C. S.; Chang, M. C. Y., Radical initiation in the class I ribonucleotide reductase: long-range proton-coupled electron transfer? *Chem. Rev.* **2003**, *103*, 2167-2202.

2. Uhlin, U.; Eklund, H., Structure of ribonucleotide reductase protein R1. *Nature* **1994**, *370*, 533-539.

3. Ge, J.; Yu, G.; Ator, M. A.; Stubbe, J., Pre-steady-state and steady-state kinetic analysis of *E. coli* class I ribonucleotide reductase. *Biochemistry* **2003**, *42*, 10071-10083.

4. Högbom, M.; Galander, M.; Andersson, M.; Kolberg, M.; Hofbauer, W.; Lassmann, G.; Nordlund, P.; Lendzlan, F., Displacement of the tyrosyl radical cofactor in ribonucleotide reductase obtained by single-crystal high-field EPR and 1.4-Å x-ray data. *Proc. Natl. Acad. Sci. U.S.A.* **2003**, *100*, 3209-3214.

5. Rappaport, F.; Boussac, A.; Force, D. A.; Peloquin, J.; Brynda, M.; Sugiura, M.; Un, S.; Britt, R. D.; Diner, B. A., Probing the coupling between proton and electron transfer in photosystem II core complexes containing a 3-fluorotyrosine. *J. Am. Chem. Soc.* **2009**, *131*, 4425-4433.

6. Seyedsayamdost, M. R.; Reece, S. Y.; Nocera, D. G.; Stubbe, J., Mono-, di-, tri-, and tetra-substituted fluorotyrosine: new probes for enzymes that use tyrosyl radicals in catalysis. *J. Am. Chem. Soc.* **2006**, *128*, 1569-1579.

7. Seyedsayamdost, M. R.; Yee, C. S.; Reece, S. Y.; Nocera, D. G.; Stubbe, J., pH rate profiles of F_nY_{356}-R2s (n = 2, 3, 4) in *Escherichia coli* ribonucleotide reductase: evidence that Y_{356} is a redox-active amino acid along the radical propagation pathway. *J. Am. Chem. Soc.* **2006**, *128*, 1562-1568.

8. Yee, C. S.; Seyedsayamdost, M. R.; Chang, M. C. Y.; Nocera, D. G.; Stubbe, J., Generation of the R2 subunit of ribonucleotide reductase by intein chemistry: insertion of 3-nitrotyrosine at residue 356 as a probe of the radical initiation process. *Biochemistry* **2003**, *42*, 14541-14552.

9. Chang, M. C. Y.; Yee, C. S.; Nocera, D. G.; Stubbe, J., Site-specific replacement of a conserved tyrosine in ribonucleotide reductase with an aniline amino acid: a mechanistic probe for a redox-active tyrosine. *J. Am. Chem. Soc.* **2004**, *126*, 16702-16703.

10. Seyedsayamdost, M. R.; Stubbe, J., Site-specific replacement of Y_{356} with 3,4-dihydroxyphenylalanine in the β2 subunit of *E. coli* ribonucleotide reductase. *J. Am. Chem. Soc.* **2006**, *128*, 2522-2523.

11. Yee, C. S.; Chang, M. C. Y.; Ge, J.; Nocera, D. G.; Stubbe, J., 2,3-Difluorotyrosine at position 356 of ribonucleotide reductase R2: a probe of long-range proton-coupled electron transfer. *J. Am. Chem. Soc.* **2003**, *125*, 10506-10507.

12. Seyedsayamdost, M. R.; Xie, J.; Chan, C. T. Y.; Schultz, P. G.; Stubbe, J., Site-specific insertion of 3-aminotyrosine into subunit $\alpha 2$ of *E. coli* ribonucleotide reductase: direct evidence for involvement of Y_{730} and Y_{731} in radical propagation. *J. Am. Chem. Soc.* **2007**, *129*, 15060-15071.

13. Davidson, V. L., What controls the rates of interprotein electron-transfer reactions. *Acc. Chem. Res.* **2000**, *33*, 87-93.

14. Kriegl, J. M.; Nienhaus, G. U., Structural, dynamic, and energetic aspects of long-range electron transfer in photosynthetic reaction centers. *Proc. Natl. Acad. Sci. U.S.A.* **2004**, *101*, 123-128.

15. Wang, H.; Lin, S.; Allen, J. P.; Williams, J. C.; Blankert, S.; Laser, C.; Woodbury, N. W., Protein dynamics control the kinetics of initial electron transfer in photosynthesis. *Science* **2007**, *316*, 747-750.

16. Barry, B. A.; Cooper, I. B.; De Riso, A.; Brewer, S. H.; Vu, D. M.; Dyer, R. B., Time-resolved vibrational spectroscopy detects protein-based intermediates in the photosynthetic oxygen-evolving cycle. *Proc. Natl. Acad. Sci. U.S.A.* **2006**, *103*, 7288-7291.

17. Vogel, R.; Siebert, F., Vibrational spectroscopy as a tool for probing protein function. *Curr. Opin. Chem. Biol.* **2000**, *4*, 518-523.

18. Haris, P. I.; Chapman, D., Does Fourier-transform infrared spectroscopy provide useful information on protein structures? *Trends Biochem. Sci.* **1992**, *17*, 328-333.

19. Arrondo, J. L. R.; Goñi, F. M., Structure and dynamics of membrane proteins as studied by infrared spectroscopy. *Prog. Biophys. Mol. Biol.* **1999**, *72*, 367-405.

20. Berthomieu, C.; Hienerwadel, R., Fourier-transform infrared (FTIR) spectroscopy. *Photosynth. Res.* **2009**, *101*, 157-170.

21. Nauman, D., FT-infrared and FT-Raman spectroscopy in biomedical research. In *Infrared and Raman spectroscopy of biological materials*, Gremlich, H.-U.; Yan, B., Marcel Dekker, Inc.: New York, 2001.

22. Miyazawa, T.; Blout, E. R., The infrared spectra of polypeptides in various conformations: amide I and II bands. *J. Am. Chem. Soc.* **1961**, *83*, 712-719.

23. Torii, H.; Tasumi, M., Infrared Spectroscopy of Biomolecules. In *Theoretical analyses of the amide I infrared bands of globular proteins*, Mantsch, H. H.; Chapman, D., Eds. Wiley-Liss: New York, 1996; pp 1-37.

24. Susi, H.; Timashef, S. N.; Stevens, L., Infrared spectra and protein conformations in aqueous solutions I. The amide I band in H_2O and D_2O solutions. *J. Biol. Chem.* **1967**, *242*, 5460-5466.

25. Engelhard, M.; Gerwert, K.; Hess, B.; Siebert, F., Light-driven protonation changes of internal aspartic acids of bacteriorhodopsin: an investigation of static and time-resolved infrared difference spectroscopy using {4-^{13}C}aspartic acid labeled purple membrane. *Biochemistry* **1985**, *24*, 400-407.

26. Gerwert, K.; Souvignier, G.; Hess, B., Simultaneous monitoring of light-induced changes in protein side-group protonation, chromophore isomerization, and backbone motion of bacteriorhodopsin by time-resolved Fourier-transform infrared spectroscopy. *Proc. Natl. Acad. Sci. U.S.A.* **1990**, *87*, 9774-9778.

27. Braiman, M. S.; Bousche, O.; Rothschild, K. J., Protein dynamics in the bacteriorhodopsin photocycle: submillisecond Fourier-transform infrared spectra of the L, M, and N photointermediates. *Proc. Natl. Acad. Sci. U.S.A.* **1991**, *88*, 2388-2392.

28. Rothschild, K. J.; Zagaeski, M.; Cantore, W. A., Conformational changes of bacteriorhodopsin detected by Fourier transform infrared difference spectroscopy. *Biochem. Biophys. Res. Commun.* **1981**, *103*, 483-489.

29. Siebert, F.; Mäntele, W.; Kreutz, W., Evidence for the protonation of two internal carboxylic groups during the photocycle of bacteriorhodopsin. Investigation by kinetic infrared spectroscopy. *FEBS Lett.* **1982**, *141*, 82-87.

30. Bagley, K.; Dollinger, G.; Eisenstein, L.; Singh, A. K.; Zimanyi, L., Fourier transform infrared difference spectroscopy of bacteriorhodopsin and its photoproducts. *Proc. Natl. Acad. Sci. U.S.A.* **1982**, *79*, 4972-4976.

31. Heberle, J.; Fitter, J.; Sass, H. J.; Büldt, G., Bacteriorhodopsin: the functional details of a molecular machine are being resolved. *Biophys. J.* **2000**, *85*, 229-248.

32. Vogel, R.; Fan, G.-B.; Sheves, M.; Siebert, F., The molecular origin of the inhibition of transduction activation in rhodopsin lacking the 9-methyl group of the retinal chromophore: a UV−Vis and FTIR spectroscopic study. *Biochemistry* **2000**, *39*, 8895-8908.

33. Zscherp, C.; Barth, A., Reaction-induced infrared difference spectroscopy for the study of protein reaction mechanisms. *Biochemistry* **2001**, *40*, 1875-1883.

34. Schweitzer-Stenner, R., Advances in vibrational spectroscopy as a sensitive probe of peptide and protein structure: a critical review. *Vib. Spectrosc.* **2006**, *42*, 98-117.

35. Noguchi, T.; Ono, T.; Inoue, Y., Detection of structural changes upon S1-to-S2 transition in the oxygen evolving manganese cluster in photosystem II by light-induced Fourier-transform infrared difference spectroscopy. *Biochemistry* **1992**, *31*, 5953-5956.

36. Steenhuis, J. J.; Barry, B. A., Protein and ligand environments of the S_2 state in photosynthetic oxygen evolution: a difference FT-IR study. *J. Phys. Chem. B* **1997**, *101*, 6652-6660.

37. Hellwig, P.; Pfitzner, U.; Behr, J.; Rost, B.; Pesavento, R. P.; van der Donk, W. A.; Gennis, R. B.; Michel, H.; Ludwig, B.; Mäntele, W., Vibrational modes of tyrosines in cytochrome *c* oxidase from *Paracoccus denitrificans*: FTIR and electrochemical studies on Tyr-D_4-labeled and on Tyr280His and Tyr35Phe mutant enzymes. *Biochemistry* **2002**, *41*, 9116-9125.

38. Nyquist, R. M.; Heitbrink, D.; Bolwien, C.; Gennis, R. B.; Heberle, J., Direct observation of protonation reactions during the catalytic cycle of cytochrome *c* oxidase. *Proc. Natl. Acad. Sci. U.S.A.* **2003**, *100*, 8715-8720.

39. Iwaki, M.; Puustinen, A.; Wikström, M. K. F.; Rich, P. R., FTIR spectroscopy and isotope labeling of the P_M intermediate of *Paracoccus denitrificans* cytochrome *c* oxidase. *Biochemistry* **2004**, *43*, 14370-14378.

40. Shao, J.; Zhou, B.; Chu, B.; Yen, Y., Ribonucleotide reductase inhibitors and future drug design. *Curr. Cancer Drug Tarets* **2006**, *6*, 409-431.

41. Stubbe, J.; van der Donk, W. A., Ribonucleotide reductases: radical enzymes with suicidal tendencies. *Chem. Biol.* **1995**, *2*, 793-801.

42. van der Donk, W. A.; Yu, G.; Pérez, L.; Sanchez, R. J.; Stubbe, J., Detection of a new substrate-derived radical during inactivation of ribonucleotide reductase from *Escherichia coli* by gemcitabine 5'-diphosphate. *Biochemistry* **1998**, *37*, 6419-6426.

43. Fisher, A. L.; Yang, F. D.; Rubin, H.; Cooperman, B. S., R2 C-terminal peptide inhibition of mammalian and yeast ribonucleotide reductase. *J. Med. Chem.* **1993**, *36*, 3859-3862.

44. Pellegrini, M.; Liehr, S.; Fisher, A. L.; Laub, P. B.; Cooperman, B. S.; Mierke, D. F., Structure-based optimization of peptide inhibitors of mammalian ribonucleotide reductase. *Biochemistry* **2000**, *39*, 12210-12215.

45. Krakoff, I. H.; Brown, N. C.; Reichard, P., Inhibition of ribonucleoside diphosphate reductase by hydroxyurea. *Cancer Res.* **1968**, *28*, 1559-1565.

46. Larsen, I. K.; Sjöberg, B. M.; Thelander, L., Characterization of the active site of ribonucleotide reductase of *Escherichia coli*, bacteriophage T4 and mammalian cells by inhibition studies with hydroxyurea analogs. *Eur. J. Biochem.* **1982**, *125*, 75-81.

47. Nordlund, P.; Sjöberg, B. M.; Eklund, H., Three-dimensional structure of the free radical protein of ribonucleotide reductase. *Nature* **1990**, *345*, 593-598.

48. Kennedy, B. J., The evolution of hydroxyurea therapy in chronic myelogenous leukemia. *Semin. Oncol.* **1992**, *19*, 21-26.

49. Vaughan, W. P.; Kris, E.; Vose, J.; Bierman, P. J.; Gwilt, P.; Armitage, J. O., Phase I/II study incorporating intravenous hydroxyurea into high-dose chemotherapy for patients with primary refractory or relapsed and refractory intermediate-grade and high-grade malignant lymphoma. *J. Clin. Oncol.* **1995**, *13*, 1089-1095.

50. Lori, F.; Malykh, A.; Cara, A.; Sun, D.; Weinstein, J. N.; Lisziewicz, J.; Gallo, R. C., Hydroxyurea as an inhibitor of human immunodeficiency virus-type I replication. *Science* **1994**, *266*, 801-805.

51. Nyholm, S.; Thelander, L.; Gräslund, A., Reduction and loss of the iron center in the reaction of the small subunit of mouse ribonucleotide reductase. *Biochemistry* **1993**, *32*, 11569-11574.

52. Pötsch, S.; Drechsler, H.; Liermann, B.; Gräslund, A.; Lassmann, G., *p*-Alkoxyphenols, a new class of inhibitors of mammalian R2 ribonucleotide reductase: possible candidates for antimelanotic drugs. *Mol. Pharmacol.* **1994**, *45*, 792-796.

53. Karlsson, M.; Sahlin, M.; Sjöberg, B. M., *Escherichia coli* ribonucleotide reductase. Radical susceptibility to hydroxyurea is dependent on the regulatory state of the enzyme. *J. Biol. Chem.* **1992**, *267*, 12622-12626.

54. Lassmann, G.; Thelander, L.; Gräslund, A., EPR stopped-flow studies of the reaction of the tyrosyl radical of protein R2 from ribonucleotide reductase with hydroxyurea. *Biochem. Biophys. Res. Commun.* **1992**, *188*, 879-887.

55. Swarts, J. C.; Aquino, M. A. S.; Han, J.-Y.; Lam, K.-Y.; Sykes, A. G., Kinetic studies on the reduction of the tyrosyl radical of the R2 subunit of *E. coli* ribonucleotide reductase. *Biochim. Biophys. Acta* **1995**, *1247*, 215-224.

56. Pötsch, S.; Sahlin, M.; Langelier, Y.; Gräslund, A.; Lassmann, G., Reduction of the tyrosyl radical and the iron center in protein R2 of ribonucleotide reductase from mouse, herpes simplex virus and *E. coli* by *p*-alkoxyphenols. *FEBS Lett.* **1995**, *374*, 95-99.

57. Han, J.-Y.; Gräslund, a.; Thelander, L.; Sykes, A. G., Kinetic studies on the reduction of the R2 subunit of mouse ribonucleotide reductase with hydroxyurea, hydrazine, phenylhydrazine, and hydroxylamine. *J. Biol. Inorg. Chem.* **1997**, *2*, 287-294.

58. Offenbacher, A. R.; Vassiliev, I. R.; Seyedsayamdost, M. R.; Stubbe, J.; Barry, B. A., Redox-linked structural changes in ribonucleotide reductase. *J. Am. Chem. Soc.* **2009**, *131*, 7496-7497.

59. Hutchison, R. S.; Betts, S. D.; Yocum, C. F.; Barry, B. A., Conformational changes in the extrinsic manganese stabilizing protein can occur upon binding to the photosystem II reaction center: an isotope editing and FT-IR study. *Biochemistry* **1998**, *37*, 5643-5653.

60. Remsen, E. E.; Freeman, J. J., A size-exclusion chromatography/FT-IR (SEC/FT-IR) technique for improved FTIR spectroscopy of proteins in D_2O solutions. *Appl. Spectrosc.* **1991**, *45*, 868-873.

CHAPTER 5

REDOX-LINKED STRUCTURAL CHANGES IN RIBONUCLEOTIDE REDUCTASE

by

[1]Adam R. Offenbacher, [1†]Ilya R. Vassiliev, [2]Mohammed R. Seyedsayamdost, [2]JoAnne Stubbe, and [1]Bridgette A. Barry

[1]School of Chemistry and Biochemistry and the Petit Institute for Bioengineering and Bioscience, Georgia Institute of Technology, Atlanta, GA 30332

[2]Departments of Chemistry and Biology, Massachusetts Institute of Technology, Cambridge, MA 02139

† - Deceased August 10, 2005

Reprinted with permission from the Journal of the American Chemical Society

Offenbacher, A. R.; Vassiliev, I. R.; Seyedsayamdost, M. R., Stubbe, J., Barry, B. A. "Redox-Linked Structural Changes in Ribonucleotide Reductase." *J. Am. Chem. Soc.* **2009**, *131*, 7496-7497.

5.1 Abstract

Ribonucleotide reductase (RNR) catalyzes the reduction of ribonucleotides to deoxyribonucleotides. Class I RNRs are composed of two homodimeric proteins, α2 and β2. The class Ia *E. coli* β2 contains dinuclear, antiferromagnetically coupled iron centers and one tyrosyl free radical, Y122•/β2. Y122• acts as a radical initiator in catalysis. Redox-linked conformational changes may accompany Y122 oxidation and provide local control of proton-coupled electron transfer reactions. To test for such redox-linked structural changes, FT-IR spectroscopy was employed in this work. Reaction-induced difference spectra, associated with the reduction of Y122• by hydroxyurea, were acquired from natural abundance, $^{2}H_4$ tyrosine, and ^{15}N tyrosine labeled β2 samples. Isotopic labeling led to the assignment of a 1514 cm^{-1} band to the υ19a ring stretching vibration of Y122 and of a 1498 cm^{-1} band to the υ7a CO stretching vibration of Y122•. The reaction-induced spectra also exhibited amide I bands, at 1661 and 1652 cm^{-1}. A similar set of amide I bands, with frequencies of 1675 and 1651 cm^{-1}, was observed when Y• was generated by photolysis in a pentapeptide, which matched the primary sequence surrounding Y122. This result suggests that reduction of Y122• is linked with structural changes at nearby amide bonds and that this perturbation is mediated by the primary sequence. To explain these data, we propose that a structural perturbation of the amide bond is driven by redox-linked electrostatic changes in the tyrosyl radical aromatic ring.

5.2 Introduction

Ribonucleotide reductase (RNR) catalyzes the reduction of ribonucleotides to deoxyribonucleotides.[1-3] Class I RNRs are composed of a 1:1 complex of two homodimeric proteins, α2 and β2. α2 contains the binding site for substrates and allosteric effectors that govern turnover rate and specificity, and β2 houses the essential

diferric-tyrosyl radical (residue 122, Y122•) cofactor.[1-4] Y122• acts as a radical initiator, generating a thiyl radical iṇ $\alpha 2$[5], ~35 Å removed.[6-8] Long distance proton-coupled electron transfer (PCET) is facilitated by a series of amino acid radical intermediates, which serve to accelerate the reaction rate into a physiologically relevant range.[9-15]

In this work, vibrational spectroscopy is used to show that electron transfer to and from the tyrosyl radical (Y122•) in RNR is coupled to a conformational change in the β2 subunit. Such redox-linked conformational changes are important because they can modulate the interaction of Y122 with its hydrogen bonding partner and provide local, structural control of its PCET reactions.

In previous work, high resolution magnetic resonance studies of Y122•[16] were performed. Comparison with the X-ray structure of reduced β2 suggested that a C_α-C_β single bond rotation may occur when Y122 is oxidized. This single bond rotation was attributed to an electrostatic repulsion between Asp-84 and Y122• and would disconnect Y122• from the hydrogen bond network at the diiron site. A Y• conformational rearrangement has also been proposed to occur with Y oxidation in pentapeptides and tyrosinate at 85 K.[17]

To identify redox-linked structural changes associated with electron transfer reactions in β2, we have performed FT-IR spectroscopy on the purified *E. coli* subunit in ^2H_2O buffer (Figures 5.7 and 5.8). FT-IR spectroscopy has emerged as a powerful tool in elucidating enzyme mechanisms (reviewed in 18). This approach has been used to study redox-active tyrosines in other proteins, such as photosystem II[19] and cytochrome *c* oxidase[20].

5.3 Materials and Methods

5.3.1 Materials

L-Tyrosine, Tris(hydroxymethyl)aminomethane hydrochloride, boric acid, sodium hydroxide, and hydrochloric acid were purchased from Sigma (St. Louis, MO). The RSYTH pentapeptide was purchased from Sigma-Genosys (The Woodlands, TX). {$^2H_4$}-tyrosine (L-tyrosine-ring-$^2H_4$, 98%), {^{15}N}-tyrosine (L-tyrosine-^{15}N, 98%) and deuterium oxide, ^2H_2O, (98%) were obtained from Cambridge Isotope Laboratories (Andover, MA). Hydroxyurea was purchased from Calbiochem (San Diego, CA).

5.3.2 Expression and Purification of the β2 Subunit of RNR

Natural abundance (NA) *E. coli* β2s were over-expressed in BL21(DE3) cells containing the pTB2 vector, as described previously.[21] The pTB2 plasmid, which is composed of the β2 gene under the control of a T7 promoter and terminator as well as an Amp^R selection marker, was transformed into the BL21(DE3) cells using the Stratagene standard protocol. A single colony of transformed cells was inoculated into 5 mL LB/Amp ([Amp] = 100 μg/mL) and grown for ~ 12 h at 37°C and 200 rpm. The starter culture was diluted 20-fold into 100 mL LB/Amp solution (500 mL shaker flask). The overnight culture (grown ~ 12 h) was diluted 20-fold into 800 mL LB/Amp solutions (typically in 2–4 x 3.2 L shaker flasks). The cultures were grown for 3 additional hours, at which point IPTG was added at a final concentration of 0.5 mM. The cells were harvested after 4 – 5 h at 37°C and 200 rpm post IPTG induction by centrifugation at 10,000 x g and 4°C for 15 min. The cell pellets were then transferred to 50 mL Falcon tube, flash frozen in liq. N_2, and stored at -80°C.

The β2 protein was typically purified from 6 – 10 g of cell pellet. All purification steps were performed at 4°C. For each g of cell pellet, 5 mL of purification buffer (50 mM Tris, 5 % glycerol, pH 7.6) was added with 1 mM PMSF (from 100 mM PMSF in isopropanol). The cells were resuspended by gentle stirring. Cells were lysed through a single passage of a French press at 14,000 psi. After lysis, sodium ascorbate and $Fe(II)(NH_4)_2(SO_4)_2$ (5 mg per g cell each; dissolved in 10 mL purification buffer) were added dropwise to the lysed cells while stirring. The cell extract was stirred for an additional 15 min to increase radical yield. The lysate was centrifuged at 15,000 x g and 4°C for 30 min to remove the cellular membrane and debris. DNA was precipitated by the dropwise addition of 0.2 volumes of 6 % streptomycin sulfate (in purification buffer) to the supernatant while stirring. The cell extract was again stirred for an additional 15 min. The DNA was then removed by centrifugation at 15,000 x g and 4°C for 35 min. Protein was precipitated by the slow (20 min) addition of 0.39 g of $(NH_4)_2SO_4$ (s) per mL supernatant while stirring. The mixture continued stirring for an additional 40 min. The protein precipitate was isolated by centrifugation at 15,000 x g and 4°C for 45 min. The protein pellet was redissolved in 10 mL purification buffer with 1 mM PMSF and subsequently desalted on a G25 (2.5 x 45 cm; 200 mL) column, which was pre-equilibrated in purification buffer. The protein was collected manually by monitoring the A_{280nm} of the eluate. The brownish, pooled eluate was loaded onto a DEAE (5 x 15 cm; 150 mL) fast flow anion exchange column, which was pre-equilibrated in purification buffer. After loading, the column was washed with 2 column volumes (CV) of purification buffer immediately followed by 1.5 CV of 110 mM NaCl (in purification buffer). The β2 protein was eluted from the DEAE column by a linear gradient (500 x

500 mL) from 100 – 500 mM NaCl (in purification buffer). Fractions containing β2, determined as Y•/β2 ≥ 0.9 (for calculation of [Y•] and [β2], vide supra), were pooled, diluted with equal volume of purification buffer, and loaded onto a Q-Sepharose (5 x 10 cm; 100 mL) column, which was pre-equilibrated with purification buffer. The β2 protein was eluted from the Q column by a linear gradient (500 x 500 mL) from 200 – 700 mM NaCl (in purification buffer). Fractions containing β2 were pooled, diluted with equal volume of purification buffer, and concentrated using a YM30 ultrafiltration device. SDS-PAGE was used to monitor the purification (Figure 5.1).

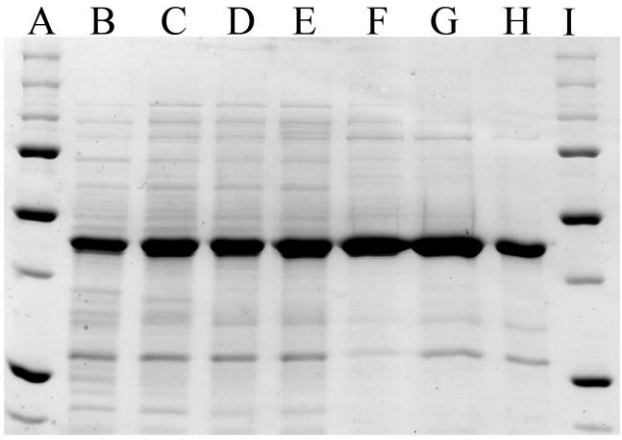

Figure 5.1. SDS-PAGE showing the purification of the *E. coli* RNR β2 subunit. Lanes: A) and I) molecular weight standards, B) cell lysate, C) after streptomycin sulfate treatment, D) after ammonium sulfate treatment, E) Sephadex G-25 eluent, F) DEAE eluent, G) Q-Sepharose eluent, and H) purified natural abundance β2.

Global incorporation of $\{^2H_4\}$-labeled tyrosine or $\{^{15}N\}$-labeled tyrosine into the β2 was accomplished using minimal media. The procedure was reported previously for 3-fluorotyrosine incorporation,[22] except that the thiamine concentration was changed to 25 mg/L and that the tyrosine concentration was changed to 600 mg/L.[23] For negative

control experiments, Met-β2, in which the tyrosyl radical is reduced and the diiron cluster remains oxidized, was produced by incubating β2 (~0.25 mM) with hydroxyurea (HU, 50 mM) at room temperature for ≥ 30 min. The HU was then removed[24] using an Amicon YM30 (Beverly, MA) concentrator. $^{2}H_2O$ buffer exchange was performed through the use of three sequential concentration and dilution steps in YM30 concentrators. The β2 sample was exchanged into $^{2}H_2O$-based buffer (Figure 5.4) to eliminate overlap of the water OH bending mode with the amide I C=O band at ~1650 cm^{-1} for the infrared experiments.[25]

5.3.3 UV-Visible Spectroscopy and Kinetic Studies

Room temperature absorbance spectra of the purified β2 sample were recorded on a Hitachi U-3000 spectrophotometer using 1 cm quartz cuvettes. The concentration of β2 (Figure 5.2A) was determined using A_{280} nm and ε ~131,000 $M^{-1}cm^{-1}$.[22] The Y• yield was determined from the absorbance at 416, 411, and 406 nm (Figure 5.2B), according to the following equation, $[Y\bullet] = \frac{A_{411nm} - \left[\frac{3\times(A_{416nm}) + 2\times(A_{406nm})}{5}\right]}{1784\,M^{-1}cm^{-1}}$.[26] The Y122• per β2 was 1.2-1.4 for the natural abundance β2 preparation, 1.0-1.3 for the $\{^{2}H_4\}$-tyrosine preparation, and 0.9-1.3 for the $\{^{15}N\}$-tyrosine preparation.

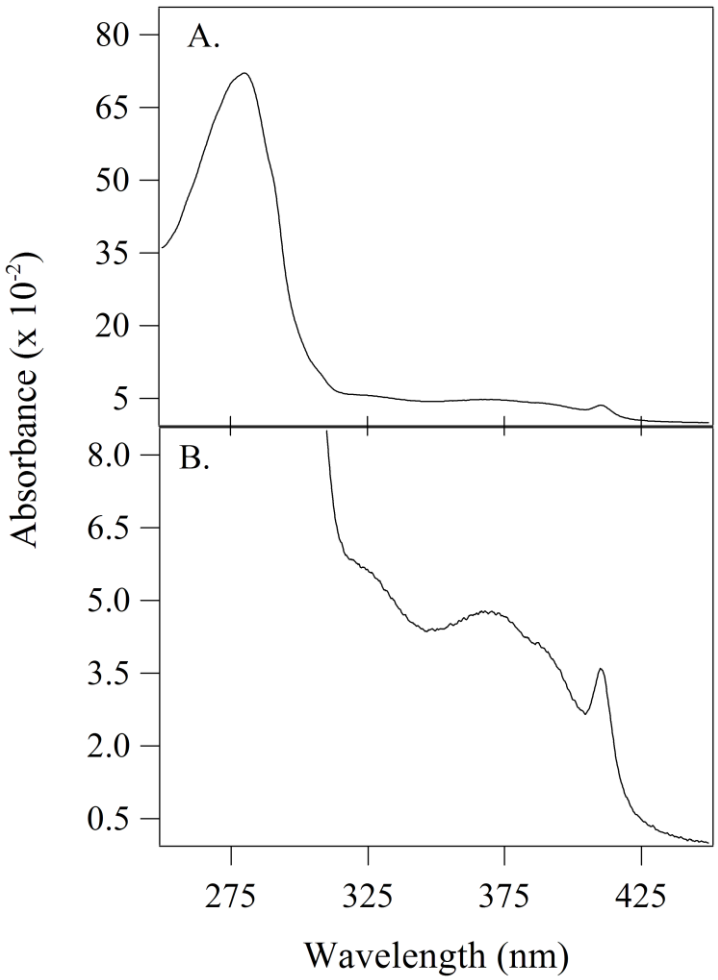

Figure 5.2. Representative UV-Visible absorbance spectrum of a purified, natural abundance β2 sample (A). In (B), the y axis was expanded by a factor of ten to show the tyrosyl radical band at 410 nm.

By monitoring the decay of the Y122• 410 nm absorption band,[27-31] the rate constants for Y122• reduction were determined (Figures 5.3 and 5.4). The second-order rate constants were obtained on a Varian Cary 50 (Varian, Walnut Creek, CA) spectrophotometer equipped with a temperature controller. The $^{1}H_2O$ or $^{2}H_2O$ buffer contained 5 mM Tris-HCl, p^{1}H or p^{2}H 7.6. The p^{1}H and p^{2}H are reported as the uncorrected meter reading. The reaction was monitored at 1.8 min intervals for 30 min at

20°C; the experiment was conducted in triplicate. The rate constant in $^{1}H_2O$ was determined to be 0.40 ± 0.06 $M^{-1}s^{-1}$, in reasonable agreement with the previously reported value of 0.33 $M^{-1}s^{-1}$.[29] The rate constant in $^{2}H_2O$ was determined to be 0.028 ± 0.003 $M^{-1}s^{-1}$.

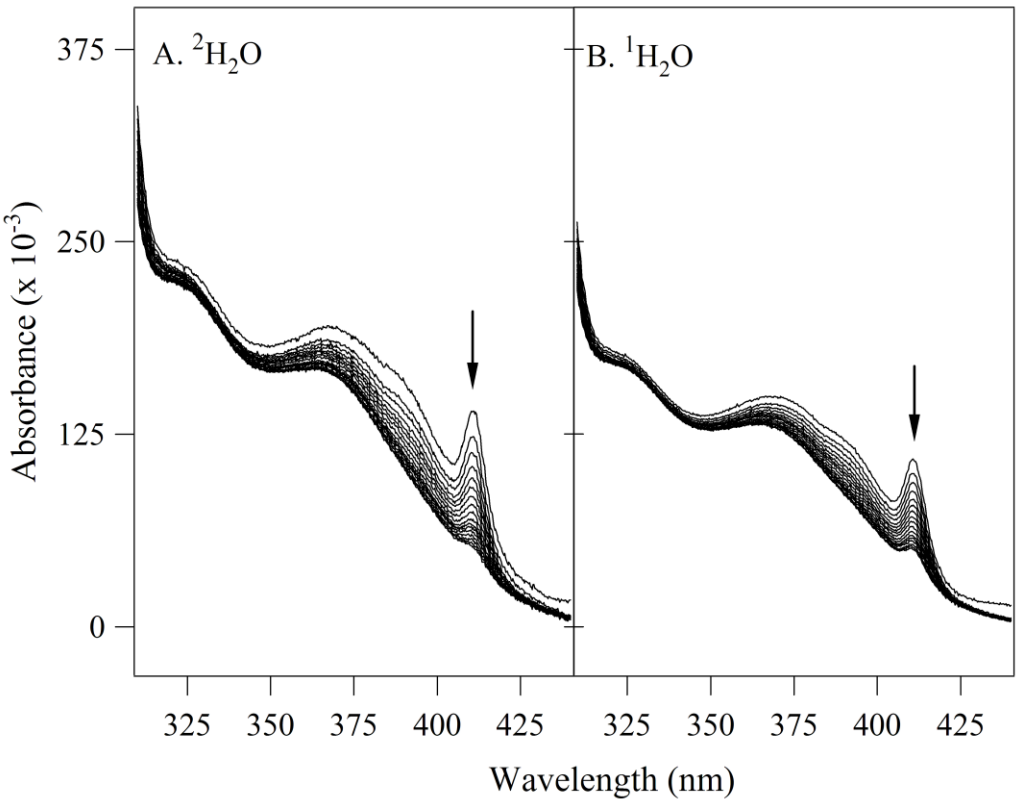

Figure 5.3. Representative examples of the UV-Visible absorbance spectra, used to derive the rate constant for Y122• reduction by HU. The temperature was 20°C, the sample was the purified, natural abundance β2 (20 μM), and the experiment was conducted either in $^{2}H_2O$ buffer with 50 mM HU (A) or $^{1}H_2O$ buffer with 2.5 mM HU (B). The loss of the Y• absorbance at 410 nm is indicated by the arrow.

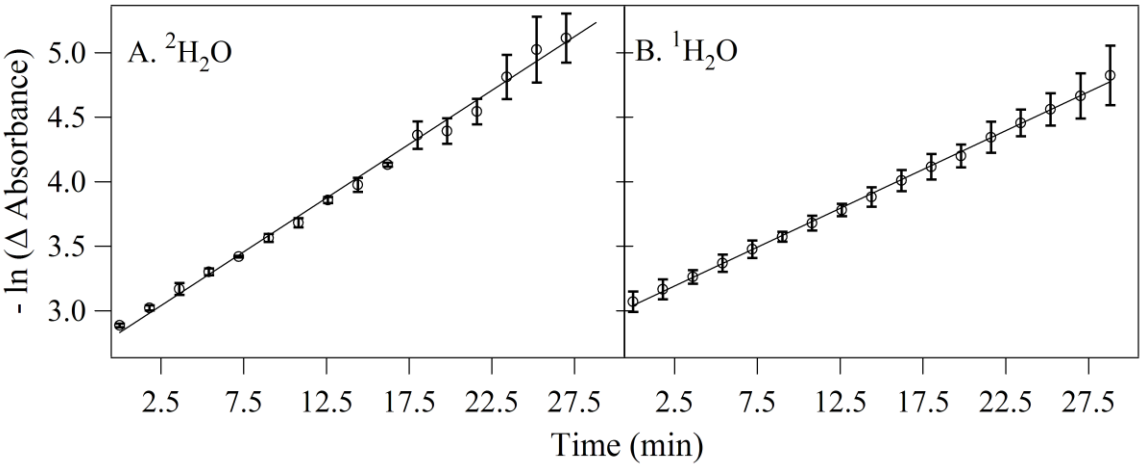

Figure 5.4. Data used to derive the averaged rate constants for Y122• reduction by HU. The decrease in A410 nm was monitored as a function of time (see example in Figure 5.3) in three separate experiments. The ΔAbs values were determined by the fitted base-line method.[31] The averaged data (three experiments) were fit to the equations, -ln(ΔAbs) = 0.0834 *t* + 2.83 (A, ^2H_2O, 50 mM HU), or -ln(ΔAbs) = 0.0602 *t* + 3.04 (B, ^1H_2O, 2.5 mM HU), where *t* is in min. The standard deviations were used to estimate the error in the measurement. The rate constant was derived by dividing through by the HU concentration.

5.3.4 Electron Paramagnetic Resonance (EPR) Spectroscopy

EPR measurements were performed to verify the incorporation of $^2H_4$-tyrosine into the β2 subunit. EPR spectra were recorded at 10 K with a Bruker (Billerica, MA) EMX X-band EPR spectrometer equipped with a standard Bruker TE cavity and an Oxford (Concord, MA) liquid helium cryostat. The natural abundance, $^2H_4$-tyrosine labeled, and Met-β2 samples were prepared at 50 μM concentrations in 5 mM Tris-^{1}HCl, p^{1}H 7.6 solutions. Another sample of natural abundance β2 was prepared as 50 μM solution in 5 mM Tris-^{2}HCl, p^{2}H 7.6. The spectrometer settings were as follows: microwave frequency, 9.44 GHz; power, 0.2 mW; center field, 3358 G; sweep width, 100

G; modulation amplitude, 3 G; modulation frequency, 100 kHz; time constant, 1310.72 ms; conversion time, 327.68 ms; resolution, 2048; number of scans, 1.

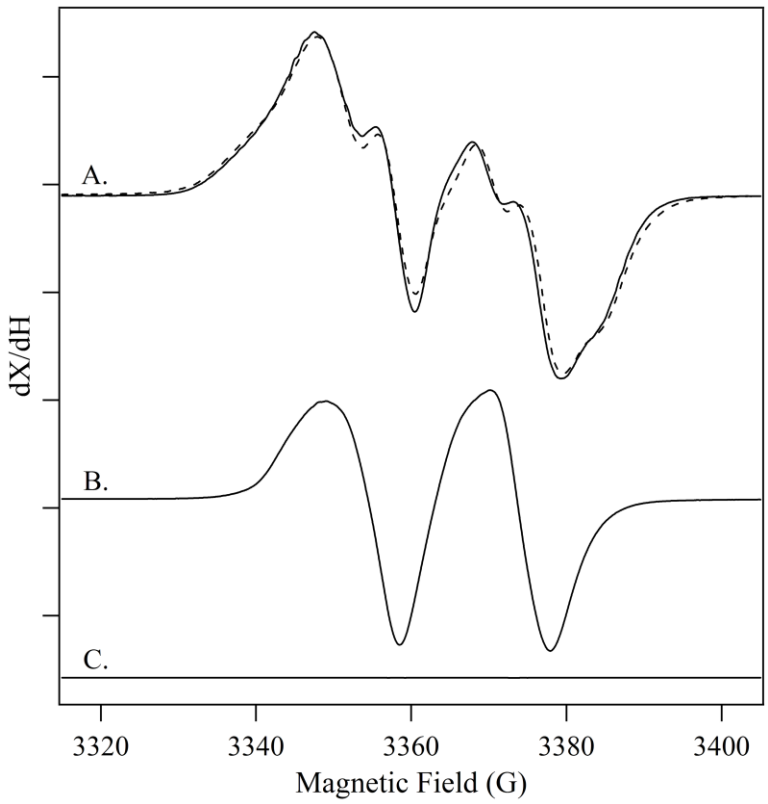

Figure 5.5. Representative EPR spectra of purified *E. coli* β2 samples recorded at 10 K. The data are natural abundance (A) and $^{2}H_4$-tyrosine labeled (B) β2. (C) is the natural abundance Met-β2 spectrum. The protein concentrations are 50 μM in 5 mM Tris-LCl, pL 7.6. In (A), the solid line represents the NA-β2 sample prepared in $^{1}H_2O$ buffer and the dashed line represents the NA-β2 sample prepared in $^{2}H_2O$ buffer.

The EPR signal of the tyrosyl radical (Y122•) for the natural abundance (NA) β2 protein is shown in Figure 5.5A. The EPR spectrum is a doublet and is similar to previously reported Y122• EPR spectra.[27] This EPR lineshape is different than that for a neutral tyrosyl radical generated from UV photolysis. The primary reason for the formation of a doublet is due to the strained ring conformation of Y122• in RNR.[32]

Exchange of the natural abundance β2 into ^2H_2O buffer (Figure 5.5A; dashed line) slightly alters the lineshape of Y122•. From previous isotopic labeling EPR and ENDOR studies,[1,32,33] the spin density for Y122• is primarily located on carbons 1', 3' and 5' and the phenoxyl oxygen in agreement with the EPR studies of tyrosinate in powder.[34-36] These EPR studies demonstrate that the spin densities for all tyrosyl radicals in Nature, transient or stable, are independent on the environment in which the radical resides. After treatment of hydroxyurea to form Met-β2 (Figure 5.5C), the EPR signal of natural abundance β2 disappears, as expected.

With $\{^2H_4\}$-tyrosine global labeling, the lineshape of the $\{^2H_4\}$-Y122• spectrum (Figure 5.5B) displays the loss of the hyperfine structure present in the NA-β2 Y122• EPR spectrum (Figure 5.5A). A similar lineshape was observed for the incorporation of the $\{3,5\text{-}^2H_2\}$-tyrosine isotopomer in β2.[37] This behavior qualitatively demonstrates that our labeling efficiency is high.

5.3.5 FT-IR Spectroscopy

FT-IR spectra were collected at 20°C on a Nicolet Magna 550 II spectrometer equipped with a MCT-A detector (Nicolet, Madison, WI). A Cavro syringe pump (GlobalFIA, Fox Island, WA) injected samples into a temperature controlled demountable sample cell (Harrick Scientific Products, Pleasantville, NY) composed of two CaF_2 windows and separated by a 6 μm spacer, stabilized by vacuum grease. One of the CaF_2 windows was customized by Spectral Systems, LLC (Hopewell Junction, NY) with a pair of through holes and equipped with nanoports (Upchurch Scientific, Oak Harbor, WA) for sample injection through the window. A 14-port selection valve allowed

for user-controlled sample injection into the sample cell from outside the FT-IR spectrometer.

To generate the reaction-induced FT-IR spectra, the reduction of Y122• was performed by addition of HU (25 μL; final concentration, 50 mM) to the oxidized (natural abundance, {$^{2}H_{4}$}-tyrosine, or {^{15}N}-tyrosine labeled)-β2 sample. The $^{2}H_{2}O$ buffer contained 5 mM Tris-^{2}HCl, p^{2}H 7.6. The FT-IR absorption spectrum in $^{2}H_{2}O$ showed the expected downshift of ~1550 cm^{-1} amide II intensity to ~1450 cm^{-1} (amide II'), indicating a substantial amount of deuterium exchange (Figure 5.6; see references 38, 39 and references therein). A negative Metβ2 control was conducted by mixture of a Metβ2 sample (225 μL; final concentration, 240-250 μM) with 25 μL HU. A negative β2 control experiment was conducted by mixture of a β2 sample with 5 mM Tris-^{2}HCl, p^{2}H 7.6 buffer (25 μL). In each case, the sample was injected into the FT-IR sample cell immediately after mixing; the sample cell was filled in approximately 30 s. Data (120 s, 595 interferograms, mirror velocity 2.5 cm s^{-1}) were collected at 4 cm^{-1} resolution. The data were acquired either immediately following (oxidized spectrum) or 8 min (reduced spectrum) after sample injection. The data were processed using a Happ-Genzel apodization function, two levels of zero filling, and a Mertz phase correction. Each data set was ratioed to an open beam background and converted to absorbance. The absorbance spectra were subtracted to generate the reaction-induced difference spectrum (oxidized-minus-reduced).

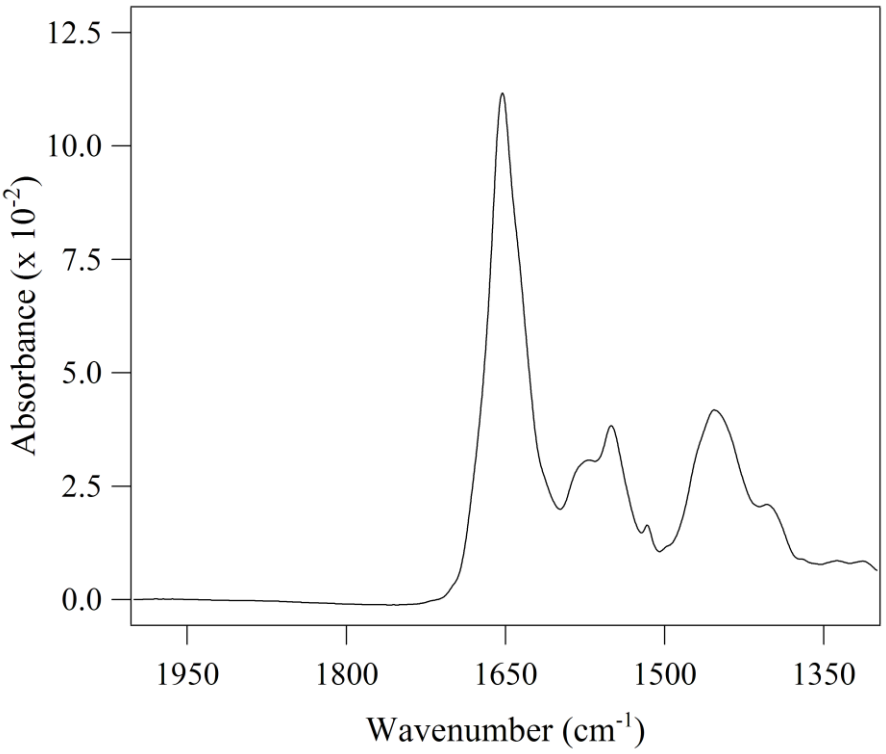

Figure 5.6 FT-IR absorbance spectrum of a natural abundance β2 (250 μM) in 5 mM Tris-^{2}HCl, p^{2}H 7.6 buffer at 20^{o}C.

For the FT-IR photolysis experiments,[17] tyrosinate or pentapeptide samples (50 mM) were prepared in 10 mM sodium borate, p^{2}H 11.0, ^2H_2O buffer. The samples (6 μL) were sandwiched between two CaF_2 windows, which were separated by a 6 μm spacer. The sample was cooled to 80 K using a Hansen (Santa Barbara, CA) liquid nitrogen cryostat. Tyrosyl radicals were generated using the 266 nm output (5 flashes) from a Surelite III Nd:YAG laser (Continuum, Santa Clara, CA) with pulse energies of 50 – 55 mJ at 10 Hz. Data were recorded before and after photolysis for 200 s at 4 cm^{-1} resolution and a 2.5 cm s^{-1} mirror velocity. The data were processed using a Happ-Genzel apodization function, two levels of zero filling, and a Mertz phase correction. The data

were ratioed to an open beam background, and absorbance spectra were generated. The reaction-induced difference spectrum was generated by subtraction of the pre-photolysis data from the post-photolysis data.

Omnic v. 5.2 (Nicolet, Madison, WI) software and Igor Pro v. 5.03(Wavemetrics, Lake Oswego, OR) software were used to process the FT-IR data.[17]

5.4 Results and Discussion

The reaction-induced difference spectrum of natural abundant β2, associated with the reduction of Y122•, is presented in Figures 5.7A and 5.8A. These data were acquired by one electron reduction of Y122• with hydroxyurea[27,29,31,40] over 10 min. Based on the rate constant in $^{2}H_2O$ (Figures 5.3 and 5.4), an estimated ~60% of Y122• is reduced during the 10 min FT-IR measurement.

In the difference spectrum shown in Figure 5.7 A, unique bands of tyrosyl radical, Y122•, will be positive features; unique bands of Y122 will be negative features. Using model compounds and DFT calculations, it has been shown that oxidation of tyrosine leads to an upshift of the CO stretching vibration to 1516 cm^{-1} (υ7a) and to perturbations of the aromatic ring stretching frequencies, at ~1600 (υ8a) and ~1500 (υ19a) cm^{-1} (Figures 3.6A and 3.7A; see ref 41 and references therein). Oxidation of the tyrosine aromatic side chain in peptides and in tyrosinate at pH 11 gave similar results for the CO and υ19a ring stretching modes (Figure 5.7D and E; references 17, 42). Previous Raman

studies of the *E. coli* and mouse β2 subunits have attributed bands at 1498[43] and 1515[44] cm^{-1}, respectively, to the CO vibration.

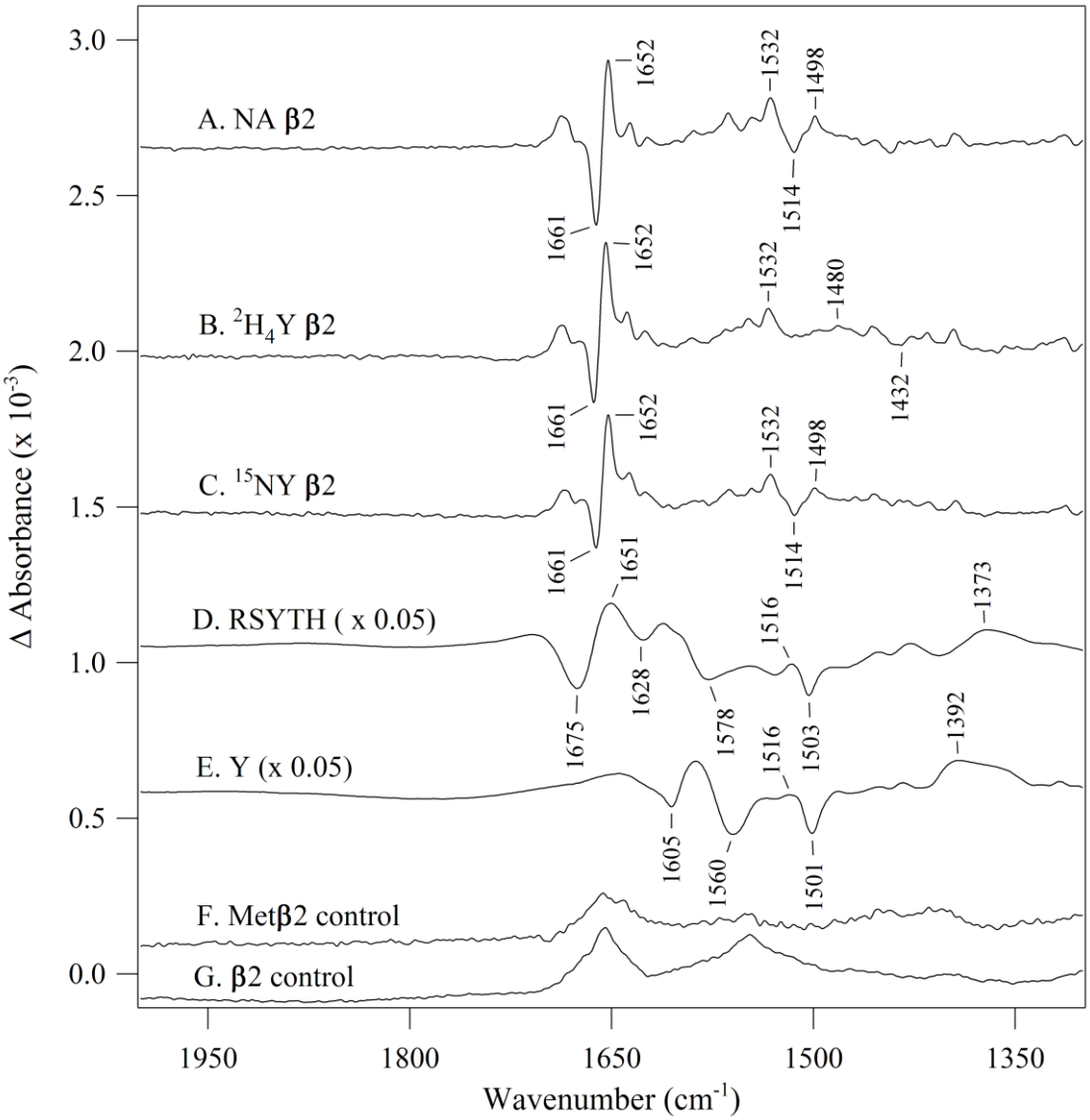

Figure 5.7. Reaction-induced FT-IR spectra, monitoring redox-linked structural changes induced by Y122• reduction with 50 mM hydroxyurea. Spectra (A-C, F and G) were acquired at 20°C in ^2H_2O buffer. In (A), the (250 μM) β2 sample was natural abundance, in (B) $^2H_4$-tyrosine labeled, and in (C) ^{15}N-tyrosine labeled. In (D) and ((E), Y• was generated using 266 nm photolysis at 80 K in the RSTYH peptide (D) or in tyrosinate (E) at p^{2}H 11. (F) is a (250 μM) Metβ2 control difference spectrum, which lacks Y122•, but was mixed with hydroxyurea. (G) is a (250 μM) β2 control difference spectrum, in which β2 was mixed with buffer, instead of hydroxyurea. The difference spectra were constructed: Y•-minus-Y. The spectra are averages from 8 (A), 6 (B), 8 (C), 5 (D), 3 (E), 6 (F), and 11 (G) samples.

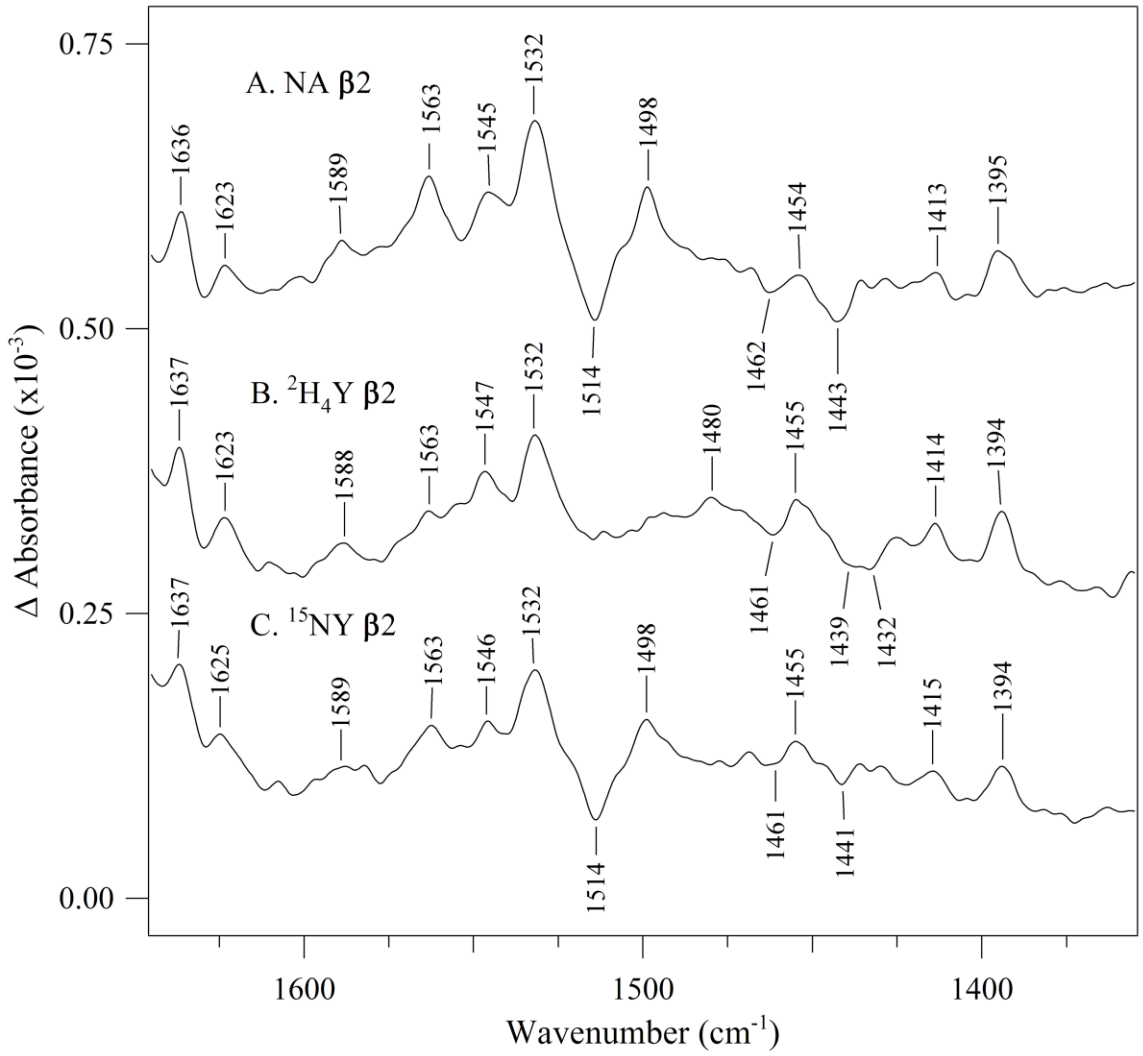

Figure 5.8. The 1700-1300 cm^{-1} region of the reaction-induced FT-IR spectrum, monitoring redox-linked structural changes induced by Y122• reduction with 50 mM hydroxyurea. Spectra 5.8A, B and C are expanded and repeated from Fig. 5.7A, B and C, respectively.

To identify Y122•/Y122 contributions to the natural abundance spectrum (Figures 5.7A and 5.8A), the β2 subunit was labeled with the $^{2}H_{4}$-tyrosine isotopomer (Figures 5.7B and 5.8B). $^{2}H_{4}$ tyrosine labeling resulted in a downshift of a negative band at 1514 cm^{-1} to 1432 cm^{-1} (Figures 5.8A and B). This band was not observed in a negative Metβ2 control (Figure 5.7F) or in a negative control, in which the β2 subunit was mixed with buffer instead of hydroxyurea (Figure 5.7G). Based on previous model compound studies and DFT calculations[41], we assign this band to a ring stretching vibration (υ19a) of Y122. From DFT calculations, he expected isotope-induced downshift is 80 cm^{-1}.[41]

$^{2}H_{4}$ labeling also resulted in a downshift of a positive band at 1498 cm^{-1} to 1480 cm^{-1} (Figures 5.8A and B). This band was not observed in the negative controls (Figure 5.7F or G) and is assigned to the CO stretching vibration (υ7a) of Y122•. From DFT calculations, the expected isotope-induced downshift is ~20 cm^{-1}.[41] The assignment of the 1498 cm^{-1} band is in agreement with previous Raman studies.[43]

These data establish that the CO vibrational band of Y122• is downshifted ~20 cm^{-1} from its frequency in Y• model compounds,[17,41] where it is observed as a positive band at 1516 cm^{-1} (Figures 5.7D and E). The symmetric ring stretching mode, υ8a, at negative 1605 cm^{-1} (Figure 5.7E) was not observed when Y• is generated in the pentapeptide (Figure 5.7D) or in β2 (Figure 5.7A).

In addition to bands associated with tyrosine oxidation, the reaction-induced spectrum in Figure 5.7A reveals coupled, oxidation-induced effects on the protein environment. For example, Figure 5.7A exhibits a negative band at 1661 cm^{-1} and a positive band at 1652 cm^{-1}. This is a spectral region characteristic of amide I C=O

vibrational bands (Figure 5.3).[25] These data suggest that Y122• reduction is coupled with a structural change in the β2 subunit.

As a first step in interpretation of the amide I spectral contributions, we studied a pentapeptide, RSYTH, matching the sequence containing Y122 in the β2 subunit.[17] The pentapeptide spectrum in $^{2}H_2O$ buffer (Figure 5.7D) exhibited several bands in the amide I region, at 1675 and 1651 cm^{-1}, which were not observed when tyrosyl radical was generated in a powder tyrosinate sample (Figure 5.7E).[17] This result suggests that electron transfer reactions are linked with a structural change in one or more peptide bonds in the pentapeptide and in the β2 sample. Because the pentapeptide is expected to have no defined structure in solution, the amino acid composition must mediate this redox-linked interaction. We propose that this conformational change occurs at adjacent peptide bonds to Y122•.

^{15}N-labeling of tyrosine in β2 was employed (Figures 5.7C and 5.8C) to test if the structural perturbation occurs at the S121-Y122 amide bond. The effect of ^{15}N labeling is expected to be detectable {for example, see ref 45}, because the amide I normal mode involves nitrogen displacement.[25] However, ^{15}N labeling had no significant effect on the reaction-induced spectrum (Figure 5.8A and C). This result is consistent with the conclusion that the redox-linked structural change does not perturb the Ser-Tyr amide linkage, but other amide bonds near Y122.

We hypothesize that the structural perturbation of the amide bond in the β2 and the pentapeptide samples is driven by an electrostatic change. Electrostatic maps predict a change in aromatic ring charge distribution.[46] An oxidation-induced change in charge distribution will lead to alterations in the C-N bond ionic character, planarity, and force

constant through a Stark effect. This interpretation is congruent with recent ESEEM studies of pentapeptide samples, which have shown composition-dependent changes in nuclear quadrapole interactions in tyrosyl radicals.[47]

Redox-linked structural changes at Y122/Y122• may partially control PCET reactions during the RNR reaction cycle.[5,16] These conformational alterations are likely to cause changes in Y122 interactions with its hydrogen bonding partner.[16] Therefore, these structural changes may play a role in regulation of Y122 midpoint potential and its reversible protonation/deprotonation reactions. This work provides spectroscopic evidence for dynamic structural changes in RNR.

5.5 Acknowledgments

This work was supported by NIH GM43273 (BAB) and GM29595 (JS). The authors are grateful to Steiner Films for the gift of mylar film, to Prof. Jake Soper for use of the Cary UV-Visible spectrophotometer, and to Derek Osborne for assistance with the FT-IR measurements.

5.6 References

1. Sjöberg, B.-M.; Reichard, P.; Gräslund, A.; Ehrenberg, A., The tyrosine free radical in ribonucleotide reductase from *Escherichia coli*. *J. Biol. Chem.* **1978**, *253*, 6863-6865.

2. Nordlund, P.; Sjöberg, B.-M.; Eklund, H., Three-dimensional structure of the free radical protein of ribonucleotide reductase. *Nature* **1990**, *345*, 593-598.

3. Stubbe, J., Ribonucleotide reductases: amazing and confusing. *J. Biol. Chem.* **1990**, *265*, 5329-5332.

4. Nordlund, P.; Eklund, H., Structure and function of the *Escherichia coli* ribonucleotide reductase protein R2. *J. Mol. Biol.* **1993**, *232*, 123-164.

5. Stubbe, J.; van der Donk, W. A., Protein radicals in enzyme catalysis. *Chem. Rev.* **1998**, *98*, 705-762.

6. Uhlin, U.; Eklund, H., Structure of ribonucleotide reductase protein R1. *Nature* **1994**, *370*, 533-9.

7. Bennati, M.; Robblee, J. H.; Mugnaini, V.; Stubbe, J.; Freed, J. H.; Borbat, P., EPR distance measurements support a model for long-range radical initiation in *E. coli* ribonucleotide reductase. *J. Am. Chem. Soc.* **2005**, *127*, 15014-15015.

8. Uppsten, M.; Färnegårdh, M.; Domkin, V.; Uhlin, U., The first holocomplex structure of ribonucleotide reductase gives new insight into its mechanism of action. *J. Mol. Biol.* **2006**, *359*, 365-377.

9. Rova, U.; Goodtzova, K.; Ingemarson, R.; Behravan, G.; Gräslund, A.; Thelander, L., Evidence by site-directed mutagenesis supports long-range electron transfer in mouse ribonucleotide reductase. *Biochemistry* **1995**, *34*, 4267-75.

10. Ekberg, M.; Sahlin, M.; Eriksson, M.; Sjöberg, B.-M., Two conserved tyrosine residues in protein R1 participate in an intermolecular electron transfer in ribonucleotide reductase. *J. Biol. Chem.* **1996**, *271*, 20655 - 20659.

11. Ekberg, M.; Pötsch, S.; Sandin, E.; Thunnissen, M.; Nordlund, P.; Sahlin, M.; Sjöberg, B.-M., Preserved catalytic activity in an engineered ribonucleotide reductase R2 protein with a nonphysiological radical transfer pathway. The importance of hydrogen bond connections between the participating residues. *J. Biol. Chem.* **1998**, *273*, 21003 - 21008.

12. Yee, C. S.; Chang, M. C.; Ge, J.; Nocera, D. G.; Stubbe, J., 2,3-difluorotyrosine at position 356 of ribonucleotide reductase R2: a probe of long-range proton-coupled electron transfer. *J. Am. Chem. Soc.* **2003**, *125*, 10506-7.

13. Seyedsayamdost, M. R.; Stubbe, J., Site-specific replacement of Y_{356} with 3,4-dihydroxyphenylalanine in the β2 subunit of *E. coli* ribonucleotide reductase. *J. Am. Chem. Soc.* **2006**, *128*, 2522-2523.

14. Seyedsayamdost, M. R.; Yee, C. S.; Reece, S. Y.; Nocera, D. G.; Stubbe, J., pH rate profiles of F_nY_{356}-R2s (n=2, 3, 4) in *Escherichia coli* ribonucleotide reductase: Evidence that Y_{356} is a redox-active amino acid along the radical propagation pathway. *J. Am. Chem. Soc.* **2006**, *128*, 1562-1568.

15. Seyedsayamdost, M. R.; Xie, J.; Chan, C. T. Y.; Schultz, P. G.; Stubbe, J., Site-specific insertion of 3-aminotyrosine into subunit α2 of *E. coli* ribonucleotide reductase: direct evidence for involvement of Y_{730} and Y_{731} in radical propagation. *J. Am. Chem. Soc.* **2007**, *129*, 15060-15071.

16. Högbom, M.; Galander, M.; Andersson, M.; Kolberg, M.; Hofbauer, W.; Lassmann, G.; Nordlund, P.; Lendzian, F., Displacement of the tyrosyl radical cofactor in ribonucleotide reductase obtained by single-crystal high-field EPR and 1.4-Å X-ray data. *Proc. Natl. Acad. Sci. U.S.A.* **2003**, *100*, 3209-3214.

17. Vassiliev, I. R.; Offenbacher, A. R.; Barry, B. A., Redox-active tyrosine residues in pentapeptides. *J. Phys. Chem. B* **2005**, *109*, 23077-23085.

18. Kötting, C.; Gerwert, K., Proteins in action monitored by time-resolved FTIR spectroscopy. *ChemPhysChem* **2005**, *6*, 881-888.

19. Kim, S.; Liang, J.; Barry, B. A., Chemical complementation identifies a proton acceptor for redox-active tyrosine D in photosystem II. *Proc. Natl. Acad. Sci. U.S.A.* **1997**, *94*, 14406-14411.

20. Iwaki, M.; Puustinen, A.; Wikström, M.; Rich, P. R., Structural and chemical changes of the P_M intermediate of *Paracoccus denitrificans* cytochrome *c* oxidase revealed by IR spectroscopy with labeled tyrosines and histidine. *Biochemistry* **2006**, *45*, 10873-10885.

21. Salowe, S. P.; Stubbe, J., Cloning, overproduction, and purification of the B2 subunit of ribonucleoside-diphosphate reductase. *J. Bacteriol.* **1986**, *165*, 363-366.

22. Seyedsayamdost, M. R.; Reece, S. Y.; Nocera, D. G.; Stubbe, J., Mono-, di-, tri-, and tetra-substituted fluorotyrosines: new probes for enzymes that use tyrosyl radicals in catalysis. *J. Am. Chem. Soc.* **2006**, *128*, 1569-1579.

23. Yee, C. S. Mechanistic investigations of the radical initiation pathway of class I ribonucleotide reductase from *Escherichia coli*. Massachusetts Institute of Technology, Cambridge, 2004.

24. Sahlin, M.; Gräslund, A.; Petersson, L.; Ehrenberg, A.; Sjöberg, B.-M., Reduced forms of the iron-containing small subunit of ribonucleotide reductase from *Escherichia coli*. *Biochemistry* **1989**, *28*, 2618-2625.

25. Krimm, S.; Bandekar, J., Vibrational spectroscopy and conformation of peptides, polypeptides, and proteins. In *Advances in Protein Chemistry*, Anfinsen, C. B.; Edsall, J. T.; Richards, F. M., Eds. Academic Press: New York, 1986; Vol. 38, pp 181-364.

26. Sneeden, J. L.; Loeb, L. A., Mutations in the R2 subunit of ribonucleotide reductase that confer resistance to hydroxyurea. *J. Biol. Chem.* **2004**, *279*, 40723-40728.

27. Ehrenberg, A.; Reichard, P., Electron spin resonance of the iron-containing protein B2 from ribonucleotide reductase. *J. Biol. Chem.* **1972**, *247*, 3485-3488.

28. Lam, K.-Y.; Fortier, D. G.; Thomson, J. B.; Sykes, A. G., Kinetics of inactivation of the tyrosine radical of the B2 subunit of *E. coli* ribonucleotide reductase. *J. Chem. Soc., Chem. Commun.* **1990**, 658-660.

29. Karlsson, M.; Sahlin, M.; Sjöberg, B. M., Escherichia coli ribonucleotide reductase. Radical susceptibility to hydroxyurea is dependent on the regulatory state of the enzyme. *J. Biol. Chem.* **1992**, *267*, 12622-12626.

30. Lassmann, G.; Thelander, L.; Gräslund, A., EPR stopped-flow studies for the reaction of the tyrosyl radical of protein R2 from ribonucleotide reductase with hydroxyurea. *Biochem. Biophys.l Res. Commun.* **1992**, *188*, 879-887.

31. Han, J. Y.; Gräslund, A.; Thelander, L.; Sykes, A. G., Kinetic studies on the reduction of the R2 subunit of mouse ribonucleotide reductase with hydroxyurea, hydrazine, phenylhydrazine and hydroxylamine. *J. Biol. Inorg. Chem.* **1997**, *2*, 287-294.

32. Bender, C. J.; Sahlin, M.; Babcock, G. T.; Barry, B. A.; Chandrashekar, T. K.; Salowe, S. P.; Stubbe, J.; Lindstoem, B.; Petersson, L., An ENDOR study of the tyrosyl free radical in ribonucleotide reductase from *Escherichia coli*. *J. Am. Chem. Soc.* **1989**, *111*, 8076-8083.

33. Hoganson, C. W.; Sahlin, M.; Sjöberg, B.-M.; Babcock, G. T., Electron magnetic resonance of the tyrosyl radical in ribonucleotide reductase from *Escherichia coli*. *J. Am. Chem. Soc.* **1996**, *118*, 4672-4679.

34. Fasanella, E. L.; Gordy, W., Electron spin resonance of an irradiated single crystal of L-tyrosine-HCl. *Proc. Natl. Acad. Sci. U.S.A.* **1969**, *62*, 299-304.

35. Sealy, R. C.; Harman, L.; West, P. R.; Mason, R. P., The electron spin resonance spectrum of the tyrosyl radical. *J. Am. Chem. Soc.* **1985**, *107*, 3401-3406.

36. Barry, B. A.; El-Deeb, M. K.; Sandusky, P. O.; Babcock, G. T., Tyrosine radicals in photosystem II and related model compounds. Characterization by isotopic labeling and EPR spectroscopy. *J. Biol. Chem.* **1990**, *265*, 20139-20143.

37. Reichard, P.; Ehrenberg, A., Ribonucleotide reductase--a radical enzyme. *Science* **1983**, *221*, 514-519.

38. Rath, P.; DeGrip, W. J.; Rothschild, K. J., Photoactivation of rhodopsin causes an increased hydrogen-deuterium exchange of buried peptide groups. *Biophys. J.* **1998**, *74*, 192-198.

39. Hutchison, R. S.; Betts, S. D.; Yocum, C. F.; Barry, B. A., Conformational changes in the extrinsic manganese stabilizing protein can occur upon binding to the photosystem II reaction center: an isotope editing and FT-IR study. *Biochemistry* **1998**, *37*, 5643-5653.

40. Larsen, I. K.; Sjöberg, B. M.; Thelander, L., Characterization of the active-site of ribonucleotide reductase of *Escherichia coli*, bacteriophage-T4 and mammalian cells by inhibition studies with hydroxyurea analogs. *Eur. J. Biochem.* **1982**, *125*, 75-81.

41. Range, K.; Ayala, I.; York, D.; Barry, B. A., Normal modes of redox-active tyrosine: conformation dependence and comparison to experiment. *J. Phys. Chem. B* **2006**, *110*, 10970-10981.

42. Ayala, I.; Range, K.; York, D.; Barry, B. A., Spectroscopic properties of tyrosyl radicals in dipeptides. *J. Am. Chem. Soc.* **2002**, *124*, 5496-5505.

43. Backes, G.; Sahlin, M.; Sjöberg, B.-M.; Loehr, T. M.; Sanders-Loehr, J., Resonance Raman spectroscopy of ribonucleotide reductase. Evidence for a deprotonated tyrosyl radical and photochemistry of the binuclear iron center. *Biochemistry* **1989**, *28*, 1923-1929.

44. Hanson, M. A.; Schmidt, P. P.; Strand, K. R.; Gräslund, A.; Solomon, E. I.; Andersson, K. K., Resonance Raman evidence for a hydrogen-bonded oxo bridge in the R2 protein of ribonucleotide reductase from mouse. *J. Am. Chem. Soc.* **1999**, *121*, 6755-6756.

45. Kim, S.; Barry, B. A., The protein environment surrounding tyrosyl radicals D• and Z• in photosystem II: a difference Fourier-transform infrared spectroscopic study. *Biophys. J.* **1998**, *74*, 2588-2600.

46. Sibert, R.; Josowicz, M.; Porcelli, F.; Veglia, G.; Range, K.; Barry, B. A., Proton-coupled electron transfer in biomimetic peptide as a model of enzyme regulatory mechanism. *J. Am. Chem. Soc.* **2007**, *129*, 4393-4400.

47. McCracken, J.; Vassiliev, I. R.; Yang, E. C.; Range, K.; Barry, B. A., ESEEM studies of peptide nitrogen hyperfine coupling in tyrosyl radicals and model peptides. *J. Phys. Chem. B* **2007**, *111*, 6586-6592.

CHAPTER 6

PROBING THE LOCAL REDOX-LINKED STRUCTURAL CHANGES IN RIBONUCLEOTIDE REDUCTASE WITH SPECIFIC ISOTOPE LABELING AND ALTERNATIVE β2 INHIBITORS

by

Adam R. Offenbacher and Bridgette A. Barry

School of Chemistry and Biochemistry and the Parker H. Petit Institute for Bioengineering and Bioscience, Georgia Institute of Technology, Atlanta, Georgia 30332

6.1 Abstract

Ribonucleotide reductase (RNR) catalyzes the reduction of ribonucleotides to deoxyribonucleotides, the rate-limiting step in DNA biosynthesis. Class Ia RNRs consist of two homodimeric proteins, α2 and β2. In α2, ribonucleotides are reduced to deoxyribonucleotides via radical chemistry initiated by a transient cysteine thiyl radical. C439• in the *E. coli* enzyme is generated by a stable tyrosyl radical Y122• located 35 Å away in β2. Structural changes are proposed to precede these reversible proton-coupled electron transfer (PCET) reactions. We have previously shown that reduction of Y122• in β2 by the exogenous radical scavenger, hydroxyurea, is linked to protein structural changes.[1] Incorporating isotopic-labeled tyrosine in β2, we are able to probe these structural changes using a reaction-induced Fourier-transform infrared (FT-IR) spectroscopic technique. FT-IR difference spectra of globally incorporated 1-{^{13}C}-labeled tyrosine yielded spectral shifts in the 1600 – 1650 cm^{-1} (amide I) and the ~1500 cm^{-1} (amide II) regions, which are distinct from natural abundance β2. These frequency shifts are consistent with amide I structural changes for the Y122-T123 amide bond. The reduction of Y122• with N-methylhydroxylamine or 4-methoxyphenol generated identical amide I frequencies to the hydroxyurea reaction in the FT-IR reaction spectra. Together, the data support that the redox-linked structural changes in the RNR tyrosyl radical occur locally and are independent of reducing agent. In addition, significant structural changes were observed in the reaction-induced FT-IR spectra among hydroxyurea, N-methylhydroxylamine, and 4-methoxyphenol. We propose that these conformational changes are a possible result from alternate pathways for Y122• reduction. These data emphasize the potential for this reaction-induced FT-IR

spectroscopic technique for resolving the subtle differences of these reaction mechanisms.

6.2 Introduction

Ribonucleotide reductase (RNR) catalyzes the radical-mediated reduction of ribonucleoside diphosphates (NDPs) to deoxyribonucleoside diphosphates (dNDPs).[2,3] There are three classes of RNRs and the mechanism for NDP reduction is universally conserved throughout all organisms.[4] Substrate reduction is initiated by a transient cysteine radical (C439•, in *E. coli* numbering). The three classes are distinguished primarily by the nature of the cysteine radical initiator. Of the three classes, class Ia, composed of mammalian and *E. coli* RNRs, is a heterodimer of homodimers, $\alpha 2$ and $\beta 2$. The large subunit, $\alpha 2$, houses the binding sites for the nucleotide substrate and effectors. In $\beta 2$, a stable tyrosyl radical (Y122•) resides adjacent to an antiferromagnetically coupled μ-oxo bridged diferric cluster. Y122• is responsible for generating the transient thiyl radical at the active site in $\alpha 2$. No structure of the active complex has yet been determined. However, a docking model of the individually solved structures of $\alpha 2$[5] and $\beta 2$[6] estimated a 35 Å distance separating these two residues. A pulsed-electron double resonance (PELDOR) spectroscopic study[7] has supported this distance, which indicates no large structural rearrangement of the complex to bring the residues closer for direct electron transfer.

A series of transient amino acid radicals (ref 8 and refs therein) have been proposed to shuttle the electron from the active site to $\beta 2$ and back. Site-directed

mutagenic studies[9-12] have unveiled the importance of these intermediates; the mechanism of these intermediates during turnover is beginning to be established through use of non-natural amino acids[13-15]. Previous kinetic studies have identified a lag phase preceding the reversible proton-coupled electron transfer (PCET) reactions required for C439• formation.[16] A physical, conformational gating was postulated to drive the PCET processes and ultimately nucleotide reduction. Since there is no crystal structure for the Y122•-containing β2 or the active complex, a model for this conformational gating process is currently unknown.

Only limited structural information is available for the active β2 protein. A high field electron paramagnetic resonance (EPR) spectroscopic study gave evidence for motion of the phenoxyl ring of Y122 along the C_α–C_β bond upon oxidation with H_2O_2.[17] Our previous work using Fourier-transform infrared (FT-IR) spectroscopy suggested that perturbations of the amide bonds surrounding Y122 are linked to reduction of the radical with hydroxyurea.[1]

In this work, we have incorporated 1-{^{13}C}-labeled tyrosine globally into the β2 subunit of the *Escherichia coli* RNR. Our reaction-induced FT-IR of the 1-^{13}CY-labeled β2 exhibits discrete spectral shifts from that of the natural abundant (NA) β2 difference spectrum. These data suggest that the 1650 – 1600 cm^{-1} bands in these reaction-induced IR spectra arise from redox-linked amide I changes in the local peptide bonds surrounding Y122. In addition, using other Y122•-reducing agents, N-methylhydroxylamine (N-MHA) and 4-methoxyphenol (4-MP), the (-) 1661/(+) 1653 cm^{-1} frequencies are identical to that of the reaction of β2 with hydroxyurea. These data

provide evidence that the redox-linked protein conformational changes in the reaction-induced FT-IR spectra are independent of reducing agent.

6.3 Materials and Methods

6.3.1 Materials

L-Tyrosine, Hepes: 4-(2-Hydroxyethyl)piperazine-1-ethanesulfonic acid, N-methylhydroxylamine hydrochloride, sodium hydroxide, and hydrochloric acid were purchased from Sigma (St. Louis, MO). 4-methoxyphenol was acquired from VWR International (Radnor, Pennsylvania). 1-{^{13}C}-tyrosine (L-tyrosine-1-^{13}C, 98%), 4-{^{13}C}-aspartic acid (D,L-aspartic acid-4-^{13}C, 99%), and deuterium oxide, ($^{2}H_2O$, 98%) were obtained from Cambridge Isotope Laboratories (Andover, MA). Hydroxyurea was purchased from Calbiochem (San Diego, CA).

6.3.2 β2 Overexpression and Purification

Escherichia coli natural abundance (NA) and isotope-labeled β2 protein was overexpressed and purified from *E. coli* BL21(DE3)/pTB2 cells, using standardized protocols. Global incorporation of {$^{2}H_4$}-, {^{15}N}-, and 1-{^{13}C}-labeled tyrosine into β2 was performed using minimal media.[1] Incorporation of 4-{^{13}C}-labeled aspartatic acid into β2 was performed as described previously for the manganese-stabilizing protein.[18] Typical yields for natural abundance (NA) β2 were 20 – 25 mg protein per g of cells. Prior to FT-IR or kinetic experiments, the protein samples were exchanged into 5 mM

Hepes, p^2H 7.6 (p^2H values are recorded as the uncorrected meter reading[19]) as previously described.[1]

6.3.3 UV-Visible Spectroscopy: Hydroxyurea, N-Methylhydroxylamine, and 4-Methoxyphenol Kinetic Studies

Room temperature UV-visible absorbance spectra of the purified *E. coli* β2 samples were recorded on a Hitachi U-3000 spectrophotometer using 1 cm quartz cuvettes. The concentration of natural abundance and isotope-labeled β2 samples were determined using ε_{280nm} ~131,000 $M^{-1}cm^{-1}$. The Y• yield was determined from the absorbance at 416, 411, and 406 nm as previously described.[1,20] The ratio of Y122• per β2 was determined to be 1.2 – 1.4 for the NA β2. By monitoring the decay of the Y122• 410 nm absorption band, the rate constants for Y122• reduction were determined for hydroxyurea (HU), N-methylhydroxylamine (N-MHA), and 4-methoxyphenol (4-MP). The second-order rate constants for these reducing agents were obtained on a Varian Cary 50 (Varian, Walnut Creek, CA) spectrophotometer equipped with a temperature controller. The ^1H_2O or ^2H_2O buffer were prepared as 5 mM Hepes, p^1H 7.6 or p^2H 7.6. The reactions were monitored at 1.8 min intervals for 30 min at 20°C; the experiments were performed in triplicate.

6.3.4 Fourier-Transform Infrared (FT-IR) Spectroscopy

Reaction-induced FT-IR spectra were collected at 20°C on a Nicolet Magna 550 II spectrometer equipped with a MCT-A detector (Nicolet, Madison, WI). A Cavro syringe pump (GlobalFIA, Fox Island, WA) injected samples into a temperature controlled demountable sample cell (Harrick Scientific Products, Pleasantville, NY) composed of

two CaF_2 windows and separated by a 6 μm spacer and stabilized with vacuum grease. One of the CaF_2 windows was customized by Spectral Systems, LLC (Hopewell Junction, NY) with a pair of through holes and equipped with nanoports (Upchurch Scientific, Oak Harbor, WA) for sample injection through the window. A 14-port selection valve allowed for user-controlled sample injection into the sample cell from outside the FT-IR spectrometer.

To generate the reaction-induced FT-IR spectra, the reduction of Y122• was performed by addition of HU (25 μL; final concentration, 50 mM) to the oxidized (natural abundance, {$^2H_4$}-tyrosine, {^{15}N}-tyrosine, 1-{^{13}C}-tyrosine, or 4-{^{13}C}-aspartic acid labeled)-β2 samples. In addition, the reduction of Y122• was performed by addition of N-MHA (25 μL; final concentration, 50 mM) or 4-MP (25 μL; final concentration, 2.5 mM) to the oxidized, natural abundance β2 samples. The ^2H_2O buffer contained either 5 mM Tris-^{2}HCl, p^{2}H 7.6 or 5 mM Hepes, p^{2}H 7.6. A negative Metβ2 control was conducted by mixture of a Metβ2 sample (225 μL; final concentration, 240-250 μM) with 25 μL HU. In each case, the sample was injected into the FT-IR sample cell immediately after manual mixing; the sample cell was filled in approximately 30 - 45 s. Data (120 s, 595 interferograms, mirror velocity 2.5 cm s^{-1}) were collected at 4 cm^{-1} resolution. The data were acquired either immediately following (oxidized spectrum) or 8 min (reduced spectrum) following sample injection. The data were processed using a Happ-Genzel apodization function, two levels of zero filling, and a Mertz phase correction. Each data set was ratioed to an open beam background and converted to absorbance spectra. The absorbance spectra were subtracted to generate the reaction-induced difference spectrum (oxidized-minus-reduced).

Photolysis-induced FT-IR spectra of tyrosinate or 4-methoxyphenol were performed at 79 K using a Hansen (Santa Barbara, CA) liquid nitrogen cryostat. Tyrosinate samples were prepared at 100 mM concentrations in 5 mM sodium borate, p^{2}H 11.0. 4-Methoxyphenol samples were prepared at 100 mM concentrations in 5 mM Hepes, p^{2}H 7.6. The 4-methoxyphenol samples were prepared in p^{2}H 7.6 buffer for comparison to the reaction-induced FT-IR spectra and the tyrosinate samples were prepared in p^{2}H 11.0 buffer for solubility. Phenoxyl radicals were generated from 5 laser flashes from 266 nm output of Surelite III (Continuum, Santa Clara, CA) Nd:YAG laser with pulse energies of 45 – 55 mJ at 10 Hz. Data were recorded before and after photolysis for 200 s at 4 cm^{-1} resolution and a 2.5 cm s^{-1} mirror velocity. The data were processed using a Happ-Genzel apodization function, two levels of zero filling, and a Mertz phase correction. The data were ratioed to an open beam background, and absorbance spectra were generated. The reaction-induced difference spectrum was generated by subtraction of the pre-photolysis data from the post-photolysis data. Omnic v. 5.2 (Nicolet, Madison, WI) software and Igor Pro v. 5.03(Wavemetrics, Lake Oswego, OR) software were used to process the reaction- and photolysis-induced FT-IR data.[21]

6.4 Results and Discussion

6.4.1 Kinetic Analysis of β2 Reduction by Hydroxyurea, N-Methylhydroxylamine, and 4-Methoxyphenol in ^2H_2O

Rate constants for β2 reducing agents such as hydroxyurea and N-methylhydroxylamine have been extensively studied both aerobically and anaerobically for the *E. coli* enzyme.[1,22-28] The reactions have been described well for the Y122•

reduction in $^{1}H_2O$, but the rate constants have not been reported for the reactions in $^{2}H_2O$. For the infrared experiments, the reactions were monitored in $^{2}H_2O$ buffer to eliminate spectral overlap of the $^{1}H_2O$ bending mode to the protein amide I region (~1650 cm^{-1}). By monitoring the decay of the Y122• 410 nm absorption band,[1,22-25,28] the rate constants for Y122• reduction were determined (Figures 6.1-6.3 and 6.6). The decay of 410 nm was determined using the fitted base-line (F.B.L.) method:

$$\Delta Abs(FBL)_{410nm} = Abs_{410nm} - \frac{Abs_{420nm} + Abs_{400nm}}{2}.$$ [28]

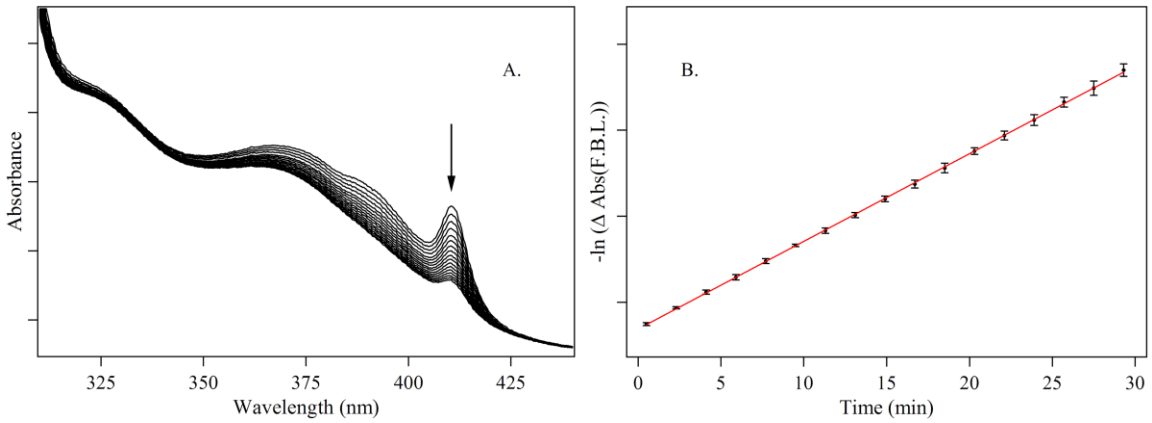

Figure 6.1. UV-visible kinetic data, which are associated with the reduction of Y122• from control β2 (40 μM) with hydroxyurea (HU, 2.5 mM), recorded at 20°C in $^{1}H_2O$ and at p^{1}H 7.6. In (A), a representative example of the UV-Visible absorbance spectra, used to derive the rate constant is shown. The loss of the Y• absorbance at 410 nm is indicated by the arrow. The *y*-axis tick marks represent 1 x 10^{-1} absorbance units. In (B) are the data used to derive the averaged rate constants for Y122• reduction by HU. The ΔAbs_{410nm} values were determined by the fitted base-line (F.B.L.) method.[28] The averaged data (three experiments) were fit (red line) to the linear equation, $y = 2.3445 + 0.050975 * t$, where t is in min. The standard deviations were used to estimate the error in the measurement. The rate constant (0.34 ± 0.01 $M^{-1}s^{-1}$) was derived by dividing through by the HU concentration. The *y*-axis tick marks represent 5 x 10^{-1} arbitrary units.

The reaction of control β2 with hydroxyurea in $^{1}H_2O$ at 20°C and p^{1}H 7.6 was monitored with UV-Vis spectroscopy (see Figure 6.1A). The natural log of the 410 nm decay using the FBL method was plotted versus time in Figure 6.1B. The kinetic data in Figure 6.1B were fit (red line) to a linear function, $y = C_0 + k_1t$, where t is in minutes. Likewise, the corresponding reaction of β2 with hydroxyurea was monitored in $^{2}H_2O$ at 2O°C (Figure 6.2).

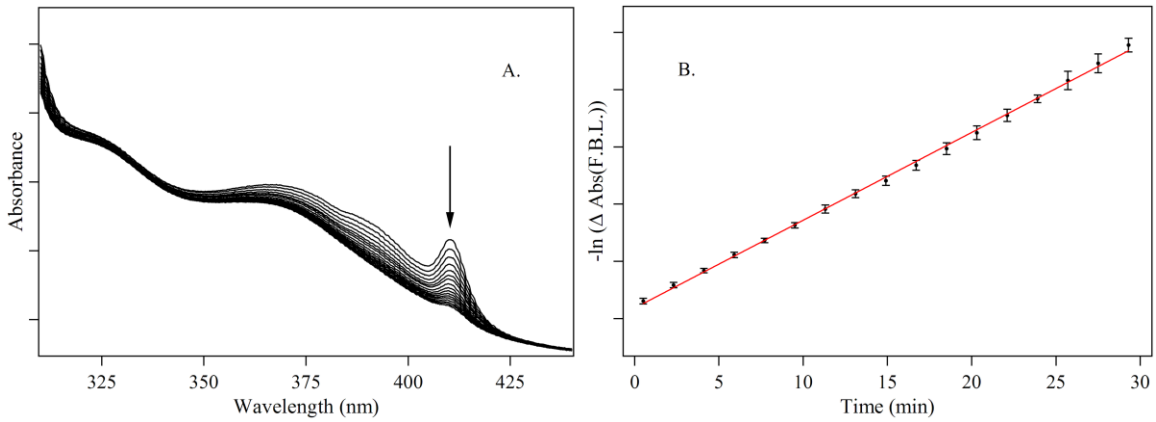

Figure 6.2. UV-visible kinetic data, which are associated with the reduction of Y122• from control β2 (40 μM) with hydroxyurea (HU, 50 mM), recorded at 20°C in $^{2}H_2O$ and at p^{2}H 7.6. In (A), a representative example of the UV-Visible absorbance spectra, used to derive the rate constant is shown. The loss of the Y• absorbance at 410 nm is indicated by the arrow. The *y*-axis tick marks represent 1 x 10^{-1} absorbance units. In (B) are the data used to derive the averaged rate constants for Y122• reduction by HU. The ΔAbs_{410nm} values were determined by the fitted base-line (F.B.L.) method.[28] The averaged data (three experiments) were fit (red line) to the linear equation, $y = 2.5931 + 0.076704 * t$, where *t* is in min. The standard deviations were used to estimate the error in the measurement. The rate constant (0.026 ± 0.001 $M^{-1}s^{-1}$) was derived by dividing through by the HU concentration. The *y*-axis tick marks represent 5 x 10^{-1} absorbance units.

From the linear fit, the rate constant for the reaction of β2-Y122• with hydroxyurea in $^{1}H_2O$ at 20°C was determined to be 0.34 ± 0.01 $M^{-1}s^{-1}$, which is in good

agreement with previously reported values of 0.33 $M^{-1}s^{-1}$ from UV-visible[24] and 0.36 $M^{-1}s^{-1}$ from EPR[29] spectroscopic studies. For the corresponding reaction in ^2H_2O from Figure 6.2, the second-order rate constant drops to 0.026 ± 0.001 $M^{-1}s^{-1}$. The resulting kinetic isotope effect ($KIE = \frac{k_{1_{H_2O}}}{k_{2_{H_2O}}}$) was calculated as 13. For the FT-IR conditions ([HU] = 50 mM), an estimated ~ 60 % reduction of Y122• was estimated during the course of the 10 min FT-IR experiments.[1]

In Figure 6.3, the reaction of control β2 with N-methylhydroxylamine in ^2H_2O is shown. The natural log plot of the 410 nm versus time is displayed in Figure 6.3B. The data in Figure 6.3B does not follow the expected linear trend for Y122• reduction. The non-linear fit to the data suggests that there are competing reactions. Incubation of the Metβ2 form with N-methylhydroxylamine in ^2H_2O (Figure 6.4) produced the appearance of a weak positive 410 nm band over 30 min. During the 30 minute incubation of the N-MHA reaction of Metβ2 in ^1H_2O (see Figure 6.5), no emergence of a 410 nm peak was observed. Moreover, mixing of the Metβ2 form with either hydroxyurea or 4-methoxyphenol in ^2H_2O also did not lead to the formation of the 410 nm feature (data not shown). The results suggest that the reaction of control β2 with N-MHA in ^2H_2O leads to reduction of Y122• and reduction of the diferric cluster with subsequent Y122 oxidation.

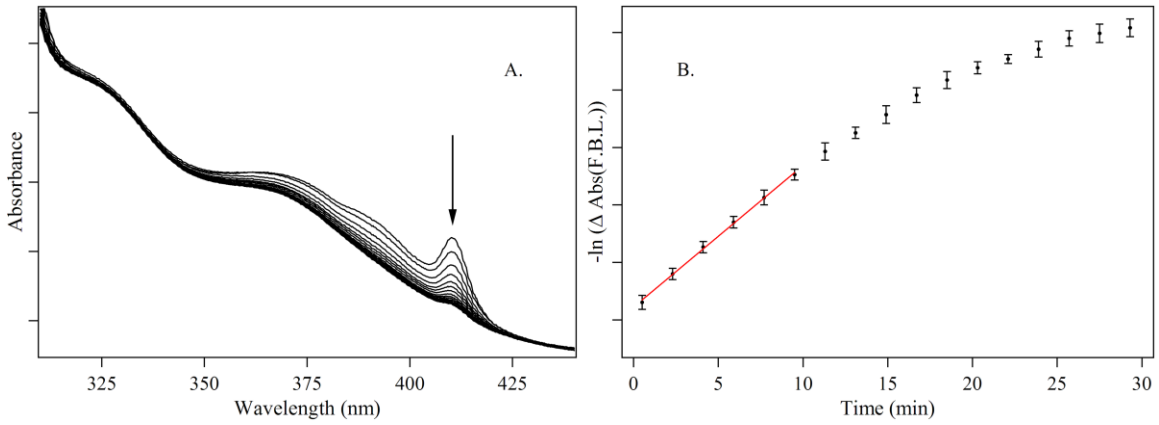

Figure 6.3. UV-visible kinetic data, which are associated with the reduction of Y122• from control β2 (40 μM) with N-methylhydroxylamine (NMHA, 50 mM), recorded at 20°C in $^{2}H_2O$ and at p^{2}H 7.6. In (A), a representative example of the UV-Visible absorbance spectra, used to derive the rate constant is shown. The loss of the Y• absorbance at 410 nm is indicated by the arrow. The *y*-axis tick marks represent 1 x 10^{-1} absorbance units. In (B) are the data used to derive the averaged rate constants for Y122• reduction by NMHA. The ΔAbs_{410nm} values were determined by the fitted base-line (F.B.L.) method.[28] The initial 10 minutes of the averaged data (three experiments) were fit (red line) to the linear equation, $y = 2.6112 + 0.12332 * t$, where t is in min. The standard deviations were used to estimate the error in the measurement. The rate constant for Y122• reduction (0.041 ± 0.001 $M^{-1}s^{-1}$) was derived by dividing through by the NMHA concentration. The *y*-axis tick marks represent 5 x 10^{-1} absorbance units.

The rate constant for the reduction of Y122• by N-methylhydroxylamine in $^{2}H_2O$ at 20°C (Figure 6.3B), was determined to be 0.041 ± 0.001 $M^{-1}s^{-1}$. This value was obtained from the linear fit of the initial 10 minutes of the reaction. Fitting the change in absorbance of the 410 nm peak versus time (Figure 6.3A) to a biexponential equation (data not shown) for the control β2 and N-MHA reaction in $^{2}H_2O$ produced a similar rate constant (0.045 ± 0.003 $M^{-1}s^{-1}$) for the first exponential (i.e. Y122• reduction). The corresponding rate constant for the reaction of control β2 with N-methylhydroxylamine in $^{1}H_2O$ at 20°C (data not shown) was determined to be 0.18 ± 0.01 $M^{-1}s^{-1}$. From these determined rates at 20°C, the KIE for N-MHA was estimated to be 4.4.

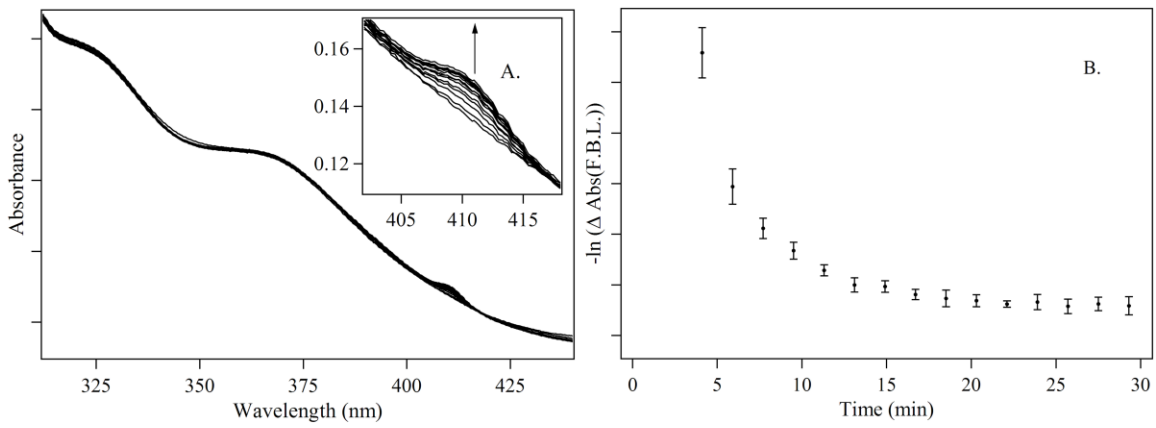

Figure 6.4. UV-visible kinetic data, which are associated with the reaction of Met-β2 (40 μM) with N-methylhydroxylamine (NMHA, 50 mM), recorded at 20°C in ^2H_2O and at p^{2}H 7.6. In (A), a representative example of the UV-Visible absorbance spectra, used to derive the rate constant is shown. The gain of the Y• absorbance at 410 nm is indicated by the arrow in the inset. The *y*-axis tick marks represent 1 x 10^{-1} absorbance units. In (B) are the data used to illustrate Y122• formation from the NMHA reaction with Metβ2. The ΔAbs_{410nm} values were determined by the fitted base-line (F.B.L.) method.[28] The standard deviations were used to estimate the error in the measurement. The *y*-axis tick marks represent 5 x 10^{-1} arbitrary units.

Gerez and Fontecave showed that the aerobic reaction of Metβ2 with hydrazine in ^1H_2O caused the re-generation of the 410 nm absorption band.[30] These previous data suggested that hydrazine can reduce the diferric cluster, even in the presence of oxygen. In the case of the Metβ2 reaction with N-MHA in ^2H_2O (Figure 6.4), aerobic reduction of the diferric cluster leads to the spontaneous reactivation of β2. The lack of reactivation of Metβ2 with N-MHA in ^1H_2O (Figure 6.5) suggests that the reduction of the diferric cluster is much slower than the reduction of Y122•. These data suggest that the second exponential for the N-MHA reaction with control β2 in ^2H_2O corresponds to the reactivation of Y122•. From the N-MHA data, we propose that the reduction of Y122• is

limited by a proton transfer, but the reduction and subsequent oxidation of the diiron cluster is not.

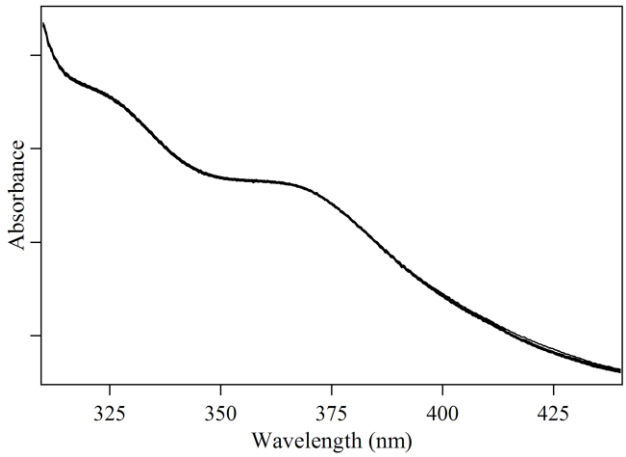

Figure 6.5. UV-visible kinetic data, which are associated with the reaction of Met-β2 (40 μM) with N-methylhydroxylamine (NMHA, 2.5 mM), recorded at 20°C in $^{1}H_2O$ and at p^{1}H 7.6. A representative example of the UV-Visible absorbance spectra is shown. The *y*-axis tick marks represent 1 x 10^{-1} absorbance units.

The reaction of control β2 and 4-methoxyphenol, monitored with UV-visible spectroscopy, is shown in Figure 6.6A. From the linear (red line) fit to the natural log plot (Figure 6.6B), the rate constant for this reaction in $^{2}H_2O$ at 20°C was determined as 0.52 ± 0.04 $M^{-1}s^{-1}$. The corresponding second-order rate constant for the reaction of control β2 with 4-methoxyphenol in $^{1}H_2O$ at 20°C (data not shown) was determined to be 0.83 ± 0.02 $M^{-1}s^{-1}$, which is within reasonable agreement to a previously reported value of 0.9 $M^{-1}s^{-1}$ using EPR spectroscopy.[29] From these rates, the KIE for 4-MP at 20°C was estimated to be ~1.6.

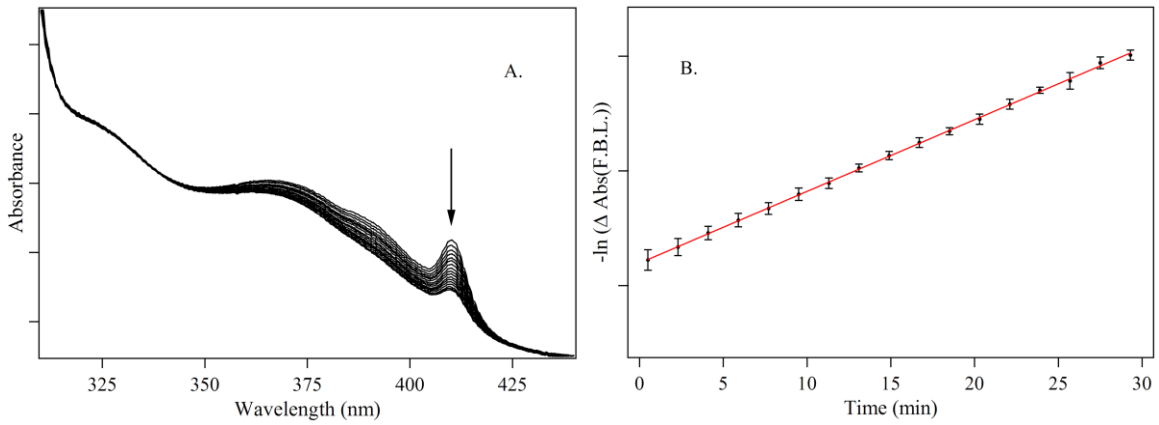

Figure 6.6. UV-visible kinetic data, which are associated with the reduction of Y122• from control β2 (40 μM) with 4-methoxyphenol (4-MP, 1 mM), recorded at 20°C in $^{2}H_2O$ and at p^{2}H 7.6. In (A), a representative example of the UV-Visible absorbance spectra, used to derive the rate constant is shown. The loss of the Y• absorbance at 410 nm is indicated by the arrow. The *y*-axis tick marks represent 1 x 10^{-1} absorbance units. In (B) are the data used to derive the averaged rate constants for Y122• reduction by 4-MP. The ΔAbs_{410nm} values were determined by the fitted base-line (F.B.L.) method.[28] The averaged data (three experiments) were fit (red line) to the linear equation, $y = 2.5985 + 0.031248 * t$, where t is in min. The standard deviations were used to estimate the error in the measurement. The rate constant (0.52 ± 0.04 $M^{-1}s^{-1}$) was derived by dividing through by the 4-MP concentration. The *y*-axis tick marks represent 5 x 10^{-1} arbitrary units.

6.4.2 Reaction-Induced FT-IR Difference Spectroscopy

Reaction-induced FT-IR spectroscopy was used to identify protein structural dynamics linked to Y122• redox changes. The FT-IR absorbance spectra for control β2, hydroxyurea (HU), N-methylhydroxylamine (N-MHA), and 4-methoxyphenol (4-MP) were recorded (Figure 6.7). The FT-IR absorption spectrum in $^{2}H_2O$ showed the expected downshift of ~1550 cm^{-1} amide II intensity to ~1450 cm^{-1} (amide II'), indicating a substantial amount of deuterium exchange (Figure 6.7; also see references 1,19,31,32).

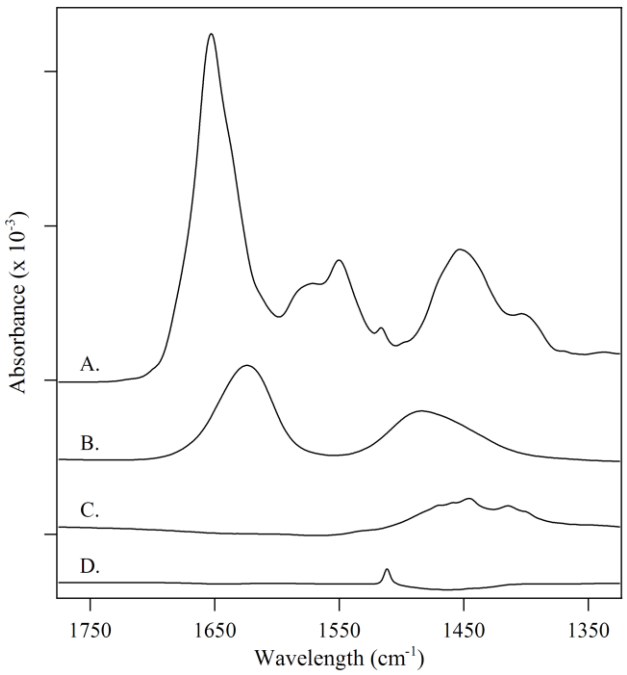

Figure 6.7. FT-IR absorbance spectra collected at 20°C. The data are (A) 250 μM natural abundance, control β2, (B) 50 mM hydroxyurea, (C) 50 mM N-methylhydroxylamine, and (D) 2.5 mM 4-methoxyphenol. All samples (A) – (D) were prepared in 5 mM Hepes, p^{2}H 7.6 buffer. The *y*-axis tick marks represent 5 x 10^{-2} absorbance units.

The reaction-induced difference FT-IR spectra of *E. coli* β2 with hydroxyurea were previously reported in Tris-^2H_2O buffer.[1] The β2 samples were mixed manually with hydroxyurea and immediately injected into the FT-IR sample cell with the GlobalFIA pump. The FT-IR data were collected as two 120 s acquisitions with a 6 min interval separating the "oxidized" and "reduced" data. These FT-IR absorption spectra were subtracted (1:1) to yield the difference spectra. *Only* those vibrational bands that are affected by the reduction of Y122• with hydroxyurea are revealed in the difference spectrum. Redox changes to tyrosine result in perturbations to the ring vibrational modes (υ_{8a} and υ_{19a}) and the CO vibration (υ_{7a}) as expected.[33-35] Unique bands attributed to the

tyrosyl radical, Y122•, are positive; whereas the reduced (singlet) tyrosine features are negative.

6.4.3 Tyrosyl radical ring and CO vibrational modes

In our previous report, the CO stretching (υ_{7a}) frequency for the light-generated tyrosyl radical in $^{2}H_2O$ solution was observed at 1516 cm^{-1},[1] similar to other model studies in $^{1}H_2O$.[21,33-37] The assignment of this band in model tyrosine was supported by specific isotope labeling[35] and density functional theory (DFT)[38] calculations. Resonance Raman studies for the *E. coli* β2 protein have assigned a ~1498 cm^{-1} band to the CO mode for Y122•.[39,40] In Figure 6.8A, the presence of a 1499 cm^{-1} positive band for the NA-β2 sample corroborates the assignment. This υ_{7a} mode of Y• is predicted to downshift by 23 cm^{-1} upon $^{2}H_{ring}$ labeling.[38] In the $^{1}H_4$–minus–$^{2}H_4$ isotope-edited spectrum (Figure 6.8A), the positive 1499 cm^{-1} peak shifts to the negative 1481 cm^{-1} feature. The -18 cm^{-1} spectral shift supports the υ_{7a} assignment.

In addition to the CO mode, the totally symmetric ring stretching mode, υ_{8a}, is also perturbed by oxidation of the phenol ring. The symmetric υ_{8a} ring stretching mode is observed at 1610 – 1600 cm^{-1} region for singlet tyrosinate and 1620 – 1610 cm^{-1} for singlet tyrosine models.[40] For Y•, the υ_{8a} mode is observed in the 1550 – 1560 cm^{-1} region.[34,35,38,41] A candidate for this mode of Y122• in β2 may be assigned to the positive 1563 cm^{-1} feature in Figure 6.8A. Our UV Raman study of control β2 led to the assignment of a 1556 cm^{-1} peak to this mode.[40] This band is sensitive to $^{2}H_{ring}$ labeling; the 1563 cm^{-1} band in the $^{1}H_4$–minus–$^{2}H_4$ isotope-edited spectrum might shift either to 1553 (Δ = -10) cm^{-1} or to 1513 (Δ = -50) cm^{-1}. The spectral shift to the υ_{8a} mode has not

been determined experimentally for the model tyrosyl radical, albeit DFT calculations predict a -38 cm^{-1} shift.[38]

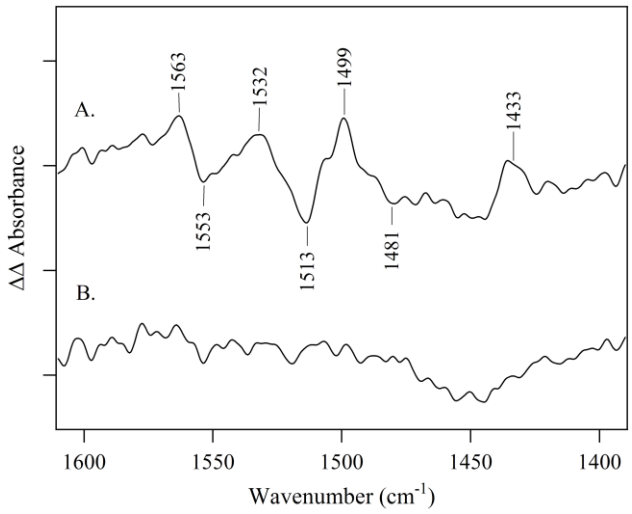

Figure 6.8. Isotope-edited FT-IR spectra of *E. coli* β2 with 50 mM hydroxyurea collected at 20°C. The data in (A) are $^{1}H_4$-minus-$^{2}H_4$ and (B) ^{14}N-minus-^{15}N tyrosine-labeled β2 samples. The $^{1}H_4$-minus-$^{2}H_4$-isotope-edited and ^{14}N-minus-^{15}N-isotope-edited FT-IR spectra of tyrosine-labeled β2 are generated from data reported previously.[1] The spectra were normalized to provide the same Y122•/β2 content. The *y*-axis tick marks represent 1 x 10^{-4} absorbance units.

6.4.4 Tyrosine ring vibrational modes

In the $^{1}H_4$Y–minus–$^{2}H_4$Y isotope-edited spectrum (Figure 6.8A), the 1513 cm^{-1} peak shifts to 1433 cm^{-1} for a spectral shift of -80 cm^{-1}. The magnitude of this downshift is in good agreement with the predicted -83 cm^{-1} shift from DFT calculations[38] for the υ_{19a} ring mode of singlet tyrosine. As expected, no tyrosine ring spectral shifts were observed for the ^{14}NY-minus-^{15}NY isotope-edited spectrum in Figure 6.8B.

Table 6.1. Assignments of β2 Vibrational Frequencies[a] with $^2H_4$ Isotope Shifts

Tyrosinate[b]		β2[c]		Assignment
	(Δexp, Δcalc)		(Δexp)	
1500	-80, -83	1513	-80	υ_{19a}

Tyrosyl radical•[b]		β2[c]		Assignment
	(Δexp, Δcalc)		(Δexp)	
1554	N.D.[d], -38	1563	N.D.[d]	υ_{8a}
1516	N.D.[d], -27	1499	-17	υ_{7a}

[a] Frequencies are in cm^{-1}. See Materials and Methods for experimental details. [b] See ref 38. [c] This work; derived from isotope-edited spectra (Figure 6.8A). [d] N.D., not determined.

6.4.5 β2 Spectral Dependence on Reducing Agent

Previously, we reported redox-linked structural changes for the reaction of control β2 with hydroxyurea.[1] Distinct features were observed at (-) 1661/(+) 1653 cm^{-1}, which were assigned to local perturbations of the amide bonds surrounding Y122. To defend the hypothesis that the spectral features in the 1650 – 1600 cm^{-1} region arise from β2 amide I changes and not from reducing agent, we sought other reducing agents that are IR invisible in this region. N-methylhydroxylamine and 4-methoxyphenol are well known, potent β2 radical scavengers. The FT-IR absorbance spectra of the two inhibitors are displayed in Figure 6.7C and 6.7D, respectively. The infrared spectra of these β2 inhibitors confirm no spectral contributions in the 1700 – 1600 cm^{-1} region.

Figure 6.9 shows the FT-IR difference spectra of hydroxyurea-treated (Figure 6.9A), N-methylhydroxylamine-treated (Figure 6.9B), and 4-methoxyphenol-treated

(Figure 6.9B) β2 samples. The frequencies in the 1600 – 1650 cm^{-1} region, specifically (-) 1661/(+) 1653 cm^{-1}, are identical. These results suggest that the amide I region of the β2 FT-IR difference spectrum is independent of the reducing agent. Therefore, the 1650 – 1600 cm^{-1} region of the β2 difference spectrum arises from the protein amide bond conformational changes (i.e. hydrogen bonding or geometry).

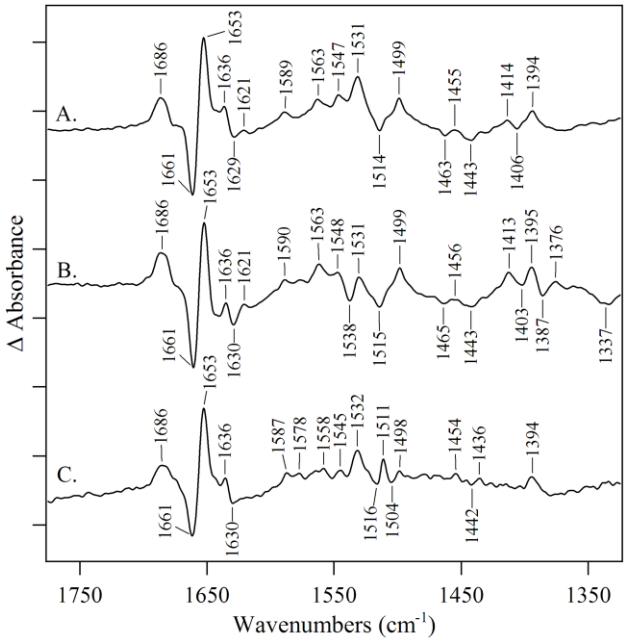

Figure 6.9. Reaction-induced FT-IR spectra of *E. coli* natural-abundance β2 collected at 20°C. The data are reactions of control β2 with (A) 50 mM hydroxyurea, (B) 50 mM N-methylhydroxylamine, and (C) 2.5 mM 4-methoxyphenol. The β2 samples were prepared at 250 μM final concentrations in 5 mM Hepes, p^2H 7.6. The spectra are averages of (A) 16, (B) 13, and (C) 4. The *y*-axis tick marks represent 2 x 10^{-4} absorbance units.

Although the amide I region are identical for the reducing agents, there are some spectral differences. Comparing the hydroxamic acids, the reactions of control β2 with hydroxyurea (Figure 6.9A) or N-methylhydroxylamine (Figure 6.9B) exhibit some

unique spectral differences. The intensities of (+) 1563, (+) 1413, and (+) 1395 cm^{-1} features are increased in Figure 6.9B compared to the hydroxyurea reaction; whereas the (+) 1531 cm^{-1} band in the N-MHA reaction loses intensity. No significant changes in intensity to the amide I or tyrosine/tyrosyl radical peaks are observed for these two hydroxamic acid derivatives. In the N-MHA reaction, shown in Figure 6.9B, new spectral features arise at (-) 1531, (-) 1387/(+) 1376, and (-) 1337 cm^{-1}.

Under anaerobic conditions, hydroxylamine has been shown to reduce the diiron cluster, albeit, on a slower time scale than Y122• reduction.[30] Reactivation of the protein was achieved when the reduced β2 was subsequently exposed to O_2. In other words, aerobic reduction of β2 with hydroxylamine in ^1H_2O, did not cause reduction of the diferric cluster.[30] From the UV-visible spectroscopy data, presented in this work, we have observed the reactivation of Metβ2 (Figure 6.4) with N-methylhydroxylamine in ^2H_2O in the presence of molecular oxygen. The conditions for the UV-visible experiments are similar to the reaction-induced FT-IR reactions (Figure 6.9B). The differences between the hydroxyurea (Figure 6.9A) and N-methylhydroxylamine (Figure 6.9B) reactions may be attributed in part to redox chemistry of the diiron center.

To investigate the spectral contributions, if any, of the reducing agents to the reaction-induced FT-IR spectra (Figure 6.9), we used 4-methoxyphenol. FT-IR spectra of the 4-methoxyphenol radical in solution can be generated using light-oxidation (see Figure 6.10B).

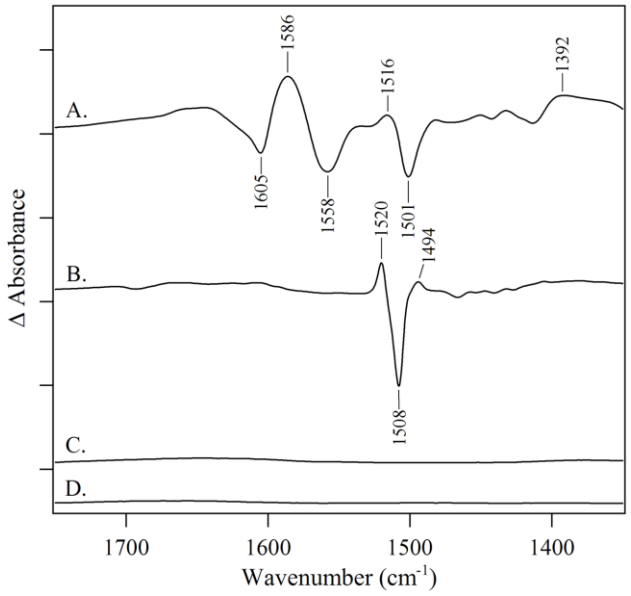

Figure 6.10. Photolysis-induced FT-IR spectra collected at 79 K. The data are (A) 100 mM tyrosinate in 5 mM Na-borate, p^2H 11.0, (B) 100 mM 4-methoxyphenol in 5 mM Hepes, p^2H 7.6, (C) 5 mM Na-borate buffer, and (D) 5 mM Hepes buffer. See Materials and Methods for details. The spectra are averages of (A) 4, (B) 4, (C) 4, and (D) 4. The *y*-axis tick marks represent 1 x 10^{-2} absorbance units.

Oxidation of tyrosinate is known to perturb the phenoxyl ring (υ_{8a}, υ_{19a}) and CO (υ_{7a}) vibrational modes. The assignments for the tyrosinate/tyrosyl radical FT-IR difference spectra have been discussed in detail, previously (see 21,35 and references within). In Figure 6.10A, the positive feature at 1516 cm^{-1} is assigned to the CO (υ_{7a}) mode for the radical.[1,21,34-38,41] For singlet tyrosinate, negative bands at 1601, 1558, and 1501 cm^{-1} are assigned to the ring vibrational modes, υ_{8a}, υ_{8b}, and υ_{19a}, respectively.[1,21,34-38,41] In comparison to tyrosinate, the photolysis-induced FT-IR spectrum of 4-methoxyphenol in Figure 6.10B is simplified. We assign the negative 1508 cm^{-1} for reduced 4-MP to a ring stretching mode and the positive 1494 cm^{-1} to the CO stretching

vibration of the 4-MP radical. As expected, we observe no changes in the sodium borate (Figure 6.10C) or Hepes (Figure 6.10D) buffer samples.

Figure 6.9C gives rise to similar features at (-) 1516/(+) 1511/(-) 1504 cm^{-1} to the model 4-methoxyphenol data in Figure 6.10B. The amide I bands (i.e. 1650 – 1600 cm^{-1} region) in Figure 6.9C are identical to the other hydroxamic acid inhibitors in Figures 6.9A and 6.9B. This result further supports the conclusion that the amide I structural changes in the reaction-induced FT-IR spectra of β2 are independent of reducing agent. The effective loss of the Y122• υ_{7a} mode at ~1498 cm^{-1} in Figure 6.9C is due to spectral overlap with a negative ~1490 cm^{-1} CO vibration from the radical 4-MP (Figure 6.10B). In comparison to the hydroxyurea reaction from Figure 6.9A, the reduction of Y122• with 4-methyphenol causes complete loss, or decreased intensity, of bands at (+) 1621, (+) 1563, (+) 1463, (-) 1443, (+) 1414, and (-) 1406 cm^{-1}. In addition, appearances of unique bands are observed at (+) 1578 and (+) 1558 cm^{-1}. These differences suggest that alternate pathways for β2 reduction may be utilized for these inhibitors.

6.4.6 Amide I and II Vibrations

Our previous studies with tyrosine-containing pentapeptides supported structural changes upon oxidation of the tyrosine residue.[1,21] The reaction-induced FT-IR spectra of the RSYTH peptide, which is the primary sequence of *E. coli* β2 surrounding Y122, yielded the set of peaks, (-) 1675/(+) 1651 cm^{-1}. Model tyrosine, which has no amide/peptide bonds, lacks these IR features. These frequencies are similar to that of NA-β2 in Figure 6.11A, suggesting that the (-) 1661/(+) 1653 cm^{-1} peaks may arise from local

amide I structural changes. To test this hypothesis, we incorporated {^{15}N}-tyrosine and 1-{^{13}C}-tyrosine globally into the β2 subunit (see Materials and Methods for details).

There are no spectral shifts in the ^{14}NY–minus–^{15}NY isotope-edited spectrum (Figure 9B). The {^{15}N} labeling of tyrosine is predicted to have no effect on the ring and CO modes of the phenoxyl radical.[38] Minimal shifts (~1-3 cm^{-1})[42,43] are expected in the amide I region for ^{15}N labeling, though no observable shifts are observed in the isotope-edited spectrum. ^{15}N-labeling is expected to have a much larger effect (~25-30 cm^{-1}) on the amide II vibration.[42,44] No spectral shifts in amide II region are observed with ^{15}N-Tyr labeling (Figure 6.8B). The lack of amide II contributions in the ^{14}N–minus–^{15}N-tyrosine isotope-edited spectrum supports that the S121-Y122 amide bond may not be involved in redox-linked structural changes of β2.[1]

Labeling of the β2 protein with 1-{^{13}C}-tyrosine causes significant changes in the FT-IR difference spectrum, compared to the natural abundance (see Figure 6.11). Subtraction of the FT-IR difference spectra of 1-{^{13}C}-tyrosine labeled β2 samples (Figure 6.11A) from natural abundance β2 (Figure 6.11A) results in the isotope-edited spectrum (Figure 6.12).

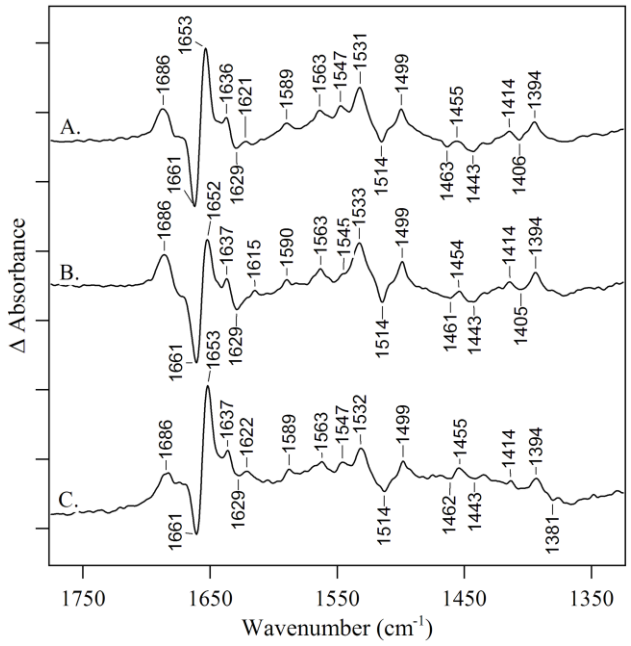

Figure 6.11. Reaction-induced FT-IR spectra of *E. coli* β2 with 50 mM hydroxyurea collected at 20°C. The data are (A) natural-abundance (NA) β2, (B) 1-{^{13}C}-tyrosine-labeled β2, and (C) 4-{^{13}C}-aspartate-labeled β2 samples. All β2 samples were prepared at 250 μM concentrations in 5 mM Hepes, p^{2}H 7.6 buffer. Spectra are averages of (A) 13, (B) 10, and (C) 6 different samples. The y-axis tick marks represent 2 x 10^{-4} absorbance units.

In the 1-^{12}CY–minus–^{13}CY isotope-edited spectrum in Figure 6.12, there are several discrete shifts in the 1700 – 1600 cm^{-1} region. In an FT-IR study of the R-minus-O of *P. denitrificans* cytochrome *c* oxidase, a set of positive bands at 1660 and 1617 cm^{-1} were assigned in part to amide I modes from tyrosine.[45] A 30 – 55 cm^{-1} shift in amide I mode is expected for specific 1-{^{13}C}-labeling of tyrosine.[31,42,44,46-49] The ^{12}C–minus–^{13}C tyrosine-isotope-edited spectrum (Figure 6.12) exhibits a significant (+) 1653 cm^{-1} band. Based upon previous studies,[31,42,44,46-49] we expect a negative feature in the 1623 – 1598 cm^{-1} range. The presence of a (-) 1614 cm^{-1} peak in Figure 6.12 supports the ^{13}C-induced shift of the amide I mode.

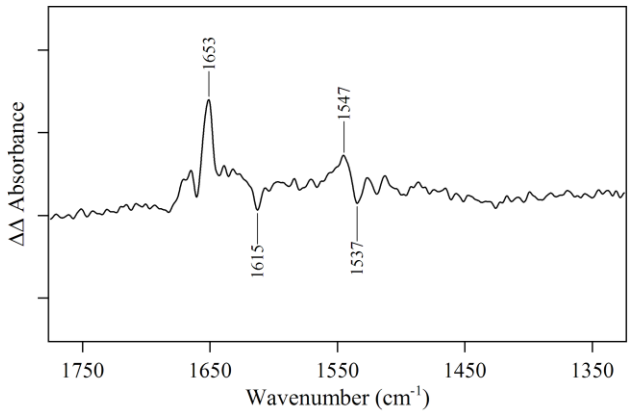

Figure 6.12. Isotope-edited FT-IR spectra of *E. coli* β2 with 50 mM hydroxyurea collected at 20°C. The data are ^{12}C-minus-^{13}C tyrosine-labeled β2 samples. The ^{12}C-minus-^{13}C-isotope-edited FT-IR spectrum of tyrosine-labeled β2 is the subtraction of Figure 6.11B from Figure 6.11A. The spectra were normalized to represent the same Y122•/β2 content prior to subtraction. The *y*-axis tick marks represent 1 x 10^{-4} absorbance units.

Kandori and coworkers observed a decrease in a 1663 cm^{-1} peak by a factor ~1/2 upon incorporation of 1-^{13}C-tyrosine in cytochrome *bo*.[50] The amplitude 1652 cm^{-1} in Figure 6.11A of NA-β2 is approximately halved upon 1-^{13}C-tyrosine incorporation (Figure 6.11B). This result further supports our assignment of the Y122-T123 amide bond involvement in the amide I structural change linked to the reduction of Y122• in β2. The higher frequency of this band (1653 cm^{-1}) indicates that the tyrosine is in an α-helical secondary structure.[48,51] These data are in good agreement with the X-ray structures of Metβ2,[6,17] which is predominantly composed of α-helix structure surrounding Y122.

In addition to amide I perturbations, there are contributions in Figure 6.12 to the amide II (C-N; ~ 1540 – 1550 cm^{-1}) region, which has also been observed previously with 1-{^{13}C}-tyrosine labeling.[50] A positive 1547 cm^{-1} band in Figure 6.12 shifts to 1537

cm^{-1} (Δ = -10 cm^{-1}). These data strongly support that the redox-linked protein conformational changes in β2 occur at nearby amide bonds surrounding Y122•. Specifically, reduction of Y122• causes perturbation of the Y122-T123 amide bond.

6.4.7 Other Vibrational Modes

The 1589-1563 and 1413-1395 cm^{-1} bands in the NA-β2 FT-IR difference spectrum in Figure 6.9A may result from the υ_{as} and υ_{s}, respectively, of the COO- for deprotonated Asp or Glu residue in $^{2}H_2O$. In $^{2}H_2O$ solutions, the COO- group of glutamate and aspartate have been observed at 1566 and 1584 cm^{-1}, respectively, for the symmetric stretch motion.[52] The protonated forms of these residues are expected at a much higher symmetric stretching frequency (1700 – 1780 cm^{-1}) range.[53] However, this mode is very sensitive to the environment and may shift + 60/- 40 cm^{-1} accordingly. Upon chelation to cations, this mode has been shown to shift as high as ~1700 cm^{-1}.[54] In this extreme case, the υ_{as} mode might be responsible for the (+) 1686 cm^{-1} band in NA-β2. The redox-induced structural changes in β2 have been linked to electrostatic-driven interactions between Y122 and D84.[1] Since D84 is chelated to the diiron cluster and is involved in interactions with Y122, it is also reasonable to assign the ~1686 cm^{-1} feature in Figure 6.9 to the υ_{as} of D84. The corresponding antisymmetric mode for deprotonated Asp/Glu is expected at ~1420 – 1400 cm^{-1}.[53,55] The exact location is dependent upon the environment and coordination. The 1413 and/or 1395 cm^{-1} vibrations might be correlated to the υas Asp or Glu vibrational mode.

To assign carboxylate contributions, β2 samples were labeled with 4-{^{13}C}-aspartic acid. The reaction-induced FT-IR spectra of these isotope-labeled β2 samples

with hydroxyurea are shown in Figure 6.12C. Based on previous reports, 65% incorporation of ^{13}C-aspartic acid is expected.[18] Compared to natural-abundance β2 difference spectrum in Figure 6.12A, possible decreases in the intensities for the (+) 1563 and (+) 1415 cm^{-1} features were discerned. These vibrational frequencies support the presence of at least one deprotonated aspartate residue. In addition, the (-) 1406 cm^{-1} in Figure 6.11A seems to vanish. The emergence of a (-) 1381 cm^{-1} peak with ^{13}C-labeling in Figure 6.11C provides evidence for structural changes to an aspartate residue. A potential downshift of 25 cm^{-1} from 1406 cm^{-1} is good agreement with 4-{^{13}C}aspartic acid labeling[56] and supports the assignment to antisymmetric stretch for deprotonated aspartate residue. Vibrational frequencies for protonated (C=O) aspartic acid residues are expected in the 1760 – 1730 cm^{-1} region.[18,53,56] We conclude that the perturbed aspartate group in Figure 6.9 is deprotonated and assign the aspartate residue to position 84. In the Metβ2 structure, D84 is within hydrogen bonding distance to Y122. Upon oxidation of tyrosine, electrostatic interactions drive rotation of the Y122.[17] D84 is a ligand to the diiron center. Structural perturbations of the aspartate-84 residue may cause structural changes to the diiron center through alterations in the electrostatic environment. Furthermore, the lack of the (+) 1563 and (+) 1414/(-) 1406 cm^{-1} features in the reaction of control β2 and 4-methoxyphenol (Figure 6.8C) suggests that aspartate residue may not be altered during the reaction. These data support the conclusion that these radical scavengers of β2 have alternate pathways for Y122• reduction.

The 1589 cm^{-1} frequency may alternatively be attributed to an arginine residue, specifically R120. The symmetric stretch of the guanidinium group of Arg has been observed around 1586 cm^{-1} in ^{2}H-exchanged samples.[52] In the protein environment,

arginine contributions have been assigned to the 1580 - 1590 cm^{-1} region.[45,57] The corresponding asymmetric stretch of the guanidinium group of arginine may contribute to the 1636 or 1623 cm^{-1} frequency in the NA-β2 difference spectrum.[53,57]

The positive features at 1686 and 1398 cm^{-1} may be attributed to the υ(C=O) and υ(CN) modes, respectively, of asparagine or glutamine.[53,57] From the Metβ2 X-ray structure, a glutamine residue at position 80 is within 5.5 Å from the reduced Y122. Movement[17] along the Cα-Cβ bond of Y122 upon oxidation could cause the Y122• and Q80 distance to shorten. Interactions with Q80 could potentially help to stabilize Y122•.

The positive 1455 cm^{-1} band could be attributed to tryptophan δCH, υCC, υCN modes. A ~1412 cm^{-1} peak is expected for tryptophan in $^{1}H_2O$ solution, but expected to downshift to 1382 upon ^{2}H-exchange.[53] However, if exchange is poor, a ~1412 cm^{-1} peak would be observed in Figure 6.9. In UV resonance Raman (UVRR), a 880 cm^{-1} W17 tryptophan mode is expected to downshift ~20 cm^{-1} in $^{2}H_2O$.[58] Based upon our UVRR study for Apoβ2-minus-Metβ2 (see Chapter 7), no spectral shift of the W17 band was observed in ^{2}H-exchanged protein samples.[40] From this study, we proposed that the exchange of the tryptophan protons is slow. Since the (+) 1414 cm^{-1} band in Figure 6.9A may arise from aspartate perturbations, tryptophan may be responsible for the (+) 1395 cm^{-1} peak.

The 1462–1461 and 1443–1439 cm^{-1} peaks could be attributed to histidine ring vibrations, which are relatively insensitive to $^{1}H/^{2}H$ exchange. A 1439 cm^{-1} peak was observed in the infrared spectrum of 4-methylimidazole.[53] Imidazole ring stretching vibrations have also been reported in the range of 1490 – 1469 cm^{-1} in both $^{1}H_2O$ and $^{2}H_2O$.[59-61]

Spectral changes to tryptophan and histidine residues support that the electronic distribution of the diferric cluster may be linked to Y122 redox changes. Perturbations of the diferric cluster could be responsible for adjusting the pK_A and/or midpoint potential of neighboring redox-active amino acids. The alterations in the electronic or electrostatic environment may further provide a mechanism of control for intraprotein proton-coupled electron transfer reactions in the β2 subunit of ribonucleotide reductase.

6.5 Conclusions

In this study, we presented redox-linked structural studies of the ribonucleotide reductase β2 subunit. When oxidized, β2 houses a stable tyrosyl radical at position 122 and a diferric cluster. Using UV-visible spectroscopy, we examined the reduction rates of Y122• using the exogenous electron donors, hydroxyurea, N-methylhydroxylamine, and 4-methoxyphenol. The hydroxamic acid derivatives, hydroxyurea and N-methylhydroxylamine, had significant kinetic isotope effects. 4-Methoxyphenol, however, did not display such a considerable ^2H_2O effect. We propose that these β2 radical scavengers may participate in different net PCET processes during Y122• reduction.

Reaction-induced FT-IR experiments gave evidence for redox-linked perturbations of local amide bonds surrounding Y122. β2 samples labeled with tyrosine isotopes supported these data and suggest that the Y122-T123 amide bond is involved. Global labeling of β2 with an aspartic acid isotope led to the tentative assignments of spectral features to a deprotonated aspartate. Structural changes to aspartate residues may

cause electrostatic and/or electronic changes to the diferric center. The redox-linked communication between tyrosine and the diferric center in β2 could serve as a means for local PCET control. Contributions from other amino acids have been discussed here. Future labeling experiments will resolve the assignments of these residues.

The dependence of the radical scavenger on β2 infrared spectra was also investigated. Amide I modes were identical for all reactions. These data support the conclusion that the amide I bands are independent of β2 inhibitor. Various spectral features, however, were different among these reactions. We propose that some of these vibrational differences are potentially a result from alternate pathways for Y122• reduction. Further experiments to determine the activation energies for these reactions may help to confirm this hypothesis. These data illustrate the potential for this reaction-induced FT-IR spectroscopic technique to resolve the subtle differences of these reaction mechanisms.

6.6 Acknowledgments

This project was supported by Award Number R01GM043273 from the National Institute of General Medical Sciences and the National Eye Institute. The authors thank Prof. J. Soper for the use of the temperature-controlled UV-visible spectrophotometer.

6.7 References

1. Offenbacher, A. R.; Vassiliev, I. R.; Seyedsayamdost, M. R.; Stubbe, J.; Barry, B. A., Redox-linked structural changes in ribonucleotide reductase. *J. Am. Chem. Soc.* **2009**, *22*, 7496-7497.

2. Thelander, L.; Reichard, P., Reduction of ribonucleotides. *Annu. Rev. Biochem.* **1979**, *48*, 133-158.

3. Stubbe, J.; van der Donk, W. A., Protein radicals in enzyme catalysis. *Chem. Rev.* **1998**, *98*, 705-762.

4. Eklund, H.; Uhlin, U.; Färnegårdh, M.; Logan, D. T.; Nordlund, P., Structure and function of the radical enzyme ribonucleotide reductase. *Prog. Biophys. Mol. Biol.* **2001**, *77*, 177-268.

5. Uhlin, U.; Eklund, H., Structure of ribonucleotide reductase protein R1. *Nature* **1994**, *370*, 533-539.

6. Nordlund, P.; Sjöberg, B.-M.; Eklund, H., Three-dimensional structure of the free radical protein of ribonucleotide reductase. *Nature* **1990**, *345*, 593-598.

7. Bennati, M.; Robblee, J. H.; Mugnaini, V.; Stubbe, J.; Freed, J. H.; Borbat, P., EPR distance measurements support a model for long-range radical initiation in *E. coli* ribonucleotide reductase. *J. Am. Chem. Soc.* **2005**, *127*, 15014-15015.

8. Stubbe, J.; Nocera, D. G.; Yee, C. S.; Chang, M. C. Y., Radical initiation in the class I ribonucleotide reductase: long-range proton-coupled electron transfer? *Chem. Rev.* **2003**, *103*, 2167-2202.

9. Rova, U.; Goodtzoba, K.; Ingemarson, R.; Behravan, G.; Gräslund, A.; Thelander, L., Evidence by site-directed mutagenesis supports long-range electron transfer in mouse ribonucleotide reductase. *Biochemistry* **1995**, *34*, 4267-4275.

10. Ekberg, M.; Sahlin, M.; Eriksson, M.; Sjöberg, B.-M., Two conserved tyrosine residues in protein R1 participate in an intermolecular electron transfer in ribonucleotide reductase. *J. Biol. Chem.* **1996**, *271*, 20655-20659.

11. Ekberg, M.; Pötsch, S.; Sandin, E.; Thunnissen, M.; Nordlund, P.; Sahlin, M.; Sjöberg, B.-M., Preserved catalytic activity in an engineered ribonucleotide reductase R2 protein with a nonphysiological radical transfer pathway. The importance of hydrogen bond connections between participating residues. *J. Biol. Chem.* **1998**, *273*, 21003-21008.

12. Rova, U.; Adrait, A.; Pötsch, S.; Gräslund, A.; Thelander, L., Evidence by mutagenesis that Tyr370 of the mouse ribonucleotide reductase R2 protein is the

connecting link in the intersubunit radical transfer pathway. *J. Biol. Chem.* **1999**, *274*, 23746-23751.

13. Chang, M. C. Y.; Yee, C. S.; Nocera, D. G.; Stubbe, J., Site-specific replacement of a conserved tyrosine in ribonucleotide reductase with an aniline amino acid: a mechanistic probe for redox-active tyrosine. *J. Am. Chem. Soc.* **2004**, *126*, 16702-16703.

14. Reece, S. Y.; Seyedsayamdost, M. R.; Stubbe, J.; Nocera, D. G., Direct observation of a transient tyrosine radical competent for initiating turnover in a photochemical ribonucleotide reductase. *J. Am. Chem. Soc.* **2007**, *129*, 13828-12830.

15. Seyedsayamdost, M. R.; Xie, J.; Chan, C. T. Y.; Schultz, P.; Stubbe, J., Site-specific insertion of 3-aminotyrosine into subunit α2 of *E. coli* ribonucleotide : direct evidence for involvement of Y_{730} and Y_{731} in radical propagation. *J. Am. Chem. Soc.* **2007**, *129*, 15060-15071.

16. Ge, J.; Yu, G.; Ator, M. A.; Stubbe, J., Pre-steady-state and steady-state kinetic analysis of *E. coli* class I ribonucleotide reductase. *Biochemistry* **2003**, *42*, 10071-10083.

17. Högbom, M.; Galander, M.; Andersson, M.; Kolberg, M.; Hofbauer, W.; Lassmann, G.; Nordlund, P.; Lendzian, F., Displacement of the tyrosyl radical cofactor in ribonucleotide reductase obtained by single-crystal high-field EPR and 1.4-Å x-ray data. *Proc. Natl. Acad. Sci. U.S.A.* **2003**, *100*, 3209-3214.

18. Sachs, R. K.; Halverson, K. M.; Barry, B. A., Specific isotope labeling and photooxidation-linked structural changes in the manganese-stabilizing subunit of photosystem II. *J. Biol. Chem.* **2003**, *278*, 44222-44229.

19. Jenson, D. L.; Barry, B. A., Proton-coupled electron transfer in photosystem II: proton inventory of a redox active tyrosine. *J. Am. Chem. Soc.* **2009**, *131*, 10567-10573.

20. Sneeden, J. L.; Loeb, L. A., Mutations in the R2 subunit of ribonucleotide reductase that confer resistence to hydroxyurea. *J. Biol. Chem.* **2004**, *279*, 40723-40728.

21. Vassiliev, I. R.; Offenbacher, A. R.; Barry, B. A., Redox-active tyrosine residues in pentapeptides. *J. Phys. Chem. B* **2005**, *109*, 23077-23085.

22. Ehrenberg, A.; Reichard, P., Electron spin resonance of the iron-containing protein B2 from ribonucleotide reductase. *J. Biol. Chem.* **1972**, *247*, 3485-3488.

23. Lam, K.-Y.; Fortier, D. G.; Thomson, J. B.; Sykes, A. G., Kinetics of inactivation of the tyrosine radical of the B2 subunit of *E. coli* ribonucleotide reductase. *J. Chem. Soc., Chem. Commun.* **1990**, 658-660.

24. Karlsson, M.; Sahlin, M.; Sjöberg, B. M., *Escherichia coli* ribonucleotide reductase. Radical susceptibility to hydroxyurea is dependent on the regulatory state of the enzyme. *J. Biol. Chem.* **1992**, *267*, 12622-12626.

25. Lassmann, G.; Thelander, L.; Gräslund, A., EPR stopped-flow studies of the reaction of the tyrosyl radical of protein R2 from ribonucleotide reductase with hydroxyurea. *Biochem. Biophys. Res. Commun.* **1992**, *188*, 879-887.

26. Nyholm, S.; Thelander, L.; Gräslund, A., Reduction and loss of the iron center in the reaction of the small subunit of mouse ribonucleotide reductase with hydroxyurea. *Biochemistry* **1993**, *32*, 11569-11574.

27. Swarts, J. C.; Aquino, M. A. S.; Han, J.-Y.; Lam, K.-Y.; Sykes, A. G., Kinetic studies on the reduction of the tyrosyl radical of the R2 subunit of *E. coli* ribonucleotide reductase. *Biochim. Biophys. Acta* **1995**, *1247*, 215-224.

28. Han, J.-Y.; Gräslund, A.; Thelander, L.; Sykes, A. G., Kinetic studies on the reduction of the R2 subunit of mouse ribonucleotide reductase with hydroxyurea, hydrazine, phenylhydrazine and hydroxylamine. *J. Biol. Inorg. Chem.* **1997**, *2*, 287-294.

29. Pötsch, S.; Sahlin, M.; Langelier, Y.; Gräslund, A.; Lassmann, G., Reduction of the tyrosyl radical and the iron center in protein R2 of ribonucleotide reductase from mouse, herpes simplex virus and *E. coli* by *p*-alkoxyphenols. *FEBS Lett.* **1995**, *374*, 95-99.

30. Gerez, C.; Fontecave, M., Reduction of the small subunit of *Escherichia coli* ribonucleotide reductase by hydrazines and hydroxylamines. *Biochemistry* **1992**, *31*, 780-786.

31. Hutchison, R. S.; Betts, S. D.; Yocum, C. F.; Barry, B. A., Conformational changes in the extrinsic manganese stabilizing protein can occur upon binding to the photosystem II reaction center: an isotope editing and FT-IR study. *Biochemistry* **1998**, *37*, 5643-5653.

32. Rath, P.; DeGrip, W. J.; Rothschild, K. J., Photoactivation of rhodopsin causes an increased hydrogen-deuterium exchange of buried peptide groups. *Biophys. J.* **1998**, *74*, 192-198.

33. Tripathi, G. N. R.; Schuler, R. H., The resonance Raman spectrum of phenoxyl radical. *J. Chem. Phys.* **1984**, *81*, 113-121.

34. Johnson, C. R.; Ludwig, M.; Asher, S. A., Ultraviolet resonance Raman characterization of photochemical transients of phenol, tyrosine, and tryptophan. *J. Am. Chem. Soc.* **1986**, *108*, 905-912.

35. Ayala, I.; Range, K.; York, D.; Barry, B. A., Spectroscopic properties of tyrosyl radicals in dipeptides. *J. Am. Chem. Soc.* **2002**, *124*, 5496-5505.

36. Mukherjee, A.; McGlashen, M. L.; Spiro, T. G., Ultraviolet resonance Raman spectroscopy and general force field analysis of phenolate and phenoxyl radical. *J. Phys. Chem.* **1995**, *99*, 4912-4917.

37. Qin, Y.; Wheeler, R. A., Density-Functional-derived structures, spin properties, and vibrations for phenol radical cation. *J. Phys. Chem.* **1996**, *100*, 10554-10563.

38. Range, K.; Ayala, I.; York, D.; Barry, B. A., Normal modes of redox-active tyrosine: conformational dependence and comparison to experiment. *J. Phys. Chem. B* **2006**, *110*, 10970-10981.

39. Backes, G.; Sahlin, M.; Sjöberg, B.-M.; Loehr, T. M.; Sanders-Loehr, J., Resonance Raman spectroscopy of ribonucleotide reductase. Evidence for a deprotonated tyrosyl radical and photochemistry of the binuclear iron center. *Biochemistry* **1989**, *28*, 1923-1929.

40. Offenbacher, A. R.; Chen, J.; Barry, B. A., *submitted*.

41. Cappuccio, J. A.; Ayala, I.; Elliott, G. I.; Szundi, I.; Lewis, J.; Konopelski, J. P.; Barry, B. A.; Einarsdóttir, Ó., Modeling the active site of cytochrome oxidase: synthesis and characterization of a cross-linked histidine-phenol. *J. Am. Chem. Soc.* **2002**, *124*, 1750-1760.

42. Haris, P. I.; Robillard, G. T.; van Dijk, A. A.; Chapman, D., Potential of ^{13}C and ^{15}N labeling for studying protein-protein interactions using Fourier transform infrared spectroscopy. *Biochemistry* **1992**, *31*, 6279-6284.

43. Noguchi, T.; Sugiura, M., Analysis of flash-induced FTIR difference spectra of the S-state cycle in the photosynthetic water-oxidizing complex by uniform ^{15}N and ^{13}C isotope labeling. *Biochemistry* **2003**, *42*, 6035-6042.

44. Zhang, M.; Fabian, H.; Mantsch, H. H.; Vogel, H. J., Isotope-edited Fourier transform infrared spectroscopy studies of calmodulin's interaction with its target peptides. *Biochemistry* **1994**, *33*, 10883-10888.

45. Iwaki, M.; Puustinen, A.; Wikström, M.; Rich, P. R., Structural and chemical changes of the P_M intermediate of *Paracoccus denitrificans* cytochrome *c* oxidase revealed by IR spectroscopy with labeled tyrosines and histidine. *Biochemistry* **2006**, *45*, 10873-10885.

46. Tadesse, L.; Nazarbaghi, R.; Walters, L., Isotopically enhanced infrared spectroscopy: a novel method for examining secondary structure at specific sites in conformationally heterogeneous peptides. *J. Am. Chem. Soc.* **1991**, *113*, 7036-7037.

47. Ludlam, C. F. C.; Sonar, S.; Lee, C.-P.; Coleman, M.; Herzfeld, J.; RajBhandary, U. L.; Rothschild, K. J., Site-directed isotope labeling and ATR-FTIR difference spectroscopy of bacteriorhodopsin: the peptide carbonyl group of Tyr 185 is structurally active during the bR--> N transition. *Biochemistry* **1995**, *34*, 2-6.

48. Decatur, S. M.; Antonic, J., Isotope-edited infrared spectroscopy of helical peptides. *J. Am. Chem. Soc.* **1999**, *121*, 11914-11915.

49. Kimura, Y.; Mizusawa, N.; Ishii, A.; Yamanari, T.; Ono, T.-A., Changes of low-frequency vibrational modes induced by universal ^{15}N- and ^{13}C-isotope labeling in S_2/S_1 FTIR difference spectrum of oxygen-evolving complex. *Biochemistry* **2003**, *42*, 13170-13177.

50. Kandori, H.; Nakamura, H.; Yamazaki, Y.; Mogi, T., Redox-induced protein structural changes in cytochrome *bo* revealed by Fourier transform infrared spectroscopy and [^{13}C]Tyr labeling. *J. Biol. Chem.* **2005**, *280*, 3281-32826.

51. Ludlam, C. F. C.; Arkin, I. T.; Liu, X.-M.; Rothman, M. S.; Rath, P.; Aimoto, S.; Smith, S. O.; Engelman, D. M.; Rothschild, K. J., Fourier transform infrared spectroscopy and site-directed isotope labeling as a probe of local secondary structure in the transmembrane domain of phospholamban. *Biophys. J.* **1996**, *70*, 1728-1736.

52. Chirgadze, Y. N.; Fedorov, O. V.; Trushina, N. P., Estimation of amino acid residue side-chain absorption in the infrared spectra of protein solutions in heavy water. *Biopolymers* **1975**, *14*, 679-694.

53. Barth, A., The infrared absorption of amino acid side chains. *Prog. Biophys. Mol. Biol.* **2000**, *74*, 141-173.

54. Deacon, G. B.; Phillips, R. J., Relationships between the carbon-oxygen stretching frequencies of carboxylate complexes and the type of carboxylate coordination. *Coord. Chem. Rev.* **1980**, *33*, 227-250.

55. Barth, A.; Zscherp, C., What vibrations tell us about proteins. *Q. Rev. Biophys.* **2002**, *35*, 369-430.

56. Englehard, M.; Gerwert, K.; Hess, B.; Kreutz, W.; Siebert, F., Light-driven protonation changes of internal aspartic acids of bacteriorhodopsin: an investigation by static and time-resolved infrared difference spectroscopy using [4-^{13}C]aspartic acid labeled purple membranes. *Biochemistry* **1985**, *24*, 400-407.

57. Ingledew, W. J.; Smith, S. M. E.; Gao, Y. T.; Jones, R. J.; Salerno, J. C.; Rich, P. R., Ligand, cofactor, and residue vibrations in the catalytic site of endothelial nitric oxide synthase. *Biochemistry* **2005**, *44*, 4238-4246.

58. Takeuchi, H.; Harada, I., Normal coordinate analysis of the indole ring. *Spectrochim. Acta* **1986**, *42A*, 1069-1078.

59. Garfinkel, D.; Edsall, J. T., Raman spectra of amino acids and related compounds. VIII. Raman and infrared spectra of imidazole, 4-methylimidazole and histidine. *J. Am. Chem. Soc.* **1958**, *80*, 3807-3812.

60. Yoshida, C. M.; Freedman, T. B.; Loehr, T. M., Resonance Raman study of cobalt(II)-imidazole complexes as models for metalloproteins. *J. Am. Chem. Soc.* **1975**, *97*, 1028-1032.

61. Caswell, D. S.; Spiro, T. G., Ultraviolet resonance Raman spectroscopy of imidazole, histidine, and $Cu(imidazole)_4^{2+}$: implications for protein studies. *J. Am. Chem. Soc.* **1986**, *108*, 6470-6477.

CHAPTER 7

PERTURBATIONS OF AROMATIC AMINO ACIDS ARE ASSOCIATED WITH IRON CLUSTER ASSEMBLY IN RIBONUCLEOTIDE REDUCTASE

by

Adam R. Offenbacher, [*]Jun Chen, and Bridgette A. Barry

Department of Chemistry and Biochemistry and the Petit Institute for Bioengineering and Bioscience, Georgia Institute of Technology, Atlanta, GA 30332

[*]*Current Address: Dalian National Laboratory for Clean Energy, Dalian Institute of Chemical Physics, Chinese Academy of Science, Dalian 116023, China*

7.1 Abstract

The β2 subunit of class Ia ribonucleotide reductases (RNR) contains an antiferromagnetically coupled μ-oxo bridged diiron cluster and a tyrosyl radical (Y122•). Reduction of ribonucleotides is initiated by long-distance proton-coupled electron transfer reactions, which generate a reduced Y122 and a transiently oxidized, active site cysteine radical. A tryptophan, W48, forms a transient tryptophan cation radical during the assembly of the iron cluster. Assembly of the diiron cluster has been proposed to be rate limited by a protein conformational change, and allosteric effects have been reported to regulate metal binding. In this study, an ultraviolet resonance Raman (UVRR) difference technique describes the structural changes, induced by the assembly of the iron cluster and by the reduction of the tyrosyl radical. Spectral contributions from aromatic amino acids are observed through UV resonance enhancement at 229 nm. Vibrational bands are assigned by comparison to histidine, phenylalanine, tyrosine, and tryptophan model compound data and by isotopic labeling of histidine in the β2 subunit. Reduction of the tyrosyl radical gives rise to Y122• Raman bands at 1499 and 1556 cm^{-1} and to Y122 Raman bands at 1170, 1199, and 1608 cm^{-1}. There is little perturbation of other aromatic amino acids when Y122• is reduced. On the other hand, assembly of the iron cluster is accompanied by protonation of histidine. In addition, structural perturbations of tyrosine and tryptophan, which are attributed to changes in tyrosine conformation and in tryptophan hydrogen bonding and dihedral angle, are observed. Analysis of the UVRR spectrum and comparison to X-ray structures suggest that the perturbed tryptophan is W48 and that the perturbed tyrosine is Y122. In summary, our work shows that

electrostatic and conformational perturbations of aromatic amino acids contribute to the structural perturbations, which are associated with metal cluster assembly in RNR.

7.2 Introduction

Ribonucleotide reductase (RNR) participates in DNA biosynthesis by reducing ribonucleotides to produce deoxyribonucleotides.[1-4] In all organisms, production of a transient cysteine radical at the active site is required for catalysis.[5] In *E. coli* and other class Ia enzymes, RNR consists of two subunits, $\alpha 2$ and $\beta 2$. A conserved tyrosine residue, Y122, is required for catalysis. The active site is located in the homodimeric $\alpha 2$ (formerly R1) subunit. The thiyl radical in $\alpha 2$ is generated by the stable tyrosyl radical (Y122•), which is adjacent to a diferric cofactor in the homodimeric $\beta 2$ (formerly R2) subunit.[6] Reduction of Y122• and subsequent oxidation of C439 is proposed to be mediated by reversible long-distance proton-coupled electron transfer (PCET) reactions.[7,8] These reactions occur over a conserved pathway and a distance of 35 Å.[7-9]

The catalytically essential Y122• forms during the activation of the apoprotein (Apo-$\beta 2$).[10] The apoprotein lacks both the iron cluster and the tyrosyl radical, but these species are spontaneously generated in the presence of Fe^{2+} and molecular oxygen.[11] During the reduction of O_2, two reducing equivalents are provided by the oxidation of the iron cluster and a third originates from the oxidation of Y122. The fourth electron most likely arises from exogenous reductant(s).[10-12] The mechanism of $\beta 2$ activation is an important process in class I RNR chemistry and is not yet fully understood {reviewed in 13}.

The crystal structures of Apo-β2 (Figure 7.1B),[14] Red-β2 (diferrous protein),[15,16] and Met-β2 (Figure 7.1A; diferric protein lacking the tyrosyl radical)[2,17] have been solved.

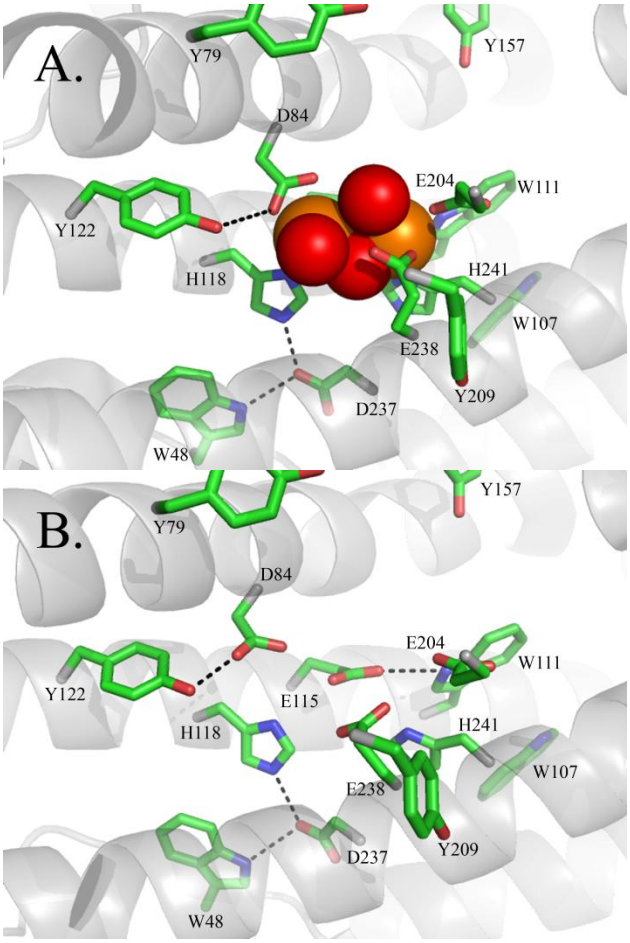

Figure 7.1. A) The coordination environment of the Met-β2 *E. coli* β2 subunit, which contains a diferric cluster and a reduced tyrosyl radical (PDB: 1RIB). All histidine, tryptophan, and tyrosine residues located within 11 Å of the cluster are shown. The iron atoms are displayed as orange spheres; the red spheres represent the oxygen atoms of water, hydroxide or oxygen that are ligated to the diiron cluster. The black, dashed lines represent hydrogen bonding interactions discussed within the text. B) The corresponding environment in the metal free (Apo-β2) *E. coli* β2 subunit (PDB coordinates were graciously provided by H. Eklund).

In analysis of the structures, removal of the iron was inferred to cause protonation of ligating histidine residues.[14] Such protonation would provide charge compensation for a cluster of formerly, ligating carboxylate groups. Local rearrangements of amino acid side chains in the vicinity of the metal site were also observed. Most notably, rotameric shifts in the conformation of aspartate and glutamate residues were evident when the Met-β2 and Apo-β2 structures were compared (Figure 7.1A and B).

Protein dynamics are proposed to play an important role in RNR. Although there is no three-dimensional structure of the fully oxidized, active protein, electron paramagnetic resonance (EPR)[17] and Fourier-transform infrared (FT-IR)[18] spectroscopic studies have given insight into the structural changes linked with Y122 redox changes. Reduction of the tyrosyl radical with hydroxyurea was observed to perturb the structure of the amide bond[18] and result in rotation of Y122.[17] In addition, carboxylate shifts occur during redox changes at the diiron cluster.[15] A slow protein conformational change has been proposed to be rate limiting in enzymatic turnover.[19] A protein conformational change has also been proposed to accompany and possibly regulate the assembly of the diferric iron cluster in RNR.[20,21]

In this study, we have used ultraviolet resonance Raman (UVRR) spectroscopy to identify structural changes associated with the assembly of the iron cluster in the *E. coli* β2 subunit and with the reduction of the tyrosyl radical. Use of UV probe wavelengths enhances spectral contributions from histidine, tyrosine, and tryptophan side chains and allows structural changes in aromatic amino acids to be directly monitored.[22-30] The resonance Raman vibrational spectrum is sensitive to changes in protonation state, hydrogen bonding, and electrostatics. Difference UVRR spectroscopy allows a focus on

the structural changes of interest. Our data provide the first spectroscopic evidence for histidine protonation upon iron removal. With metal cluster assembly, significant differences are also induced in the structure and/or local environment of tyrosine and tryptophan residues. These experiments give new information concerning conformational changes, which are coupled with metal binding in RNR.

7.3 Materials and Methods

7.3.1 Materials

L-Tyrosine, L-tryptophan, L-histidine, L-phenylalanine, succinic acid, HEPES: 4-(2-Hydroxyethyl)piperazine-1-ethanesulfonic acid, boric acid, lithium hydroxide, 8-hydroxyquinoline-5-sulfonic acid, sodium hydroxide and hydrochloric acid were obtained from Sigma (St. Louis, MO). Deuterium oxide, $^{2}H_2O$ (98%), and $^{15}N_3$ L-histidine:HCl:H_2O (98%) were purchased from Cambridge Isotope Laboratories (Andover, MA). Hydroxyurea was obtained from Calbiochem (San Diego, CA).

7.3.2 *E. coli* β2 Overexpression, Purification, and ^{15}N Histidine Labeling

Escherichia coli wild-type β2 protein was overexpressed and purified (Figure 7.3, black line) from *E. coli* BL21(DE3) cells transformed with pTB2, using protocols previously described.[18,31] The resulting yield was 60 - 120 mg protein per liter. Met-β2, the form of the protein with a reduced tyrosyl radical and an oxidized diiron cluster (Figure 7.3, blue line), was prepared by incubating with and subsequently removing hydroxyurea as described.[18] The iron-free form of the protein (Apo-β2; Figure 7.3, red

line) was generated by dialyzing Met-β2 (2 mL, 100 μM) against an iron chelator, lithium 8-hydroxyquinoline-6-sulfonate (400 mL), as described.[11,32] The chelator was removed by dialysis against 50 mM Tris-HCl, 5% glycerol, pH 7.6 and subsequent chromatography on a desalting Sephadex G25 column. The ferrozine method of iron quantitation showed that at least 92% of the iron was removed by this treatment in the natural abundance sample. All protein samples were exchanged into 5 mM HEPES, NaOL, pL 7.6 through four sequential concentration and dilution steps using an Amicon (Beverly, MA) YM30 concentrator.

^{15}N histidine labeling was accomplished by overexpressing and purifying β2 from the histidine auxotroph, AW608Thr(DE3)/pTB2 (Figure 7.2).

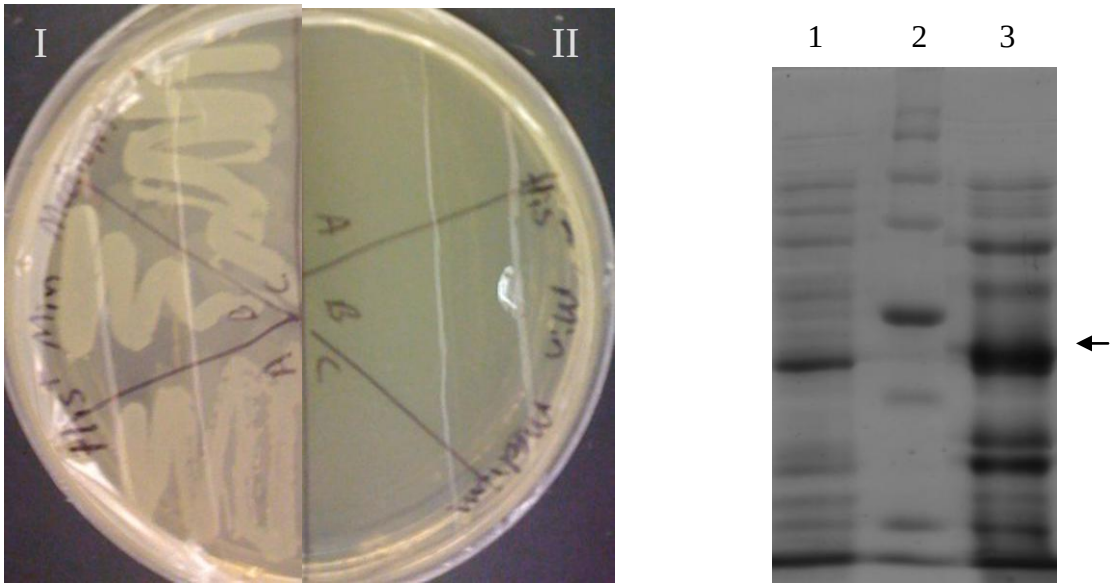

Figure 7.2. Characterization of *E. coli* histidine auxotroph, AW608Thr. *Left*: AW608Thr cells plated on minimal media in the presence (I) and absence (II) of histidine. The letters A, B, and C designate three single colonies. *Right*: SDS-PAGE of natural abundance β2 expression from AW608Thr(DE3)/pTB2 cells. Lane 1 is pre-induction with IPTG, lane 2 is molecular markers (MW: 250, 150, 100, 75, **50**, 37, and 25 kDa), and lane 3 is post-induction with IPTG. The arrow represents the expected migration of β2 (monomer size: 43.5 kDa)

E. coli AW608Thr cells were lysogenized with λDE3 using a kit from Novagen (Madison, WI) to incorporate the T7 gene. The minimal media used for incorporation of $^{15}N_3$ histidine was the same as described previously,[33] except 135 mg/L of labeled histidine was supplemented. The resulting yield was about 50 mg protein per liter. Using this method, incorporation of ^{15}N into histidine has been confirmed previously by NMR spectroscopy.[34,35]

7.3.3 UV-Visible Spectroscopy

Absorption spectra of the purified *E. coli* β2 protein were collected at room temperature on a Hitachi U-3000 spectrophotometer in 1 cm quartz cuvettes. The concentrations of the control, Met-β2, and Apo-β2 forms (Figure 7.3A) were determined using the $A_{280\ nm}$ and ε = 131, 131, and 120 $mM^{-1}\ cm^{-1}$, respectively. The Y• yield for the control β2 protein was determined as previously described.[36] In the natural abundance preparation, quantitation yielded 1.1 – 1.4 Y• per dimer. In the $^{15}N_3$ histidine preparations, quantitation yielded 0.7 Y• per dimer.

7.3.4 UV Raman experiments

UVRR spectra at 229 nm were recorded at room temperature using a Raman microscope system (Renishaw inVia, Hoffman Estates, IL) and 8 cm^{-1} spectral resolution.[37,38] The 250 μW, 229 nm probe beam was generated from a frequency-doubled Ar ion laser (Cambridge LEXEL 95, Fremont, CA). Samples were recirculated through a jet nozzle with a 0.12 mm diameter to prevent UV damage. Control experiments at 400 μW UV probe power showed no significant alterations in the UVRR

difference spectrum, Apo-β2-minus-Met-β2, supporting the conclusion that the samples were undamaged by the lower power, 250 μW UV probe beam. Protein samples were prepared at 50 μM concentrations and were exchanged into 5 mM HEPES, NaOL, pL 7.6 (p^2H reported as the uncorrected meter reading[39]) prior to UVRR measurements. To generate Raman difference spectra (Figure 7.9), UVRR data, recorded on the same day (Figure 7.4), were subtracted and averaged. The background signal of the buffer was adopted as an internal intensity standard in this subtraction. Amino acid samples were prepared at 1 (tyrosine and tryptophan) or 20 (histidine and phenylalanine) mM concentrations in 5 mM HEPES (pL 7.5; Y, W, F, H), borate (pL 11.0; Y, H) or succinate (pL 4.0; H).

7.4 Results

7.4.1 UV absorption spectra of β2

In Figure 7.3, we present the UV visible absorption spectra of control, Met-β2 and Apo-β2 samples, which are similar to previous reports.[11,40] The control β2 absorbance spectrum (Figures 7.3A and B, black line) is defined by characteristic peaks at 325, 370, 390 and 410 nm. The μ-oxo bridged iron cluster contributes to the shoulder at 325 and the band at 370 nm.[11,41,42] The tyrosyl radical (Y122•) displays a characteristic sharp 410 nm band with a weak, broad 390 nm shoulder.[42,43] The Met-β2 state of the protein lacks the stable tyrosyl radical and therefore does not exhibit the 410 nm band (Figures 7.3A and B, blue line). When iron is removed, there is complete loss of spectral features over 300 nm, as expected for Apo-β2 (Figures 7.3A and B, red line).

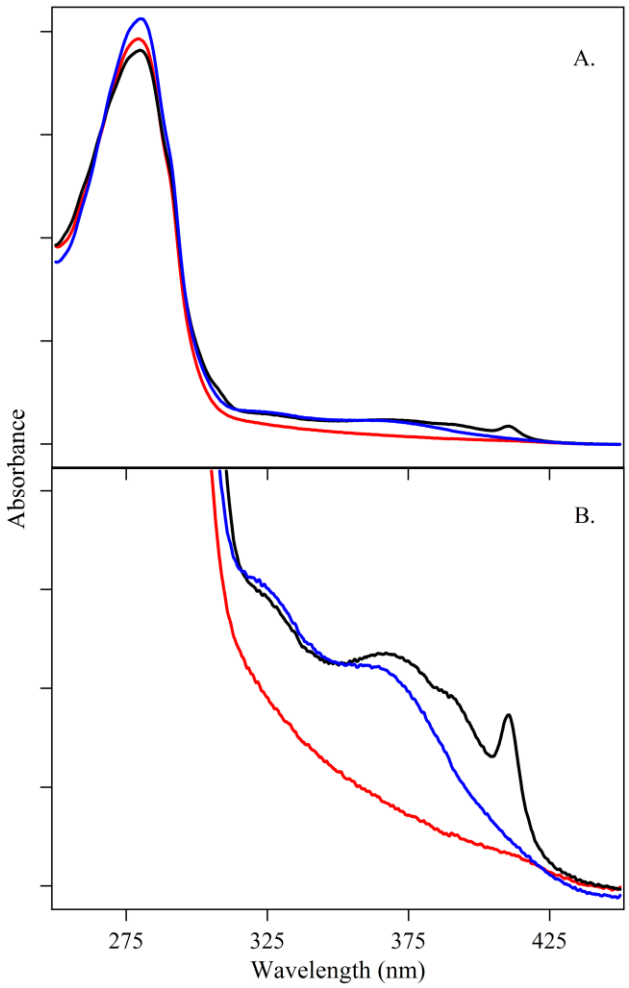

Figure 7.3. Room temperature UV-Visible absorbance spectra of *E. coli* β2 samples. In both panels, the black line represents control β2, the blue line represents Met-β2, and the red line represents Apo-β2. The samples were prepared at 7.5 μM in 5 mM HEPES, p^1H 7.6. The spectra in panel (B) are multiplied by a factor of 10. The *y*-axis tick marks represent 2.5 x 10^{-1} absorbance units.

7.4.2 UVRR Spectra of β2

In Figure 7.3, we present the UVRR spectra of the control (Figure 7.4A), Met-β2 (Figure 7.4B), and Apo-β2 (Figure 7.4C) samples. The spectra were acquired with 229 nm excitation and at room temperature on a flowing sample. Overall, the UVRR spectra of the control, Met-β2, and Apo-β2 forms are similar (Figure 7.4). At 229 nm excitation,

the vibrational bands of tryptophan and tyrosine are expected to be resonantly enhanced due to the overlap of the Raman probe with the B_b and L_a electronic transitions,[44-47] respectively. Histidine and phenylalanine have weaker Raman signals at this excitation wavelength due to their π_1-π_1* (histidine) and L_a (phenylanine) electronic transitions at ~207 nm.[22,45] To investigate the origin of the observed frequencies in the β2 subunit spectra (Figure 7.4), model compound UVRR data were acquired from tyrosine (Figure 7.5), tryptophan (Figure 7.6), phenylalanine (Figure 7.7), and histidine (Figure 7.8).

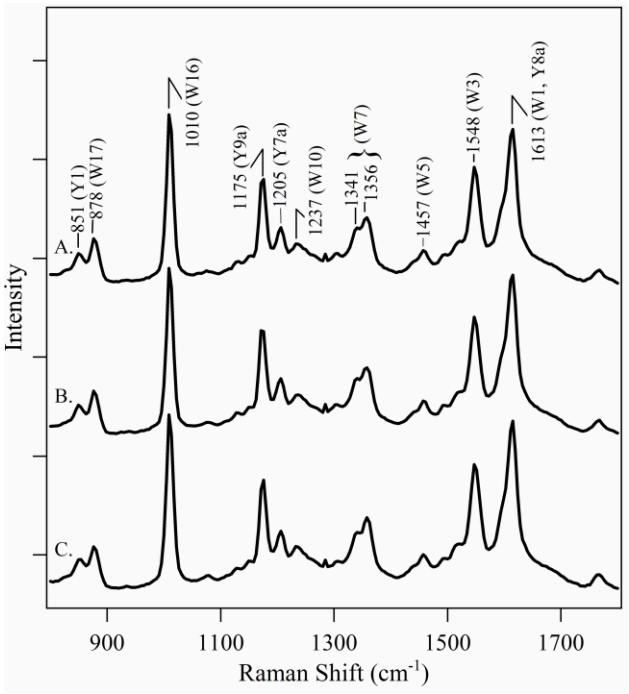

Figure 7.4. UVRR spectra of *E. coli* β2 collected with a 250 μW, 229 nm beam for a 21 min exposure time. The data were collected from control (A), Met-β2 (B), and Apo-β2 (C) samples. The protein concentrations were 50 μM in 5 mM HEPES, p^{1}H 7.6. The spectra are representative data recorded from one sample. The *y*-axis tick marks represent 1 x 10^4 intensity units.

7.4.4 Model Compound Data: Tyrosine and Tyrosinate

In Figure 7.5, we present the UVRR spectra of tyrosine acquired in ^1H_2O buffers (blue) at p^{1}H 7.5 (panel A) and p^{1}H 11 (panel B) and in ^2H_2O buffers (green) at p^{2}H 7.5 (panel A) and p^{2}H 11 (panel B). In Figure 7.5A (p^{1}H 7.5, blue), the 1614 and 1600 cm^{-1} bands are assigned to the symmetric Y8a and to asymmetric Y8b ring stretching modes of protonated tyrosine in ^1H_2O (Table 7.1). The Y8b mode shifts to 1589 cm^{-1} with ^{2}H-exchange (see Figure 7.5 inset). The Y7a' CO vibrational mode, expected at ~1250 cm^{-1}, is not well resolved in the UVRR spectra with 229 nm excitation.[25] The 1208 cm^{-1} band in Figure 6.5A is assigned to the Y7a C_{ring}–CH_2 stretch of Tyr.[45] The 1179 cm^{-1} band in Figure 7.5A is attributed to the Y9a CH bending mode. The 822/849 cm^{-1} doublet for tyrosine is assigned to a Fermi resonance between the overtone Y16 (CH bending) band and the υ1 (ring breathing) mode. The 822 cm^{-1} feature shifts to 814 cm^{-1} when exchanged into ^2H_2O (Figure 7.5A, green line).

In tyrosinate, the Y8a and Y8b ring stretching modes downshift to 1606 and 1555 cm^{-1} (Figure 7.5B), respectively, with the loss of the phenolic proton. The 1208 cm^{-1} C_{ring}–CH_2 mode is unaffected by the deprotonation of tyrosine; the Y9a mode is shifted from 1179 cm^{-1} (tyrosine) to 1176 cm^{-1} (tyrosinate). The Y1 band (849 cm^{-1}) is not perturbed by the protonation state of tyrosine. However, the 2×Y16 feature is shifted to 827 cm^{-1} for tyrosinate and is the only tyrosinate feature sensitive to ^{2}H-exchange (Δ = -13 cm^{-1}, Figure 7.5B, compare blue and green).

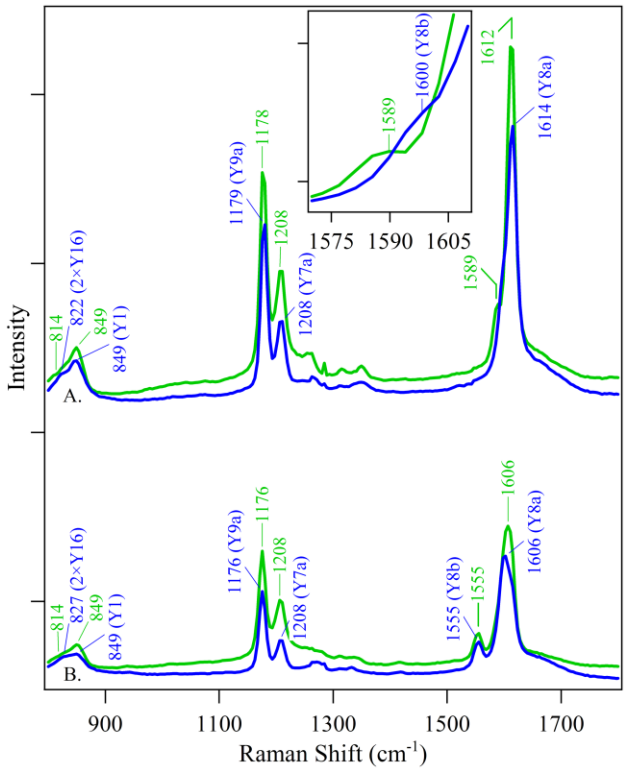

Figure 7.5. UVRR spectra of 1 mM tyrosine collected with a 250 μW, 229 nm beam for a 21 min exposure time. The tyrosine was dissolved in (A) 5 mM HEPES, pL 7.5 or (B) 5 mM borate, pL 11.0. The *inset* is the expansion of the 1570 – 1610 cm^{-1} region of (A) to highlight the Y8b mode. The spectra in blue were collected in $^{1}H_2O$, and the spectra in green were collected in $^{2}H_2O$ at the corresponding pL. The spectra are averages of data obtained from 3 separate samples. The *y*-axis tick marks represent 1 x 10^4 intensity units.

7.4.5 Model Compound Data: Tryptophan

In Figure 7.6, we present the UVRR spectra of tryptophan acquired in $^{1}H_2O$ buffers (blue) and in $^{2}H_2O$ buffers (green) at pL 7.5 (Table 6.1). In Figure 7.6, the 1618 cm^{-1} band is assigned to the W1 phenyl ring mode, analogous to the benzene-derived υ8a mode.[23] Excitation profiles for tryptophan show that the W2 mode (υ8b-like), expected at 1575 cm^{-1}, is not well resolved with 229 nm excitation.[48] This band is not observed in Figure 7.6. The 1550 cm^{-1} band is assigned to the W3 pyrrole ring stretching mode. The weak 1460 cm^{-1} feature arises from the tryptophan W5 mode. The Fermi W7 doublet at

1343/1360 cm^{-1} is composed of a fundamental and an out-of-plane combination band.[49] This doublet sharpens at ~1360 cm^{-1} with increasing hydrophobicity. An increase in intensity is observed for this band with ^{2}H-exchange (Figure 6.6, green). The pronounced 1011 cm^{-1} (W16) band is attributed to an out of phase benzene and pyrrole ring breathing mode.[50] The 880 cm^{-1} tryptophan band (W17) is an indole vibration with a large contributing NH pyrrole bending motion, which results in sensitivity to H-bonding.[51] A downshift to 862 cm^{-1} is observed in $^{2}H_2O$ (Figure 7.6, green). In addition to the ^{2}H-sensitivity of the W17 mode, the intensities of the W3, W7, W16, and W18 bands increase in $^{2}H_2O$ (Figure 7.6, green).

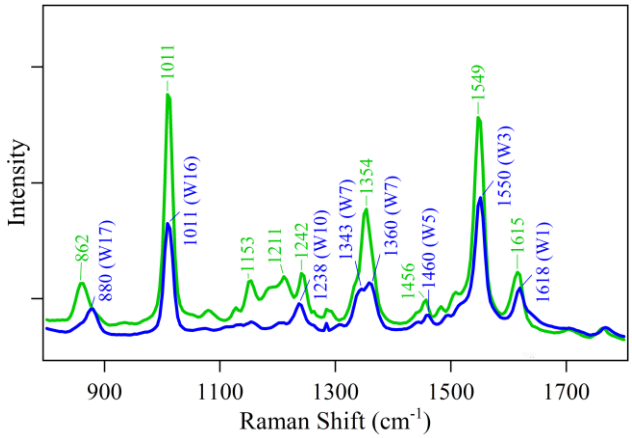

Figure 7.6. UVRR spectra of 1 mM tryptophan collected with a 250 μW, 229 nm beam for a 21 min exposure time. The tryptophan was dissolved in 5 mM HEPES, pL 7.5. The spectrum in blue was collected in $^{1}H_2O$, and the spectrum in green was collected in $^{2}H_2O$. The spectra are averages of data obtained from 3 separate samples. The *y*-axis tick marks represent 1 x 10^{4} intensity units.

7.4.6 Model Compound Data: Phenylalanine

In Figure 7.7, we present the UVRR spectrum of phenylalanine. The ring vibrations of phenylalanine (Figure 7.7) include the symmetric F8a mode at 1603 cm^{-1}

and the asymmetric F8b mode (shoulder at ~1585 cm^{-1}). The 1206 cm^{-1} feature is assigned to the symmetric C_{ring}–CH_2 (υ13) stretching vibrational mode.[45] The F9a mode of phenylalanine is observed at 1184 cm^{-1} in Figure 7.7. The ring breathing mode, F12, of phenylalanine is assigned to the 1003 cm^{-1} band.[52] The shoulder at 1032 cm^{-1} corresponds to the F18a mode.[45] The phenylalanine F8a ring stretch contribution at 1603 cm^{-1} (Figure 7.7) overlaps with the tyrosine Y8b (Figure 7.5; ~1600 cm^{-1}) ring vibrational mode. This F8a mode is among the most intense spectral features derived from phenylalanine at this Raman excitation wavelength (see Figure 7.7). However, in these 229 nm probe spectra, the υ8a scattering ratio is ~34 for tyrosine (Figure 7.5A, blue) compared to phenylalanine (Figure 7.7), similar to previous reports.[48] Therefore, phenylalanine is expected to make minimal contribution to the UVRR spectra (Figure 7.4) and to the difference UVRR spectra (Figure 7.9) of the β2 subunit.

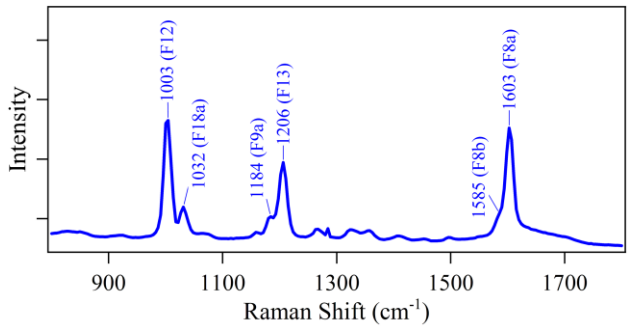

Figure 7.7. UVRR spectrum of 20 mM phenylalanine collected with a 250 μW, 229 nm beam for a 21 min exposure time. The phenylalanine was dissolved in 5 mM HEPES, p^1H 7.5. The spectrum is an average of data obtained from 3 separate samples. The *y*-axis tick marks represent 5 x 10^3 intensity units.

7.4.6 Model Compound Data: Histidine

In Figure 7.8, we present the UVRR spectra of histidine in $^{1}H_2O$ (blue) and $^{2}H_2O$ (green) buffers and at pL 4.0 (panel A), pL 7.5 (panel B) and pL 11.0 (panel C). Extensive pH dependence is observed (Table 7.1), as previously described.[53,54]

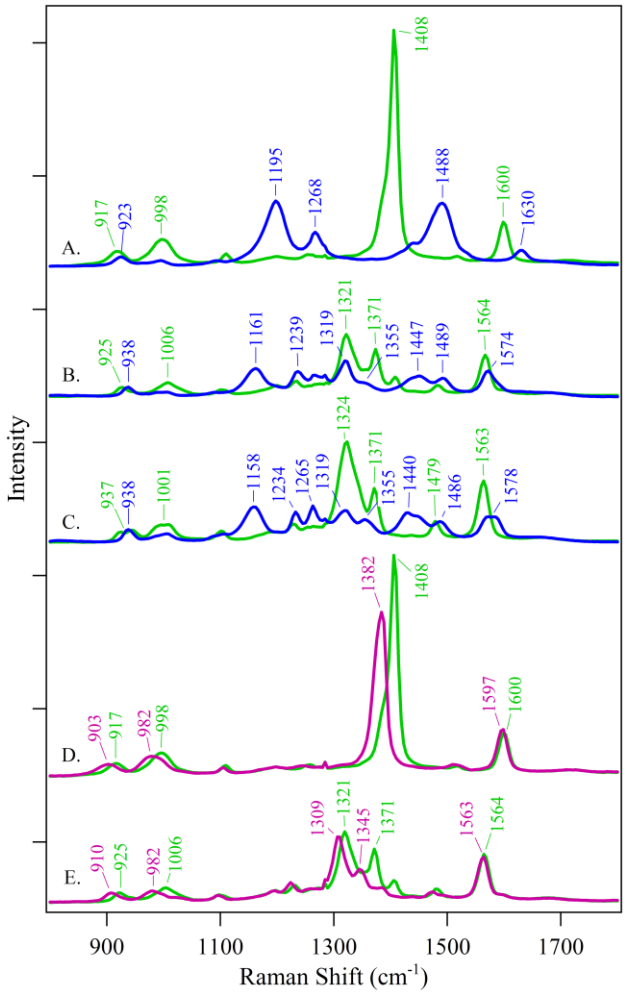

Figure 7.8. UVRR spectrum of 20 mM histidine collected with a 250 μW, 229 nm beam for a 21 min exposure time. The histidine was dissolved in (A) 5 mM succinate, pL 4.0, (B) 5 mM HEPES, pL 7.5, or (C) 5 mM borate, pL 11.0. The spectra in blue were collected in $^{1}H_2O$, and the spectra in green were collected in $^{2}H_2O$ at the corresponding pL. In D and E, the effects of ^{15}N labeling in 5 mM succinate, p^{2}H 4.0 (D) and in 5 mM HEPES, p^{2}H 7.5 (E) are shown. Data in green were acquired from natural abundance histidine; data in pink were acquired from $^{15}N_3$ labeled histidine. The spectra are averages of data obtained from 3 separate samples. The *y*-axis tick marks represent 4 x 10^4 intensity units.

The UVRR data for protonated histidine in ^1H_2O solution (Figure 7.8A, pL 4.0, blue line) exhibits 5 bands at 1630 (υC=C + υC=N), 1488 (δN–H), 1268 (δ=C–HN), 1195 (υNτ–C_2–Nπ + δN–H), and 923 (δC–H) cm^{-1}. The UVRR data for deprotonated histidine in ^1H_2O (Figures 7.8B and C, blue lines) are more complex. At p^{1}H 7.5, the bands are 1574 (υC=C), 1489 (δN-H), 1447 (δCH_2), 1355 (shoulder; υC=N + υC–C(Nπ)), 1319 (υC=N + υC–N(Nτ)), 1239 (δ=C–H + υ=C–N), 1161 (υ=C–N + δN–H), and 938 (δ ring) cm^{-1}. At p^{1}H 11, the pattern is similar with bands at 1578 (υC=C + υC=N(Nπ); υC=C + δN-H(Nτ)), 1486 (δN-H), 1440 (δCH_2), 1355 (υC=N + υC–C(Nπ)), 1319 (υC=N + υC–N(Nτ)), 1265 (δ=C–H(Nπ)), 1234 (δ=C–H + υ=C–N), 1158 (υ=C–N + δN–H), and 938 (δ ring) cm^{-1}.

For deprotonated histidine in ^2H_2O (Figures 7.8B and C, green), the intensities of the 1321, 1371, and 1564 cm^{-1} peaks increase. For protonated histidine in ^2H_2O (Figure 7.8A, green), there is a predominant 1408 cm^{-1} peak arising from the υ(Nτ–C_2–Nπ) mode.[22,55-57] The 1408 cm^{-1} band provides a structural marker for protonated histidine in exchanged proteins.

7.4.7 UVRR Difference Spectra

Based on the model compound data discussed above, we conclude that the UVRR spectra of the β2 samples (Figure 7.4) are dominated by vibrational modes from tyrosine and tryptophan. The assignments of the bands are summarized as labels in Figure 7.4.

In Figure 7.9, we present difference UVRR spectra for the control, Met-β2, and Apo-β2 samples. The difference spectra were constructed by subtraction of data,

recorded on the same day and using an internal standard, as described in the Materials and Methods section.

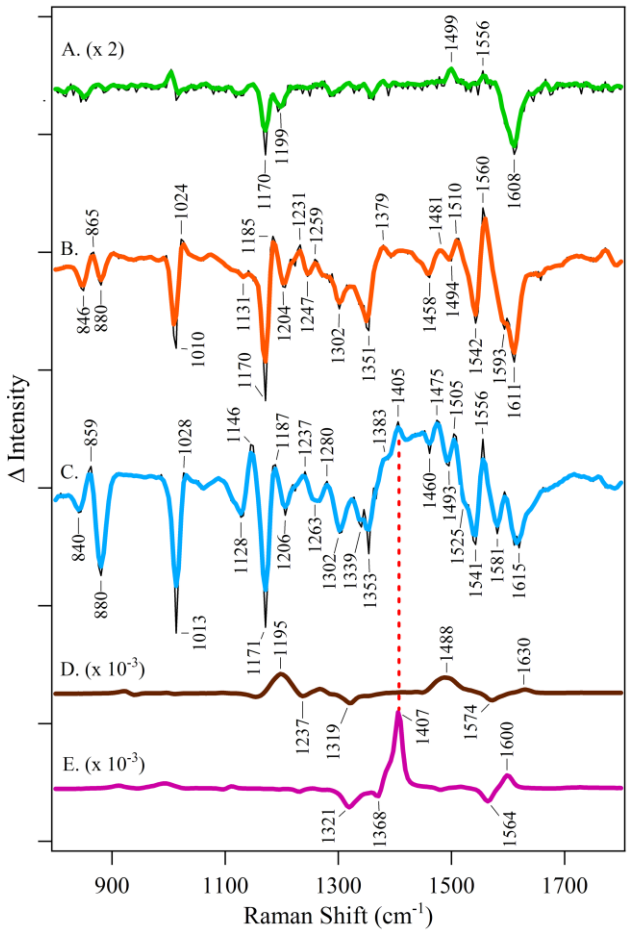

Figure 7.9. UVRR difference spectra of *E. coli* β2 samples. The data are control-minus-Met-β2 in 5 mM HEPES, p^{1}H 7.6 (A), Apo-β2-minus-Met-β2 in 5 mM HEPES, p^{1}H 7.6 (B), Apo-β2-minus-Met-β2 in 5 mM HEPES, p^{2}H 7.6 (C). (D) and (E) show the protonation spectrum of histidine in ^1H_2O and ^2H_2O, respectively, and correspond to a subtraction of p^{1}H 4-minus-p^{1}H 7.5 and p^{2}H 4-minus-p^{2}H 7.5 in Figure 7.8. The spectrum in (A) was multiplied by 2 and the spectra in (D) and (E) have been multiplied by 10^{-3} for comparison. The green, orange, and light blue lines correspond to a three adjacent point smoothing fit to the raw (thin black line) data.[38] The spectra are averages of data obtained from (A) 10, (B) 10, (C) 10, (D) 3, and (E) 3 samples. The protein concentrations were 50 μM, and the histidine concentration was 20 mM. The *y*-axis tick marks represent 1 x 10^3 intensity units.

In these difference spectra, observed spectral features correspond to vibrational bands that are perturbed by tyrosyl radical reduction (Met-β2 samples) (Figure 7.9A) or by iron cluster removal (Apo-β2 samples) (Figures 7.9B and C). Use of difference spectroscopy allows focus on spectral perturbations induced by reduction of the radical or by iron cluster assembly, respectively. Data in Figures 7.9A and B were acquired in $^{1}H_2O$ buffer; data in Figure 7.9C were acquired in $^{2}H_2O$ buffer. Figures 7.9D and E present model compound difference spectra, constructed from data associated with the protonation of histidine in $^{1}H_2O$ (Figure 7.9D) or $^{2}H_2O$ (Figure 7.9E) buffers. These difference spectra were constructed by a direct one to one subtraction of the data in Figure 7.8.

7.4.8 Spectral changes induced by Y122• reduction, relative to a control sample

In the control-minus-Met-β2 difference spectrum (Figure 7.9A), unique Y122• contributions are positive bands, while unique Y122 contributions are negative bands. Oxidation of the tyrosine is expected to perturb CO stretching and aromatic ring stretching vibrations.[58-61] Both tyrosine and tyrosyl radical are resonantly enhanced with 229 nm excitation, because tyrosyl radical reduction shifts the L_a electronic transition from ~240 to 220 nm.[62] A previous UV Raman study of the tyrosyl radical *in vitro* assigned the Y7a CO stretching mode at 1510 cm^{-1} and the υ8a ring stretching mode at 1565 cm^{-1}.[59] A previous infrared study of the tyrosyl radical *in vitro* assigned the Y7a CO stretching mode at 1516 cm^{-1} and the Y8a ring stretching mode at 1554 cm^{-1}.[61,63]

In Figure 7.9A, the positive 1499 cm^{-1} feature is assigned to the Y7a mode of Y122•. This assignment is supported by previous visible Raman[64] and FT-IR[18] studies of

RNR. In the FT-IR study, isotopic labeling of tyrosine was used to assign the Y7a band.[18] The 1499 cm^{-1} frequency is significantly downshifted compared to the CO frequency observed in model compounds and is upshifted from some of the reported frequencies for the photosystem II tyrosyl radicals.[65,66] Therefore, this CO frequency is diagnostic for the production of Y122•. In Figure 7.9A, a weak positive band at 1556 cm^{-1} is assigned to the ring stretching (Y8a) vibration of Y122•.[61,63]

The control-minus-Met-β2 difference spectrum (Figure 7.9A) also exhibits negative bands at 1608, 1199, and 1170 cm^{-1}, which we assign to the reduced tyrosine, Y122. The 1608 cm^{-1} band is assigned to the Y8a mode. While tryptophan (W1 at 1618 cm^{-1}) and phenylalanine (F8a at 1602 cm^{-1}) may also make a contribution at 1608 cm^{-1}, phenylalanine has minimal resonance enhancement,[48] and the tryptophan W1 band is also weak with 229 nm Raman excitation. Y122 is protonated in the reduced state, and either hydrogen bonded weakly to D84[17] or not hydrogen bonded.[2] The observed 1608 cm^{-1} frequency is between the frequency expected for a protonated (1614 cm^{-1}) and a deprotonated (1606 cm^{-1}) tyrosine. The Y8a and Y8b modes of tyrosine are not strongly influenced by hydrogen bonding.[25] The frequency of this band may be influenced by Stark effects, induced by the presence of the metal cluster.[67] The Y8b asymmetric mode (~1600 cm^{-1}; Figure 7.5A inset) overlaps with the Y8a band and is thus not resolvable in Figure 7.9A.

In Figure 7.9A, we assign the 1199 and 1170 cm^{-1} bands to tyrosine C_{ring}-CH_2- (Y7a) and CH bending (Y9a) deformation modes of Y122, respectively. The Y9a frequency for a protonated tyrosine is expected at approximately 1179 cm^{-1} (Figure 7.5). Frequency shifts are not related to hydrogen bonding, but Y9a may downshift to 1170

cm^{-1} as the Y–OH hydrogen swings to an out-of-plane configuration.[25] An out-of-plane configuration is consistent with the X-ray structure of Met-β2 that assigns Y122 and D84 as hydrogen bonding partners.[17]

The Y7a C_{ring}-CH_2- stretch of tyrosine acts as a hydrogen bond sensor in proteins, because the mode has a ∂COH component. For model tyrosine in solution, this band is observed at ~1210 cm^{-1} in non-hydrogen bonding or for proton accepting, hydrogen bonded tyrosine and at ~1205 cm^{-1} in proton donating, hydrogen bonded tyrosine.[25] In Figure 7.9A, this band is observed at 1199 cm^{-1}, suggesting that the Y122 forms a hydrogen bond in the Met-β2 state. This observation is consistent with the high-resolution X-ray structure {17 but see ref 2}.

The intensity of the Y9a tyrosine feature band at 1170 cm^{-1} is approximately 10,000 counts in the control β2 UVRR spectrum (Figure 7.4A). The signal shown in Figure 7.9A is multiplied by 2 for comparison purposes. After correction for this, the intensity of the Y9a band in the control-minus-Met-β2 difference spectrum (Figure 7.9A) is approximately 320 counts. Because there are 32 tyrosine residues in the β2 dimer,[68] we conclude that ~1 tyrosine residue contributes to the control-minus-Met-β2 difference spectrum in Figure 7.9A. This result is consistent with an assignment of this band to Y122. Our UV-Vis spectrophotometric characterization of the natural abundance β2 preparation gave a yield of 1.1 – 1.4 Y• per dimer. This experiment supports the conclusion that difference UV Raman spectroscopy can be used to monitor redox changes at Y122 in the β2 subunit. The spectrum is dominated by the bands associated with tyrosyl radical reduction, with little perturbation to other aromatic amino acid residues.

7.4.9 Spectral changes induced by iron cluster removal, relative to a Met-β2 sample: perturbations of tryptophan

The Apo-β2-minus-Met-β2 difference spectrum (Figure 7.9B) displays spectral alterations due to iron cluster assembly. No significant contribution from Y122• reduction will be observed, because the tyrosyl radical is reduced under both sets of conditions. In Figure 7.9B and C, we present the Apo-β2-minus-Met-β2 difference spectra acquired in $^{1}H_2O$ and in $^{2}H_2O$ buffer, respectively. As expected, significant differences are observed when compared to the control-minus-Met-β2 data (Figure 7.9A). Assignments are summarized in Table 7.1.

Comparison of the model compound data in Figures 7.5–7.8 to Figure 7.9B supports the assignment of bands at 880 (-)/865 (+)/846 (-) and 1010 (-)/1024 (+) cm^{-1} to the W17 and W16 bands of tryptophan, respectively (Figure 7.9B and Table 7.1). As expected, $^{2}H_2O$ solvent isotope effects are observed for these spectral features (Figure 7.6). Negative bands at 1351 (-), 1542 (-), and 1611 (-) cm^{-1} in Figure 6.9B are also assignable to tryptophan, with possible overlapping contributions from tyrosine for the 1611 and 1542 cm^{-1} bands. In Figure 7.9C, bands at 1128 (-) and 1146 (+) cm^{-1} are attributed to ^{2}H exchanged tryptophan, based on comparison to the model compound spectra in $^{2}H_2O$ (Figure 7.6).

There are 14 tryptophan residues in the β2 dimer (7 residues in each monomer).[68] The total intensity of the W16 band (~1010 cm^{-1}) in Figure 7.4 is approximately 17,000 counts. The intensity of the 1010 cm^{-1} W16 band in the Apo-β2-minus-Met-β2 difference is approximately 700 counts. This analysis suggests that at least one tryptophan residue is perturbed and contributes to the difference spectrum (Figures 7.9B and C).

Table 7.1. Assignments for Selected Vibrational Bands in the Apo-β2-minus-Met-β2 Difference Spectrum and in Model Compound Data

A. Tyrosine Modes

E. coli β2[a] υ (cm^{-1})		Assignment[b]	Model data, pL 7.5[c] υ (cm^{-1})	
{^1H_2O}	{^2H_2O}		{^1H_2O}	{^2H_2O}
(-) 1611	(-) 1615	Y8a (8a ring stretch)	1614	1612
(-) 1593	(-) 1581	Y8b (8b ring stretch)	1600	1589
(-) 1204	(-) 1206	Y7a (C-CH_3)	1208	1208
(-) 1170/ (+)1185	(-) 1171/ (+)1187	Y9a (CH deform)	1179	1176

B. Tryptophan Modes

E. coli β2[a] υ (cm^{-1})		Assignment[b]	Model data, pL 7.5[c] υ (cm^{-1})	
{^1H_2O}	{^2H_2O}		{^1H_2O}	{^2H_2O}
(-) 1611	(-) 1615	W1 (benzene ring stretch)	1618	1615
(+) 1560/ (-) 1542	(+) 1556/ (-) 1541	W3 (pyrrole ring stretch)	1550	1549
(-) 1458	(-) 1460	W5 (19a ring stretch)	1460	1456
(+) 1024/ (-) 1010	(+) 1028/ (-) 1013	W16 (benzene ring breath)	1011	1011
(-) 880/ (+) 865/ (-) 846	(-) 880/ (+) 859/ (-) 840	W17 (indole/NH bend)	880	862

C. Histidine Modes

E. coli β2[a] υ (cm^{-1})		Assignment[b]	Model data, pL 4.0[c] υ (cm^{-1})	
{^1H_2O}	{^2H_2O}		{^1H_2O}	{^2H_2O}
N.O.[d]	(+) 1405	υ(Nτ–C_2–Nπ)	N.O.[d]	1408

[a] The Apo-β2-minus-Met-β2 UVRR difference spectra can be found in Figure 7.9B (^1H_2O) and 7.9C (^2H_2O). [b]Assignment based on previous studies for Tyr, Trp, and His.[22,23,44-46,53,55,56,59,61,63,69] [c]UVRR spectra for Tyr, Trp, and His can be found in Figures 7.5, 7.6, and 7.8, respectively. [d]Not observed.

The 880 cm^{-1} W17 tryptophan Raman band is expected to downshift ~20 cm^{-1} with ^{2}H exchange.[51] In agreement, our model compound results (Figure 7.6) show an 18 cm^{-1} downshift on exchange. However, only a moderate shift of 0-6 cm^{-1} is observed for the W17 bands in the Apo-β2-minus-Met-β2 difference spectrum (Figure 7.9C). This result suggests that the ^{2}H exchange rate of the perturbed tryptophan is slow.[70] However, the intensity increases in other bands with ^{2}H exchange (Figure 7.9C) are consistent with the scattering increases observed for exchanged tryptophan in solution (see Figure 7.6 for comparison). This phenomenon is not observed in the tyrosine model data (Figure 7.5) and is diagnostic of exchanged tryptophan.

It should be noted that these spectra are not consistent with the generation of a tryptophan radical under these conditions.[59,69,71,72] Removing an electron or hydrogen atom from the tryptophan side chain significantly alters vibrational frequencies from the indole ring, due to changes in CC and CN bond distances.[69,72] In the neutral tryptophan radical, a 200 cm^{-1} downshift of the W3 band has been reported.[72] A 100 cm^{-1} downshift of the W3 mode had been calculated for the tryptophan cation radical.[69] Shifts of the W1, W5, W16, and W17 modes are also expected. For example, the W1, W16, and W17 modes downshifted 26, 17 and 4 cm^{-1}, respectively, in the neutral tryptophan radical.[72]

7.4.10 Spectral changes induced by iron cluster removal, relative to a Met-β2 sample: perturbations of tyrosine

Bands at 1542 (-) and 1611 (-) cm^{-1} in Figure 7.9B may have overlapping contributions from tyrosine. Supporting the assignment to tyrosine, the negative 1593 cm^{-1} Y8b mode (Figure 7.9B) shifts to 1581 cm^{-1} with ^{2}H-exchange (Figure 7.9C). Similar behavior for Y8b is observed for tyrosine in solution (Figure 7.5A and inset).[73]

Bands at 1170 (-) and 1185 (+) in Figure 6.9B are assignable to a tyrosine perturbation (Table 7.1). In addition, a negative band at 1204 cm^{-1} also may contain a contribution from tyrosine. The intensity of the Y9a tyrosine feature at 1170 cm^{-1} (Figure 7.9B) corresponds to approximately 7% of the total tyrosine signal, observed in control β2 (Figure 7.4). Because dimeric β2 contains 32 tyrosine residues,[68] this result suggests that two tyrosine residues contribute to the tyrosine signal changes observed in Figure 7.9B. These two tyrosines may be Y122 (in chain A and B), which are located within 6 Å of the iron cluster. The 1204 cm^{-1} frequency for tyrosine Y7a in Figure 7.9B is different from the 1199 cm^{-1} frequency observed in the control-minus-Met-β2 spectrum (Figure 7.9A). This may be due to an overlapping spectral perturbation from the positive band at 1185 cm^{-1} in Figure 7.9B. Observation of a tyrosine Y7a band at 1204 cm^{-1} supports the conclusion that the perturbed tyrosine residue(s) is hydrogen bonded in the Met-β2 state.[17]

7.4.11 Spectral changes induced by iron cluster removal, relative to a Met-β2 sample: perturbations of histidine

With ^2H exchange of protonated histidine in solution, the $\upsilon(N\tau\text{-}C_2\text{-}N\pi)$ symmetric stretch intensifies and shifts to 1408 cm^{-1} (Figure 7.8A, green and references 22, 55, 56). Figure 7.9D and E are difference spectra, associated with the protonation of histidine *in vitro*. A 1407 cm^{-1} band dominates the difference spectrum acquired in ^2H_2O buffer (Figure 7.9E), but is not observed in ^1H_2O buffer (Figure 7.9D). Similarly, a 1405 cm^{-1} band is observed in the ^2H exchanged Apo-β2-minus-Met-β2 difference spectrum (Figure 7.9C, Table 7.1), but not in ^1H_2O buffer (Figure 7.9B). This observation provides evidence for protonation of histidine with metal cluster removal from the β2 subunit.

To confirm this interpretation, the β2 subunit was labeled with $^{15}N_3$ histidine (Figure 7.10B) and compared to a natural abundance sample (Figure 7.10A). As shown in Figure 7.8D for histidine *in vitro*, ^{15}N labeling of histidine results in a 26 cm^{-1} downshift of the 1408 cm^{-1} band. This downshift is expected from previous studies.[74] Figures 7.10A and B show a similar downshift (1405 (+) to 1381 (+) cm^{-1}) in the $^{15}N_3$ histidine labeled Apo-β2-minus-Met-β2 spectrum. We conclude that histidine ligands protonate when the iron is removed from the β2 subunit. The other vibrational bands of histidine are not observed, because these bands are not as intense as the 1408 cm^{-1} band and are less sensitive to $^{15}N_3$ labeling (Figure 7.8D).

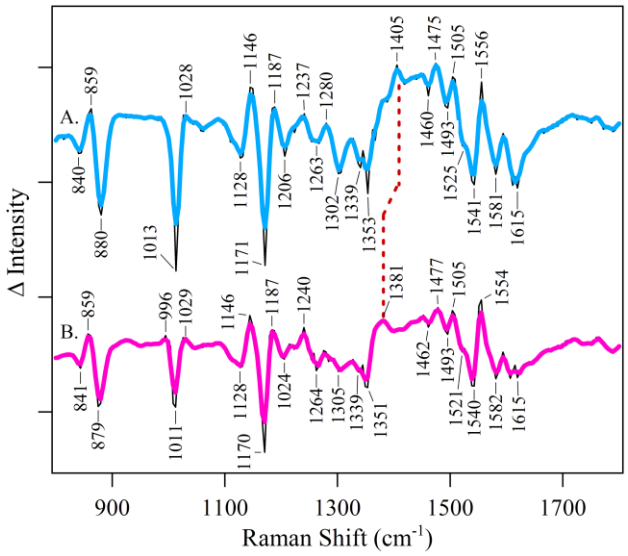

Figure 7.10. UVRR difference spectrum of *E. coli* β2 samples, showing the effect of $^{15}N_3$ histidine labeling. The data are natural abundance Apo-β2-minus-Met-β2 in 5 mM HEPES, p^2H 7.6 (A) and ^{15}N-histidine labeled Apo-β2-minus-Met-β2 in 5 mM HEPES, p^2H 7.6 (B). The spectrum in (A) is reproduced from Figure 7.9C, for comparison. The light blue and purple lines correspond to a three adjacent point smoothing fit to the raw (thin black line) data.[38] The spectra are averages of data obtained from 10 separate samples. The protein concentrations were 50 μM. The *y*-axis tick marks represent 1 x 10^3 intensity units.

7.5 Discussion

7.5.1 Conformational gating in electron transfer proteins

Conformational control limits electron transfer reactions in some enzymes, but little is known concerning the associated conformational landscape in most proteins {reviewed in 75}. In RNR, a slow, rate-limiting conformational change has been proposed to precede substrate reduction[8,19] and accompany assembly of the metal cluster.[20] Carboxylate shifts accompany redox changes at the RNR metal center;[15,76] such rearrangements also occur during catalysis in other non-heme, diiron proteins[77,78] and in photosystem II.[79] Structural changes have been shown to precede redox reactions at the photosynthetic oxygen-evolving complex.[80,81] Pretuning of the protein matrix has been proposed to play a role in photosynthetic electron transfer in the bacterial reaction center.[82] In cytochrome P450, it has been proposed that there is a rugged energy landscape for conformational sampling.[83] Vibrational spectroscopy provides a method to describe the structural changes, induced by electron transfer reactions, in these proteins.

7.5.2 Structure of the metal-free β2 subunit

In RNR, formation of the iron cluster occurs by binding ferrous ions to a folded protein, followed by metal oxidation. In the ferric form, the net +6 formal charge on the two iron ions is compensated by two negative charges provided by a bridging O^{2-} and by the ligating, negatively charged Asp 84, Glu 115, Glu 204, and Glu 238 side chains. Structures of the diferric (Met-β2, Figure 7.1A), diferrous (Red-β2), and metal free (Apo-β2, Figure 7.1B) form of the β2 subunit are available.[2,14-17] The structure of the metal-free β2 subunit shows that the carboxylates at the iron site change their rotameric

conformation when the iron is removed.[14] Changes in the position and content of bound water molecules are also observed. pK_A shifts may occur, and low barrier hydrogen bonds between carboxylate groups may form. These changes may compensate for destabilizing electrostatic effects.[76] While protonation state could not be directly resolved at the available structural resolution, it was proposed that histidine residues protonate when the iron is removed from the β2 subunit.[76]

7.5.3 Protein conformational changes are expected to accompany diiron cluster assembly

Reaction of Apo-β2 with Fe^{2+}, O_2, and excess reductant generates 1.2 tyrosyl radicals per β2 subunit and a Fe^{+2}/Y122• stoichiometry of 3.3.[84] The metal cluster binding site is 10 Å from the surface, and there is no obvious channel through which metal can access the binding site.[14] Each β monomer contains two inequivalent iron binding sites, Fe_A and Fe_B, which have a 5 fold difference in metal affinity.[21,85] Intermediates in the assembly process can be detected {reviewed in ref 13}. When reducing equivalents are abundant, an intermediate, X, accumulates with a rate constant of 8 s^{-1} and decays with the formation of the diferric cluster (0.8 s^{-1}).[20] X corresponds to an oxo-bridged Fe^{3+} Fe^{4+} dimetal center; this species generates the tyrosyl radical by oxidation of Y122.[10,20,84,86-88] When reducing equivalents are limiting, a transient signal from a W48 tryptophan cation radical, which presumably reduces a $Fe^{4+}Fe^{4+}$ species, can be detected.[89,90] $W48H^+$• can also oxidize Y122 to generate the tyrosyl radical.[89]

Because the rate constant for formation of X is independent of the concentrations of reactants, it was proposed that the 8 s^{-1} first order rate constant reflects a protein conformational change.[20] Subsequent work has shown that binding of metal to the high

affinity Fe_B site causes a global conformational change, which inhibits iron binding to the other β protomer.[21,91] Filling the Fe_B site also has been reported to inhibit metal binding to the Fe_A site[21] through an allosteric effect.

7.5.4 UVRR spectroscopy reveals protein conformational changes, associated with metal cluster assembly

In this work, we describe structural changes, which are linked to the assembly of the iron cluster and to the reduction of the tyrosyl radical in RNR. To acquire these results, we performed UVRR experiments. Spectral contributions from tyrosine, tryptophan, and histidine were resonantly enhanced using a UV Raman probe beam. The vibrational frequencies and intensities of these amino acids are structural markers in proteins.[29,92,93] UVRR has previously been applied to other enzymes to monitor electron transfer reactions,[38] protonation changes,[94,95] folding,[96], allosteric conformational changes,[92] and dynamics.[97,98] Contributions from carboxylic acid side chains (Figure 7.11) are not detectable with UV probe wavelengths.

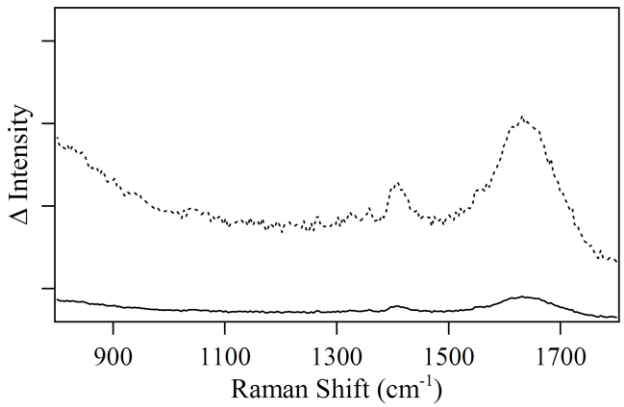

Figure 7.11. UVRR spectrum of 20 mM aspartate collected with a 250 μW, 229 nm beam for a 21 min exposure time. Aspartic acid was dissolved in 5 mM Hepes, p^1H 7.5. The tick y-axis tick marks represent 4 x 10^3 intensity units.

In the first experiment described here, the vibrational difference spectrum associated with the reduction of Y122• was measured. This experiment establishes the validity of the difference Raman technique, because the spectrum exhibits expected vibrational bands of Y122• and Y122. In the second experiment described here, the vibrational difference spectrum associated with the removal of the metal cluster was measured. Our results show that assembly of the metal cluster is associated with protonation of histidines and with perturbations of tyrosine and tryptophan. Further, from the UVRR spectrum of Li-8-hydroxyquinoline-5-sulfonate-Fe (Figure 7.12), no spectral features from the chelator are contributing to Figure 7.9, as expected.

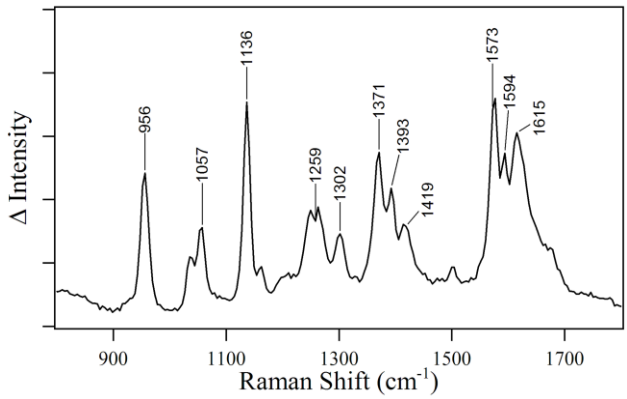

Figure 7.12. UVRR spectrum of a sample of lithium 8-hydroxyquinoline-5-sulfonate bound to iron collected with a 250 μW, 229 nm beam for a 3 min exposure time. The chelator-iron sample was collected from the G25 column following the elution of Apo-β2. The tick y-axis tick marks represent 1 x 10^3 intensity units.

7.5.5 Reduction of Y122

The control-minus-Met-β2 spectrum reflects redox changes to Y122, as expected. In particular, we observe the diagnostic CO (υ7a-1499 cm^{-1}) and ring stretching (υ8a-1556 cm^{-1}) vibrations of the tyrosyl radical, Y122• and several normal modes, at 1170,

1199, and 1608 cm^{-1}, arising from the reduced tyrosine, Y122. The upshift of the CO vibration to 1499 cm^{-1} from the ~1250 cm^{-1} CO frequency expected in singlet tyrosine is caused by the delocalization of spin density onto the phenolic oxygen.[58] Recently, it has been shown that redox changes to Y122 result in perturbations of the amide bond.[18] In RNR, Y122 oxidation causes a loss of hydrogen bond communication to the diiron cluster and rotation of the aromatic ring.[17] The trigger for the observed conformational changes may be the change in hydrogen bonding interactions between Y122•/Y122 and D84[17] or the electrostatic changes induced by Y122• reduction.[99] Our results show that these conformational changes have little effect on the other aromatic amino acid residues in the vicinity of Y122.

7.5.6 Deprotonation of histidine is associated with assembly of the metal cluster

Clustering of negatively charged amino acids in the interior of proteins is unusual. Therefore, it has been proposed that protonation of histidines compensates for charge differences induced by loss of iron.[76] Histidine protonation may serve to reduce the extent of conformational changes associated with metal cluster disassembly. Alternatively, the polar nature of the metal binding site, which is located 10Å from the surface of the protein, might lead to dipolar relaxation.

Our UVRR Raman data provide evidence for histidinium in the Apo-β2 subunit, even at slightly alkaline pH (i.e. pH 7.6). The presence of a protonated histidine at pH 7.6 suggests an environmental influence, which increases the pK_A of the histidine side chain. This hypothesis is supported by the p^2H-dependence of the intensity of the positive 1405 cm^{-1} peak as shown in Figure 7.13. Based on these data, the pK_A of the

histidine residues are between 6.0 and 8.0. An increase in histidine pK_A could be due to the negative charges on the carboxylate ligands, which will tend to stabilize the protonated form of the imidazole side chains. The only histidine residues within 11 Å of the cluster are the ligating histidines, H118 and H241 (Figure 7.1). Therefore, we conclude that the charge states of H118 and H241 change with metal cluster assembly.

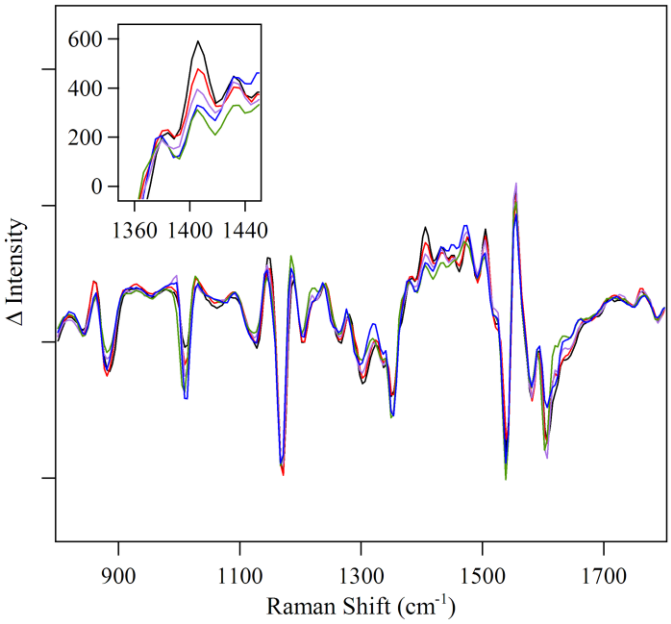

Figure 7.13. UVRR difference spectra of *E. coli* β2 samples. The data are Apo-β2-minus-Met-β2 collected in 5 mM MES, p^2H 6.5 (black), in 5 mM TRIS, p^2H 7.6 (red), in 5 mM TRIS, p^2H 8.0 (lilac), in 5 mM TRIS, p^2H 8.5 (green), and in 5 mM TRIS, p^2H 9.0 (blue). The inset shows the dependence of the + 1405 cm^{-1} peak (protonated histidine) as a function of p^2H. The spectra are averages of data obtained from (black) 10, (red) 9, (lilac) 9, (green) 9, and (blue) 9 samples. The protein concentrations were 50 μM. The *y*-axis tick marks represent 1 x 10^3 intensity units.

7.5.7 Tryptophan hydrogen bonding and conformational changes are associated with assembly of the metal cluster

Our UVRR data provide evidence for a perturbation of tryptophan with metal cluster removal. Alterations both in the frequency and the intensity of vibrational bands are observed. Changes in the Raman intensities or frequency shifts correlate with alterations in the tryptophan environment. For tryptophan, frequency and/or intensity are influenced by indole ring orientation,[100] hydrogen bonding,[101] and cation-π interactions.[102] In particular, the frequencies of the W1, W3, W7, and W17 bands shift down with increasing dielectric and hydrogen bonding. For example, the W3 band downshifted 5 cm^{-1} when solvating cyclohexane (1562 cm^{-1}) was compared to solvating water (1557 cm^{-1}).[101] The frequency of the W3 band is also a conformation marker,[101] with a range of approximately 20 cm^{-1} for the tryptophan conformational angles found in most proteins.[93]

In our data, a second derivative shaped feature, 846 (-)/865 (+)/ 880 (-) cm^{-1} (W17) is observed in the Apo-β2-minus-Met-β2 difference spectrum (Figure 7.9B). Our interpretation is that a derivative shaped band increases frequency with metal cluster removal. Increasing frequency for the W17 mode has been shown to be correlated with a weakening of tryptophan hydrogen bonding and a lower dielectric constant.[24,101,103] W17 has been reported at ≥883 cm^{-1} in weak or non-hydrogen-bonded environments and at ~877 cm^{-1} in high dielectric and strong hydrogen bonding environments.[103,104] Therefore, the observed frequencies in the Apo-β2-minus-Met-β2 difference spectrum suggest a shift from increased dielectric or strong hydrogen bonding in the Met-β2 state (846 cm^{-1}) to weak hydrogen bonding or low dielectric in the Apo-β2 state (880 cm^{-1}).

There are three tryptophan residues, W111, W107, and W48, within 11 Å of the

iron cluster (Figure 7.1). W48, which has been linked to Y122• formation and substrate-induced PCET, is ~ 9 Å from the nearest iron atom. W48 participates in a potential hydrogen bonding network with one of the histidine ligands (Figure 7.1) and forms a transient tryptophan cation radical under some conditions.[89,90] W48 exchanges protons with Asp237, adjacent to Glu238, potentially to mediate PCET directionality.[8,105] W107 is 9 Å and W111 is 4 Å from the iron cluster, but these tryptophans are not predicted to be in a hydrogen bonding network (Figure 7.1).

The W3 band at ~1550 cm^{-1} is a conformation marker for tryptophan.[24] The frequency of this band is affected by the torsion angle, $\chi^{2,1}$ about the C_2=C_3-C_β-C_α linkage. The correlation, $\upsilon(W3) = 1542 + 6.7(\cos 3\times|\chi^{2,1}|+1)^{1/2}$, between the frequency of the W3 band and tryptophan dihedral angle can be used to aid in the assignment of the Raman bands.[106] The dihedral angles of W48, W107, and W111 in the Met-β2 form of the β2 subunit are -78°, -120°, and 18°, respectively.[17] Given these values for the dihedral angles, the negative 1542 cm^{-1} peak in Figure 7.9B can be attributed to W48 in Met-β2. In Apo-β2, the dihedral angle of W48 is -88°,[14] therefore, the frequency is expected around ~1550 cm^{-1}. A candidate vibrational band for W48 in Apo-β2 is the positive feature at 1560 cm^{-1}.

To summarize, analysis of W17 frequency provides spectroscopic evidence that there is a decrease in tryptophan hydrogen bonding, when the Apo-β2 is compared to the Met-β2 state. The frequency of the W3 band in the Met-β2 state suggests that this tryptophan may be W48. The decrease in hydrogen bonding in the Apo-β2 state could be an electrostatic effect, driven by the generation of positive charge on histidine, which will destabilize a partial positive charge on W48 (Figure 7.1). Analysis of the W3 frequency

change suggests that W48 undergoes a conformational alteration when the Apo-β2 and Met-β2 states are compared.

These results can be compared to the Apo-β2 and Met-β2 X-ray structures.[2,14,15,17] Removal of the metal cluster changes the dihedral angle of W48 by -10° in chain A and by $+2^{o}$ in chain B. The change in dihedral angle is chain A consistent with our UVRR results, which indicate a change in conformation for one tryptophan. The dihedral angle of W107 changes by -3^{o} in both chains. Further, the removal of the cluster perturbs the dihedral angle of W111 by -5° (chain A) and -10° (chain B). The distance between W48 and Asp237 changes from 2.9 to 3.1 Å, consistent with our UVRR results indicating a change in hydrogen bonding. The distance between W111 and E204 and W111 and E115 changes from 3.0 to 3.8 Å and from 3.4 to 3.2 Å, respectively, when the Met-β2 and Apo-β2 forms of the protein are compared.

However, other possible explanations of the spectrum cannot be excluded. For example, the indole ring of W111 is only 4 Å from the diiron cluster and cannot be excluded as a contributor to the spectrum. The origin of the overall decrease of intensity, observed for the 1010 cm^{-1} tryptophan band, is not known. Change in metal content may lead to alterations in the mechanism of resonance enhancement, which is complex in this spectral region.[44,45,48]

7.5.8 A tyrosine conformational change is associated with assembly of the metal cluster

Perturbations of bands at 1170 (-) and 1185 (+) are observed in the Apo-β2-minus-Met-β2 difference spectrum, and these bands are diagnostic of structural perturbations to tyrosine. There are three tyrosine residues within 11 Å of the iron

cluster, redox active Y122, Y209, and Y157 (Figure 7.1). Y122 has a hydrogen bonding interaction with Asp84, which is in turn within hydrogen bonding distance of ligating His118 (Figure 7.1).[17] The high resolution structure of Met-β2 supports a weak hydrogen bond between Tyr122 and Asp84.{17 but see 2}. Iron removal induces a shortening of the distance between the two residues from 3.3 to 2.7 Å.[14] This change suggests a strengthening of the hydrogen bond between the Y122 and D84 residues in the Apo-β2 form of the β2 subunit. However, the Y9a frequency is influenced mainly by the Y–OH configuration,[25] so we attribute the spectral change in tyrosine bands to a conformational alteration in Y122. Redox driven changes in conformation have been reported for Y122 previously.[17,18]

7.5.9 Comparison of metal cluster assembly in RNR with other diiron nonheme proteins

Diferric nonheme proteins, such as ribonucleotide reductase (RNR), soluble methane monooxygenase hydroxylase (MMOH), and stearoyl acyl carrier protein Δ^9 desaturase (Δ9D) catalyze a diverse range of reactions. MMOH is responsible for oxidizing methane to methanol,[107,108] whereas Δ9D introduces a double bond between carbons 9 and 10 of stearoyl-ACP as the first step in fatty acid biosynthesis.[109] Although the functions of these enzymes differ, they each have a similar diiron center with coordination from two histidine and four carboxylate residues.[110] In all three cases, the iron center is buried in the protein, and assembly of the cluster could disrupt the conformation of the protein through electrostatic effects. During catalytic turnover, the diiron center cycles among several oxidation states, and the structure of the active site accommodates these differences by rearrangement of carboxylate ligands.[77,78,110]

X-ray structures of the metal-free MMOH[111] and Δ9D[112] have been reported. The global changes observed in the structure of the metal-free proteins are relatively minor, when compared to their respective holoenzymes. In metal-free MMOH, the metal coordinating ligands demonstrate more flexibility compared to the holo-MMOH protein. Some of the normally coordinating carboxylates are disordered. The rotameric position of one ligating carboxylate, Glu 114, is altered and permits its hydrogen bonding to two water molecules. The disorder of some of the carboxylate groups in metal-free MMOH may suggest a lack of charge compensation. As opposed to the carboxylate ligands, the histidine ligands are highly ordered, and protonation of the histidines was considered unlikely.[111] The structure of the metal-free Δ9D protein also shows little difference from the structure of the ferrous enzyme. Buried carboxylates shift positions slightly and are within hydrogen bonding distance of each other, suggesting that they may be protonated. As with the metal-free MMOH structure, the protonation state of histidine in Apo-Δ9D was not clear.

In Apo-β2, there are conserved hydrogen bonding networks involving W48-D237-H118 and Y122-D84 that may assist in stabilizing the metal binding site. Metal-free MMOH lacks these conserved networks, which may cause increased structural flexibility. Overall, the metal-free forms of these nonheme diiron proteins exhibit stable structures, even in the absence of charges provided by the metal clusters. Thus, all three proteins have evolved to accommodate assembly of the metal cluster in a folded form of the protein. Our RNR study demonstrates the potential of UVRR studies of other nonheme diiron proteins.

7.6 Summary

The conformational perturbations to tryptophan, tyrosine, and histidine residues, measured here, are associated with assembly of the iron cluster. These changes are caused by alterations in charge distribution, hydrogen bonding, and configuration. Such conformational plasticity is likely to play a role in facilitating the assembly of the metal cluster and these structural changes are likely to contribute to the conformational change, which has previously been proposed[20] to accompany metal binding and oxidation.

7.7 Acknowledgments and notes

The authors thank Prof. JoAnne Stubbe and Ellen Minnihan for helpful discussions and for providing protocols for metal-free β2 production. The authors thank Prof. John Markeley and Dr. Fariba Assadi-Porter for providing AW608Thr cells and Prof. H. Eklund and Prof. P. Nordlund for sharing the coordinates of the Apo-β2 structure. This project was supported by Award Number R01GM043273 from the National Institute of General Medical Sciences and the National Eye Institute.

7.8 References

1. Thelander, L.; Reichard, P., Reduction of ribonucleotides. *Annu. Rev. Biochem.* **1979**, *48*, 133-158.

2. Nordlund, P.; Sjöberg, B.-M.; Eklund, H., Three-dimensional structure of the free radical protein of ribonucleotide reductase. *Nature* **1990**, *345*, 593-598.

3. Jordan, A.; Reichard, P., Ribonucleotide reductases. *Annu. Rev. Biochem.* **1998**, *67*, 71-98.

4. Stubbe, J.; van der Donk, W. A., Protein radicals in enzyme catalysis. *Chem. Rev.* **1998**, *98*, 705-762.

5. Stubbe, J., Ribonucleotide reductases: amazing and confusing. *J. Biol. Chem.* **1990**, *265*, 5329-5332.

6. Stubbe, J.; Riggs-Gelasco, P., Harnessing free radicals: formation and function of the tyrosyl radical in ribonucleotide reductase. *Trends Biochem. Sci.* **1998**, *23*, 438-443.

7. Uhlin, U.; Eklund, H., Structure of ribonucleotide reductase protein R1. *Nature* **1994**, *370*, 533-539.

8. Stubbe, J.; Nocera, D. G.; Yee, C. S.; Chang, M. C. Y., Radical initiation in the class I ribonucleotide reductase: long-range proton-coupled electron transfer? *Chem. Rev.* **2003**, *103*, 2167-2202.

9. Bennati, M.; Robblee, J. H.; Mugnaini, V.; Stubbe, J.; Freed, J. H.; Borbat, P., EPR distance measurements support a model for long-range radical initiation in *E. coli* ribonucleotide reductase. *J. Am. Chem. Soc.* **2005**, *127*, 15014-15015.

10. Bollinger, J. M., Jr.; Edmondson, D. E.; Huynh, B. H.; Filley, J.; Norton, J. R.; Stubbe, J., Mechanism of assembly of the tyrosyl radical-dinuclear iron cluster cofactor of ribonucleotide reductase. *Science* **1991**, *253*, 292-298.

11. Atkin, C. L.; Thelander, L.; Reichard, P.; Lang, G., Iron and free radical in ribonucleotide reductase: exchange of iron and Mössbauer spectroscopy of the protein B2 subunit of the *E. coli* enzyme. *J. Biol. Chem.* **1973**, *248*, 7464-7472.

12. Elgren, T. E.; Lynch, J. B.; Juarez-Garcia, C.; Münck, E.; Sjöberg, B.-M.; Que, L., Jr., Electron transfer associated with oxygen activation in the B2 protein of ribonucleotide reductase from *Escherichia coli*. *J. Biol. Chem.* **1991**, *266*, 19265-19268.

13. Stubbe, J., Di-iron-tyrosyl radical ribonucleotide reductases. *Curr. Opin. Chem. Biol.* **2003**, *7*, 183-188.

14. Åberg, A.; Nordlund, P.; Eklund, H., Unusual clustering of carboxyl side chains in the core of iron-free ribonucleotide reductase. *Nature* **1993**, *361*, 276-278.

15. Logan, D. T.; Su, X.-D.; Åberg, A.; Regnström, K.; Hajdu, J.; Eklund, H.; Nordlund, P., Crystal structure of reduced protein R2 of ribonucleotide reductase:

the structural basis for oxygen activation at a dinuclear iron site. *Structure* **1996**, *4*, 1053-1064.

16. Voegtli, W. C.; Sommerhalter, M.; Saleh, L.; Baldwin, J.; Bollinger, J. M., Jr.; Rosenzweig, A. C., Variable coordination geometries at the diiron(II) active site of ribonucleotide reductase R2. *J. Am. Chem. Soc.* **2003**, *125*, 15822-15830.

17. Högbom, M.; Galander, M.; Andersson, M.; Kolberg, M.; Hofbauer, W.; Lassmann, G.; Nordlund, P.; Lendzlan, F., Displacement of the tyrosyl radical cofactor in ribonucleotide reductase obtained by single-crystal high-field EPR and 1.4-A x-ray data. *Proc. Natl. Acad. Sci. U.S.A.* **2003**, *100*, 3209-3214.

18. Offenbacher, A. R.; Vassiliev, I. R.; Seyedsayamdost, M. R.; Stubbe, J.; Barry, B. A., Redox-linked structural changes in ribonucleotide reductase. *J. Am. Chem. Soc.* **2009**, *131*, 7496-7497.

19. Ge, J.; Yu, G.; Ator, M. A.; Stubbe, J., Pre-steady-state and steady-state kinetic analysis of *E. coli* class I ribonucleotide reductase. *Biochemistry* **2003**, *42*, 10071-10083.

20. Tong, W. H.; Chen, S.; Lloyd, S. G.; Edmondson, D. E.; Huynh, B. H.; Stubbe, J., Mechanism of assembly of the diferric cluster-tyrosyl radical cofactor of *Escherichia coli* ribonucleotide reductase from the diferrous form of the R2 subunit. *J. Am. Chem. Soc.* **1996**, *118*, 2107-2108.

21. Pierce, B. S.; Hendrich, M. P., Local and global effects of metal binding within the small subunit of ribonucleotide reductase. *J. Am. Chem. Soc.* **2005**, *127*, 3613-3623.

22. Caswell, D. S.; Spiro, T. G., Ultraviolet resonance Raman spectroscopy of imidazole, histidine, and $Cu(imidazole)_4^{2+}$: implications for protein studies. *J. Am. Chem. Soc.* **1986**, *108*, 6470-6477.

23. Harada, I.; Takeuchi, H., *Spectroscopy of Biological Systems*. Wiley: New York, 1986; Vol. 13, p 157.

24. Miura, T.; Takeuchi, H.; Harada, I., Tryptophan Raman bands sensitive to hydrogen bonding and side chain conformation. *J. Raman Spectrosc.* **1989**, *20*, 667-671.

25. Takeuchi, H.; Watanabe, N.; Satoh, Y.; Harada, I., Effects of hydrogen bonding on the tyrosine Raman bands in the 1300-1150 cm^{-1} region. *J. Raman Spectrosc.* **1989**, *20*, 233-237.

26. Takeuchi, H.; Kimura, Y.; Koitabashi, I.; Harada, I., Raman bands of *N*-deuterated histidinium as markers of conformation and hydrogen bonding. *J. Raman Spectrosc.* **1991**, *22*, 233-236.

27. Ames, J. B.; Ros, M.; Raap, J.; Lugtenburg, J.; Mathies, R. A., Time-resolved ultraviolet resonance Raman studies of protein structure: application to bacteriorhodopsin. *Biochemistry* **1992**, *31*, 5328-5334.

28. Rodgers, K. R.; Su, C.; Subramaniam, S.; Spiro, T. G., Hemoglobin R→T structural dynamics from simultaneous monitoring of tyrosine and tryptophan

time-resolved UV resonance Raman signals. *J. Am. Chem. Soc.* **1992**, *114*, 3697-3709.

29. Austin, J. C.; Jordan, T.; Spiro, T. G., Ultraviolet resonance Raman studies of proteins and related model compounds. In *Biomolecular spectroscopy*, Clark, R. J. H.; Hester, R. E., Eds. John Wiley & Sons Ltd.: New York, 1993; pp 55-125.

30. Nagai, M.; Wajcman, H.; Lahary, A.; Nakatsukasa, T.; Nagatomo, S.; Kitagawa, T., Quarternary structure sensitive tyrosine residues in human hemoglobin: UV resonance Raman studies of mutants at α140, β35, β145 tyrosine. *Biochemistry* **1999**, *38*, 1243-1251.

31. Salowe, S. P.; Stubbe, J., Cloning, overproduction, and purification of the B2 subunit of ribonucleoside-diphosphate reductase. *J. Bacteriol.* **1986**, *165*, 363-366.

32. Seyedsayamdost, M. R. Investigation of the mechanism of radical propagation in *E. coli* ribonucleotide reductase by site-specific incorporation of unnatural amino acids. Massachusetts Institute of Technology, Cambridge, 2008.

33. Xia, B.; Cheng, H.; Skjeldal, L.; Coghlan, V. M.; Vickery, L. E.; Markley, J. L., Multinuclear magnetic resonance and mutagenesis studies of the histidine residues of human mitochondrial ferredoxin. *Biochemistry* **1995**, *34*, 180-187.

34. Xia, B.; Pikus, J. D.; Xia, W.; McClay, K.; Steffan, R. J.; Chae, Y. K.; Westler, W. M.; Markley, J. L.; Fox, B. G., Detection and classification of hyperfine-shifted ^{1}H, ^{2}H, and ^{15}N resonances of the Rieske ferredoxin component of toluene 4-monooxygenase. *Biochemistry* **1999**, *38*, 727-739.

35. Rotsaert, F. A. J.; Pikus, J. D.; Fox, B. G.; Markley, J. L.; Sanders-Loehr, J., N-isotope effects on the Raman spectra of Fe_2S_2 ferredoxin and Rieske ferredoxin: evidence for structural rigidity of metal sites. *J. Biol. Inorg. Chem.* **2003**, *8*, 318-326.

36. Sneeden, J. L.; Loeb, L. A., Mutations in the R2 subunit of ribonucleotide reductase that confer resistence to hydroxyurea. *J. Biol. Chem.* **2004**, *279*, 40723-40728.

37. Chen, J.; Barry, B. A., Ultraviolet resonance Raman microprobe spectroscopy of photosystem II. *Photochem. Photobiol.* **2008**, *84*, 815-818.

38. Chen, J.; Bender, S. L.; Keough, J. M.; Barry, B. A., Tryptophan as a probe of photosystem I electron transfer reactions: a UV resonance Raman study. *J. Phys. Chem. B Letters* **2009**, *113*, 11367-11370.

39. Jenson, D. L.; Barry, B. A., Proton-coupled electron transfer in photosystem II: proton inventory of a redox active tyrosine. *J. Am. Chem. Soc.* **2009**, *131*, 10567-10573.

40. Brown, N. C.; Eliasson, R.; Reichard, P.; Thelander, L., Spectrum and iron content of protein B2 from ribonucleoside diphosphate reductase. *Eur. J. Biochem.* **1969**, *9*, 512-518.

41. Garbett, K.; Darnall, D. W.; Klotz, I. M.; Williams, R. J. P., Spectroscopy and structure of hemerythrin. *Arch. Biochem. Biophys.* **1969**, *135*, 419-434.

42. Petersson, L.; Gräslund, A.; Ehrenberg, A.; Sjöberg, B. M.; Reichard, P., The iron center in ribonucleotide reductase from *Escherichia coli*. *J. Biol. Chem.* **1980**, *255*, 6706-6712.

43. Nyholm, S.; Thelander, L.; Gräslund, A., Reduction and loss of the iron center in the reaction of the small subunit of mouse ribonucleotide reductase with hydroxyurea. *Biochemistry* **1993**, *32*, 11569-11574.

44. Rava, R. P.; Spiro, T. G., Selective enhancement of tyrosine and tryptophan resonance Raman spectra via ultraviolet laser excitation. *J. Am. Chem. Soc.* **1984**, *106*, 4062-4064.

45. Rava, R. P.; Spiro, T. G., Resonance enhancement in the ultraviolet Raman spectra of aromatic amino acids. *J. Phys. Chem.* **1985**, *89*, 1856-1861.

46. Ludwig, M.; Asher, S. A., Ultraviolet resonance Raman excitation profiles of tyrosine: dependence of Raman cross sections on excited-state intermediates. *J. Am. Chem. Soc.* **1988**, *110*, 1005-1011.

47. Sweeny, J. A.; Asher, S. A., Tryptophan UV resonance Raman excitation profiles. *J. Phys. Chem.* **1990**, *94*, 4784-4791.

48. Fodor, S. P. A.; Copeland, R. A.; Grygon, C. A.; Spiro, T. G., Deep-ultraviolet Raman excitation profiles and vibronic scattering mechanisms of phenylalanine, tyrosine and tryptophan. *J. Am. Chem. Soc.* **1989**, *111*, 5509-5518.

49. Harada, I.; Miura, T.; Takeuchi, H., Origin of the doublet at 1360 and 1340 cm^{-1} in the Raman spectra of tryptophan and related compounds. *Spectrochim. Acta A* **1986**, *42*, 307-312.

50. Hirakawa, A. Y.; Nishimura, Y.; Matsumoto, T.; Nakanishi, M.; Tsuboi, M., Characterization of a few Raman lines of tryptophan. *J. Raman Spectrosc.* **1978**, *7*, 282-287.

51. Takeuchi, H.; Harada, I., Normal coordinate analysis of the indole ring. *Spectrochim. Acta* **1986**, *42A*, 1069-1078.

52. Asher, S. A.; Ludwig, M.; Johnson, C. R., UV resonance Raman excitation profiles of the aromatic amino acids. *J. Am. Chem. Soc.* **1986**, *108*, 3186-3197.

53. Mesu, J. G.; Visser, T.; Soulimani, F.; Veckhuysen, B. M., Infrared and Raman spectroscopic study of pH-induced structural changes of L-histidine in aqueous environment. *Vib. Spectrosc.* **2005**, *39*, 114-125.

54. Pflüger, F.; Hernández, B.; Ghomi, M., Vibrational analysis of amino acids and short peptides in hydrated media. VII. Energy landscapes, energetic and geometrical features of L-histidine with protonated and neutral side chains. *J. Phys. Chem. B* **2010**, *114*, 9072-9083.

55. Tasumi, M.; Harada, I.; Takamatsu, T.; Takahashi, S., Raman studies of L-histidine and related compounds in aqueous solutions. *J. Raman Spectrosc.* **1982**, *12*, 149-151.

56. Gregoriou, V. G.; Jayaraman, V.; Hu, X.; Spiro, T. G., FT-IR difference spectroscopy of hemoglobins A and Kempsey: evidence that a key quaternary interaction induces protonation of asp .beta.99. *Biochemistry* **1995**, *34*, 6876-6882.

57. Zhao, X.; Wang, D.; Spiro, T. G., A UV resonance Raman monitor of histidine protonation in proteins: Bohr protons in hemoglobin. *J. Am. Chem. Soc.* **1998**, *120*, 8517-8518.

58. Tripathi, G. N. R.; Schuler, R. H., The resonance Raman spectrum of phenoxyl radical. *J. Chem. Phys.* **1984**, *81*, 113-121.

59. Johnson, C. R.; Ludwig, M.; Asher, S. A., Ultraviolet resonance Raman characterization of photochemical transients of phenol, tyrosine, and tryptophan. *J. Am. Chem. Soc.* **1986**, *108*, 905-912.

60. Qin, Y.; Wheeler, R. A., Similarities and differences between phenoxyl and tyrosine phenoxyl radical structures, vibrational frequencies, and spin densities. *J. Am. Chem. Soc.* **1995**, *117*, 6083-6092.

61. Ayala, I.; Range, K.; York, D.; Barry, B. A., Spectroscopic properties of tyrosyl radicals in dipeptides. *J. Am. Chem. Soc.* **2002**, *124*, 5496-5505.

62. Bent, D. V.; Hayon, E., Excited state chemistry of aromatic amino acids and related peptides. I. Tyrosine. *J. Am. Chem. Soc.* **1975**, *97*, 2599-2606.

63. Range, K.; Ayala, I.; York, D.; Barry, B. A., Normal modes of redox-active tyrosine: conformation dependence and comparison to experiments. *J. Phys. Chem. B* **2006**, *110*, 10970-10981.

64. Backes, G.; Sahlin, M.; Sjöberg, B.-M.; Loehr, T. M.; Sanders-Loehr, J., Resonance Raman spectroscopy of ribonucleotide reductase. Evidence for a deprotonated tyrosyl radical and photochemistry of the binuclear iron center. *Biochemistry* **1989**, *28*, 1923-1929.

65. Kim, S.; Barry, B. A., Vibrational spectrum associated with the reduction of tyrosyl radical D• in photosystem II: a comparative biochemical and kinetic study. *Biochemistry* **1998**, *37*, 13882-13892.

66. Ayala, I.; Kim, S.; Barry, B. A., A difference Fourier transform infrared study of tyrosyl radical Z• decay in photosystem II. *Biophys. J.* **1999**, *77*, 2137-2144.

67. Suydam, I. T.; Boxer, S. G., Vibrational Stark effects calibrate the sensitivity of vibrational probes for electric fields in proteins. *Biochemistry* **2003**, *42*, 12050-12055.

68. Carlson, J.; Fuchs, J. A.; Messing, J., Primary structure of the *Escherichia coli* ribonucleoside diphosphate reductase operon. *Proc. Natl. Acad. Sci. U.S.A.* **1984**, *81*, 4294-4297.

69. Walden, S. E.; Wheeler, R. A., Structural and vibrational analysis of indole by density functional and hybrid Hartree-Fock/density functional methods. *J. Chem. Soc., Perkin Trans. 2* **1996**, 2653-2662.

70. Liu, G.; Grygon, C. A.; Spiro, T. G., Ionic strength dependence on cytochrome *c* structure and Trp-59 H/D exchange from ultraviolet resonance Raman spectroscopy. *Biochemistry* **1989**, *28*, 5046-5050.

71. Gurudas, U.; Schelvis, J. P. M., Resonance Raman spectroscopy of the neutral radical Trp_{306} in DNA photolyase. *J. Am. Chem. Soc.* **2004**, *126*, 12788-12789.

72. Shafaat, H. S.; Leigh, B. S.; Tauber, M. J.; Kim, J. E., Resonance Raman characterization of a stable tryptophan radical in an azurin mutant. *J. Phys. Chem. B* **2009**, *113*, 382-388.

73. Copeland, R. A.; Spiro, T. G., Ultraviolet resonance Raman spectra of cytochrome *c* conformational states. *Biochemistry* **1985**, *24*, 4960-4968.

74. Zhao, X.; Chen, R.; Deng, Q.; Mabrouk, P. A.; Spiro, T. G., UV resonance Raman probe of heme-bound imidazole established by labeling of hemoglobin. *Isr. J. Chem.* **2000**, *40*, 15-20.

75. Davidson, V. L., What controls the rates of interprotein electron-transfer reactions. *Acc. Chem. Res.* **2000**, *33*, 87-93.

76. Andersson, M. E.; Högbom, M.; Rinaldo-Matthis, A.; Blodig, W.; Liang, Y.; Persson, B.-O.; Sjöberg, B.-M.; Su, X.-D.; Nordlund, P., Structural and mutational studies of the carboxylate cluster in iron-free ribonucleotide reductase. *Biochemistry* **2004**, *43*, 7966-7972.

77. Kurtz, D. M., Jr., Structural similarity and functional diversity in diiron-oxo proteins. *J. Biol. Inorg. Chem.* **1997**, *2*, 159-167.

78. Sazinsky, M. H.; Lippard, S. J., Correlating structure with function in bacterial multicomponent monooxygenases and related diiron proteins. *Acc. Chem. Res.* **2006**, *39*, 558-566.

79. Steenhuis, J. J.; Hutchison, R. S.; Barry, B. A., Alterations in carboxylate ligation at the active site of photosystem II. *J. Biol. Chem.* **1999**, *274*, 14609-14616.

80. Haumann, M.; Liebish, P.; Müller, C.; Barra, M.; Grabolle, M.; Dau, H., Photosynthetic O_2 formation tracked by time-resolved X-ray experiments. *Science* **2005**, *310*, 1019-1021.

81. Barry, B. A.; Cooper, I. B.; De Riso, A.; Brewer, S. H.; Vu, D. M.; Dyer, R. B., Time-resolved vibrational spectroscopy detects protein-based intermediates in the photosynthetic oxygen evolving cycle. *Proc. Natl. Acad. Sci. U.S.A.* **2006**, *103*, 7288-7291.

82. Wang, H.; Lin, S.; Allen, J. P.; Williams, J. C.; Blankert, S.; Laser, C.; Woodbury, N. W., Protein dynamics control the kinetics of initial electron transfer in photosynthesis. *Science* **2007**, *316*, 703-704.

83. Hay, S.; Brenner, S.; Khara, B.; Quinn, A. M.; Rigby, S. E. J.; Scrutton, N. S., Nature of the energy landscape for gated electron transfer in a dynamic redox protein. *J. Am. Chem. Soc.* **2010**, *132*, 9738-9745.

84. Bollinger, J. M., Jr.; Tong, W. H.; Ravi, N.; Huynh, B. H.; Edmondson, D. E.; Stubbe, J., Mechanism of assembly of the tyrosyl radical-diiron(III) cofactor of *E. coli* ribonucleotide reductase. 2. Kinetics of the excess Fe^{2+} reaction by optical, EPR and Mössbauer spectroscopies. *J. Am. Chem. Soc.* **1994**, *116*, 8015-8023.

85. Bollinger, J. M., Jr.; Chen, S.; Parkin, S. E.; Mangravite, L. M.; Ley, B. A.; Edmondson, D. E.; Huynh, B. H., Differential iron(II) affinity of the sites of the diiron cluster in protein R2 of *Escherichia coli* ribonucleotide reductase: tracking the individual sites through the O_2 activation sequence. *J. Am. Chem. Soc.* **1997**, *119*, 5976-5977.

86. Burdi, D.; Sturgeon, B. E.; Tong, W. H.; Stubbe, J.; Hoffman, B. M., Rapid freeze-quench ENDOR of the radical X intermediate of *Escherichia coli* ribonucleotide reductase using $^{17}O_2$, $H_2{}^{17}O$, and $^{2}H_2O$. *J. Am. Chem. Soc.* **1996**, *118*, 281-282.

87. Sturgeon, B. E.; Burdi, D.; Chen, S.; Huynh, B. H.; Edmondson, D. E.; Stubbe, J.; Hoffman, B. M., Reconsideration of X, the diiron intermediate formed during cofactor assembly in *E. coli* ribonucleotide reductase. *J. Am. Chem. Soc.* **1996**, *118*, 7551-7557.

88. Willems, J.-P.; Lee, H.-I.; Burdi, D.; Doan, P. E.; Stubbe, J.; Hoffman, B. M., Identification of the protonated oxygenic ligands of ribonucleotide reductase intermediate X by Q-band $^{1,2}H$ CW and pulsed ENDOR. *J. Am. Chem. Soc.* **1997**, *119*, 9816-9824.

89. Baldwin, J.; Krebs, C.; Ley, B. A.; Edmondson, D. E.; Huynh, B. H.; Bollinger, J. M., Jr., Mechanism of rapid electron transfer during oxygen activation in the R2 subunit of *Escherichia coli* ribonucleotide reductase. 1. Evidence for a transient tryptophan radical. *J. Am. Chem. Soc.* **2000**, *122*, 12195-12206.

90. Krebs, C.; Chen, S.; Baldwin, J.; Ley, B. A.; Patel, U.; Edmondson, D. E.; Huynh, B. H.; Bollinger, J. M., Jr., Mechanism of rapid electron transfer during oxygen activation in the R2 subunit of *Escherichia coli* ribonucleotide reductase. 2. Evidence for and consequences of blocked electron transfer in the W48F variant. *J. Am. Chem. Soc.* **2000**, *122*, 12207-12219.

91. Pierce, B. S.; Elgren, T. E.; Hendrich, M. P., Mechanistic implications for the formation of the diiron cluster in ribonucleotide reductase provided by quantitative EPR spectroscopy. *J. Am. Chem. Soc.* **2003**, *125*, 8748-8759.

92. Hu, X.; Spiro, T. G., Tyrosine and tryptophan structure markers in hemoglobin ultraviolet resonance Raman spectra: mode assignments via subunit-specific isotope labeling of recombinant protein. *Biochemistry* **1997**, *36*, 15701-15712.

93. Takeuchi, H., Raman structural markers of tryptophan and histidine side chains. *Biopolymers* **2003**, *72*, 305-317.

94. Asher, S. A.; Larkin, P. J.; Teraoka, J., Ultraviolet resonance Raman and absorption difference spectroscopy of myoglobins - titration behavior of individual tyrosine residues. *Biochemistry* **1991**, *30*, 5944-5954.

95. Wu, Q.; Li, F. B.; Wang, W. X.; Hecht, M. H.; Spiro, T. G., UV Raman monitoring of histidine protonation and H-H-2 exchange in plastocyanin. *J. Inorg. Biochem.* **2002**, *88*, 381-387.

96. Sanchez, K. M.; Neary, T. J.; Kim, J. E., Ultraviolet resonance Raman spectroscopy of folded and unfolded states of an integral membrane protein. *J. Phys. Chem. B* **2009**, *112*, 9507-9511.

97. Zhu, L. Y.; Kim, J.; Mathies, R. A., Picosecond time-resolved Raman system for studying photochemical reaction dynamics: application to the primary events in vision. *J. Raman Spectrosc.* **1999**, *30*, 777-783.

98. Balakrishnan, G.; Weeks, C. L.; Ibrahim, M.; Soldatova, A. V.; Spiro, T. G., Protein dynamics from time resolved UV Raman spectroscopy. *Curr. Opin. Struct. Biol.* **2009**, *18*, 623-629.

99. Sibert, R.; Josowicz, M.; Porcelli, F.; Veglia, G.; Range, K.; Barry, B. A., Proton-coupled electron transfer in a biomimetic peptide as a model of enzyme regulatory mechanisms. *J. Am. Chem. Soc.* **2007**, *129*, 4393-4400.

100. Takeuchi, H.; Matsuno, M.; Overman, S. A.; Thomas, G. J., Jr., Raman linear intensity difference of flow-oriented macromolecules: orientation of the indole ring of tryptophan-26 in filamentous virus *fd*. *J. Am. Chem. Soc.* **1996**, *118*, 3498-3507.

101. Matsuno, M.; Takeuchi, H., Effects of hydrogen bonding and hydrophobic interactions on the ultraviolet resonance Raman intensities of indole ring vibrations. *Bull. Chem. Soc. Jpn.* **1998**, *71*, 851-857.

102. Okada, A.; Miura, T.; Takeuchi, H., Protonation of histidine and histidine-tryptophan interaction in the activation of the M2 ion channel from influenza A virus. *Biochemistry* **2001**, *40*, 6053-6060.

103. Miura, T.; Takeuchi, H.; Harada, I., Characterization of individual tryptophan side chains in proteins using Raman spectroscopy and hydrogen-deuterium exchange kinetics. *Biochemistry* **1988**, *27*, 88-94.

104. Kochendoerfer, G. G.; Kaminaka, S.; Mathies, R. A., Ultraviolet resonance Raman examination of the light-induced protein structural changes in rhodopsin activation. *Biochemistry* **1997**, *36*, 13153-13159.

105. Reece, S. Y.; Hodgkiss, J. M.; Stubbe, J.; Nocera, D. G., Proton-coupled electron transfer: the mechanistic underpinning for radical transport and catalysis in biology. *Philos. Trans. R. Soc., B* **2006**, *361*, 1351-1364.

106. Maruyama, T.; Takeuchi, H., Water accessibility to the tryptophan indole N-H sites of gramicidin A transmembrane channel: detection of positional shifts of tryptophans 11 and 13 along the channel axis upon cation binding. *Biochemistry* **1997**, *36*, 10993-11001.

107. Lipscomb, J. D., Biochemistry of the soluble methane monooxygenase. *Annu. Rev. Microbiol.* **1994**, *48*, 371-399.

108. Baik, M.-H.; Newcomb, M.; Friesner, R. A.; Lippard, S. J., Mechanistic studies on the hydroxylation of methane by methane monooxygenase. *Chem. Rev.* **2003**, *103*, 2385-2420.

109. Fox, B. G.; Lyle, K. S.; Rogge, C. E., Reactions of the diiron enzyme stearoyl-acyl carrier protein desaturase. *Acc. Chem. Res.* **2004**, *37*, 421-429.

110. Solomon, E. I.; Brunold, T. C.; Davis, M. I.; Kemsley, J. N.; Lee, S.-K.; Lehnert, N.; Neese, F.; Skulan, A. J.; Yang, Y.-S.; Zhou, J., Geometric and electronic structure/function correlations in non-heme iron enzymes. *Chem. Rev.* **2000**, *100*, 235-349.

111. Sazinsky, M. H.; Merkx, M.; Cadieux, E.; Tang, S.; Lippard, S. J., Preparation and X-ray structures of metal-free, dicobalt and dimanganese forms of soluble methane monooxygenase hydroxylase from *Methylococcus capsulatus* (Bath). *Biochemistry* **2004**, *43*, 16263-16276.

112. Moche, M.; Shanklin, J.; Ghoshal, A.; Linqvist, Y., Azide and acetate complexes plus two iron-depleted crystal structures of the diiron enzyme Δ9 stearoyl-acyl carrier protein desaturase. Implications for oxygen activation and catalytic intermediates. *J. Biol. Chem.* **2003**, *278*, 25072-25080.

CHAPTER 8

CONCLUSIONS

Redox-active tyrosine residues are important mediators of proton-coupled electron transfer (PCET) reactions in biology.[1] Tyrosyl radicals, generated from single electron oxidation of tyrosine, are necessary for PCET-linked catalysis in photosystem II,[2] cytochrome *c* oxidase,[3,4] and ribonucleotide reductase.[5] The roles and properties of the tyrosyl radicals in these enzymes are significantly different. For example, Y122• of ribonucleotide reductase is stable for 2 weeks at 4°C,[6] while Y_Z• of photosystem II is a transient radical with a lifetime on the micro- to millisecond timescale.[7] The environmental factors that control PCET processes involving tyrosine residues are beginning to be elucidated.{for examples, see 8,9}

In cytochrome *c* oxidase, the functional role of the unique post-translational modified tyrosine-histidine covalent-link during O_2 reduction has not yet been resolved. Copper-containing model compounds were synthesized to mimic the active site geometry of the cross-linked moiety.[10] UV-visible spectrophotometric titrations of the compounds gave pK_A values of the copper-containing model compound and tyrosine as 7.7 and ~10, respectively. These results demonstrated the capacity for the tyrosine-histidine cross-link to participate as a proton donor in the enzyme. The photolysis-induced infrared spectra of these model compounds were consistent with the formation of phenoxyl radicals in the absence or presence of a ligated copper ion. With the aid of ^{13}C isotope labeling, we have provided unambiguous assignment of the υC–O vibrational mode for the phenoxyl radical in the models. This assignment may be a useful structural marker to identify the

potential presence of an oxidized tyrosine-histidine in future FT-IR studies of cytochrome *c* oxidase.

Protein secondary structure has previously been proposed to facilitate long-distance electron transfer reactions.[11] Previous work in our lab using tyrosine-containing dipeptides had suggested that the amide bonds surrounding the tyrosine may influence electron transfer reactions.[12] To test this hypothesis, we designed pentapeptide model compounds to match the primary sequence of tyrosine 161 (Y_Z) of D1 subunit of photosystem II ($IY_{161}PIG$) and of tyrosine 122 of the β2 subunit of ribonucleotide reductase ($RSY_{122}TH$). At cryogenic temperatures, we measured the photolysis-induced infrared changes of four different pentapeptide sequences and compared to model tyrosine. New spectral features were observed in the amide I region of the FT-IR difference spectra for these pentapeptides when compared to tyrosine. These data demonstrated that the peptide electronic structure is perturbed upon redox changes to tyrosine residues and these electrostatic-driven structural changes are dependent on the amino acid content.

These model studies illustrated the importance of the local structure in facilitating biological PCET reactions. In the protein matrix, conformational dynamics have been proposed to limit or to couple to aromatic amino acid-linked radical transport to prevent build-up of reactive oxygen species.[13] In this work, we describe the development of a novel reaction-induced infrared spectroscopic technique to monitor protein structural dynamics associated with electron transfer reactions in ribonucleotide reductase and other enzyme systems. Ribonucleotide reductase catalyzes the formation of DNA monomers through ribonucleotide reduction.[14] In class Ia enzymes, generation of a cysteine radical

at the active site in the α2 subunit is required to initiate substrate reduction. This C• is formed from Y122• in the β2 subunit through reversible long-distance (35 Å) PCET reactions.[5,15-17] These reactions have been hypothesized to be gated by conformational changes.[18]

Using the novel reaction-induced vibrational method, we have identified amide I structural changes linked to electron transfer reactions in the β2 subunit of ribonucleotide reductase. In comparison to the photolysis-induced infrared spectra of RSYTH, which is the pentapeptide matching the primary sequence of Y122, a similar set of amide I peaks were observed. These data suggested that the structural changes in β2 are caused by local peptide bond perturbations surrounding Y122. To confirm these results, we prepared β2 samples globally labeled with $^{13}C_{carbonyl}$-tyrosine. The positive feature in the natural abundance β2 infrared spectra shifted from 1653 cm^{-1} to 1624 cm^{-1}, consistent with the tyrosine amide assignment. The isotope data support the conclusion that the protein conformational changes are local and redox-linked to tyrosine. We propose that these structural dynamics are linked to changes in the electrostatic communication between Tyr122 and Asp84. The interactions may be important in controlling the local PCET reactions.

In addition, we have identified structural changes that are associated with diiron cluster assembly in the β2 subunit of ribonucleotide reductase using ultraviolet (UV) resonance Raman spectroscopy. From comparison of UV Raman data to the X-ray structures of β2, we have assigned changes in the tryptophan and tyrosine vibrational bands to alterations in side-chain conformations and hydrogen bonding interactions, respectively. Moreover, for the first time, we have provided spectroscopic evidence for

the protonation of histidine in the metal-free (Apo-β2) ribonucleotide reductase. To confirm these data, we labeled β2 samples with $^{15}N_3$-histidine using a histidine auxotroph. UV Raman spectra of the ^{15}N-histidine labeled β2 samples showed a positive feature shifted -24 cm^{-1}. To explain these data, the histidine must have an elevated pK_A. These findings demonstrate the ability of the UV resonance Raman technique to determine histidine protonation states in other metal-binding proteins.

The structural information gathered for ribonucleotide reductase in this work provides a better understanding of the mechanisms for PCET reactions and metal assembly in RNR. From the Y122• redox-linked studies, we have developed a current working model for these structural changes. In the reduced state Y122 is within hydrogen bonding distance to D84.[15] Upon oxidation, the more electronegative nature of the tyrosyl radical phenoxyl ring[8] causes repulsion with the deprotonated aspartic acid at position 84. The electrostatic repulsion drives movement of the phenoxyl ring via a Cα-Cβ rotation. We propose that this interaction causes changes in the molecular geometry of the Tyr122-Thr123 amide bond. A recent work postulates that the conformational changes surrounding the diiron cluster rate-limit the PCET processes required for nucleotide reduction.[19] Our work suggests that the local protein structure plays a critical role in controlling electron transfer reactions involving tyrosine in ribonucleotide reductase. The conclusion is emphasized through the studies with model compounds. The tyrosine-containing pentapeptide model compounds underscored the importance of the composition for tyrosyl radical-mediated electron transfer reactions. In the tyrosine-histidine cross-link mimicking compounds, the effect of this unique structure in C*c*O on the functional and spectroscopic properties of tyrosine was shown. It follows that these

studies highlight the significance of protein structure and dynamics on the function of proton-coupled electron transfer reactions that control catalysis in many biological systems.

Future experiments, however, to investigate the structural changes that precede the PCET reactions in ribonucleotide reductase are necessary. Reaction-induced FT-IR spectroscopic studies involving the holoenzyme are already being designed. The use of incorporated unnatural amino acids to change the rate-limiting step of nucleotide reduction from a conformational change to an electron transfer reaction may be necessary to study the details of the electron transfer pathway.[20] These future studies will aid in the elucidation of the mechanisms for the PCET reactions in ribonucleotide reductase.

Perhaps the most interesting outcome to follow from the ribonucleotide reductase experiments is the potential, future application of the reaction-induced FT-IR spectroscopic study on the various β2 inhibitors towards the design and development of novel anti-cancer drugs. Current models for the reduction of Y122• using radical scavengers, such as hydroxyurea, have been established through kinetic studies. These previous experiments do not provide a thorough mechanism of action. A detailed analysis of the mechanism of RNR inhibitors and development and application of techniques to monitor the reaction of these inhibitors is required. Our reaction-induced FT-IR spectroscopic technique has demonstrated the ability to distinguish the structural changes of these reactions at room temperatures. Future isotope labeling experiments will aid in the elucidation of the mechanisms and pathways for Y122• reduction. An understanding of these inhibitors' modes of action may lead to the development of more effective clinical treatments of cancer.

8.1 References

1. Barry, B. A.; Einarsdóttir, Ó., Insights into the structure and function of redox-active tyrosines from model compounds. *J. Phys. Chem. B* **2005**, *109*, 6972-6981.

2. Boerner, R. J.; Barry, B. A., Isotopic labeling and EPR spectroscopy show that a tyrosine residue is the terminal electron donor, Z, in manganese-depleted photosystem II preparations. *J. Biol. Chem.* **1993**, *268*, 17151-17154.

3. Das, T. K.; Pecoraro, C.; Tomson, F. L.; Gennis, R. B.; Rousseau, D. L., The post-translational modification in cytochrome *c* oxidase is required to establish a functional environment of the catalytic site. *Biochemistry* **1998**, *37*, 14471-14476.

4. Pinakoulaki, E.; Pfitzner, U.; Ludwig, B.; Varotsis, C., The role of the cross-link his-tyr in the functional properties of the binuclear center in cytochrome *c* oxidase. *J. Biol. Chem.* **2002**, *277*, 13563-13568.

5. Stubbe, J.; Nocera, D. G.; Yee, C. S.; Chang, M. C. Y., Radical initiation in class I ribonucleotide reductase: long-range proton-coupled electron transfer? *Chem. Rev.* **2003**, *103*, 2167-2201.

6. Atkin, C. L.; Thelander, L.; Reichard, P.; Lang, G., Iron and free radical in ribonucleotide reductase: exchange of iron and Mössbauer spectroscopy of the protein B2 subunit of the *Escherichia coli* enzyme. *J. Biol. Chem.* **1973**, *248*, 7464-7472.

7. Dekker, J. P.; Plijter, J. J.; Ouwehand, L.; Gorkom, H. J. V., Kinetics of manganese redox transitions in the oxygen-evolving apparatus of photosynthesis. *Biochim. Biophys. Acta* **1984**, *325*, 483-503.

8. Sibert, R.; Josowicz, M.; Porcelli, F.; Gianluigi, V.; Range, K.; Barry, B. A., Proton-coupled electron transfer in a biomimetic peptide as a model of enzyme regulatory mechanisms. *J. Am. Chem. Soc.* **2007**, *129*, 4393-4400.

9. Sibert, R.; Josowicz, M.; Barry, B. A., Control of proton and electron transfer in *de novo* designed, biomimetic β hairpins. *ACS Chem. Biol.* **2010**.

10. White, K. N.; Sen, I.; Szundi, I.; Landaverry, Y. R.; Bria, L. E.; Konopelski, J. P.; Olmstead, M. M.; Einarsdóttir, Ó., Synthesis and structural characterization of cross-linked histidine-phenol Cu(II) complexes as cytochrome *c* oxidase active site models. *Chem. Commun.* **2007**, 3252-3254.

11. Gray, H. B.; Winkler, J. R., Electron tunneling through proteins. *Quart. Rev. Biophys.* **2003**, *36*, 341-372.

12. Ayala, I.; Range, K.; York, D.; Barry, B. A., Spectroscopic properties of tyrosyl radicals in dipeptides. *J. Am. Chem. Soc.* **2002**, *124*, 5496-5505.

13. Davidson, V. L., What controls the rates of interprotein electron-transfer reactions. *Acc. Chem. Res.* **2000**, *33*, 87-93.

14. Jordan, A.; Reichard, P., Ribonucleotide reductases. *Annu. Rev. Biochem.* **1998**, *67*, 71-98.

15. Nordlund, P.; Sjöberg, B.-M.; Eklund, H., Three-dimensional structure of the free radical protein of ribonucleotide reductase. *Nature* **1990**, *345*, 593-598.

16. Uhlin, U.; Eklund, H., Structure of ribonucleotide reductase protein R1. *Nature* **1994**, *370*, 533-539.

17. Reece, S. Y.; Hodgkiss, J. M.; Stubbe, J.; Nocera, D. G., Proton-coupled electron transfer: the mechanistic underpinning for radical transport and catalysis in biology. *Phil. Trans. R. Soc. B* **2006**, *361*, 1351-1364.

18. Ge, J.; Yu, G.; Ator, M. A.; Stubbe, J., Pre-steady-state and steady-state kinetic analysis of *E. coli* class I ribonucleotide reductase. *Biochemistry* **2003**, *42*, 10071-10083.

19. Yokoyama, K.; Uhlin, U.; Stubbe, J., A hot oxidant, 3-NO_2Y_{122} radical, unmasks conformational gating in ribonucleotide reductase. *J. Am. Chem. Soc.* **2010**, *132*, 15368-15379.

20. Seyedsayamdost, M. R.; Xie, J.; Chan, C. T. Y.; Schultz, P. G.; Stubbe, J., Site-specific insertion of 3-aminotyrosine into subunit of $\alpha 2$ of *E. coli* ribonucleotide reductase: direct evidence for involvement of Y_{730} and Y_{731} in radical propagation. *J. Am. Chem. Soc.* **2007**, *129*, 15060-15071.

VITA

ADAM R. OFFENBACHER

OFFENBACHER was born in Lima, Ohio. He attended public schools in Elida, Ohio and received a B.S. in Biochemistry with High Distinction from Ohio Northern University, Ada, Ohio in 2005 before coming to Georgia Tech to pursue a doctorate in Chemistry. When he is not working on his research, Mr. Offenbacher enjoys spending time with his dog, Petey, woodworking, cooking, riding motorcycles, and playing soccer, paintball or racquetball.